

Optical Feedback System for Smart Laserosteotome

Inaugural dissertation

to

be awarded the degree of Dr. sc. med.

presented at

the Faculty of Medicine

of the University of Basel

by

Hamed Abbasi

from Tehran, Iran

Basel, 2020

Original document stored on the publication server of the University of Basel
edoc.unibas.ch

Approved by the Faculty of Medicine

on application of

Prof. Dr. Azhar Zam, University of Basel, *First examiner*

Prof. Dr. Philippe C. Cattin, University of Basel, *Second examiner*

Prof. Dr. Raphael Guzman, University Hospital Basel, *Further advisor*

Prof. Dr. Conor L. Evans, Harvard Medical School, *External expert*

Basel, 14th December 2020

Prof. Dr. Primo Leo Schär

Dean

To my parents, Fatemeh, and Mohammad.

Contents

List of acronyms and abbreviation.....	vii
Acknowledgments	xiii
Summary.....	xiv
Zusammenfassung.....	xv
Chapter 1: Introduction	1
1.1 Motivation.....	2
1.2 Contribution.....	2
1.3 Outline	3
Chapter 2: Background	5
2.1 Medical background.....	6
2.2 Physical and technical background	7
2.2.1 Laser-tissue interaction	7
2.2.2 Optical feedback methods for tissue analysis	11
2.2.3 Laser-induced breakdown spectroscopy (LIBS).....	12
Chapter 3: Differentiating bone from surrounding soft tissues using laser-induced breakdown spectroscopy (LIBS).....	18
3.1 Plasma plume expansion dynamics in a nanosecond Nd:YAG laserosteotome	19
3.2 Differentiation of femur bone from surrounding soft tissue using laser-induced breakdown spectroscopy as a feedback system for smart laserosteotomy	28
Chapter 4: Monitoring laser-induced thermal damage during laserosteotomy: Using LIBS to detect carbonization and dehydration	38
4.1. Effect of cooling water on ablation during Er:YAG laserosteotomy of hard bone	39
4.2 Laser-induced breakdown spectroscopy as a potential tool for auto carbonization detection in laserosteotomy	45
4.3. Pilot ex vivo study of laser-induced breakdown spectroscopy to detect bone dehydration: An approach for irrigation feedback in laserosteotomy	54
Chapter 5: Real-time closed-loop tissue-specific laserosteotomy.....	59
5.1. Combined Nd:YAG and Er:YAG lasers for real-time closed-loop tissue-specific laser osteotomy.....	60
5.2. A simple acoustic-cased method for lens-to-sample distance adjustment in μ LIBS.....	79
Chapter 6: Development of miniaturized laser-induced breakdown spectroscopy (mini-LIBS) probe for endoscopic smart laserosteotomy.....	81

6.1. Simulation of Echellogram using Zemax OpticStudio and Matlab for LIBS	82
6.2. Highly flexible fiber delivery of high peak power nanosecond Nd:YAG laser beam for flexiscopic applications	91
6.3. All-fiber-optic LIBS system for tissue differentiation: A prospect for endoscopic smart laser surgery	110
Chapter 7: Discussion and conclusion	120
7.1 Discussion.....	121
7.2 Future Work	122
7.3 Conclusion.....	123
Appendix I:	124
Appendix II:	127
List of peer-reviewed publications and presentations on the Ph.D. topic.....	131
Curriculum Vitae	135
Bibliography	136

List of acronyms and abbreviation

1D:	one dimensional
2D:	two dimensional
A:	aperture
AN:	air nozzle
Ar:	argon
AUC:	area under curve
BD:	beam dump
BP:	beam profiler
BS:	beam shaper
C:	carbon
C ₂ :	carbon to carbon bonding
Ca:	calcium
CARS:	coherent anti-Stokes Raman scattering
CCD:	charged coupled device
CF-LIBS:	calibration-free laser-induced breakdown spectroscopy
CL:	collimating lens
Cl:	chlorine
cm:	centimeter
CN:	carbon to nitrogen bonding
CNN:	convolutional neural network
CO ₂ :	carbon dioxide
CT:	computed tomography
CV:	cross-validated
CW:	continuous wave
DFA:	discriminant function analysis
DH:	deuterium-halogen

DM:	dichroic mirror
DOE:	diffractive optical element
DRS:	diffuse reflectance spectroscopy
EESI-MS:	extractive electrospray ionization mass spectrometry
EFL:	effective focal length
EM:	energy meter
Er:YAG:	erbium-doped yttrium aluminium garnet (Er:Y ₃ Al ₅ O ₁₂)
Er,Cr:YSGG:	erbium, chromium-doped yttrium, scandium, gallium and garnet
ETFE:	ethylene tetrafluoroethylene
F:	fluorine
FBG:	fiber Bragg grating
Fe:	iron
FEL:	free-electron laser
FFPE:	formalin-fixed paraffin-embedded
FL:	focusing lens
FO-LIBS:	fiber-optic laser-induced breakdown spectroscopy
FoV:	field of view
fs:	femtosecond
FSR:	free spectral range
FWHM:	full width at half maximum
GPa:	gigapascal
GUI:	graphical user interface
GW:	gigawatt
H:	hydrogen
HgAr:	mercury-argon
Ho:YAG:	holmium-doped yttrium aluminum garnet
Hz:	hertz
ICCD:	intensified charged coupled device

IL:	imaging lens
IR:	infrared
K:	potassium
KNN:	k-nearest neighbors
Kr:	krypton
KW:	kilowatt
Laser:	light amplification by stimulated emission of radiation
LIBS:	laser-induced breakdown spectroscopy
LIDT:	laser-induced damage threshold
LIPS:	laser-induced plasma spectroscopy
LTE:	local thermal (thermodynamic) equilibrium
LTSD:	lens-to-sample distance
LWIR:	longwave infrared
M:	mirror
mBR:	minimum bending radius
MCP:	microchannel plate
MEMS:	micro-electro-mechanical systems
Mg:	magnesium
min:	minute
MIR:	mid-infrared
MIRACLE:	Minimally Invasive Robot-Assisted Computer-guided LaserosteotomE
MIS:	minimally invasive surgery
mJ:	millijoule
mL:	milliliter
mm:	millimeter
MP:	moving plate
MR:	magnetic resonance
MS:	mass spectrometry

ms:	millisecond
MW:	megawatt
N:	nitrogen
NA:	numerical aperture
Na:	sodium
ND:	natural density filter
Nd:Glass:	neodymium-doped glass
Nd:YVO ₄ :	neodymium-doped yttrium orthovanadate (Nd:Vanadate)
Nd:YAG:	neodymium-doped yttrium aluminum garnet (Nd:Y ₃ Al ₅ O ₁₂)
Ne:	neon
NIR:	near infrared
NIST:	national institute of standards and technology
ns:	nanosecond
O:	oxygen
OAP:	off-axis parabolic
OD:	optical density
OES:	optical emission spectroscopy
OCT:	optical coherence tomography
OPO:	optical parametric oscillator
OR:	operating room
PbSe:	lead selenide
PC:	personal computer
PC:	principal component
PCA:	principal component analysis
PIV:	particle image velocimetry
PMT:	photomultiplier tube
ps:	picosecond
PZE:	piezo-electric

Q-SVM:	quadratic support vector machine
REIMS:	rapid evaporative ionization mass spectrometry
ROC:	receiver operating characteristic
RPE:	retinal pigment epithelial
s:	second
SD:	standard deviation
SHG:	second harmonic generator
SNR:	signal-to-noise ratio
SP:	stationary plate
SPL:	sound pressure level
Sr:	strontium
SRLIBS:	spatial-resolved laser-induced breakdown spectroscopy
SS-OCT:	swept-source optical coherence tomography
SVM:	support vector machine
TC:	thermal camera
T _e :	electron temperature
T _g :	general gas temperature
Ti:Sapphire:	titanium-sapphire (Ti:Al ₂ O ₃)
TIR:	total internal reflection
Tm:YAG:	thulium doped yttrium aluminum garnet
Tm:YAP:	thulium-doped yttrium aluminum perovskite
TRLIBS:	time-resolved laser-induced breakdown spectroscopy
TS:	translation stage
TTL:	transistor–transistor logic
um:	micrometer (micron)
us:	microsecond
UV:	ultraviolet
VIS:	visible

Yb:KYW: ytterbium-doped potassium yttrium tungstate
Yb:Glass: ytterbium-doped glass
Yb-doped: ytterbium-doped
Zn: zinc
 μ LIBS: micro laser-induced breakdown spectroscopy

Acknowledgments

Carrying out this study was only possible due to the contribution and cooperation of a number of people. I would like to take this opportunity to acknowledge them.

First and foremost, I would like to express my sincere gratitude to my first thesis advisor, Prof. Dr. Azhar Zam, for the opportunity to work on this thesis with the Biomedical Laser and Optics Group (BLOG). It was very exciting to work on such an interesting project with BLOG. I learned about biomedical optics from Azhar, both in his course and also through our weekly meetings. Azhar's door was always open, even for daily discussion. I appreciate the time and the energy he spent on this thesis. I am also thankful to my second thesis advisor, Prof. Dr. Philippe C. Cattin. Philippe helped me regarding the required signal processing and data analysis. I learned about state-of-the-art machine learning methods from Philippe, both from his course and also from our monthly meetings. Moreover, I am very grateful to Prof. Dr. Raphael Guzman, another advisor of this thesis, who guided me from a medical point of view. I appreciate the time that he spent during our meetings, despite his busy schedule. Raphael, a surgeon, guided me towards developing a device that would be intuitive and useful for the potential end-users (surgeons). In addition, I would like express gratitude to Prof. Dr. Georg Rauter. For part of the project, we worked together and shared equipment. Thanks to the opportunity to attend international conferences/schools, I was able to meet great researchers in the field, extend my network, and get inspired by my discussions with them. I appreciate those who helped me find the answers to my questions and gave me great ideas, especially Prof. Dr. Steven Jacques from the University of Washington. It was my pleasure to meet, discuss, and learn from Steven.

I would like to acknowledge Prof. Dr. Conor L. Evans from Harvard University for kindly being the external expert/examiner of this thesis and evaluating this doctoral thesis. A great thanks also goes to Prof. Dr. Pablo Sinues, for chairing the defense. Additionally, I gratefully acknowledge funding from the Werner Siemens Foundation through the Minimally Invasive Robot-Assisted Computer-guided Laserosteotome (MIRACLE) project.

For more than four years, I worked in the department of biomedical engineering (DBE) under the flagship project of the department, MIRACLE. There, I enjoyed working with other students, interns, postdoctoral research associates, and other colleagues from different groups, especially from BLOG (former and current members). Thank you all for the pleasant atmosphere in our working area. We shared facilities, labs, workshop, kitchen, dining area, classrooms, and so on. I enjoyed working in a multidisciplinary area while learning from all my colleagues, especially through our journal club, summer/winter school, retreat, and other meetings. The chance to work directly with a few master students gave me experience, joy, and additional insights, thanks to Antoine, Negin, and Matin.

Last but not least, I would like to sincerely thank my friends and family for their generous support and never-ending motivation during my Ph.D.

Summary

Compared to traditional mechanical tools for bone cutting (osteotomy), laser offers several benefits, including functional cutting geometry (high axial and lateral resolution), contactless interaction without pushing (no momentum), reduced trauma, and consequently, accelerated healing. While pre-operative planning can help point the laser beam in the right direction, lack of real-time feedback about the type of tissue being cut risks iatrogenic damage due to body/laser movement or any other unexpected error. Therefore, real-time feedback during laserosteotomy is essential in order to avoid damage to adjacent soft tissues. Equally vital is the ability to monitor laser-induced thermal damage in order to control the irrigation system used for rehydrating and cooling down the tissue during laserosteotomy. Laser-induced thermal damage (e.g., carbonization) can slow down the cutting procedure and prolong the healing process. In this thesis study, an optical feedback mechanism based on laser-induced breakdown spectroscopy (LIBS) was developed to serve as a powerful label-free method for elemental analysis. For this purpose, a custom-made, high-resolution, broadband Echelle spectrometer with high optical throughput was developed. The portable LIBS system, coupled with multivariate spectrochemical analysis, was able to differentiate bone from its surrounding soft tissue (namely, bone marrow, muscle, and fat) and to detect laser-induced thermal damage — both with high accuracy in a single-shot measurement without any sample preparation. The feedback system was integrated into an efficient bone cutting system and was tested in a real-time closed-loop manner, to stop the ablation laser when it encountered the adjacent soft tissues that should be preserved, *in situ*. In the end, the system was miniaturized by delivering the high peak power laser beam through a highly flexible bend-insensitive fiber system with a tiny half-ball lens at the tip. The same optical fiber system was used to collect plasma emissions and transfer them to the spectrometer for analysis. The all-fiber LIBS system developed provides a stand-alone miniaturized feedback mechanism suitable for intraoperative tissue characterization in a minimally-invasive endoscopic procedure. This thesis study was part of the MIRACLE (Minimally Invasive Robot-Assisted Computer-guided LaserosteotomE) project, which aims to develop a robotic endoscope to perform laser-based, contact-free bone surgery.

Zusammenfassung

Im Vergleich zu herkömmlichen mechanischen Werkzeugen zum Knochenschneiden (Osteotomie) bieten Laser mehrere Vorteile, einschließlich funktioneller Schnittgeometrie (hohe axiale und laterale Auflösung), kontaktlose Interaktion ohne Druck (kein Impuls), reduziertes Trauma und folglich beschleunigte Heilung. Während die präoperative Planung dazu beitragen kann, den Laserstrahl in die richtige Richtung zu lenken, besteht bei fehlender Echtzeit-Rückmeldung zu Art und Charakteristik des zu schneidenden Gewebes die Gefahr einer iatrogenen Schädigung aufgrund von Bewegungen zwischen Körper und Laser oder anderen möglichen unvorhergesehenen Fehlern. Daher ist eine Echtzeit-Rückmeldung bei der Laserosteotomie unerlässlich, um Schäden an benachbarten Weichteilen zu vermeiden. Da laserinduzierte thermische Schäden (z. B. Karbonisierung) den Schneidvorgang verlangsamen und den Heilungsprozess verlängern können, ist die Überwachung der laserinduzierten thermischen Schäden von entscheidender Bedeutung um das Spülsystem zu steuern, das zur Rehydratisierung und Abkühlung des Gewebes während der Laserosteotomie verwendet wird. In dieser Dissertation wurde ein optischer Rückkopplungsmechanismus basierend auf laserinduzierter Durchbruchspektroskopie (LIBS) als markerfreie und leistungsstarke elementare Analysemethode entwickelt. Zu diesem Zweck wurde ein maßgeschneidertes, hochauflösendes Breitband-Echelle-Spektrometer mit hohem optischen Durchsatz entwickelt. Das entwickelte tragbare LIBS-System konnte in Verbindung mit einer multivariaten spektrochemischen Analyse Knochen vom umgebenden Weichgewebe, nämlich Knochenmark, Muskel und Fett, unterscheiden und laserinduzierte thermische Schäden mit hoher Genauigkeit bei der Einzelschussmessung erkennen, ohne jegliche Probenvorbereitung. Das Rückkopplungssystem wurde in ein effizientes Knochenschneidsystem integriert und in Echtzeit in einem geschlossenen Regelkreis getestet um den Ablationslaser zu stoppen, sobald dieser auf benachbarte, zu bewahrende Weichteile trifft. Am Ende wurde das System miniaturisiert, indem der Laserstrahl mit hoher Spitzenleistung durch ein hochflexibles, biegeunempfindliches Fasersystem und eine winzige Halbkugellinse an dessen Spitze abgegeben wurde. Das gleiche optische Fasersystem wurde verwendet, um die Plasmaemission zu sammeln und zur Analyse auf das Spektrometer zu übertragen. Das entwickelte All-Fiber-LIBS-System bietet einen eigenständigen miniaturisierten Rückkopplungsmechanismus, der für die intraoperative Gewebecharakterisierung in einem endoskopischen minimalinvasiven Verfahren geeignet ist. Diese Dissertation war Teil des Projekts MIRACLE (kurz für Minimally Invasive Robot-Assisted Computer-guided LaserosteotomE) mit dem Ziel, ein Roboterendoskop für die laserbasierte kontaktfreie Knochenchirurgie zu entwickeln.

Chapter 1: Introduction

1.1 Motivation

Archeological studies reveal that the earliest evidence of bone-cutting (osteotomy) comes from Champ-Durand (France) and dates back to Neolithic times (3400-3000 BC) [1]. Since then, humans have achieved a high degree of mastery of surgical techniques, yet basic osteotomy tools have not been significantly improved. Instead, modern osteotomy tools are essentially powered versions of old-style instruments [2, 3]. Mechanical tools (e.g., burs, saws, and drills) are still commonly used for cutting bones. Due to the many side effects of using conventional osteotomy tools — e.g., mechanical vibrations, poor surface evenness, limited cutting geometry, high amount of heat production, potential contamination, and high material loss — alternative solutions are being sought. Lasers seem to be a perfect candidate for replacing conventional saws and drills in osteotomy procedures [3-9]. Comparative studies reveal that lasers could overcome the limitations of conventional tools, effectively ablate with significantly higher bone repair (i.e., accelerate early new bone formation) ratios than burs or piezo-electric (PZE) osteotomes [10-18].

Although lasers offer several benefits over traditional osteotomy tools, they pose a risk of causing collateral damage to the neighboring tissues if feedback about the type of tissue being cut is not provided. Likewise, to avoid laser-induced thermal damage to the tissue, it is vital to use a cooling system and to have sufficient feedback for monitoring thermal damage [19]. In order to avoid such damages, several approaches have been developed based on the optical properties of the ablated tissues. Optical methods include laser-induced breakdown spectroscopy (LIBS) [20-26], diffuse reflectance spectroscopy (DRS) [27-32], Raman spectroscopy [32-36], autofluorescence spectroscopy [37, 38], optical coherence tomography (OCT) [39, 40], speckle analysis [41-43], shockwave measurement [44, 45], combustion/pyrolysis light analysis [46-48], and random lasing [49]. While extensive research has been carried out on this topic, none of the studies mentioned could simultaneously fulfill the complete set of requirements for a minimally-invasive laserosteotomy feedback mechanism. These requirements include the ability to differentiate bone from its surrounding tissues and monitor laser-induced thermal damages in real-time, the ability to work in a closed-loop fashion in combination with an efficient ablation laser, and the possibility to be inserted inside the narrow channel of a flexible endoscope for non(semi)-destructive, minimally-invasive tissue monitoring.

The aim of this thesis research was to offer a method capable of providing optical feedback on the type and characteristics of the tissue being cut during laser bone surgery. The method should be able to differentiate bone from its surrounding tissues, detect different levels of laser-induced thermal damage (dehydration and carbonization), function in a non(semi)-destructive way, and allow for miniaturization.

1.2 Contribution

By the time that this project had started, a few studies had been conducted using LIBS (the method chosen to provide optical feedback for this thesis work), with the aim of providing feedback to differentiate bone from other tissues. The studies were mainly carried out by a research group in

Friedrich-Alexander-Universität Erlangen-Nürnberg [20-24]. Their investigations showed the potential of using LIBS to differentiate bone from other soft tissues, namely muscle, fat, skin, nerve, mucosa, liver, tendon, as well as cartilage. The studies covered differentiation between all soft tissues surrounding bone, except bone marrow. To the best of my knowledge, research on the use of LIBS for monitoring thermal damage had not been done. Therefore, I opted to examine the use of LIBS to differentiate bone from its surrounding soft tissues (including bone marrow) and to detect laser-induced thermal damage (dehydration and carbonization). It is worth mentioning that the previous LIBS studies had been performed using commercially available spectrometers (general purpose). Therefore, a custom-made, high-resolution, high-throughput Echelle spectrometer was developed in order to optimize performance for the dedicated application and to reduce costs. None of the previously published manuscripts reported combining or integrating a closed-loop feedback mechanism within an efficient ablation system. Therefore, the real-time, closed-loop feedback process developed here was integrated into an efficient Er:YAG ablation system. Last but not least, the laser beam was transmitted using a flexible fiber delivery system, which to the best of my knowledge, provides the most flexible fiber delivery system, capable of tolerating peak power levels for nanosecond pulses.

1.3 Outline

This thesis comprises six chapters. Following this introductory chapter, Chapter 2: Background explains the medical basis of the thesis research, and the physical and technical principles underlying the instruments and methods developed. Chapters 3 to 6, present publications arising from this thesis research; each section starts with a brief introduction regarding the state of the art and motivation of the work, followed by the publication. Chapter 3: Tissue Differentiation presents two conference proceeding publications; in the first, the dynamic of laser-driven plasma over time is explored [50], and in the second, a time-resolved LIBS is carried out to differentiate bone from its surrounding tissues [51]. Chapter 4: Thermal Damage Monitoring presents publications arising from this thesis work related to detecting dehydration and carbonization. It starts with a conference proceeding publication that shows the importance of cooling water in laserosteotome [52], and continues with a peer-reviewed journal publication demonstrating the possibility of using LIBS for detecting carbonization [53]. The chapter concludes with a conference proceeding publication that shows the applicability of LIBS for differentiating fresh bone from dehydrated bone [54]. The studies presented in chapters 3 and 4 were conducted in “offline mode”, meaning that the data was collected and stored on a PC, and analyzed afterward. Chapter 5: Closed-Loop Operation presents a peer-reviewed journal publication describing the combination of a low-energy Nd:YAG laser for tissue differentiation and high-energy Er:YAG laser for efficient ablation [55]. Tissue differentiation was performed in a real-time and closed-loop fashion, thanks to a mechanical shutter that blocked the Er:YAG beam path when it encountered a tissue to be preserved. In this study, the energy of the Nd:YAG laser was reduced so as not to ablate non-target tissues. The method, known as laser-induced breakdown thresholding, provided a non-destructive, real-time, closed-loop tissue differentiation mechanism. The chapter ends with a short conference proceeding publication that introduces a method for lens-to-sample distance adjustment while

using a low-energy Nd:YAG for plasma formation [56]. Chapter 6: Miniaturization includes a conference proceeding paper published as a book chapter, and two peer-reviewed journal publications [57-59]. The book chapter presents a simulation for designing a tailor-made Echelle spectrometer dedicated to the specific application of this thesis work. The journal publications present the process of instrumenting the designed spectrometer and a flexible fiber delivery system for transmitting high power Q-switched laser pulses, together with performing fiber optic LIBS for tissue differentiation. The thesis concludes with a discussion and conclusion in Chapter 7. Information about the author, as well as a list of relevant publications and presentations can be found at the end of the thesis.

Chapter 2: Background

2.1 Medical background

Bone has three functions in the human body: protecting vital organs (such as brain and bone marrow), regulating mineral homeostasis, and providing mechanical support for locomotion [60]. Any abnormality in the feature or shape of a bone in the body might limit or prevent the bone's functionality. To correct such abnormalities, surgery, including bone cutting, might be required. Osteotomy, defined as the surgical cutting of bone, is a routine orthopedic procedure. Osteotomy is also applied in the field of cranio-maxillofacial surgery, neurosurgery, otolaryngology, traumatology, and spinal column surgery [4-6]. To cut bone efficiently, it is necessary to know its composition and its properties (physical, thermal, mechanical, etc.). Bone's primary composition includes collagen, water, and a bioceramic similar to hydroxyapatite ($\text{Ca}_{10}(\text{PO}_4)_6(\text{OH}_2)$), which forms concentric lamellar structures known as osteons [4]. Bone is a calcified tissue composed of approximately 60% inorganic components (primarily crystalline hydroxyapatite), 27–30% organic components (30 proteins, with type I collagen being the most abundant at >90%), and 10–13% water [60, 61]. By volume, the inorganic constituents account for about 40% of the tissue, while the organic components make up approximately 35%. The remaining 25% is due to the presence of water in the bone. By weight, the inorganic components, the organic components, and water account for roughly 60%, 30%, and 10%, respectively [60]. The difference between the volume and weight ratios is explained by the different densities of the components of the bone. Also, the properties of the bone itself differ from cortical to cancellous bone. The density of cortical bone is 1800–2000 kg/m^3 , while that of cancellous bone is reportedly 300–975 kg/m^3 . The modulus and the strength of bone differ between the cortical and cancellous parts. While the specific heat capacity of both cortical and cancellous bone is within the range of 1100–1260 J/kg.K , cortical bone has greater thermal conductivity (0.41–0.63 vs. 0.12–0.31 W/m.K) [62]. Cortical bones form approximately 80% of the human skeleton, while the remaining 20% comprises cancellous bones [63]. Bone composition is similar to that of enamel and dentine, and is likewise considered to be a hard tissue [64]. Hard materials are more challenging to cut than soft tissues, which can be cut by a scalpel alone. Initially, mechanical tools similar to those used for cutting other hard materials (metals, wood, stone, etc.) were used to cut bone as well. Traditional mechanical tools (e.g., saws, chisels, and drills) used for bone cutting — the gold standard in osteotomy for thousands of years — are operated manually and require a certain degree of mechanical force to function, such as grinding or hammering [65]. Thanks to the force provided by electric motors, traditional manual mechanical tools gave way to electric ones over the past centuries. Electric saws and drills help surgeons to cut the bone more precisely, with less effort and in a shorter time. However, as electric saws and drills still employ a mechanical force (contact mode cutting), many of the disadvantages of mechanical tools remained unchanged (e.g., high chance of contamination, metal abrasion, bone fragmentation, and thermal damage). Saws and drills can also create an amorphous, mineral-rich carbon layer on the bone surface and change the mineralized matrix, which leads to a prolonged healing process [66, 67]. Several non-traditional techniques for osteotomy have been proposed and examined over the last few decades, including machining based on microwave, ion beam, ultrasonic, PZE, and water jet [3]. Some of these techniques improved performance by reducing bleeding and requiring less frequent tool sterilization. While some of the limitations of

traditional machining tools were overcome, other new issues and restrictions arose (e.g., the need for a vacuum during ion beam machining and the dangers posed to surgeon and patient while using hazardous microwave radiation) [62]. Water jet and PZE tools were more promising. By cooling down the tissue while cutting, water jets reduce thermal damage [68]. However, optimizing machining parameters is a challenge due to deviation of the water jet while machining, and the chances of breaking or moving the bone are high, particularly for thin bone segments, such as those close to the mandible [3]. Laser beams do not deflect while traveling and do not carry momentum. Momentum is defined as the mass of the object times the velocity of the object. Photons have no mass; thus laser light does not carry momentum and interacts with materials without pushing them, in a contactless manner. Without pushing, body movements during surgery are minimized and, as a result, an intraoperative image guidance system can perform with less error. Several studies have compared the performance of laserosteotomy, traditional mechanical tools, and PZE bone cutting tools. Laser beams offer high spatial resolution (both axial and lateral), allowing for a high degree of freedom when cutting. This freedom offers major advantages in surgeries, especially oral and maxillofacial surgery, and when an implant is used to replace part of the bone. Microstructural analysis (e.g., micro-computed tomography (CT) and histological examinations) showed that more new mineralized bone formed after cutting bone with laser than after cutting bone with PZE [17]. Accelerated healing is also reported for laserosteotomy [14]. In one animal study, radiological and histological examinations revealed primary gap healing in sheep two months post-laserosteotomy, and almost no visible osteotomy gap after three months [18]. Laserosteotomies are assisted by computers and robots to provide better control based on a patient-specific, pre-planned program largely derived from CT and magnetic resonance (MR) images. While preplanning can direct the laser to the required area, a lack of real-time monitoring risks iatrogenic damage due to body movement or any other possible unpredicted error. Therefore, real-time feedback is vital in laserosteotomy to avoid any damage to adjacent bone and surrounding soft tissues. Miniaturization of the system would allow for minimally invasive surgery using endoscopes. This thesis research was conducted as part of the MIRACLE project [69], which aims to develop a robotic endoscope to perform contact-free bone surgery with laser light.

2.2 Physical and technical background

2.2.1 Laser-tissue interaction

Although it took almost half a century to experimentally demonstrate the idea of coherent light stimulation [70], a year after this demonstration [71], the first medical application of laser was reported in 1961 [72]. In that instance, a pulsed ruby laser with a peak power of 200W (100mJ/500us) was used to burn retinal tissue in a rabbit. In this ophthalmological application, the laser created a hot zone on the tissue to yield a photothermal interaction.

Depending on the applied energy, spot size, and pulse duration of a laser, different phenomena may occur when the laser interacts with biological tissues [73-75]. When a pulsed laser interacts with the tissue, there might be a nonlinear absorption of the light; thus, the type of interaction can be changed quickly by changing the parameters of the laser [76]. A laser-tissue interaction map

explains the underlying principle of the work. The laser-tissue interaction map was initially introduced by J. Boulnois in 1986 [77]. Later, this map was reproduced and modified on different occasions by other researchers [73, 78, 79]. Due to limited access to ultra-short laser pulses, the initial map included four main phenomena, namely: (I) photochemical (mainly for CW lasers only), (II) photothermal (including coagulation, vaporization, carbonization, and melting), (III) photoablative, and (IV) photomechanical (electro-mechanical). Basically, the different phenomena are the result of laser energy converting to different kinds of energy: chemical, thermal, and mechanical [80]. In most of the recently reproduced maps, the electro-mechanical section (using short and ultra-short laser pulses) is divided into two parts: photodisruption and plasma-induced ablation (it should be noted that there is no consensus on that particular terminology, and other terms are also used). In both photodisruption and plasma-induced ablation, the tissue is ionized, and a localized plasma from the tissue material is produced at the ablation zone (breakdown). The difference is the higher impact of mechanical effects in photodisruption (the term disruption originates from the Latin word “ruptus”, meaning ruptured) [79]. Mechanical effects produce shockwaves (high-pressure gradients moving at supersonic speed at the shock front) in all tissues, cavitation (explosive vaporization involving negative tensile waves that disrupt a material, causing successive expansion and collapse due to strong compression of water and carbon oxides) in soft tissues, and jet formation (only in fluids) near a solid boundary during collapse from cavitation [81, 82]. Figure 1 offers a representation of the laser-interaction map from [79].

The exact interaction mechanism a tissue will undergo depends on several laser parameters; these include pulse duration and applied power density, the two main parameters in the two-dimensional Laser-tissue interaction map. Moreover, tissue properties like absorption, transmission, scattering, reflection (all wavelength-dependent), heat conduction, heat capacity, and tissue density also determine the type of interaction. The variety of optical and mechanical properties of different kinds of tissue widens the borders shown in Figure 1. This means that a specific laser parameter can lead to two different interactions for two different tissues. The optical breakdown formed by nanosecond pulses is always associated with a shock wave (for both hard and soft tissues) and cavitation (only for soft tissues) even at the very threshold. Electro-mechanical ablation generates relatively powerful thermoelastic tensile pressure, which can produce cavitation inside the irradiated medium; its amplitude is a function of the absorption coefficient of the medium and the power density of the applied laser beam [83]. Considering all the differences among the mechanical and physical properties of hard and soft tissues, the fact that cavitation (negative tensile pressure disruption) occurs only in soft tissues, and that up to one-fourth of the applied energy will be consumed in cavitation [79], higher energy is required to start the breakdown of soft tissues (different required dosimetry based on the tissue optics [84]) at specific pulse durations.

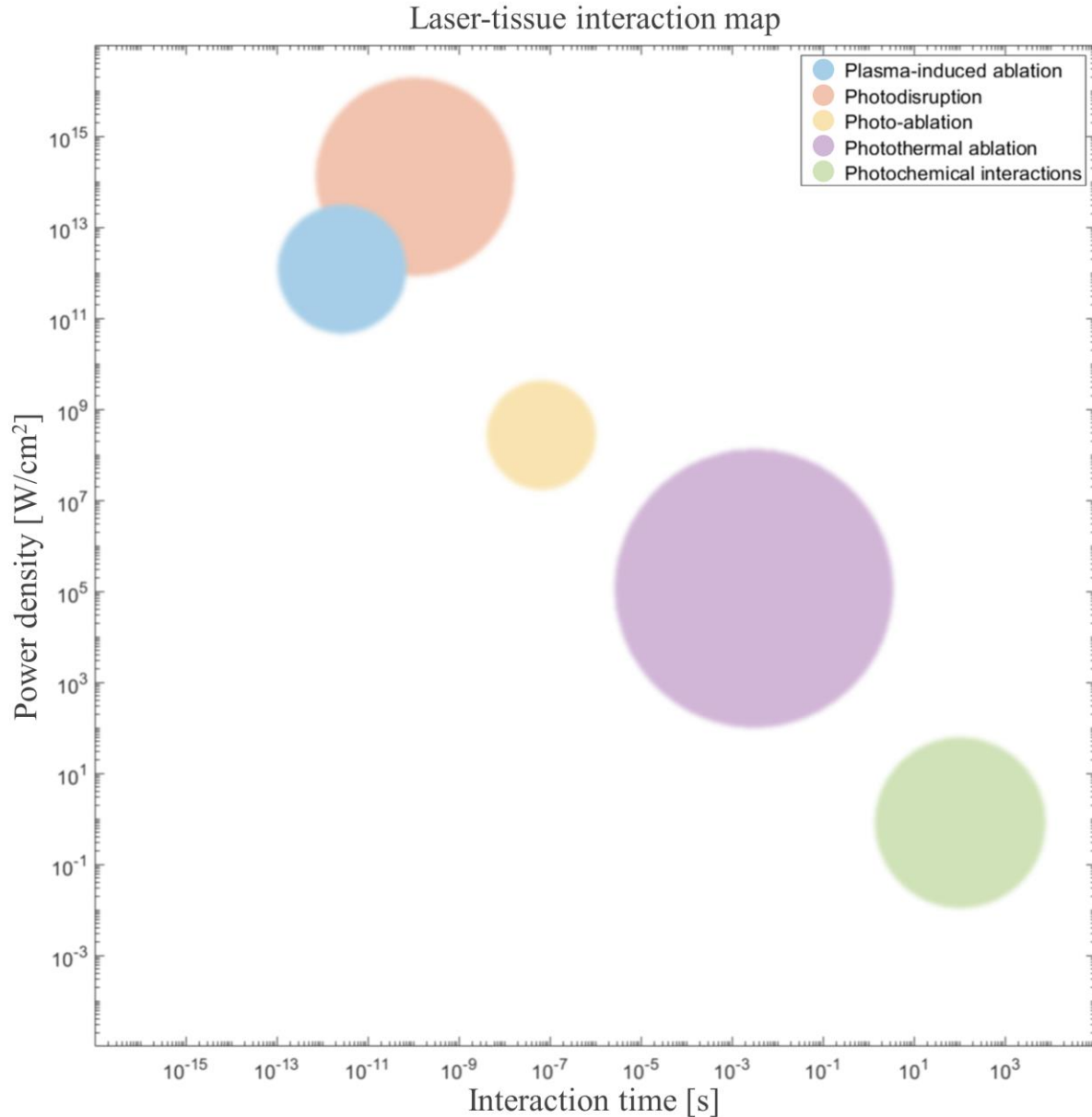


Fig. 1. Laser-tissue interaction map.

Short (ns) and ultra-short pulsed (ps-fs) laser ablation is associated with plasma formation. Monitoring the characteristics of this plasma provides some information about the material (please refer to Section 2.2.2, below). Therefore, these kinds of lasers are suited to providing monitoring feedback during the ablation process. More importantly, the ablation would be thermally confined, so thermal damage is less likely to occur. However, since a big portion of laser energy is used for plasma formation, not all of the energy contributes to ablation. Therefore, the ablation efficiency of short and ultra-short pulsed lasers is not as high as that of long-pulsed lasers. Consequently, in terms of ablation efficiency, lasers with a longer pulse duration are preferred for osteotomy [85]. Yet, if the pulse duration is longer than the thermal relaxation time of bone (typically below 80 μ s [86]), thermal damage is likely to occur [66, 87-89]. Moreover, spatial resolution in ultra-short laser

osteotomy is higher than with longer pulses [90]. Therefore, a laser with a pulse duration shorter than the thermal relaxation time of bone and long enough to avoid plasma formation would provide the fastest ablation, with less need for cooling [91]. Since such a laser is typically associated with low energy, a combination of high-energy laser (higher pulse duration) and an irrigation system (for cooling down the tissue) are preferred [92-95]. In addition to pulse duration, laser wavelength plays an important role in tissue optics, as the optical phenomena that occur in tissue (absorption, transmission, scattering, reflection) are wavelength dependent. Figure 2 shows the absorption coefficient of hydroxyapatite and water (together, around 70% of bone composition). The wavelength of the lasers most commonly used for osteotomy are marked in the figure as well, namely, the Yb-doped fiber laser, Nd:Vanadate Nd:YVO4/Nd:YAG (first and second harmonics at 1064 nm and 532 nm) [96-102]; the Ti:Sapphire at 800 nm [90, 98, 103-105] (alternatively 775 nm [13, 106] or 1053 nm [107]); the fiber femtosecond laser at 1030 nm [23] (the Yb:KYW at 1030 nm [108, 109], the Nd:Glass at 1054 nm [110] and the Yb:Glass laser at 1040 nm [98, 111] provide similar wavelengths, 1027 nm exists as well [112]); the Ho:YAG laser at 2120 nm [113, 114] (Tm:YAG and Tm:YAP lasers provide similar wavelengths and can be used for osteotomy as well [115, 116]); the Er,Cr:YSGG laser at 2780 nm [117-120]; the Er:YAG at 2940 nm [8-10], free-electron laser (FEL) at 6100 nm and 6450 nm [121]; and finally the CO₂ laser at 9300 nm, 9600 nm and 10600 nm [122-125].

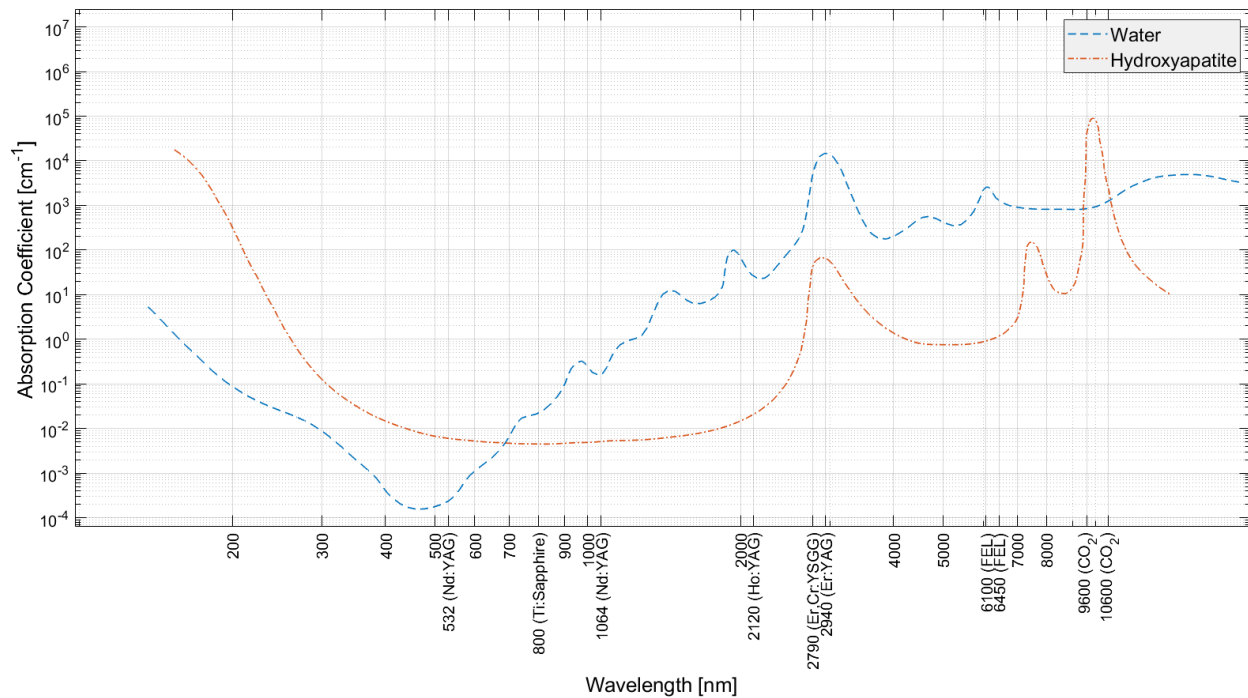


Fig.2. Absorption coefficient of hydroxyapatite and water at different wavelengths, representation from [64].

As shown in Fig. 1, the highest absorption peaks of water and hydroxyapatite are at 3,000nm and 10,000nm. Consequently, Er:YAG and CO₂ lasers with peaks around these wavelengths are readily absorbed by bone and, accordingly, achieve higher ablation efficiency, compared to other

wavelengths. The Er:YAG laser is often preferred over the CO₂ gas laser with a bigger cavity (bigger size). The Nd:YAG/YVO₄ laser is also widely used in osteotomy, since water is transparent to its wavelength (particularly frequency-doubled Nd:YAG at 532 nm); therefore, it can be used to ablate under water [99, 100, 126]. Since ablation is a threshold-based phenomenon, the spot size of the laser beam on the bone plays a key role as well. Spot size defines the fluence (peak energy density) and irradiance (peak power density) of the laser beam. Thus, the spot size on the bone surface should be adjusted in a way that fulfils the threshold condition. Spot size can be altered by utilizing lenses with different focal lengths. The focusability of the laser beam (defined by M² of the laser) influences spot size as well. It is worth mentioning that a smaller spot size is typically preferred, since it creates a smaller gap during ablation, resulting in less mass removal, and consequently, faster bone healing after surgery. Smaller spot sizes are achieved by using short focal length lenses, which result in a shorter Rayleigh length, which in turn limits the depth of focus. Hence, a tradeoff between spot size and Rayleigh length must be considered. A more detailed discussion of the types and properties of lasers in osteotomy can be found in a book chapter [5], not included in this thesis.

2.2.2 Optical feedback methods for tissue analysis

As mentioned previously, it is vital to monitor the tissue being cut during surgery [127-129]. Several methods have been introduced to either differentiate tissues from each other (like differentiating bone from surrounding soft tissues) or to detect some characteristics of the tissue (like detecting cancerous parts of the tissue) with the goal of using the information collected as a feedback mechanism during surgical interventions. Feedback methods can be categorized as contact and noncontact. In contact methods, the sensor itself or the part that collects data for the sensor is attached to the tissue. In noncontact methods, data is collected from a distance. The disadvantage of contact methods is the risk of contamination. Contact feedback methods include using PZE accelerometers (to detect vibrations) [46-48, 130], bioimpedance sensing [131-137], and DRS [27-32], among others. The advantage of DRS is that it collects information from both the surface tissue and the layer behind it, since the reflected spectrum comes from diffused scattered light inside the tissue. The penetration depth (wavelength-dependent) can reach the millimeter range, and is typically equal to the distance of two embedded fibers in the probe. Contact feedback methods are suitable for monitoring a contact tissue cutting method. DRS, for example, is typically connected to an electrosurgical knife [138-143]. However, DRS can be used in a noncontact mode, as well [28, 29, 144, 145]. Electrical monitoring (voltage-current measurements) is another way to provide information about the tissue under the cut during electrosurgery with electric scalpels [146, 147]. Note that electrosurgical knives can cut soft tissues only. Optical emission spectroscopy (OES) of the plasma generated at the tip of the electric scalpel is an alternative way of monitoring the tissue under the cut during the surgery, and is considered to be a noncontact method [146-150]. Analyzing the smoke (also known as surgical ablation plume/vapor/debris/aerosol) produced during electrosurgery has also been proposed as a means of tissue identification, using differential ion mobility spectrometry (DMS) [151, 152], extractive electrospray ionization mass spectrometry (EESI-MS) [153], and rapid evaporative ionization mass spectrometry (REIMS) [154-157]. Analyzing the smoke produced during laser ablation with a mass spectrometer has been reported as well

[158-163]. The device developed for the investigation was recently integrated into the da Vinci surgical system [164]. While the approach is an interesting one, the size of the sampling probe (0.3 to 1 cm) presents a challenge for endoscopic applications, especially considering that the probe sits alongside the optic used to transfer the required laser energy to the sample. Furthermore, the time-lapse between the onset of laser irradiation and the detection of ions by the MS instrument (0.4 to 1.5 s), as well as a delay for signal disappearance after deactivating the laser (3.5 to 7.9 s) [158] runs counter to the goal of a fast sampling rate. The delay due to droplet transfer time (1.7 to 8.9 s [164]), together with a long accumulation time in the ion trap (up to approximately half a second [158]), makes this device incompatible with the sampling rate of lasers typically used in laserosteotomy. Other noncontact feedback methods are combustion/pyrolysis light analysis [46-48], random lasing [49], OCT [39, 40], spectroscopic methods including LIBS [20-26], spontaneous Raman [32-36], and autofluorescence [37, 38], as well as acoustic-based monitoring methods that use a microphone/transducer [165-167], fiber Bragg grating (FBG) [166, 168], speckle analysis [41-43], Fabry-Pérot [44] and/or Mach-Zehnder interferometer [45]. Considering the fact that laserosteotomy is a noncontact optical tissue cutting method, a noncontact optical feedback method would be the most compatible. Of the optical feedback methods, autofluorescence, DRS, LIBS, and Raman are capable of providing label-free information regarding the chemical composition of the tissue being cut. Both LIBS and Raman offer extensive information about the characteristics of the tissue; the former provides mainly atomic information, while the latter provides molecular information. However, due to the low cross-section of Raman scattering, the integration required for spontaneous Raman spectroscopy is typically high (e.g., 5 s [32, 33] or 10 s [36]), which makes it unsuitable for real-time monitoring of tissue under the cut during laserosteotomy. Other Raman methods, like Kerr-gated time-resolved Raman spectroscopy [169, 170] and coherent anti-Stokes Raman scattering (CARS) [171-173], are recent fast-growing methods capable of providing information in a much shorter time; however, their experimental setup is bulky and costly. LIBS is a powerful analytical method, and was chosen to monitor laserosteotomy for this thesis work.

2.2.3 Laser-induced breakdown spectroscopy (LIBS)

History: A few years after the invention of the laser, the production of luminous plasma while using a laser was reported in 1962 [174-176]. Approximately, twenty years after the first observation, the technique of performing OES on laser-driven luminous plasma was dubbed LIBS (laser-induced breakdown spectroscopy) by Leon J. Radziemski and Tim R. Loree from the Los Alamos National Laboratories, New Mexico, USA [177, 178]. In the late 1980s, when the technique arrived in Europe, it was renamed LIPS (laser-induced plasma spectroscopy) [179]. This double denomination endured until the year 2000, when a decision was made to discontinue the acronym LIPS, in favor of the original name, LIBS, at the First International Conference on Laser-Induced Plasma and Applications, held in Pisa [179].

Fundamentals: Plasma, the fourth state of matter, is an ionized gas consisting of active particles, reactive species, and temporary fields (e.g., ions, electrons, free radicals, heat, acoustic waves, electromagnetic fields). Based on the thermodynamic equilibrium between ions and electrons,

plasma can be categorized as thermal (the electron temperature (T_e) equal to the general gas temperature (T_g), i.e., $T_e \approx T_g$) or nonthermal (i.e., $T_e \gg T_g$) [180-183]. In LIBS, ionization is induced by a focused short or ultra-short laser pulse (ns to fs). In LIBS plasma, the radiation is not at thermal equilibrium. Therefore, a LIBS plasma where all processes are at thermal equilibrium, except for the radiation, is said to be at local thermal (thermodynamic) equilibrium (LTE) [179, 184]. The plasma is at LTE when the radiative processes (responsible for energy loss in plasma) are negligible compared to collisional processes (responsible for the thermalization of the plasma). The excited species in laser-driven plasma emit radiation that grants information about the quantitative and qualitative properties of the material under the laser beam. By measuring the frequency/wavelength of the light emitted from the plasma, the chemical composition of the material under the laser beam is revealed [185, 186].

Working principle: LIBS is a powerful atomic analytical technique for real-time identification [187]. The setup is composed of a Q-switched or mode-locked laser; a high-resolution spectrometer, typically Echelle; and some optics to guide the light. After illuminating the sample with a focused laser pulse, a localized plasma is created. An optical setup (typically optical fiber) collects the light emitted from the plasma created and delivers it to the spectrometer. The collected spectrum includes some peaks, the intensity of which correspond to the chemical composition of the material under the laser beam [188]. Figure 3 shows a typical LIBS spectrum collected from a bone sample. By comparing the wavelength of the observed peaks with reference wavelengths, the presence of specific atoms in the material can be concluded. The most commonly used database for LIBS wavelengths is the Handbook of Basic Atomic Spectroscopic Data from the National Institute of Standards and Technology (NIST) [189]. By applying advanced chemometrics, even samples with a high degree of similarity can be differentiated. One of the big advantages of LIBS over other analytical techniques is that it requires minimal sample preparation; in most cases, the sample is put under the laser beam directly, without any preparation [187], making rapid analysis possible. LIBS can be applied to multiple sample states, solid, liquid, or gas. By adjusting the energy of the laser, plasma can be created and analyzed in all states of matter. The data acquisition time is very short (typically less than a millisecond), as is the data processing time (in the tens to hundreds of milliseconds range, depending on the applied algorithm and the power of the connected computer). LIBS works in the atmospheric environment, in contrast to many other analytical techniques that require a vacuum. The LIBS setup is robust, meaning that it can uphold its performance even during long-distance transport. For this reason, it has been largely used for on-site analysis. Even NASA has sent a LIBS system, the “ChemCam LIBS instrument”, to Mars for analysis, due to the robustness of the system during transport. The device has been operating on the Mars Curiosity Rover for more than 2700 sols (more than seven and a half terrestrial years) [179, 190].

Biomedical applications of LIBS: Given the high sensitivity of LIBS and its ability to detect trace elements, typically ppm as the limit of detection (LOD), it has been widely used for biological and medical investigations [191, 192]. For example, LIBS has been extensively employed for direct analysis of human blood serum [193, 194] and whole blood samples [195, 196]. Other biomedical

applications of LIBS include cancer diagnosis [197-199], trace element detection in biological tissues [200-202], cell and protein analysis [203-205], bioterrorism threat investigations [206, 207], and biological tissue analysis [208-210]. LIBS also has been used for bacteria detection [211-214].

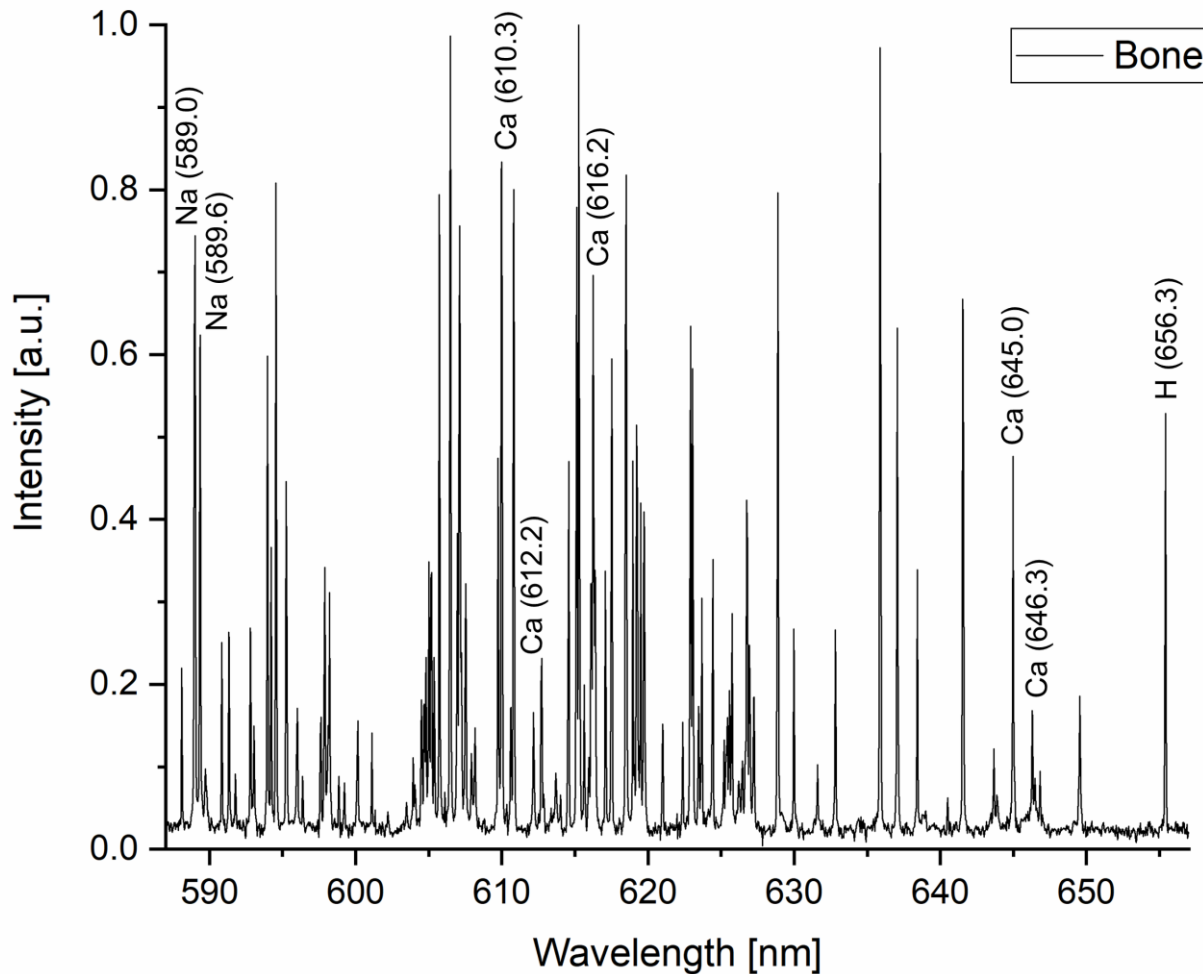


Fig. 3. Typical LIBS spectrum collected from a bone sample.

LIBS instrumentation:

The main components required for LIBS are a pulsed laser for optical breakdown, a spectrometer/monochromator for resolving different wavelengths, a detector, and delivery optics for delivering both laser light to the sample and plasma light to the spectrometer. The delivery optics can be based on free-space or on optical fibers. Figure 4 shows the most commonly used LIBS setups.

In Figure 4, part (a) shows the setup, where both laser and spectrometer work based on free-space optics. In the setup, plasma light is collected with an angle (typically 45 or 90 degrees) in reference to the laser beam direction; however, inline (on-axis) collection is also possible with a dichroic mirror (alternatively, a pierced mirror can be used). This setup is not used very often, since most of the available spectrometers are fiber-fed. Part (b) shows the most common LIBS setup, where

the laser is in free-space, but light collection is based on an optical fiber. Part (c) shows an all-fiber LIBS setup, where both illumination and collection are performed using optical fibers. This setup is often used with a fiber laser. If the output of the laser is not directly in fiber, then an additional coupling optic is required. Part (d) shows an all-fiber LIBS setup, whereby utilizing a dichroic mirror (or, alternatively, a pierced mirror), a single optical fiber illuminates the sample and simultaneously collects the plasma light. This setup is most suitable for endoscopic applications, where the limited space inside the narrow channel of the endoscope should be dedicated to optical fibers.

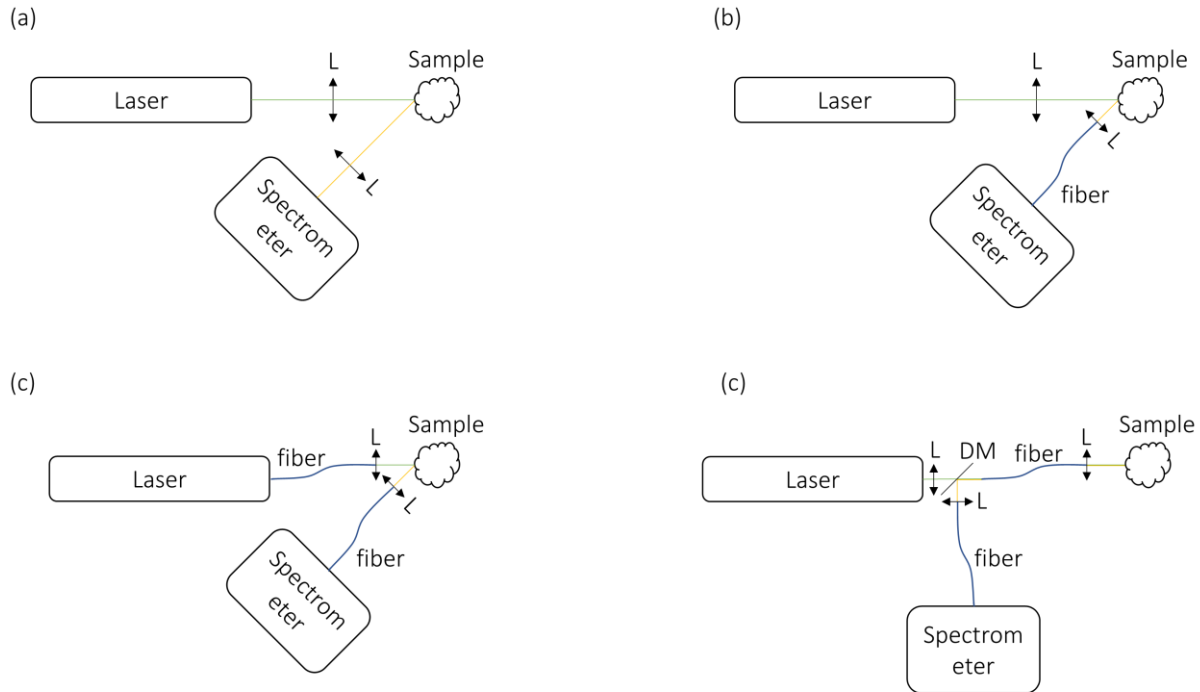


Fig. 4. The most commonly used LIBS setups. L: Lens, DM: Dichroic mirror. The detector (inside/attached to the spectrometer) is not shown.

As discussed previously, a LIBS-suitable laser should be able to interact with tissue in a way that provides plasma-mediated ablation (see the laser-tissue interaction map in Section 2.2.1). For this reason, Q-switched and mode-locked lasers capable of providing short (ns) to ultra-short (fs) pulses are among the most commonly used for LIBS. The lens and mirror used to deliver the laser beam should have a high laser-induced damage threshold (LIDT) in order to avoid damage caused by a high-power laser pulse. Laser line coated optics are the most suitable for this purpose. The most challenging task is delivering the laser pulse with optical fibers, since the fibers require a higher LIDT than the lens and mirror used in the setup. This requirement is due to the fact that the laser beam is focused inside the fibers and, as a result, the fibers must tolerate higher irradiance (peak power density). Further discussion of optical fiber challenges and solutions is provided in Chapter 6.

Theoretically, LIBS can detect all of the elements of the periodic table; for each element, several emission lines at different frequencies are possible (based on the energy difference between the

different electronic states of the atom). To handle the quantity of lines expected from a LIBS spectrum, a high-resolution spectrometer ($\ll 1\text{nm}$) is required to avoid overlap between the different lines. Moreover, the wavelengths of the lines lie in the entire visible (Vis) regime, and also in part of the ultraviolet (UV) and near-infrared (NIR) regimes. Therefore, in addition to high resolution, wide bandwidth ($> 500\text{nm}$) is also required to cover all of the emission lines. By employing a high optical throughput spectrometer, line intensity (peak intensity) will be higher, allowing for a higher signal-to-noise ratio (SNR). Considering the limited size of the detector, achieving both high resolution and wide bandwidth is impossible without having a mechanical moving part in a one dimensional (1D) classical spectrometer [215]. Note that since LIBS plasma emits within a very short time, and part of the emission should be blocked (the reason for which will be discussed shortly after this topic), snapshot spectroscopy is required. Consequently, the whole spectrum should be captured at once (no mechanical movement). Hence, a specific type of spectrometer (2D) is required for LIBS. Figure 5 shows different spectrometer designs.

As shown in Figure 5., the type (a) spectrometer lines are well-resolved, but only a limited number of lines can be captured [216, 217]. Type (b) is similar to type (a) with an additional mechanical moving part. In this type of spectrometer, typically, either the diffraction grating (e.g., Czerny-Turner design) rotates or the detector moves linearly; photomultiplier tubes (PMT) are widely used as a detector in this type of spectrometer. Type (b) is suitable for phenomena with constant radiations (no change in the spectrum over time). Type (c) can capture the whole spectrum at once (snapshot), but the lines are not well-resolved. In this type of spectrometer, either diffraction grating with low groove density or a prism is used, with the aim of not opening the spectrum beyond the width of the detector (CCD/CMOS) [218]. Type (c) is typically used for applications with no sharp/narrow peak in the spectrum, e.g., fluorescence [219]. In 1D spectrometers (types a to c), either 1D detectors (linear camera) are used, or the pixels are vertically binned [220]. In type (d) spectrometers, the spectrum is opened in 2D; therefore, it requires a 2D detector as well. Two main approaches are available for 2D spectroscopy, either using multiple grating side-by-side [221-225] (or, alternatively, multi-segment grating [226]) or using an Echelle (French for “ladder”) grating [227-232]. For the former, a slicing mirror is used, while the later employs a second diffraction grating or a prism (cross-dispenser) to separate different diffracted lines. An in-depth discussion of Echelle spectrometer design is provided in Chapter 6.

As mentioned earlier, LIBS plasma emits within a very short time. Soon after optical breakdown, some continuum emission dominates the LIBS spectrum, mainly bremsstrahlung radiation given off by electrons and recombination in of the plasma [233]. The next chapter outlines the experimental demonstration of this process. To record continuum emission-free spectra, resolved techniques are used, including spatial-resolved (SRLIBS) and time-resolved LIBS (TRLIBS) [234]. Initially, fast shutters/choppers were employed to block continuum emission in LIBS; later, intensified CCDs (ICCD) capable of gated imaging were introduced for measuring in TRLIBS [187, 235-237].

In an ICCD, the incoming photons hit a photocathode (photon to electron conversion). Then, the electrons generated pass through a plate connected to a high potential (voltage), called a

microchannel plate (MCP). The connected potential allows electrons for multiplication (providing gain). Fast gating (ns to ps) can be achieved by fast switching the potential connected to the MCP. Therefore, a triggering signal (normally TTL) with low jitter from a master device (the laser itself or a delay generator) is required to control the ICCD (slave). In the end, electrons are converted back to photons after reaching a phosphor screen. Therefore, both gaining and gating are achieved with ICCD [236].

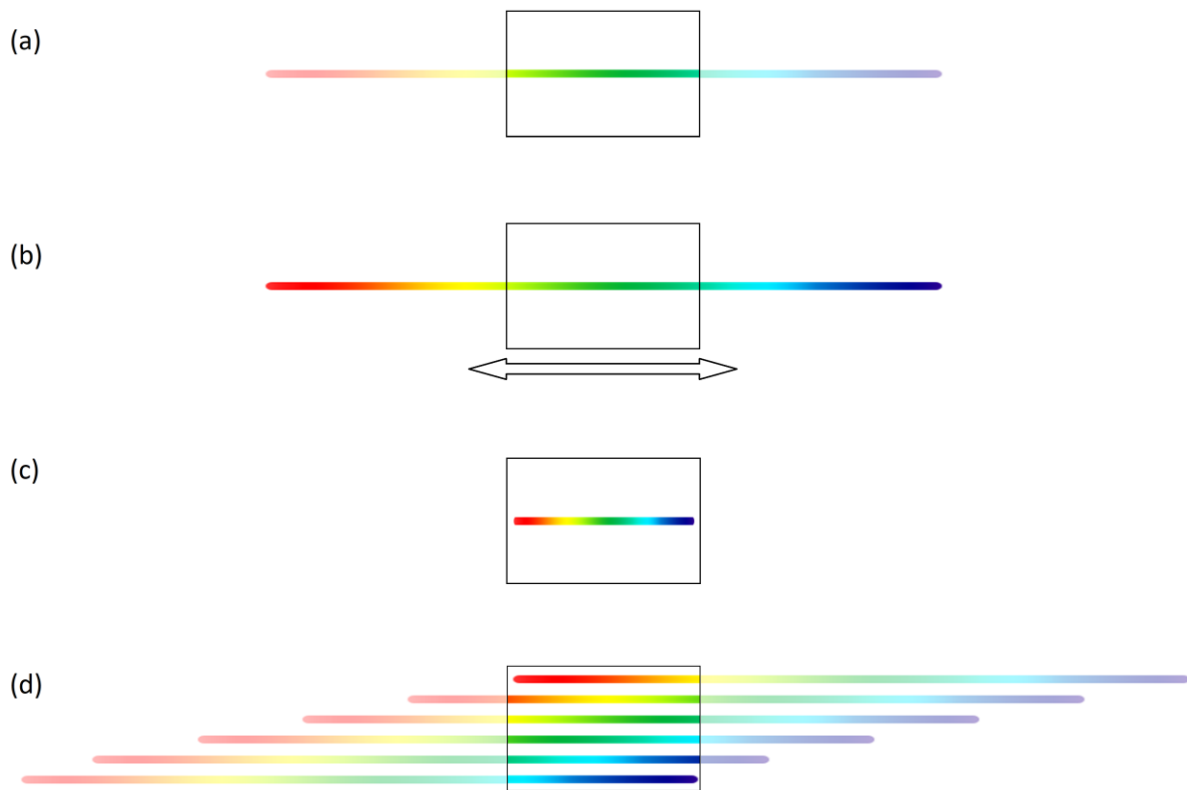


Fig. 5. Different spectrometer designs. (a) 1D, snapshot, high resolution, narrow bandwidth, (b) 1D, non-snapshot, high resolution, wide bandwidth, (c) 1D, low resolution, high bandwidth, (d) 2D, snapshot, high resolution, high bandwidth.

Chapter 3:
Differentiating bone from surrounding soft tissues using laser-
induced breakdown spectroscopy (LIBS)

3.1 Plasma plume expansion dynamics in a nanosecond Nd:YAG laserosteotome

This section presents a publication from a conference proceeding where we studied the dynamics of laser-driven plasma over time. By observing the dynamics of plasma plume expansion, we were able to experimentally determine the best time frame for opening the gate of the camera in LIBS for bone. The goals were to block the continuum emission at the beginning of plasma formation and to achieve the most intense signal while measuring. The results of this section were used to perform TRLIBS, described in the next section.

Publication: Hamed Abbasi, Georg Rauter, Raphael Guzman, Philippe C. Cattin, and Azhar Zam "Plasma plume expansion dynamics in nanosecond Nd:YAG laserosteotome", *Proc. SPIE* 10505, High-Speed Biomedical Imaging and Spectroscopy III: Toward Big Data Instrumentation and Management, 1050513 (20 February 2018); <https://doi.org/10.1117/12.2290980>

Copyright notice: Copyright 2018 Society of Photo-Optical Instrumentation Engineers (SPIE).

PROCEEDINGS OF SPIE

[SPIDigitalLibrary.org/conference-proceedings-of-spie](https://spiedigitallibrary.org/conference-proceedings-of-spie)

Plasma plume expansion dynamics in nanosecond Nd:YAG laserosteotome

Hamed Abbasi, Georg Rauter, Raphael Guzman,
Philippe C. Cattin, Azhar Zam

Hamed Abbasi, Georg Rauter, Raphael Guzman, Philippe C. Cattin, Azhar Zam, "Plasma plume expansion dynamics in nanosecond Nd:YAG laserosteotome," Proc. SPIE 10505, High-Speed Biomedical Imaging and Spectroscopy III: Toward Big Data Instrumentation and Management, 1050513 (20 February 2018); doi: 10.1117/12.2290980

SPIE.

Event: SPIE BiOS, 2018, San Francisco, California, United States

Plasma plume expansion dynamics in nanosecond Nd:YAG laserosteotome

Hamed Abbasi^{*a}, Georg Rauter^b, Raphael Guzman^c, Philippe C. Cattin^d, Azhar Zam^{†a}

^a Biomedical Laser and Optics Group, Department of Biomedical Engineering, University of Basel, Gewerbestrasse 14, CH-4123 Allschwil, Switzerland

^b Bio-Inspired RObots for Medicine-Lab., Department of Biomedical Engineering, University of Basel, Gewerbestrasse 14, CH-4123 Allschwil, Switzerland

^c Department of Neurosurgery, University Hospital Basel, Spitalstrasse 21, CH-4056 Basel, Switzerland

^d Center for medical Image Analysis and Navigation, Department of Biomedical Engineering, University of Basel, Gewerbestrasse 14, CH-4123 Allschwil, Switzerland

ABSTRACT

In minimal invasive laser osteotomy precise information about the ablation process can be obtained with LIBS in order to avoid carbonization, or cutting of wrong types of tissue. Therefore, the collecting fiber for LIBS needs to be optimally placed in narrow cavities in the endoscope. To determine this optimal placement, the plasma plume expansion dynamics in ablation of bone tissue by the second harmonic of a nanosecond Nd:YAG laser at 532 nm has been studied. The laser-induced plasma plume was monitored in different time delays, from one nanosecond up to one hundred microseconds. Measurements were performed using high-speed gated illumination imaging. The expansion features were studied using illumination of the overall visible emission by using a gated intensified charged coupled device (ICCD). The camera was capable of having a minimum gate width (Optical FWHM) of 3 ns and the timing resolution (minimum temporal shift of the gate) of 10 ps. The imaging data were used to generate position–time data of the luminous plasma-front. Moreover, the velocity of the plasma plume expansion was studied based on the time-resolved intensity data. By knowing the plasma plume profile over time, the optimum position (axial distance from the laser spot) of the collecting fiber and optimal time delay (to have the best signal to noise ratio) in spatial-resolved and time-resolved laser-induced breakdown spectroscopy (LIBS) can be determined. Additionally, the function of plasma plume expansion could be used to study the shock wave of the plasma plume.

Keywords: Fast photography, time-resolved, plasma plume, laserosteotome

1. INTRODUCTION

LIBS feedback systems for laserosteotomy could help surgeons avoid cutting a wrong tissue or make it carbonized [1-9]. Laserosteotomes connected to such a feedback system are so-called smart laserosteotomes [10]. Although compared to traditional mechanical tools for cutting bones, laserosteotomes already have several benefits including minimal invasiveness, non-contact interaction, functional cuts and accelerated healing [11-15], making them smart can further improve the level of safety of the current systems [16]. In minimally invasive interventions there is little space, so the placement of the fiber with respect to an observable laser plume is critical [17-20]. This study aims to determine the optimal placement of the fiber with respect to a plasma that is easily accessible due to an ablation process carried out in open air. While most of the similar previous research has carried out to observe the expansion dynamics of the plasma from the side view (perpendicular to the laser beam) [21-23], this study aims to observe the plasma profile from frontal view. The reason for selecting the front view is the fact that in endoscopic laserosteotomy, observing the plasma zone from the side view needs much more optical components and as a result makes the endoscopes thicker. The expansion

* hamed.abbasi@unibas.ch; phone +41 (0)61 207 54 61; <http://dbe.unibas.ch/blog>

† azhar.zam@unibas.ch; phone +41 (0)61 207 54 60; <http://dbe.unibas.ch/blog>

behavior of the laser-driven plasma plume involves several processes such as shielding effects, electron-ion recombination, attenuation, and shock wave formation. Thus, the plasma behavior depends on laser parameters and environmental conditions including the type of sample that is ablated by the laser [24-26]. Therefore, the plasma expansion dynamic for different samples should be studied individually in order to determine the appropriate time delay and appropriate position of the collecting fiber (optimal signal to noise ratio) in time-resolved and spatial-resolved LIBS feedback systems. In this study, the emission intensities of plasma for the axial area (FWHM) as a function of delay were measured by means of high-speed gated illumination imaging with a nanosecond gated ICCD during nanosecond Nd:YAG bone ablation to find out the best possible time delay and axial distance of collection optic in smart laserosteotomes.

2. MATERIALS AND METHODS

2.1 Bone samples

In this study, fresh femur porcine bones were used. The bones were kept in the deep freezer (-18° centigrade) between the scarification to the starting day of the experiment. Four hours before the experiment, the bones were moved to the refrigerator (+ 4° centigrade). The experiments were done at room temperature after removing the surrounding soft tissue with a surgical scalpel.

2.2 Optical setup

Figure 1 shows the schematic of the experimental setup. A Q-switched Nd:YAG laser (Q-smart 450, Quantel) running in its second harmonic at 532 nm with 5 ns pulse duration was used to generate plasma in the air and at the surface of the bone. The laser was operated at 200 mJ per pulse and 1 Hz repetition rate. The first harmonic of the laser was separated and blocked using a nonlinear crystal (C), and a beam blocker (D) installed right after the harmonic generator, respectively. The initial output beam of the laser (E) (6.5 mm diameter, < 0.5 mrad divergence) was horizontally directed to a dichroic mirror (G) placed at 45 degree to the laser line. The reflected light was directed to the surface of the sample from the side by placing a convex lens (H) between the dichroic mirror and the sample (I). This focusing lens provides a spot size in the order of a couple of hundreds of micrometers at the sample surface. The image of the generated plasma (J) was passed through the mentioned convex lens and dichroic mirror first and was focused by an imaging lens (M) to the ICCD (N) (PI-MAX4, Princeton Instruments) after filtering through a laser line filter (L) (532 nm blocker). Both focusing and collimating lenses had a focal length of +40 mm for providing magnification of 1 to have an appropriate field of view. The ICCD was synchronized with the Q-switch of the laser through the internal delay generator of the ICCD to apply a desired time delay (Q-switch as a master and the camera as a slave). Although the camera had the ability of time delay adjustment with picosecond resolution, due to having 1 ns jitter of Q-switch TTL pulse output, different time delays ranging from 1 nanosecond to 100 microseconds were set. The gain and the gate of the ICCD were set to fill 90% of the available counts of the camera (16-bit digitization) to avoid non-linearity effects which normally happen near the saturation.

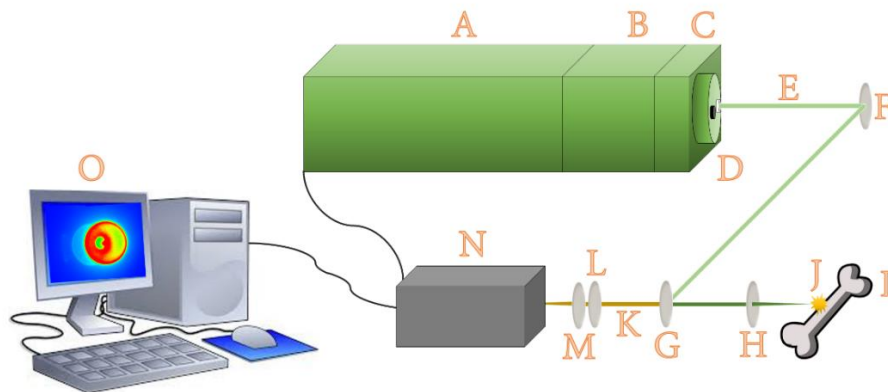


Figure 1. The schematics of the optical setup for investigating ionization front. A: Laser (pulsed Nd:YAG), B: Second harmonic generator, C: Harmonic separator, D: First harmonic blocker, E: Laser beam, F: Laser line mirror, G: Dichroic mirror, H: Convex lens, I: Sample, J: Generated plasma, K: Plasma emission light, L: Notch filter, M: Convex lens, N: ICCD, O: Computer.

3. RESULTS

3.1 Imaging of the generated plasma in air

Figure 1 shows the images of the generated plasmas in the air with different time delays ranging from 1 ns to 10 μ s. The time delay shown in the top-left corner of the pictures is the time between starting point of the generation of the plasma and opening the gate of the ICCD. Imaging at each time delay was repeated five times, and the images were found to be reproducible in both shape and size. Rapid expansion is observable in the first tens of nanoseconds after the generation of the plasma, and afterwards, the plasma size was roughly constant. Table 1 shows the average size of the generated plasma in the air in millimeters, including standard deviation of five different measurements at each time delay.

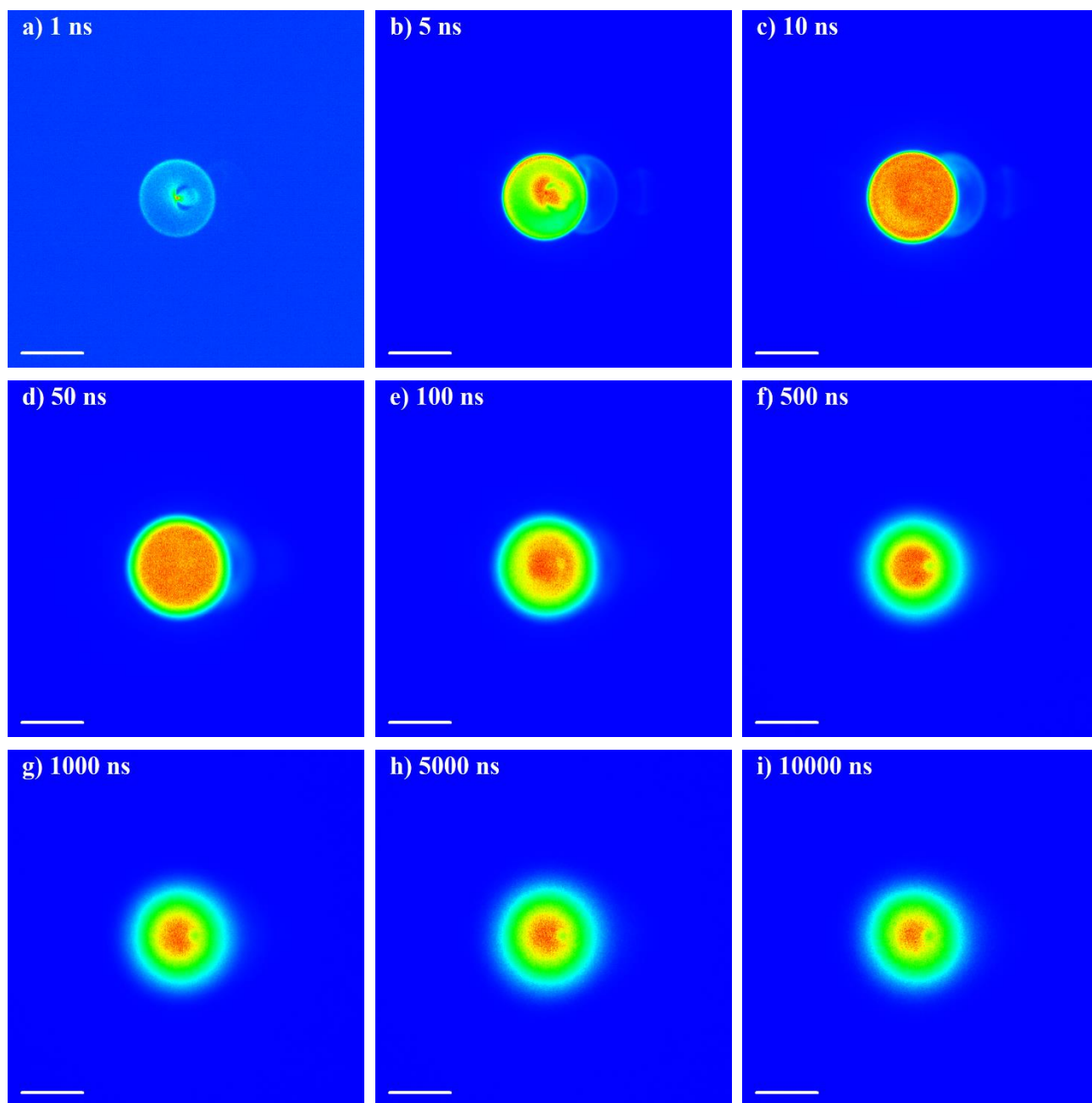


Figure 2. Images of the generated plasma in the air with different time delay. The scale bar at the corner is 2 mm in all images. Images are depicted in full-scale auto-contrast mode (Blue: minimum intensity, Red: maximum intensity).

3.2 Imaging of the generated plasma at the surface of the bone

Figure 2 shows the images of the plasma generated at the surface of the bone with different time delays ranging from 1 ns to 10 μ s. The time delay shown in the top-left corner of the pictures is the time between starting point of the generation of the plasma and opening the gate of the ICCD. Imaging at each time delay was repeated five times, and similar to the measurements above, the images were found to be reproducible in both shape and size. The generated plasmas at the surface of the bone were bigger and brighter in comparison to the plasma generated in the air. High velocity expansion was observed in the first tens of nanoseconds after the generation of the plasma and later a slower expansion was observed. Table 1 shows the average size of the generated plasma at the surface of the bone in millimeter, including standard deviation of five different measurements at each time delay.

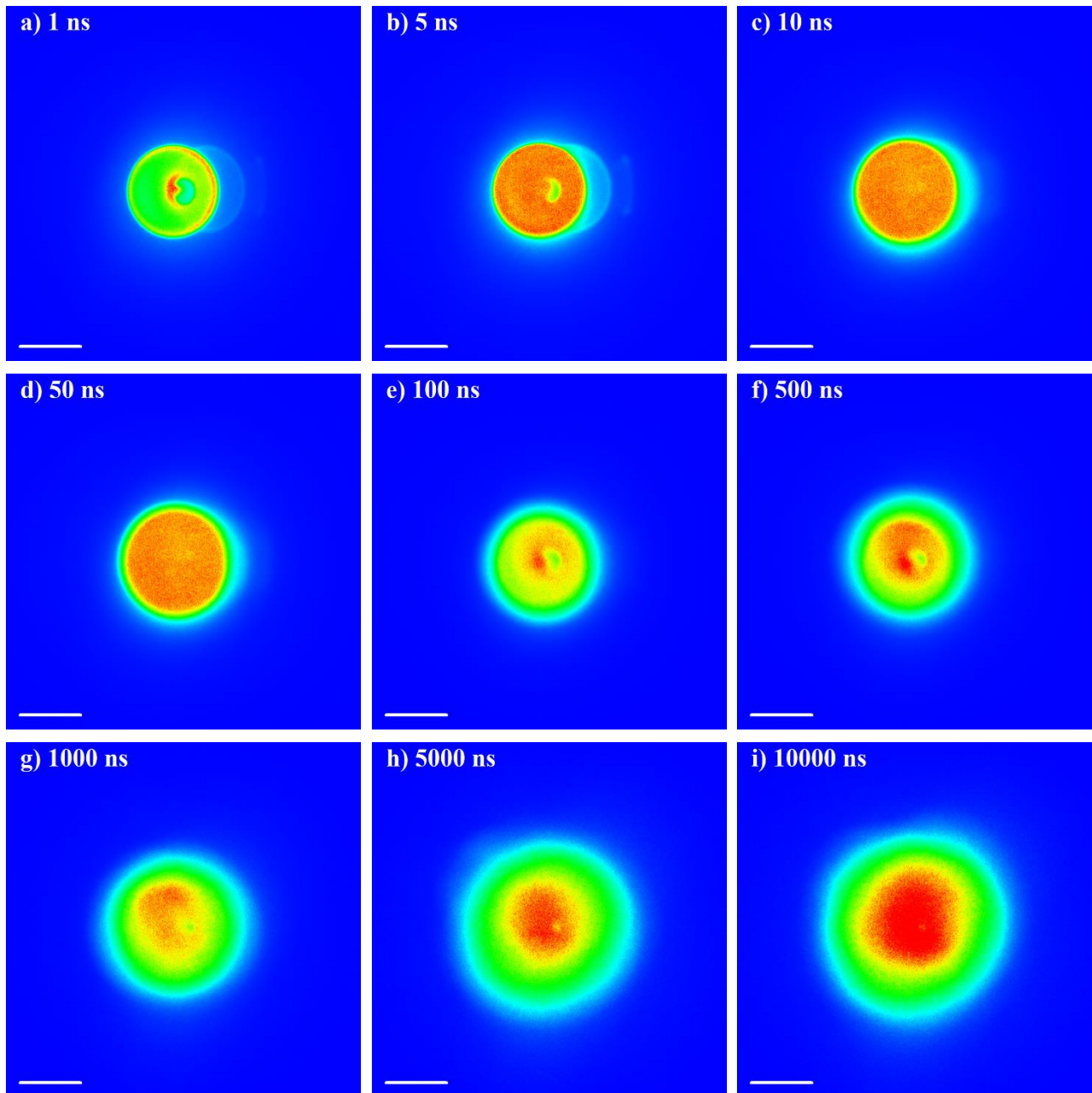


Figure 3. Images of the generated plasma at the surface of the bone with different time delay. The scale bar at the corner is 2 mm in all images. Images are depicted in full-scale auto-contrast mode (Blue: minimum intensity, Red: maximum intensity).

Table 1. The average size (FWHM) of the generated plasmas in the air and at the surface of the bone.

Time delay [ns]	Size of the plasma generated in the air [mm]	Size of the plasma generated at the surface of the bone [mm]
1	2.32± 0.04	2.88± 0.04
5	2.67± 0.04	3.07± 0.01
10	2.87± 0.01	3.38± 0.02
50	2.96± 0.01	3.64± 0.02
100	2.56± 0.02	3.07± 0.01
500	2.24± 0.02	3.17± 0.06
1000	2.19± 0.03	3.69± 0.02
5000	2.23± 0.05	3.99± 0.07
10000	2.13± 0.07	4.42± 0.17

3.3 Plasma fading

It was observed that plasma exists for tens of microseconds and then it gradually fades. It is worth mentioning that the fading happened in the air earlier than the bone. Figure 4 shows a typical plasma image of the bone sample, right before fading (100 μ s delay). As can be seen from the image, the central part fades earlier than outer part, since the ionized particles in the central part of the plasma have a higher lifetime as compare to those in the outer parts.

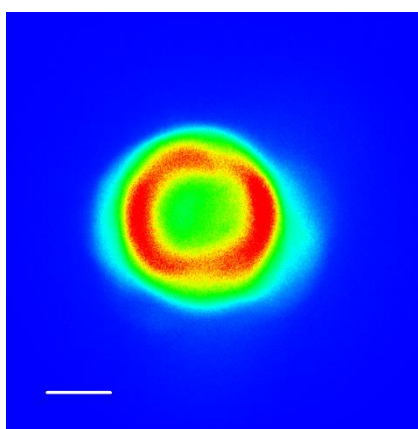


Figure 4. A typical image of the generated plasma at the surface of the bone right before fading. The scale bar at the corner is 2 mm. The image is depicted in optimal-scale auto-contrast mode (Blue: minimum intensity, Red maximum intensity).

4. DISCUSSION

It was observed that the size of the plasma generated at the surface of the bone was bigger and brighter in comparison to the plasma generated in the air in all time delays. This could be related to the fact that more particles could be ionized in the bone sample, whereas in air there are not so many particles that effectively can be ionized. Additionally, a rapid expansion with very high velocity was observed in the first tens of nanoseconds after the generation of the plasma in both samples, confirming a high level of Bremsstrahlung emission in this timescale. Therefore, a time delay of more than hundreds of nanoseconds is necessary to prevent covering the atomic plasma lines by the continuum emission in time-resolved laser-induced breakdown spectroscopy (TRLIBS) of bone samples. In the beginning of the plasma generation in

the bone, the size of plasma is less than 3.66 mm. Based on this result, if the collection fiber is placed 1.83 mm away from the center of the plasma, it would collect a high level of Bremsstrahlung-free emissions in spatial-resolved laser-induced breakdown spectroscopy (SRLIBS). However, the idea needs to be confirmed experimentally in the future. Moreover, it was observed that the plasma exists up to some hundreds of microseconds in bone samples. This observation indicates that using the laser with a repetition rate of more than 10 kHz could result in plasma shielding effects and consequently reduce the ablation efficiency due to the absorption of the laser light by the plasma itself. In addition, having different sizes and fading times between bone and air samples shows the potential of high-speed gated illumination imaging of plasma for auto-focus applications which results in having thinner cuts and more reproducible LIBS spectra for smart laserosteotomes. Finally, it should be noted that all of the experiments in this study were done with a fixed energy, pulse duration, and wavelength. Thus, the effect of changing the mentioned parameter on the results should be examined in future to optimally place the collecting fiber in narrow cavities in the endoscope of smart laserosteotomes for in vivo experiments.

5. CONCLUSION

The dynamics of the plasma plume is essential to determine the appropriate position of the collecting fiber (to have the best signal to noise ratio) in LIBS feedback systems of laserosteotomes. The emission intensities of plasma for an axial view (FWHM) as a function of delay were measured by means of high-speed gated illumination imaging with a nanosecond gated ICCD during porcine femur bone ablation with a nanosecond Nd:YAG laserosteotome. Results of the expansion dynamic of the generated plasma at the surface of the bone suggest to either have a time delay of more than hundreds of nanoseconds in TRLIBS or to put the collecting fiber ca. 1.83 mm away from the central part of the ablation zone in SRLIBS to have the best signal to noise ratio. Moreover, the results of the fading time study, which was longer in bone samples as compared to the air, suggest using lasers with a repetition rate of 10 kHz or less to avoid plasma shielding effects for nanoseconds Nd:YAG laserosteotomy.

ACKNOWLEDGMENTS

The authors gratefully acknowledge funding of the Werner Siemens Foundation through the MIRACLE (short for Minimally Invasive Robot-Assisted Computer-guided LaserosteotomE) project. Moreover, the authors are particularly appreciative of the assistance given by Ms. Lina Beltrán.

REFERENCES

- [1] Mehari, F., Rohde, M., Knipfer, C., Kanawade, R., Klämpfl, F., Adler, W., Stelzle, F. and Schmidt, M., "Laser induced breakdown spectroscopy for bone and cartilage differentiation-ex vivo study as a prospect for a laser surgery feedback mechanism," *Biomedical optics express*, 5(11), pp.4013-4023 (2014).
- [2] Mehari, F., Rohde, M., Kanawade, R., Knipfer, C., Adler, W., Klämpfl, F., Stelzle, F. and Schmidt, M., "Investigation of the differentiation of ex vivo nerve and fat tissues using laser-induced breakdown spectroscopy (LIBS): Prospects for tissue-specific laser surgery," *Journal of biophotonics*, 9(10), pp.1021-1032 (2016).
- [3] Henn, K., Gubaidullin, G.G., Bongartz, J., Wahrburg, J., Roth, H. and Kunkel, M., "A spectroscopic approach to monitor the cut processing in pulsed laser osteotomy," *Lasers in medical science*, 28(1), pp.87-92 (2013).
- [4] Ferraz de Menezes, R., Harvey, C.M., Márquez de Martínez Gerbi, M.E., Smith, Z.J., Smith, D., Ivaldi, J.C., Phillips, A., Chan, J.W. and Wachsmann-Hogiu, S., "Fs-laser ablation of teeth is temperature limited and provides information about the ablated components," *Journal of Biophotonics*, 10(10), pp. 1292-1304 (2017).
- [5] Han, J.H., Moon, Y., Lee, J.J., Choi, S., Kim, Y.C. and Jeong, S., "Differentiation of cutaneous melanoma from surrounding skin using laser-induced breakdown spectroscopy," *Biomedical optics express*, 7(1), pp.57-66 (2016).
- [6] Yueh, F.Y., Zheng, H., Singh, J.P. and Burgess, S., 2009. "Preliminary evaluation of laser-induced breakdown spectroscopy for tissue classification," *Spectrochimica Acta Part B: Atomic Spectroscopy*, 64(10), pp.1059-1067.

- [7] Jeong, D.C., Tsai, P.S. and Kleinfeld, D., "Prospect for feedback guided surgery with ultra-short pulsed laser light," *Current opinion in neurobiology*, 22(1), pp.24-33 (2012).
- [8] Abbasi, H., Rauter, G., Guzman, R., Cattin, P.C. and Zam, A., "Laser-induced breakdown spectroscopy as a potential tool for auto carbonization detection in laserosteotomy," Submitted (2018).
- [9] Nguendon, H.K., Faivre, N., Meylan, B., Shevchik, S., Rauter, G., Guzman, R., Cattin, P.C., Wasmer, K. and Zam, A. "Characterization of ablated porcine bone and muscle using laser-induced acoustic wave method for tissue differentiation," *Proc. SPIE 10417*, pp. 104170N1-10 (2017).
- [10] Huang, H., Yang, L.M., Bai, S. and Liu, J., "Smart surgical tool," *Journal of biomedical optics*, 20(2), pp.028001-028001 (2015).
- [11] Jowett, N., Wöllmer, W., Reimer, R., Zustin, J., Schumacher, U., Wiseman, P.W., Mlynarek, A.M., Böttcher, A., Dalchow, C.V., Lörincz, B.B. and Knecht, R., "Bone ablation without thermal or acoustic mechanical injury via a novel picosecond infrared laser (PIRL)," *Otolaryngology--Head and Neck Surgery*, 150(3), 385-393 (2014)
- [12] Moslemi, N., Shahnaz, A., Masoumi, S., Torabi, S. and Akbari, S., "Laser-Assisted Osteotomy for Implant Site Preparation: A Literature Review," *Implant dentistry*, 26(1), pp.129-136 (2017).
- [13] Beltrán, L., Abbasi, H., Rauter, G., Friederich, N., Cattin, P. and Zam, A., "Effect of laser pulse duration on ablation efficiency of hard bone in microseconds regime," *Proc. SPIE 10453*, pp. 104531S1-6 (2017).
- [14] Abbasi, H., Beltrán, L., Rauter, G., Guzman, R., Cattin, P.C. and Zam, A., "Effect of cooling water on ablation in Er: YAG laserosteotomy of hard bone," *Proc. SPIE 10453*, pp. 104531I1-4 (2017).
- [15] Tulea, C.A., Caron, J., Gehlich, N., Lenenbach, A., Noll, R. and Loosen, P., "Laser cutting of bone tissue under bulk water with a pulsed ps-laser at 532 nm," *Journal of biomedical optics*, 20(10), 105007-105007 (2015).
- [16] Abbasi, H., Rauter, G., Guzman, R., Cattin, P.C. and Zam, A., "Differentiation of femur bone from surrounding soft tissue using laser-induced breakdown spectroscopy as a feedback system for Smart Laserosteotomy," accepted to be published in *Proc. SPIE* (2018).
- [17] Burgner, J., [Robot assisted laser osteotomy], KIT Scientific Publishing (2010).
- [18] Burgner, J., Müller, M., Raczkowski, J. and Wörn, H., "Ex vivo accuracy evaluation for robot assisted laser bone ablation," *The International Journal of Medical Robotics and Computer Assisted Surgery*, 6(4), pp.489-500 (2010).
- [19] Sotsuka, Y., Nishimoto, S., Tsumano, T., Kawai, K., Ishise, H., Kakibuchi, M., Shimokita, R., Yamauchi, T. and Okihara, S.I., "The dawn of computer-assisted robotic osteotomy with ytterbium-doped fiber laser," *Lasers in medical science*, 29(3), pp.1125-1129 (2014).
- [20] Stübinger, S., Landes, C., Seitz, O. and Sader, R., "Er: YAG laser osteotomy for intraoral bone grafting procedures: a case series with a fiber-optic delivery system," *Journal of periodontology*, 78(12), pp.2389-2394 (2007).
- [21] Nahen, K. and Vogel, A., "Plume dynamics and shielding by the ablation plume during Er: YAG laser ablation," *Journal of Biomedical Optics*, 7(2), pp.165-178 (2002).
- [22] Verhoff, B., Harilal, S.S., Freeman, J.R., Diwakar, P.K. and Hassanein, A., "Dynamics of femto-and nanosecond laser ablation plumes investigated using optical emission spectroscopy," *Journal of Applied Physics*, 112(9), p.093303 (2012).
- [23] Camacho, J.J., Diaz, L., Marin-Roldan, A., Moncayo, S. and Caceres, J.O., "Plume Dynamics of Laser-Produced Swine Muscle Tissue Plasma," *Applied spectroscopy*, 70(7), pp.1228-1238 (2016).
- [24] Vogel, A. and Venugopalan, V., "Mechanisms of pulsed laser ablation of biological tissues," *Chemical reviews*, 103(2), pp.577-644 (2003).
- [25] Vogel, A., Aplitz, I., Freidank, S. and Dijkink, R., "Sensitive high-resolution white-light Schlieren technique with a large dynamic range for the investigation of ablation dynamics," *Optics letters*, 31(12), pp.1812-1814 (2006).
- [26] Nazeri, M., Majd, A.E., Massudi, R., Tavassoli, S.H., Mesbahinia, A. and Abbasi, H., "Laser-Induced Breakdown Spectroscopy Via the Spatially Resolved Technique Using Non-Gated Detector," *Journal of Russian Laser Research*, 37(2), pp.164-171 (2016).

3.2 Differentiation of femur bone from surrounding soft tissue using laser-induced breakdown spectroscopy as a feedback system for smart laserosteotomy

TRLIBS experiment was carried out to differentiate bone from its surrounding tissues (muscle and fat). We were able to capture LIBS spectra with a very good SNR. We observed 21 reproducible atomic emission lines, including calcium (Ca), sodium (Na), potassium (K), zinc (Zn), hydrogen (H), iron (Fe), oxygen (O), chlorine (Cl), and nitrogen (N). In addition, a molecular line of carbon to nitrogen bonding (CN) was observed in the recorded spectra. Later, we applied a DFA algorithm to the data and managed to differentiate tissues from each other with good accuracy.

Publication: Hamed Abbasi, Georg Rauter, Raphael Guzman, Philippe C. Cattin, and Azhar Zam "Differentiation of femur bone from surrounding soft tissue using laser-induced breakdown spectroscopy as a feedback system for smart laserosteotomy", *Proc. SPIE* 10685, Biophotonics: Photonic Solutions for Better Health Care VI, 1068519 (17 May 2018); <https://doi.org/10.1117/12.2309473>

Copyright notice: Copyright 2018 Society of Photo-Optical Instrumentation Engineers (SPIE).

PROCEEDINGS OF SPIE

SPIDigitalLibrary.org/conference-proceedings-of-spie

Differentiation of femur bone from surrounding soft tissue using laser induced breakdown spectroscopy as a feedback system for smart laserosteotomy

Hamed Abbasi, Georg Rauter, Raphael Guzman, Philippe C. Cattin, Azhar Zam

Hamed Abbasi, Georg Rauter, Raphael Guzman, Philippe C. Cattin, Azhar Zam, "Differentiation of femur bone from surrounding soft tissue using laser induced breakdown spectroscopy as a feedback system for smart laserosteotomy," Proc. SPIE 10685, Biophotonics: Photonic Solutions for Better Health Care VI, 1068519 (17 May 2018); doi: 10.1117/12.2309473

SPIE.

Event: SPIE Photonics Europe, 2018, Strasbourg, France

Differentiation of femur bone from surrounding soft tissue using laser-induced breakdown spectroscopy as a feedback system for Smart Laserosteotomy

Hamed Abbasi^{*a}, Georg Rauter^b, Raphael Guzman^c, Philippe C. Cattin^d, Azhar Zam^{†a}

^a Biomedical Laser and Optics Group, Department of Biomedical Engineering, University of Basel, CH-4123 Allschwil, Switzerland

^b Bio-Inspired RObots for MEDicine-Lab, Department of Biomedical Engineering, University of Basel, CH-4123 Allschwil, Switzerland

^c Department of Neurosurgery, University Hospital Basel, CH-4056 Basel, Switzerland

^d Center for medical Image Analysis and Navigation, Department of Biomedical Engineering, University of Basel, CH-4123 Allschwil, Switzerland

ABSTRACT

Although laserosteotomes have become generally accepted devices in surgical applications, they still suffer from a lack of information about the type of tissue currently being ablated; as a result, critical structures of the body under or near the focal spot of the laser beam are prone to inadvertent ablation. The lack of information about the properties of the ablated tissue can be solved by connecting the laserosteotome to an optical detection setup which can differentiate various types of tissues, especially bone from connective soft tissues. This study examines the applicability of laser-induced breakdown spectroscopy (LIBS) as a potential technique to differentiate bone from surrounding soft tissue (fat and muscle). In this experiment, fresh porcine femur bone, muscle, and fat were used as hard and soft tissue samples. The beam of a nanosecond frequency-doubled Nd:YAG laser was used to ablate the tissue samples and generate the plasma. The plasma light emitted from the ablated spot, which corresponds to the recombination spectra of ionized atoms and molecules, was gathered with a collection optic (including a reflective light collector and a fiber optic) and sent to an Echelle spectrometer for resolving the atomic composition of the ablated sample. Afterwards, Discriminant Function Analysis (DFA) based on the ratio of the intensity of selected peak pairs was performed to classify three sample groups (bone, muscle, and fat). Lastly, the sensitivity, specificity, and accuracy of the proposed method were calculated. Sensitivity and specificity of 100 % and 99 % were achieved, respectively, to differentiate bone from surrounding soft tissue.

Keywords: Laserosteotome, minimally invasive surgery, feedback, LIBS, tissue differentiation, DFA, smart surgery

1. INTRODUCTION

In comparison to well established mechanical instruments for cutting bone, laserosteotomes provide several important benefits like functional cuts, minimal invasiveness, non-contact interaction, and accelerated healing [1-10]. At the same time, they still suffer from a lack of feedback on the type and properties of the tissue being cut; as a result, critical structures of the body under the laser line are prone to iatrogenic damage [11-15]. The lack of information on the type of tissue being ablated by the laserosteotome limits its application as a minimally invasive osteotomy tool. In order to advance the range of applications for laserosteotomes, there is a need for a feedback control system that can provide accurate information on the type and properties of the tissue being cut. Such feedback mechanisms can rely on photoacoustic, spectroscopic or OCT-based measurements [16-21]. Hereby, the potential spectroscopic methods include diffuse reflectance, laser-induced breakdown, Raman, and fluorescence spectroscopy [22-26]. Among them, laser-induced breakdown spectroscopy (LIBS), as a powerful analytical technique, seems to be most promising to us since it enables using the same laser as during the cutting process. Authors have recently shown that LIBS feedback systems for laserosteotomy could help surgeons avoid

* hamed.abbasi@unibas.ch; phone +41 (0)61 207 54 61; <http://dbe.unibas.ch/blog>

† azhar.zam@unibas.ch; phone +41 (0)61 207 54 60; <http://dbe.unibas.ch/blog>

carbonizing bone [18]. Moreover, LIBS has shown its potential to differentiate between healthy and carious teeth [27, 28], bone and spinal cord [29, 30], bone and cartilage [31], nerve and fat [32], as well as nerve and gland [33]. Laserosteotomes connected to such a feedback system are so-called smart laserosteotomes [34]. Making laserosteotomes smart can further improve their efficiency and safety. This study aims to examine LIBS to differentiate hard femur bone from surrounding soft tissue (muscle and fat) as a feedback system for smart laserosteotomy. A high-resolving power ($\lambda/\Delta\lambda$ of 4000) Echelle spectrometer connected to an intensified CCD (ICCD) was employed to collect the plasma emission spectrum. Fresh hard pig bone, muscle, and fat were ablated with 5 ns laser pulses at 532 nm, while simultaneously the laser-driven plasma plume was monitored spectroscopically with a fixed time delay. Finally, canonical discriminant function analysis was employed to provide a function to classify groups of samples. Receiver Operating Characteristic (ROC) analysis was performed additionally to confirm the performance of the proposed classifier later on.

2. MATERIALS AND METHODS

2.1 Specimens

In this study, fresh femur porcine samples (bone, muscle, and fat) bought from a local supermarket were used. The specimens were kept in the deep freezer (-18°C) between the scarification to the day of the experiment. Four hours before the experiment, specimens were moved to the refrigerator ($+4^{\circ}\text{C}$). The tissue types were separated with a surgical scalpel and rinsed in tap water prior to the experiments.

2.2 LIBS setup

Figure 1 shows the schematic of the LIBS setup. A flash-lamp pumped Q-switched Nd:YAG laser (Q-smart 450, QuanteI) running in its second harmonic at 532 nm (5 ns pulse duration) was used to ablate the specimens. The laser was operated at 108 mJ energy per pulse and 1 Hz repetition rate. The fundamental harmonic of the laser (1064 nm) was separated and blocked using a nonlinear crystal (C) and a beam blocker (D) installed right after the harmonic generator, respectively. The initial output beam of the laser (E) (6.5 mm diameter) was horizontally directed to a convex lens (F) placed perpendicular to the laser line. The focused light was directed to the surface of the specimen from the side. This focusing lens provides a spot size in the order of hundreds of micrometers at the specimen surface. The emitted light from the produced plasma (H) with a diameter of ca. 3 mm [35] was collected by a light collector placed at 45-degree angle in reference to the laser beam (I), passed through an optical fiber (J) and finally guided to a high-resolution Echelle spectrometer (K) that sent the spectrometer data forward to the computer (L). The spectrometer was empowered with a 16-bit ICCD with a built-in delay generator and adjustable gain. The ICCD (as a slave) was synchronized with the Q-switch of the laser (as a master) with the jitter of 1 ns. The gate delay of 5 μs was applied to avoid collecting continuum emissions which could cover the LIBS peaks [36]. The LIBS spectra were integrated for 1 ms. The CCD-sensor was cooled down to -30°C to reduce the background noise level. Also, the experiment was run at the same temperature that was employed to calibrate the spectrometer ($+25^{\circ}\text{C}$) to avoid misalignment caused by thermal expansion/contraction of the system.

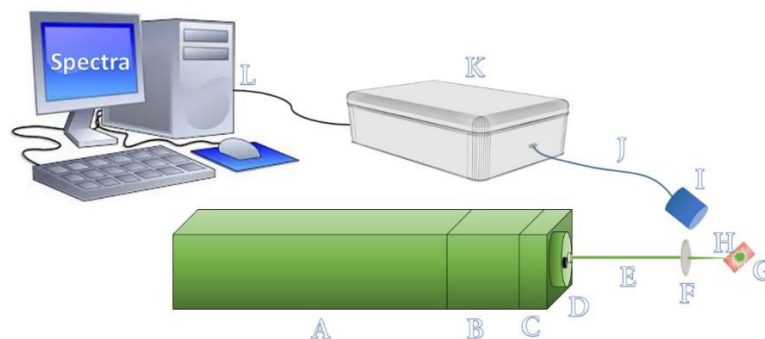


Figure 1. The schematics of the LIBS setup. A: Laser (nanosecond Nd:YAG), B: Second harmonic generator, C: Harmonic separator, D: First harmonic beam blocker, E: Output beam, F: Focusing lens, G: Specimen, H: Generated plasma, I: Light collector, J: Optical fiber, K: Echelle spectrometer, L: Computer.

2.3 Data analysis

The specimens were separated into three groups: femur bone as a hard tissue sample and femur muscle and fat as surrounding soft tissue samples. Each group consisted of 5 specimens; 50 shots were recorded from each specimen. In total, 750 spectra were recorded, 250 from each group. Then, to determine the atomic composition of the samples, the emission lines in the recorded LIBS spectra of all groups of samples were mapped with the atomic spectra database of the National Institute of Standards and Technology (NIST) [37]. After finding the related lines of the emitted atomic elements, the wavelengths and the intensities of reproducible peaks were stored in a separate file. Later on, the ratio between the intensity of the stored peaks was calculated and used as input of Discriminant Function Analysis (DFA) to generate functions to classify sample groups. This ratio-based analysis allows for more robust results, as it is more stable than data based on absolute intensity values in the spectra of a given tissue type [18]. Afterwards, the performance of the employed classifier was evaluated using ROC analysis. Additionally, statistical parameters of the classifier including the true positive rates (sensitivity), true negative rates (specificity), positive predictive values (precision), negative predictive values and accuracy were calculated between different sample pairs (i.e., hard-soft tissue pair, bone-muscle pair, bone-fat pair and fat-muscle pair).

3. RESULTS

Figure 2 shows LIBS spectra of bone, muscle and fat samples. Each depicted spectrum is the average of 250 measurements without any background reduction.

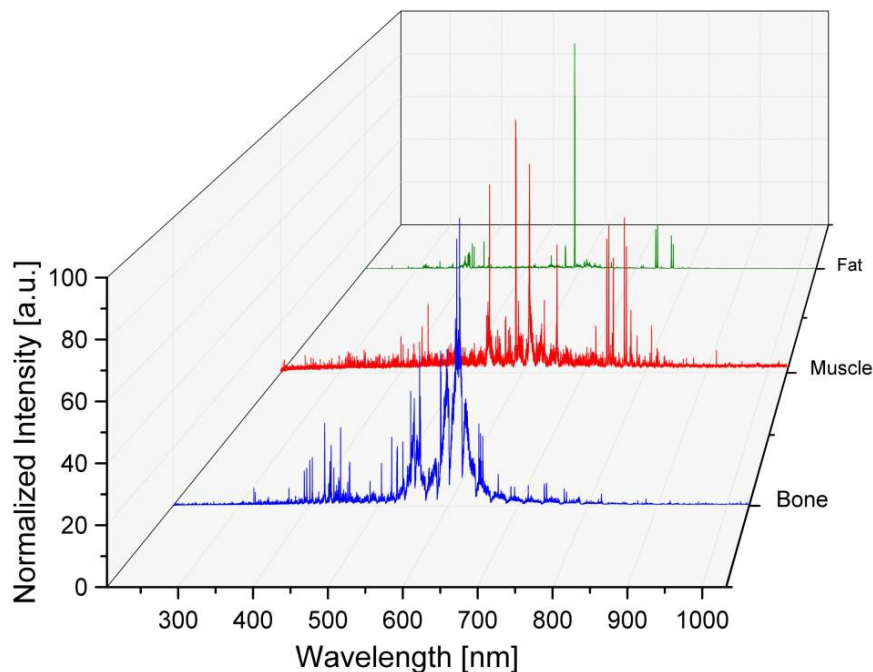


Figure 2. Average LIBS spectra of hard and soft tissue samples (bone in blue, muscle in red and fat in green).

The recorded spectra may include emission lines of the elements found in the ambient air. In the collected spectra, 21 reproducible atomic emission lines were observed including calcium (Ca), sodium (Na), potassium (K), zinc (Zn), hydrogen (H), iron (Fe), oxygen (O), chlorine (Cl), and nitrogen (N). In addition, a molecular line of carbon to nitrogen bonding (CN) was observed in the recorded spectra. The observed lines were in agreement with the lines described in literature [26-34]. Later on, based on the 22 chosen peak intensities, 231 intensity ratios were generated using permutation

without repetition. These 231 generated ratios were used as input for DFA. Figure 3 shows the result of the employed canonical DFA.

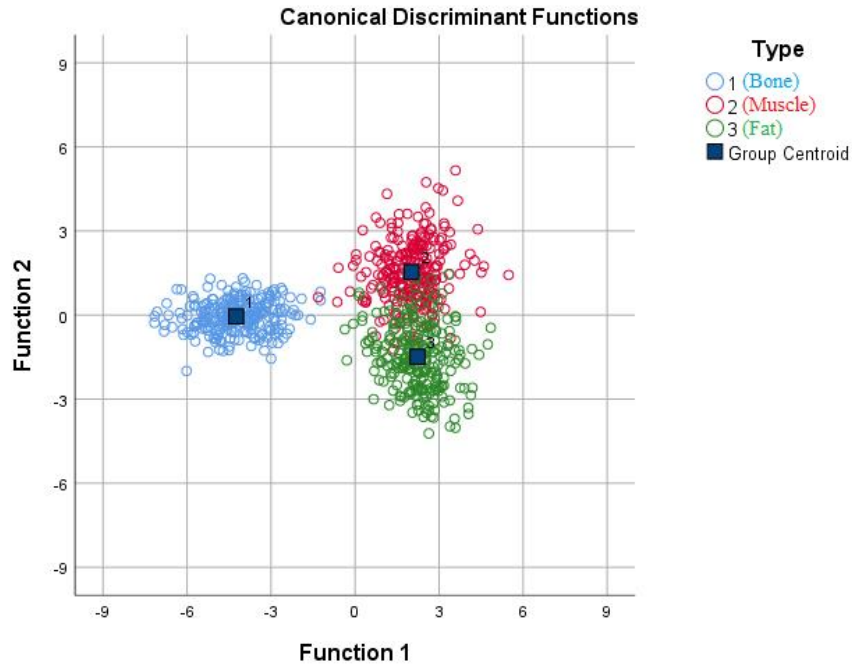


Figure 3. Result of employed canonical DFA to classify groups of samples (bone in blue, muscle in red and fat in green).

In Figure 3, function 1 enables the classification between hard (bone) and soft tissues (muscle and fat) classes and function 2 provides classification between muscle and fat classes. By employing function 1, all 250 bone spectra were correctly classified as bone, 249 muscle as muscle and only 1 as bone and also all 250 fat spectra as fat. By employing function 2, out of 250 recorded muscle spectra, 228 of them were classified as muscle, and 22 as fat, also out of the 250 recorded fat spectra, 223 of them were correctly classified as fat and 27 as muscle. Table 1 shows the peak ratios that had the highest contribution to the functions, sorted from lowest to highest Wilks' Lambda.

Table 1. The peak ratios with most contribution to the functions, sorted from lowest to highest Wilks' Lambda (from highest to lowest contribution). I means single ionized atomic line, P means persistent line and M means Molecular line.

#	Ratio
1	Ca I (P) @ 616.2 nm / K I (P) @ 769.9 nm
2	Ca I (P) @ 612.2 nm / K I (P) @ 769.9 nm
3	Ca I (P) @ 610.3 nm / CN (M) @ 388 nm
4	Ca I (P) @ 616.2 nm / K I (P) @ 766.5 nm
5	Ca I (P) @ 558.9 nm / CN (M) @ 388 nm
6	Ca I (P) @ 610.3 nm / K I (P) @ 769.9 nm
7	Ca I (P) @ 612.2 nm / K I (P) @ 766.5 nm

Table 1 clearly shows that atomic lines of calcium and potassium, as well as the molecular line of carbon to nitrogen bonding, had the highest contribution to differentiate groups of samples. Table 2 shows the statistical parameters of the classifier between different pairs of groups.

Table 2. Statistical parameters of the classifier between different pairs of groups.

	Hard (Bone)-Soft (Muscle and Fat) Tissue Pair	Bone-Muscle Pair	Bone-Fat Pair	Fat-Muscle Pair
True Positive Rate (Sensitivity)	100 %	100 %	100 %	90.0 %
True Negative Rate (Specificity)	99.8 %	99.6 %	100 %	91.2 %
Positive Predictive Value (Precision)	99.6 %	99.6 %	100 %	91.1 %
Negative Predictive Value	100 %	100 %	100 %	90.1 %
Accuracy	99.9 %	99.8 %	100 %	90.6 %

It is clear from Table 2 that all groups of samples were classified with an accuracy of more than 90 %. Additionally, a ROC analysis was performed, and the Area Under Curve (AUC) was calculated afterwards. Figure 4 shows the result of the ROC analysis for different pairs of samples.

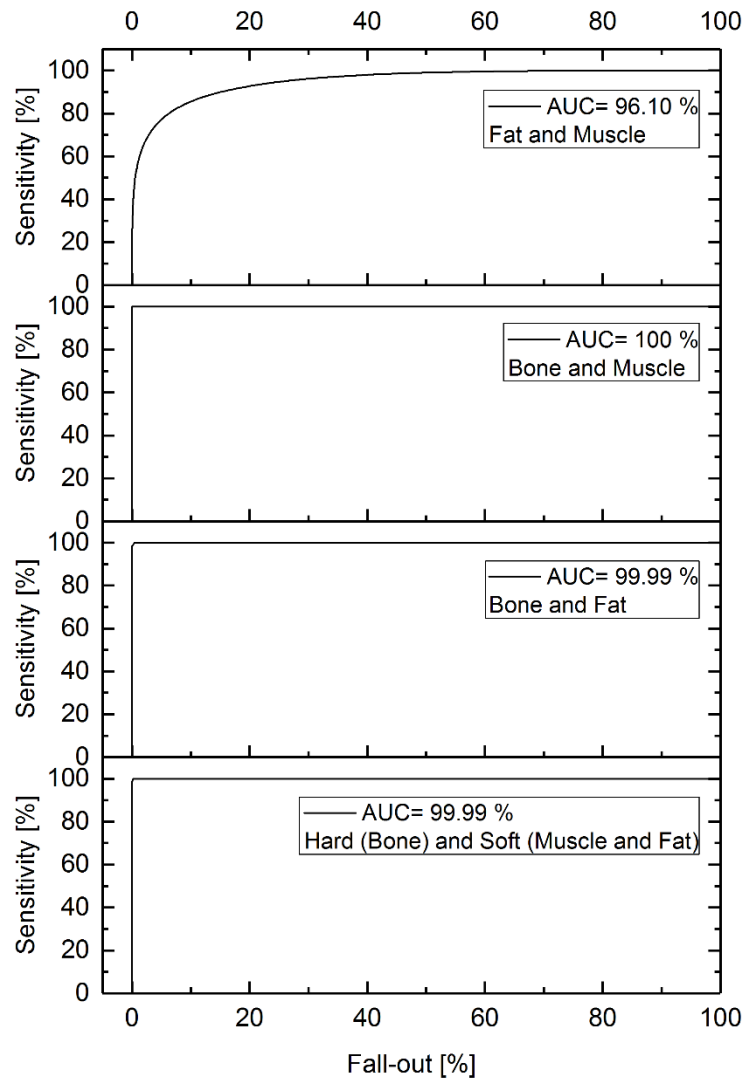


Figure 4. Result of ROC analysis for different pairs of samples.

4. DISCUSSION

Laser-induced breakdown spectroscopy showed reliable results to differentiate porcine femur bone from surrounding soft tissue in *ex vivo* conditions. Since the accuracy of the classifier to detect surrounding soft tissues was high (more than 99.99 %) the *ex vivo* results are likely to transfer to *in vivo* conditions. Nevertheless, the obtained accuracy from the *ex vivo* conditions is expected to decrease for *in vivo* experiments, where tissues are surrounded by rinsing solutions (e.g., blood) during the clinical procedures. A possible approach to overcome the influence of rinsing solutions in *in vivo* conditions could be utilizing a double-pulse LIBS setup, where the first pulse can remove the superficial liquid on the focal spot and the second pulse can quickly reach the target surface before the target area is refilled with liquid that would falsify the results. While the primary aim of the study was to differentiate soft from hard tissue, the applicability of LIBS to differentiate internally between soft tissue groups (muscle and fat) was examined as well; the accuracy of internal soft tissue differentiation was close to 90 %. A possible reason for this decrease in the accuracy of muscle-fat pair differentiation could be the existence of connective tissue in between soft tissues. Employing either more advanced classification methods or a more robust LIBS setup, such as LIBS being connected to an auto-focus system, might result in even higher classification accuracy for internal soft tissue differentiation. Alternatively, considering the average of multiple spectra for the analysis or employing a fiber with less absorption in UV might improve the accuracy further. Finally, it is noteworthy that the area under the ROC curve of the fat-muscle pair was higher than 96 %. This suggests that depending on the application, either more sensitivity (true positive rate) or specificity (true negative rate) are achievable by moving the threshold line.

5. CONCLUSION

Laserosteotomes have to efficiently and safely cut bones without damaging the surrounding soft tissues, and therefore, the type of tissue being cut has to be identified. One viable option is to include real-time feedback mechanisms in the cutting process. This study examined the applicability of LIBS for differentiating femur bone from surrounding soft tissue (muscle and fat) by monitoring the laser-driven plasma generated during a nanosecond pulse ablation using a frequency-doubled Nd:YAG laser at 532 nm. The observed atomic and molecular emissions in the recorded LIBS spectra of both hard and soft classes were in agreement with literature. Also, the preliminary results of this study demonstrate that LIBS is a powerful technique for differentiating surrounding soft tissue from hard bone. Sensitivity and specificity of 100 % and 99 % were achieved, respectively.

ACKNOWLEDGMENTS

The authors gratefully acknowledge funding of the Werner Siemens Foundation through the Minimally Invasive Robot-Assisted Computer-guided Laserosteotomy (MIRACLE) project. In addition, the authors appreciate the assistance given by Dr. Maryam Bahreini.

REFERENCES

- [1] Jowett, N., Wöllmer, W., Reimer, R., Zustin, J., Schumacher, U., Wiseman, P.W., Mlynarek, A.M., Böttcher, A., Dalchow, C.V., Lörinicz, B.B. and Knecht, R., "Bone ablation without thermal or acoustic mechanical injury via a novel picosecond infrared laser (PIRL)," *Otolaryngology--Head and Neck Surgery*, 150(3), 385-393 (2014)
- [2] Panduric, D.G., Juric, I.B., Music, S., Molčanov, K., Sušic, M. and Anic, I., "Morphological and ultrastructural comparative analysis of bone tissue after Er: YAG laser and surgical drill osteotomy," *Photomedicine and laser surgery*, 32(7), 401-408 (2014).
- [3] Strassl, M., Wieger, V., Brodoceanu, D., Beer, F., Moritz, A. and Wintner, E., "Ultra-short pulse laser ablation of biological hard tissue and biocompatibles," *JLMN-Journal of Laser Micro/Nanoengineering*, 3(1), 30-40 (2008).
- [4] Moslemi, N., Shahnaz, A., Masoumi, S., Torabi, S. and Akbari, S., "Laser-Assisted Osteotomy for Implant Site Preparation: A Literature Review," *Implant dentistry*, 26(1), 129-136 (2017).

- [5] Lo, D.D., Mackanos, M.A., Chung, M.T., Hyun, J.S., Montoro, D.T., Grova, M., Liu, C., Wang, J., Palanker, D., Connolly, A.J. and Longaker, M.T., "Femtosecond plasma mediated laser ablation has advantages over mechanical osteotomy of cranial bone," *Lasers in surgery and medicine*, 44(10), 805-814 (2012).
- [6] Beltrán, L., Abbasi, H., Rauter, G., Friederich, N., Cattin, P. and Zam, A., "Effect of laser pulse duration on ablation efficiency of hard bone in microseconds regime," *Proc. SPIE 10453*, 104531S1-6 (2017).
- [7] Abbasi, H., Beltrán, L., Rauter, G., Guzman, R., Cattin, P.C. and Zam, A., "Effect of cooling water on ablation in Er: YAG laserosteotome of hard bone," *Proc. SPIE 10453*, 104531I1-4 (2017).
- [8] Tulea, C.A., Caron, J., Gehlich, N., Lenenbach, A., Noll, R. and Loosen, P., "Laser cutting of bone tissue under bulk water with a pulsed ps-laser at 532 nm," *Journal of biomedical optics*, 20(10), 105007 (2015).
- [9] Plötz, C., Schelle, F., Bourauel, C., Frentzen, M. and Meister, J., "Ablation of porcine bone tissue with an ultrashort pulsed laser (USPL) system," *Lasers in medical science*, 30(3), 977-983 (2015).
- [10] Bernal, L.M.B., Shayeganrad, G., Kosa, G., Zelechowski, M., Rauter, G., Friederich, N., Cattin, P.C. and Zam, A., "Performance of Er: YAG laser ablation of hard bone under different irrigation water cooling conditions" *Proc. SPIE10492*, 104920B (2018).
- [11] Yueh, F.Y., Zheng, H., Singh, J.P. and Burgess, S., "Preliminary evaluation of laser-induced breakdown spectroscopy for tissue classification," *Spectrochimica Acta Part B: Atomic Spectroscopy*, 64(10), 1059-1067 (2009).
- [12] Jeong, D.C., Tsai, P.S. and Kleinfeld, D., "Prospect for feedback guided surgery with ultra-short pulsed laser light," *Current opinion in neurobiology*, 22(1), 24-33 (2012).
- [13] Henn, K., Gubaidullin, G.G., Bongartz, J., Wahrburg, J., Roth, H. and Kunkel, M., "A spectroscopic approach to monitor the cut processing in pulsed laser osteotomy," *Lasers in medical science*, 28(1), 87-92 (2013).
- [14] Kanawade, R., Mehari, F., Knipfer, C., Rohde, M., Tangermann-Gerk, K., Schmidt, M. and Stelzle, F., "Pilot study of laser induced breakdown spectroscopy for tissue differentiation by monitoring the plume created during laser surgery—An approach on a feedback Laser control mechanism, " *Spectrochimica Acta Part B: Atomic Spectroscopy*, 87, 175-181 (2013).
- [15] Kanawade, R., Mehari, F., Klämpfl, F., Rohde, M., Knipfer, C., Tangermann-Gerk, K., Adler, W., Schmidt, M. and Stelzle, F., "Qualitative tissue differentiation by analysing the intensity ratios of atomic emission lines using laser induced breakdown spectroscopy (LIBS): prospects for a feedback mechanism for surgical laser systems," *Journal of biophotonics*, 8(1-2), 153-161 (2015).
- [16] Nguendon, H.K., Faivre, N., Meylan, B., Shevchik, S., Rauter, G., Guzman, R., Cattin, P.C., Wasmer, K. and Zam, A. "Characterization of ablated porcine bone and muscle using laser-induced acoustic wave method for tissue differentiation," *Proc. SPIE 10417*, 104170N1-10 (2017).
- [17] Nguendon, H.K., Rauter, G., Guzman, R., Cattin, P.C. and Zam, A., "Comparison of acoustic shock waves generated by micro and nanosecond lasers for a smart laser surgery system," *Proc. SPIE 10484*, 104840P (2018).
- [18] Abbasi, H., Rauter, G., Guzman, R., Cattin, P.C. and Zam, A., "Laser-induced breakdown spectroscopy as a potential tool for auto carbonization detection in laserosteotomy," *Journal of biomedical optics*, 23(7), 071206 (2018).
- [19] Lenz, M., Krug, R., Dillmann, C., Stroop, R., Gerhardt, N.C., Welp, H., Schmieder, K. and Hofmann, M.R., "Automated differentiation between meningioma and healthy brain tissue based on optical coherence tomography ex vivo images using texture features," *Journal of biomedical optics*, 23(7), 071205 (2018).
- [20] Davari, S.A., Masjedi, S., Ferdous, Z. and Mukherjee, D., "In-vitro analysis of early calcification in aortic valvular interstitial cells using Laser-Induced Breakdown Spectroscopy (LIBS)," *Journal of biophotonics*, 11(1), 201600288 (2018).
- [21] Teran-Hinojosa, E., Sobral, H., Sánchez-Pérez, C., Pérez-García, A., Alemán-García, N. and Hernández-Ruiz, J., "Differentiation of fibrotic liver tissue using laser-induced breakdown spectroscopy," *Biomedical optics express*, 8(8), 3816-3827 (2017).
- [22] Reisner, L.A., King, B.W., Klein, M.D., Auner, G.W. and Pandya, A.K., "A prototype biosensor-integrated image-guided surgery system," *The International Journal of Medical Robotics and Computer Assisted Surgery*, 3(1), 82-88 (2007).
- [23] Ashok, P.C., Giardini, M.E., Dholakia, K. and Sibbett, W., "A Raman spectroscopy bio-sensor for tissue discrimination in surgical robotics, " *Journal of biophotonics*, 7(1-2), 103-109 (2014).
- [24] Krause, F., Braun, A., Brede, O., Eberhard, J., Frentzen, M. and Jepsen, S., "Evaluation of selective calculus removal by a fluorescence feedback-controlled Er: YAG laser in vitro," *Journal of clinical periodontology*, 34(1), 66-71 (2007).

- [25] Gill, R.K., Smith, Z.J., Lee, C. and Wachsmann-Hogiu, S., "The effects of laser repetition rate on femtosecond laser ablation of dry bone: a thermal and LIBS study," *Journal of biophotonics*, 9(1-2), 171-180 (2016).
- [26] Lee, J.J., Moon, Y., Han, J.H. and Jeong, S., "Analysis of major elements in pigmented melanocytic chicken skin using laser-induced breakdown spectroscopy," *Journal of biophotonics*, 10(4), 523-531 (2017).
- [27] Gazmeh, M., Bahreini, M. and Tavassoli, S.H., "Discrimination of healthy and carious teeth using laser-induced breakdown spectroscopy and partial least square discriminant analysis," *Applied optics*, 54(1), 123-131 (2015).
- [28] Gazmeh, M., Bahreini, M., Tavassoli, S.H. and Asnaashari, M., "Qualitative analysis of teeth and evaluation of amalgam elements penetration into dental matrix using laser induced breakdown spectroscopy," *Journal of lasers in medical sciences*, 6(2), 67-73 (2015).
- [29] Kim, B.M., Feit, M.D., Rubenchik, A.M., Gold, D.M., Darrow, C.B., Marion, J.E. and Da Silva, L.B., "Plasma luminescence feedback control system for precise ultrashort pulse laser tissue ablation," *Proc. SPIE 3255*, 92-98, (1998).
- [30] Kim, B.M., Feit, M.D., Rubenchik, A.M., Mammini, B.M. and Da Silva, L.B., "Optical feedback signal for ultrashort laser pulse ablation of tissue," *Applied Surface Science*, 127, 857-862 (1998).
- [31] Mehari, F., Rohde, M., Knipfer, C., Kanawade, R., Klämpfl, F., Adler, W., Stelzle, F. and Schmidt, M., "Laser induced breakdown spectroscopy for bone and cartilage differentiation-ex vivo study as a prospect for a laser surgery feedback mechanism," *Biomedical optics express*, 5(11), 4013-4023 (2014).
- [32] Mehari, F., Rohde, M., Kanawade, R., Knipfer, C., Adler, W., Klämpfl, F., Stelzle, F. and Schmidt, M., "Investigation of the differentiation of ex vivo nerve and fat tissues using laser-induced breakdown spectroscopy (LIBS): Prospects for tissue-specific laser surgery," *Journal of biophotonics*, 9(10), 1021-1032 (2016).
- [33] Mehari, F., Rohde, M., Knipfer, C., Kanawade, R., Klämpfl, F., Adler, W., Oetter, N., Stelzle, F. and Schmidt, M., "Investigation of Laser Induced Breakdown Spectroscopy (LIBS) for the Differentiation of Nerve and Gland Tissue—A Possible Application for a Laser Surgery Feedback Control Mechanism," *Plasma Science and Technology*, 18(6), 654-660 (2016).
- [34] Huang, H., Yang, L.M., Bai, S. and Liu, J., "Smart surgical tool," *Journal of biomedical optics*, 20(2), 028001 (2015).
- [35] Abbasi, H., Rauter, G., Guzman, R., Cattin, P.C. and Zam, A., "Plasma plume expansion dynamics in nanosecond Nd: YAG laserosteotome," *Proc. SPIE 10505*, 1050513, (2018).
- [36] Nazeri, M., Majd, A.E., Massudi, R., Tavassoli, S.H., Mesbahinia, A. and Abbasi, H., "Laser-Induced Breakdown Spectroscopy Via the Spatially Resolved Technique Using Non-Gated Detector," *Journal of Russian Laser Research*, 37(2), 164-171 (2016).
- [37] Sansonetti, J.E. and Martin, W.C., "Handbook of basic atomic spectroscopic data," *Journal of Physical and Chemical Reference Data*, 34(4), 1559-2259 (2005).

Chapter 4:
Monitoring laser-induced thermal damage during
laserosteotomy: Using LIBS to detect carbonization and
dehydration

4.1. Effect of cooling water on ablation during Er:YAG laserosteotomy of hard bone

Initially, we investigated the effect of using cooling water during Er:YAG laserosteotomy of bone. We experimentally showed that bone under long-pulse Er:YAG irradiation can survive for only a few pulses without irrigation. We also experimentally showed that an Er:YAG beam cannot pass a layer of water beyond approximately 1 mm (energy dependent). The result was orally presented at the Third International Conference on Applications of Optics and Photonics, 2017, Faro, Portugal, and later published in Proc. SPIE.

Publication: Hamed Abbasi, Lina Beltrán, Georg Rauter, Raphael Guzman, Philippe C. Cattin, and Azhar Zam "Effect of cooling water on ablation in Er:YAG laserosteotomy of hard bone", *Proc. SPIE* 10453, Third International Conference on Applications of Optics and Photonics, 104531I (22 August 2017); <https://doi.org/10.1117/12.2272138>

Copyright notice: Copyright 2017 Society of Photo-Optical Instrumentation Engineers (SPIE).

PROCEEDINGS OF SPIE

[SPIDigitalLibrary.org/conference-proceedings-of-spie](https://spiedigitallibrary.org/conference-proceedings-of-spie)

Effect of cooling water on ablation in Er:YAG laserosteotome of hard bone

Hamed Abbasi, Lina Beltrán, Georg Rauter, Raphael Guzman, Philippe C. Cattin, et al.

Hamed Abbasi, Lina Beltrán, Georg Rauter, Raphael Guzman, Philippe C. Cattin, Azhar Zam, "Effect of cooling water on ablation in Er:YAG laserosteotome of hard bone," Proc. SPIE 10453, Third International Conference on Applications of Optics and Photonics, 104531I (22 August 2017); doi: 10.1117/12.2272138

SPIE.

Event: Third International Conference on Applications of Optics and Photonics, 2017, Faro, Portugal

Effect of Cooling Water on Ablation in Er:YAG Laserosteotome of Hard Bone

Hamed Abbasi*^a, Lina Beltrán^a, Georg Rauter^b, Raphael Guzman^c, Philippe C. Cattin^d, Azhar Zam*^a

^a Biomedical Laser and Optics Group, Department of Biomedical Engineering, University of Basel, Gewerbestrasse 14, CH-4123 Allschwil, Switzerland

^b Bio-Inspired RObots for Medicine-Lab., Department of Biomedical Engineering, University of Basel, Gewerbestrasse 14, CH-4123 Allschwil, Switzerland

^c Department of Neurosurgery, University Hospital Basel, Basel, Switzerland

^d Center for Medical Image Analysis and Navigation, Department of Biomedical Engineering, University of Basel, Gewerbestrasse 14, CH-4123 Allschwil, Switzerland

ABSTRACT

The aim of this paper is to examine the effect of pig bone immersion in different levels of cooling water during laser ablation with a Er:YAG laser. The laser worked at 2940 nm wavelength and 10 Hz repetition rate in microseconds pulse duration regime. The bone was immersed in different levels of cooling water in a sample container for preventing carbonization. The bone samples were ablated with fixed deposited energy to investigate at which water level Er:YAG lasers start ablating bone through a layer of water. Results showed that the maximum level of water that laser can pass through to start the ablation nonlinearly depends on pulse energy.

Keywords: Laserosteotome, ablation, carbonization, cooling water, porcine bone, Er:YAG, microsecond pulse, minimally invasive surgery

1. INTRODUCTION

Smart surgical tools are devices that can help surgeons reduce possible medical errors. Reducing medical errors are important [1]. Some of these lethal medical errors can occur during surgery; therefore, developing smart surgical tools that prevent medical errors is necessary. A laserosteotome would be one such smart surgical system that can help surgeons in cutting hard and soft tissues in a safe and efficient manner. Laserosteotomes are applied in the fields of orthopedics, cranio-maxillofacial surgery, neurosurgery, otolaryngology, traumatology, and spine surgery. By performing this kind of minimal invasive osteotomies (bone cuts) the duration of hospital stays and rehabilitation is expected to be reduced. In comparison with mechanical tools, it has been proven that laserosteotomes have significant advantages such as non-contact interaction, minimal invasiveness, precise and small cuts based on pre-operative planning, functional cut geometry (smart cuts), accelerated healing, and less trauma [2-4]. However, without using any cooling agent soon after starting the ablation the bone would start to carbonize and bone healing will be impeded, therefore some kind of cooling system is necessary in combination with laserosteotome. In our current setup, we use an Er:YAG laser because it is one of the best lasers for cutting the bones [2]. The principle of bone ablation with Er:YAG lasers is based on laser energy absorption by water in the bone. So simply immersing the bone in water for cooling will only lead to an evaporation of the surrounding water, but not to cutting of bone. This behavior strongly depends on the wavelength of the laser. Lasers at other wavelengths would allow bone cutting inside water [5]. Moreover, it has been shown that different water cooling conditions of spray systems in Er:YAG laser ablation of hard dental tissues influence ablation efficiency [6]. The aim of this paper is to investigate limitation of water cooling conditions (maximum level of cooling water) that would still allow laser ablation with Er:YAG lasers. Knowing the maximum water level that still allows bone ablation is important for adjusting the diameter of the cooling water droplet in spray systems or the height of water in a running water systems for irrigation in Er:YAG laserosteotomes.

*hamed.abbasi@unibas.ch; phone +41 (0)61 207 54 61; <http://dbe.unibas.ch/blog>

*azhar.zam@unibas.ch; phone +41 (0)61 207 54 60; <http://dbe.unibas.ch/blog>

2. METHODOLOGY

2.1 Bone sample

In this paper, fresh porcine bone parts from the femur of Swiss pigs were used to minimize the post-mortem changes as much as possible. The bones were kept in the deep freezer between the scarification of the animal to the starting day of the experiment. The temperature of the freezer was set to -18° centigrade. Four hours before the starting of the experiment, the bones were moved from freezer to the refrigerator which was set to $+4^{\circ}$ centigrade. Soft tissues were removed from the surface of the bones using a surgical scalpel.

2.2 Laser

A pulsed Er:YAG (Erbium-doped yttrium aluminium garnet) laser which emits an infrared beam at 2940 nm was used in this experiment. The laser is a flash lamp pumped Er:YAG laser that emits pulses in the microseconds regime. The laser could emit a laser beam with a repetition rate in the range of 10 to 50 Hz. In this paper, the repetition rate was set to 10 Hz. The output pulse energy of the laser was adjustable. Moreover, the pulse duration of the laser was adjustable, but not in an independent manner, as soon as applying any change to the pulse duration, the pulse energy of the laser was changed and vice versa. We selected seven different pulse energies (7 different pulse durations) for the experiment in which the specification can be seen in Table 1.

Table 1. Parameters of the experiments.

Number of the experiment	Parameters of the laser				
	Pulse energy [mJ]	Pulse duration [μ s]	Pulse Power [kW]	Repetition rate [Hz]	Average power [W]
1	100	201	0.50	10	1.0
2	160	246	0.65	10	1.6
3	220	286	0.77	10	2.2
4	260	321	0.81	10	2.6
5	300	360	0.83	10	3.0
6	340	402	0.85	10	3.4
7	380	436	0.87	10	3.8

The pulse energy of the laser was measured using a power meter (ES220C sensor connected to PM100D meter, Thorlabs). Moreover, the pulse duration and repetition rate of the laser were checked using a PbSe fixed gain detector (PDA20H, Thorlabs) connected to a precise scopometer (Fluke 190-504). An IR reflective neutral density filter (NDIR20A, Thorlabs) and an IR band pass filter (FB3000-500, Thorlabs) were used for reducing the power at the detector and filtering the flash pump pollution, respectively, during measurement of the pulse durations and repetition rates.

2.3 Optical setup

The laser line was focused on the surface of the bones using an uncoated CaF₂ plano-convex lens (WG51050, Thorlabs) with a focal length of +80.0 mm. This focusing system provides a spot size in the order of a couple of hundreds of micrometers at the focal length of the lens. A broadband sapphire window with an anti-reflection coating (WG31050-D, Thorlabs) was put right after the lens to prevent any possible damage to the surface of the lens. The laser line was vertically directed to the surface of the bone from above by placing a gold mirror (ME05-M01, Thorlabs) between the laser head and the focusing lens, while bones were in a cylindrical container with a diameter of 77 mm. Figure 1. Shows the schematic of the experimental setup.

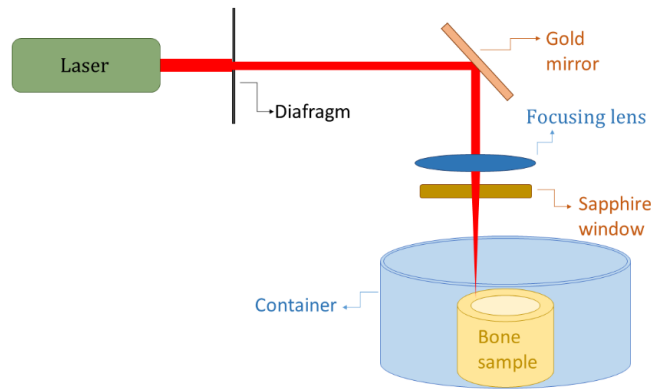


Figure 1. The schematic of the experimental setup.

A precise syringe was used to add/remove the water into the container for realizing different heights of water above the bone. The laser pulses were started as soon as the bone was covered with 2 mm of water above the surface. Over time, the water was gradually removed from the container. As soon as an ablation process was initiated (observed) the extraction of water was stopped and the height of the water over the bone was calculated based on the amount of extracted water. In this way, the maximum height of water through which the laser can initiate bone ablation was obtained.

3. RESULTS

It is clear that the more energy is applied the higher is the ablation efficiency. For example, we measured the ablated volume of the bones with three different energies, 220, 260 and 310 mJ after 5 seconds of laser radiation and ablated volumes were 0.25, 0.38 and 0.61 mm³ respectively. For these three different energies, 114 mL/min water spray was used as cooling system. The ablated volumes were measured using a microCT (computed tomography, Skyscan) system. The resolution of the CT system was isotropically 18 μm. Mainly, this paper is going to answer the question that what is the maximum height of water that laser can pass through to start the ablation process. Figure 2 shows the diagram of different applied energies (in the horizontal axis) vs. height of the water above the bone (in the vertical axis). Each experiment was done three times and each repetition was done on a different bone. The error bar is also depicted in the diagram. As becomes clear in the diagram, the maximum height of the water increases nonlinearly by increasing the energy. A polynomial fit which is visible in the diagram with red color shows nonlinearity of the behavior.

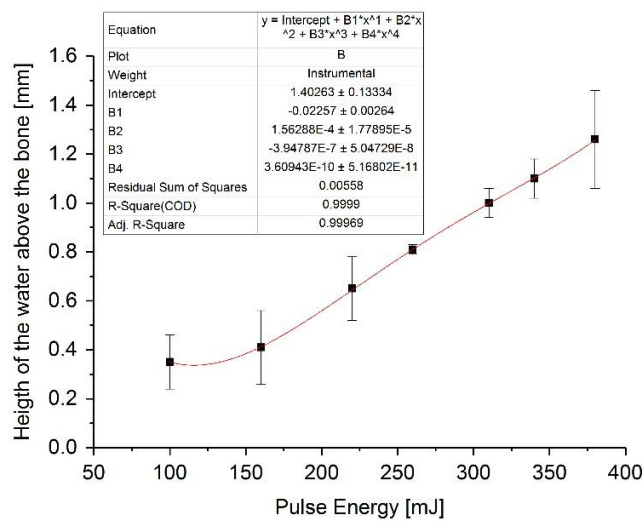


Figure 2. The height of the water above the bone for different applied pulse energies.

4. CONCLUSION

Laser pulses with higher energy leads to a higher ablation efficiency (ablated bone volume per laser pulse). In this experiment, more volume was ablated at higher energy levels, as expected. However, the aim of this paper was not to measure the ablation efficiency. The main aim of this paper was to find the maximum height of water that laser can pass through to start the ablation process. It was observed that the maximum height of the water above the bone increased by increasing the energy in a nonlinear manner. The obtained data is useful to design any kind of irrigation cooling system. The diameter of the droplet of water in spray system or height of water in running water mode can be determined using these results. We observed that without using cooling water, the bone immediately starts to carbonize and therefore some kind of cooling system is necessary for any laserosteotome. It could be observed that the maximum height of the water above the bone to start the ablation process is in the order of 1 mm. This low height of water is not enough to cover/fill the spot again with water after the first couple of laser pulses. The reasons seem to be that the generated air pressure close to the spot point of the ablation expels water; also, the bone surface is hydrophobe and prevents water from entering the ablation spot. Therefore, the irrigation system should be either realized in form of a running water or a spray system. The obtained laser-water interaction result of this paper can help to design any different cooling systems for Er:YAG laserosteotomes.

ACKNOWLEDGMENTS

The authors gratefully acknowledge funding of the Werner Siemens Foundation through the MIRACLE project. Moreover, the authors gratefully acknowledge Mr. Marek Zelechowski for his help in code writing to operate the laser.

REFERENCES

- [1] Makary, M.A. and Daniel, M., "Medical error—the third leading cause of death in the US, " *Bmj*, 353, 2139-2139 (2016).
- [2] Jowett, N., Wöllmer, W., Reimer, R., Zustin, J., Schumacher, U., Wiseman, P.W., Mlynarek, A.M., Böttcher, A., Dalchow, C.V., Lörincz, B.B. and Knecht, R., "Bone ablation without thermal or acoustic mechanical injury via a novel picosecond infrared laser (PIRL), " *Otolaryngology--Head and Neck Surgery*, 150(3), 385-393 (2014).
- [3] Baek, K.W., Deibel, W., Marinov, D., Griessen, M., Dard, M., Bruno, A., Zeilhofer, H.F., Cattin, P. and Juergens, P., "A comparative investigation of bone surface after cutting with mechanical tools and Er:YAG laser," *Lasers in surgery and medicine*, 47(5), 426-432 (2015).
- [4] Beltrán, L., Abbasi, H., Rauter, G., Friederich, N. F., Cattin, P. and Zam. A. "Effect of laser pulse duration on ablation efficiency of hard bone in microseconds regime" the III International Conference on Applications in Optics and Photonics (2017).
- [5] Tulea, C.A., Caron, J., Gehlich, N., Lenenbach, A., Noll, R. and Loosen, P., "Laser cutting of bone tissue under bulk water with a pulsed ps-laser at 532 nm, " *Journal of biomedical optics*, 20(10), 105007-105007 (2015).
- [6] Kuščer, L. and Diaci, J., "Measurements of erbium laser-ablation efficiency in hard dental tissues under different water cooling conditions, " *Journal of biomedical optics*, 18(10), 108002-108002 (2013).

4.2 Laser-induced breakdown spectroscopy as a potential tool for auto carbonization detection in laserosteotomy

After showing the importance of an irrigation system (Section 4.1), we demonstrated that LIBS can automatically detect carbonization in laser-irradiated bone. A possible error in the irrigation system can cause carbonization, therefore such feedback can stop further carbonization. The result of this work was published in the Journal of Biomedical Optics (SPIE).

Publication: Hamed Abbasi, Georg Rauter, Raphael Guzman, Philippe C. Cattin, and Azhar Zam "Laser-induced breakdown spectroscopy as a potential tool for autocarbonization detection in laserosteotomy," *Journal of Biomedical Optics* 23(7), 071206 (2 March 2018). <https://doi.org/10.1117/1.JBO.23.7.071206>

Copyright notice: Copyright 2018 Society of Photo-Optical Instrumentation Engineers (SPIE).

Laser-induced breakdown spectroscopy as a potential tool for autcarbonization detection in laserosteotomy

Hamed Abbasi
Georg Rauter
Raphael Guzman
Philippe C. Cattin
Azhar Zam

Laser-induced breakdown spectroscopy as a potential tool for autocarbonization detection in laserosteotomy

Hamed Abbasi,^{a,*} Georg Rauter,^b Raphael Guzman,^c Philippe C. Cattin,^d and Azhar Zam^{a,*}

^aBiomedical Laser and Optics Group, Department of Biomedical Engineering, University of Basel, Allschwil, Switzerland

^bBio-Inspired Robots for Medicine-Laboratory, Department of Biomedical Engineering, University of Basel, Allschwil, Switzerland

^cDepartment of Neurosurgery, University Hospital Basel, Basel, Switzerland

^dCenter for Medical Image Analysis and Navigation, Department of Biomedical Engineering, University of Basel, Allschwil, Switzerland

Abstract. In laserosteotomy, it is vital to avoid thermal damage of the surrounding tissue, such as carbonization, since carbonization does not only deteriorate the ablation efficiency but also prolongs the healing process. The state-of-the-art method to avoid carbonization is irrigation systems; however, it is difficult to determine the desired flow rate of the air and cooling water based on previous experiments without online monitoring of the bone surface. Lack of such feedback during the ablation process can cause carbonization in case of a possible error in the irrigation system or slow down the cutting process when irrigating with too much cooling water. The aim of this paper is to examine laser-induced breakdown spectroscopy as a potential tool for autocarbonization detection in laserosteotomy. By monitoring the laser-driven plasma generated during nanosecond pulse ablation of porcine bone samples, carbonization is hypothesized to be detectable. For this, the collected spectra were analyzed based on variation of a specific pair of emission line ratios in both groups of samples: normal and carbonized bone. The results confirmed a high accuracy of over 95% in classifying normal and carbonized bone.

© 2018 Society of Photo-Optical Instrumentation Engineers (SPIE) [DOI: [10.1117/1.JBO.23.7.071206](https://doi.org/10.1117/1.JBO.23.7.071206)]

Keywords: laser-induced breakdown spectroscopy; laserosteotomy; carbonized bone; smart surgery; feedback; differentiation.

Paper 170634SSR received Sep. 29, 2017; accepted for publication Feb. 12, 2018; published online Mar. 2, 2018.

1 Introduction

Over the past several years, there has been a particular interest in the development of laser surgery systems due to the advantages offered by laser-based cutting, including minimal invasiveness, noncontact interaction, precise and small cuts, functional cut geometry as well as less trauma.¹⁻⁶ Moreover, in comparison to other mechanical procedures, such as conventional surgery, bone showed faster healing after interventions with laserosteotomes.⁷ Studying the effect of different laser parameters on quality and efficiency of laser cutting in both soft and hard tissues is a topic of present interest.⁸⁻¹³ Although laserosteotomy has become a generally accepted technique in various surgical applications, this technique has two main drawbacks: lack of real-time information about depth of the cut and lack of information about the properties of the ablated tissue; as a result, critical structures of the body under or near the focal spot of the laser beam are prone to iatrogenic damage. In addition, to be a practical tool, clinical lasers have to be safe and effective in removing tissue with limited collateral damage. To reduce the thermal damage to the surrounding tissue, it is vital to use a cooling system to avoid carbonization. Carbonization happens when the tissue is heated up and all the water content is evaporated. Carbonization occurs not only in hard tissues but also in soft tissues. Carbonization not only reduces the ablation efficiency but also prolongs healing.^{14,15}

Lack of real-time information about depth of the cut can be solved by combining the laser surgery system with a coaxial real-time optical coherence tomography setup,^{16,17} and lack of information about the properties of the ablated tissue can be improved by connecting the system to an optical detection setup.¹⁸ Therefore, having a real-time feedback method to detect the possible carbonization in case of any possible error in the irrigation system is needed.

The potential optical detection methods to investigate the properties of the tissues include optoacoustic-based measurements^{19,20} and also spectroscopy-based measurements, including diffuse reflectance,^{21,22} laser-induced breakdown,²³⁻²⁵ Raman,^{26,27} and fluorescence spectroscopy.^{28,29} Among the above-mentioned optical methods, laser-induced breakdown spectroscopy (LIBS) showed its potential to detect the type of tissue with high accuracy. In LIBS, the light emitted from the ablation spot, which corresponds to the recombination spectra of ionized atoms and molecules, is collected with a spectrometer to resolve the atomic composition of the ablated sample. LIBS has been applied to differentiate between different tissue pairs with a high sensitivity and specificity (normally ranging from 70% to 100%), such as cartilage and cortical bone,³⁰ nerve and gland,³¹ nerve and fat³² as well as differentiation between oral soft and hard tissues.³³ Due to the compelling performance of LIBS in tissue characterization, we assume that applying LIBS also for detecting carbonization in laser surgery will be possible while tissue characterization can be performed in parallel.

*Address all correspondence to: Hamed Abbasi, E-mail: hamed.abbasi@unibas.ch; Azhar Zam, E-mail: azhar.zam@unibas.ch

The aim of this study is to differentiate between normal and carbonized hard porcine bone samples by monitoring the laser-driven plasma generated during a nanosecond pulse ablation using a frequency-doubled nanosecond Nd:YAG laser. A high-resolving power echelle spectrometer connected to an intensified CCD (ICCD) was employed to detect carbonization. The ICCD was capable of collecting LIBS signals with high temporal resolution (ps) and also short integration time (ns) to measure spectra for the classification of the samples. The analytical approach of calculating ratios of values of specific pairs of emission lines was taken to perform the differentiation between two groups of samples: normal (noncarbonized) and carbonized porcine bone. Then the sensitivity, specificity, and accuracy of the method were calculated afterward. Based on the results of the current study, we aim at proceeding LIBS-based carbonization detection also in real time. A successful real-time autodetection of carbonization in laserosteotomy will increase the safety of laserosteotomes. Additionally, this proof of principle study is intended to pave the way for *in vivo* experiments with an LIBS-based autcarbonization detection system in laser surgery.

2 Materials and Methods

2.1 Sample Preparation

Fresh porcine femur bone was used as a sample in this experiment. The bone samples were kept in a freezer between the slaughtering of the pig to the starting day of the experiment. The temperature of the freezer was set to -18°C . Four hours before starting the experiment, the bones were moved from the freezer to the refrigerator ($+4^{\circ}\text{C}$). Soft tissues were removed from the bone's surface using a surgical scalpel. Five bisected bones with the height of ca. 3 cm were used as samples. One half of each sample was irradiated by a microsecond Er:YAG laser (DPM-15, 3mikron, Pantec, Liechtenstein) with a pulse energy of 90 mJ and a 10-Hz repetition rate for 30 s without any cooling water to create a carbonized layer on the bone's surface; the other half of the bone remained untouched as a noncarbonized reference sample. To confirm bone carbonization and assess the carbon bonding, Raman spectroscopy was employed. Er:YAG bone ablation at $3\ \mu\text{m}$ is based on absorption of the laser beam mainly by the water content of the bone. In contrast, with Nd:YAG ($0.5\ \mu\text{m}$) lasers, ablation is mainly based on hydroxyapatite absorption.^{15,34} Therefore, in Er:YAG ablation without rewetting the ablation area, the surface of the bone will carbonize faster.

2.2 Ethics Committee Approval

Ethics committee approval was not necessary for this work as the bone samples were commercially available as regular food obtained from the local slaughterhouse.

2.3 Laser Setup

Usually, LIBS measurement systems consist of two main parts: an ablating laser with an appropriate focusing setup and a spectrometer with the appropriate optics for collecting the emission light. A delay generator can be added to the setup optionally to have a time-resolved measurement with higher signal-to-noise ratio. Spatially resolved measurement is an alternative method to increase the signal-to-noise ratio in LIBS.³⁵ In this experiment, a flash-lamp-pumped Nd:YAG laser (Q-smart 450,

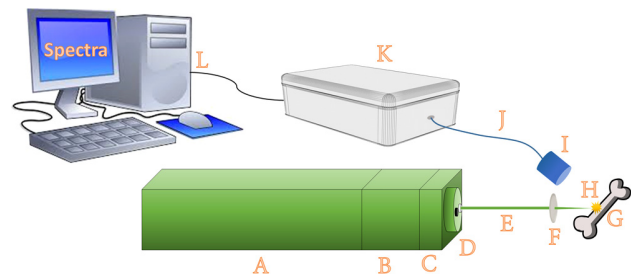


Fig. 1 Schematics of the LIBS setup: A, laser (flash-lamp-pumped Nd:YAG), B, second-harmonic generator; C, harmonic separator; D, beam blocker; E, laser beam; F, focusing lens; G, bone sample; H, generated plasma; I, light collector; J, fiber optic; K, spectrometer (echelle); and L, computer.

Quantel, France) running in its second harmonics of 532 nm with 5-ns pulse duration was used to ablate both normal and carbonized bone samples. The 1064-nm mode of the beam was separated and blocked using a nonlinear crystal, and a beam blocker installed right after the harmonic generator, respectively. The laser was operated at 108 mJ per pulse and 1-Hz repetition rate. The initial output beam of the laser with 6.5-mm diameter was directly focused onto the sample's surface using an uncoated CaF₂ planoconvex lens (LA5458, Thorlabs) with a focal length of 80 mm.

2.4 Spectroscopy Setup

An echelle spectrometer with a wavelength range of 200 to 975 nm connected to an ICCD was used to reveal the spectral distribution of the laser-generated plasma light. The spectral resolution ($\lambda/\Delta\lambda$) of the spectrometer was more than 4000. The CCD was cooled down to -30°C to reduce the background noise level. A fiber optic with a $50\text{-}\mu\text{m}$ core connected to a UV-NIR light collector with an F -number of 2 was used to guide the plasma light into the spectrometer. A gate delay of $1\ \mu\text{s}$ between the laser shot and opening of the intensifier was applied to remove the continuum emission of the plasma. The gate width was set to $200\ \mu\text{s}$. Both gate delay and width were applied using the internal delay generator of the ICCD. Figure 1 shows the schematic of the LIBS setup.

2.5 Data Analysis

The bone samples were separated into two groups based on their carbonization: normal bone as a control group and carbonized bone as a test group. Each group consisted of five bones. One hundred shots were recorded from each side, 50 from the normal side and 50 from the carbonized side. In total, 500 spectra were recorded, 250 from each group. Then, to determine the elemental composition of the bone samples, the atomic emissions in the recorded LIBS spectra of both normal and carbonized bones were mapped with the National Institute of Standards and Technology atomic emission database.³⁶ After finding the related peaks of the different atomic elements, the wavelengths and the intensities of those reproducible peaks, which appeared in both groups, were stored in a separate file. Among the stored peaks, two peaks with the highest reproducible ratio difference in two groups of samples among all 500-recorded spectra were selected. Finally, the ratio between the intensity of the selected peak pairs was calculated, and a ratio threshold was found to have a maximum accuracy (maximum number of true positive

and also true negative). The analysis aims to determine the class membership within the normal and carbonized bone groups. This ratio analysis allows for more robust results, as it is more stable than the absolute or normalized intensity of emission lines in the spectra of a given tissue type.³² The performance of the classifier was evaluated using receiver operating characteristic (ROC). Moreover, statistical parameters of the classifier, including true positive rate (sensitivity), true negative rate (specificity), positive predictive value (precision), negative predictive value, and accuracy, were calculated for each sample separately and also totally for all collected spectra.

3 Results

The elements detected in the bone samples through LIBS were identified as carbon (C), hydrogen (H), oxygen (O), calcium (Ca), sodium (Na), magnesium (Mg), zinc (Zn), and strontium (Sr). In addition to the atomic emission line of carbon, a molecular line of carbon-to-carbon bonding (C_2) was also observed. This result is in line with results described in literature.^{30–32,37–44} Note that the collected spectra may include emission lines of the elements found in the ambient air. Interestingly, the higher concentration of carbon in carbonized samples was not only observed in the average intensity of pure carbon emission line (13.77 for carbonized samples as compared with 3.15 for normal samples) but also in the carbon-related molecular emissions of the C_2 (10.12 for carbonized samples as compared with 4.38 for normal samples). Moreover, a reduction in the emission intensity of the hydrogen line was observed in the carbonized sample compared to the normal one (from 9.08 to 5.05). Decreasing hydrogen emission intensity and increasing carbon emission intensity seem to indicate that the bone has dried out and will be followed by subsequent carbonization if not properly rehydrated before continuing with the laser ablation. In addition to the atomic and molecular LIBS, Raman spectroscopy results also show a change in the carbon bonding. The

Raman spectra of normal and carbonized bones are shown in Fig. 2.

As shown in Fig. 2, the Raman spectra of normal and carbonized bone samples, which both are normalized to the carbon-to-carbon bonding intensity at 1589 cm^{-1} (highlighted by light yellow in the picture),^{45–47} show a significant reduction in the C–H bonding between 2870 to 3010 cm^{-1} ^{46–49} and also O–H bonding between 3380 to 3530 cm^{-1} ^{45,46,50} of the carbonized bone sample. Moreover, there is some reduction in intensity of the bonding of the carbonized bone related with phosphate ($PO_4^{3-}\nu_2$) around 422 cm^{-1} , double peak of phosphate antisymmetric bending frequency ($PO_4^{3-}\nu_4$) around 566 and 636 cm^{-1} , proline around 835 cm^{-1} , phosphate ($PO_4^{3-}\nu_1$) around 883 cm^{-1} , phosphate ($PO_4^{3-}\nu_3$) around 1024 cm^{-1} , amide III (primarily from the in-phase combination of NH in-plane bend and CN stretch) around 1288 cm^{-1} , pentosidine around 1495 cm^{-1} , and amide I (primarily from the C=O stretch and C–H bending) around 1687 cm^{-1} .^{48,49,51–53} Results of the Raman spectroscopy are in a good agreement with molecular LIBS. Increase in carbon concentration of the carbonized bone sample (obtained from atomic LIBS data) in combination with results of the Raman and molecular LIBS, which show bonding of carbon to carbon has not broken while that of carbon to other elements have broken, indicates that the carbonization has occurred in the carbonized samples.

Figures 3(a) and 3(b) show LIBS spectra of normal and carbonized bone samples, respectively.

As shown in Figs. 3(a) and 3(b), the ratio of the intensities between the sodium (Na) peak at 321.2 nm (from $2s^22p^53p$ to $2s^22p^53s$) and the calcium peak at 612.2 nm (from $3p^64s5s$ to $3p^64s4p$) is different in normal and carbonized bone. These two prominent peaks with a high difference in intensity ratio in two groups of samples, which had the lowest Wilks' lambda between the observed peak pairs, can be used for differentiation between carbonized and noncarbonized bone. Figure 4 shows

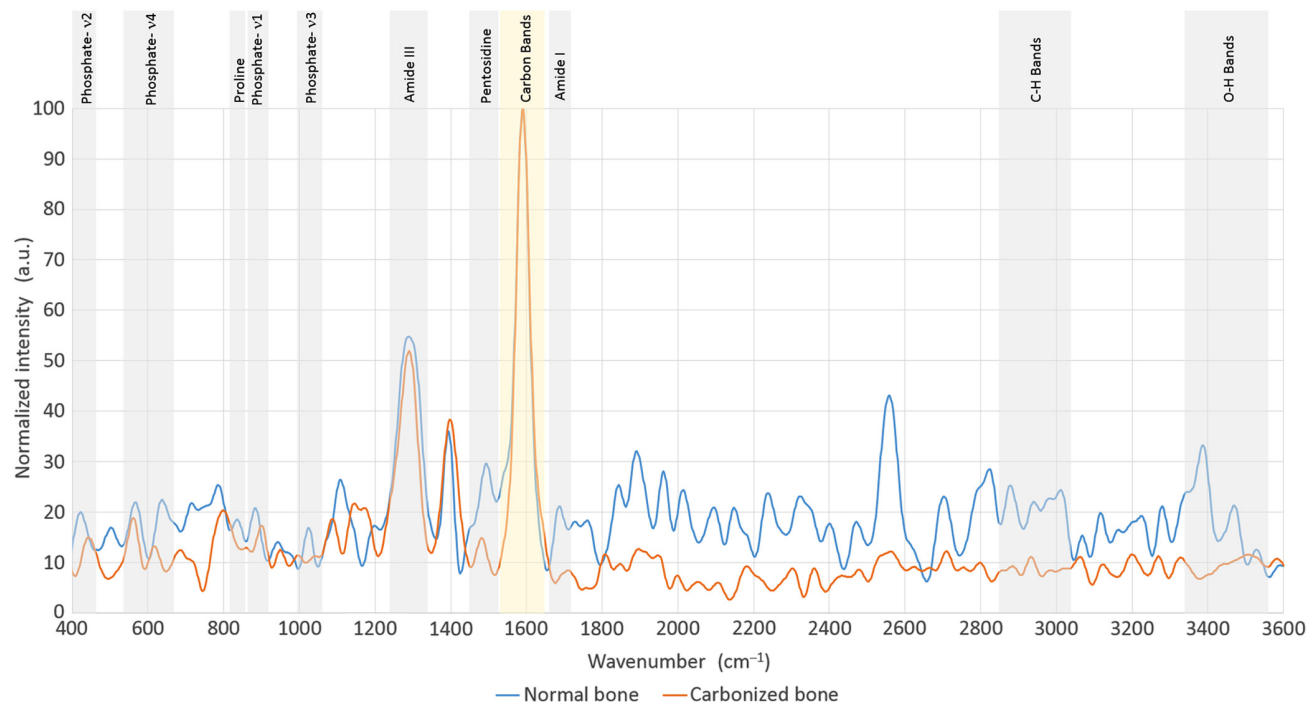


Fig. 2 Raman spectra of normal and carbonized bone samples.

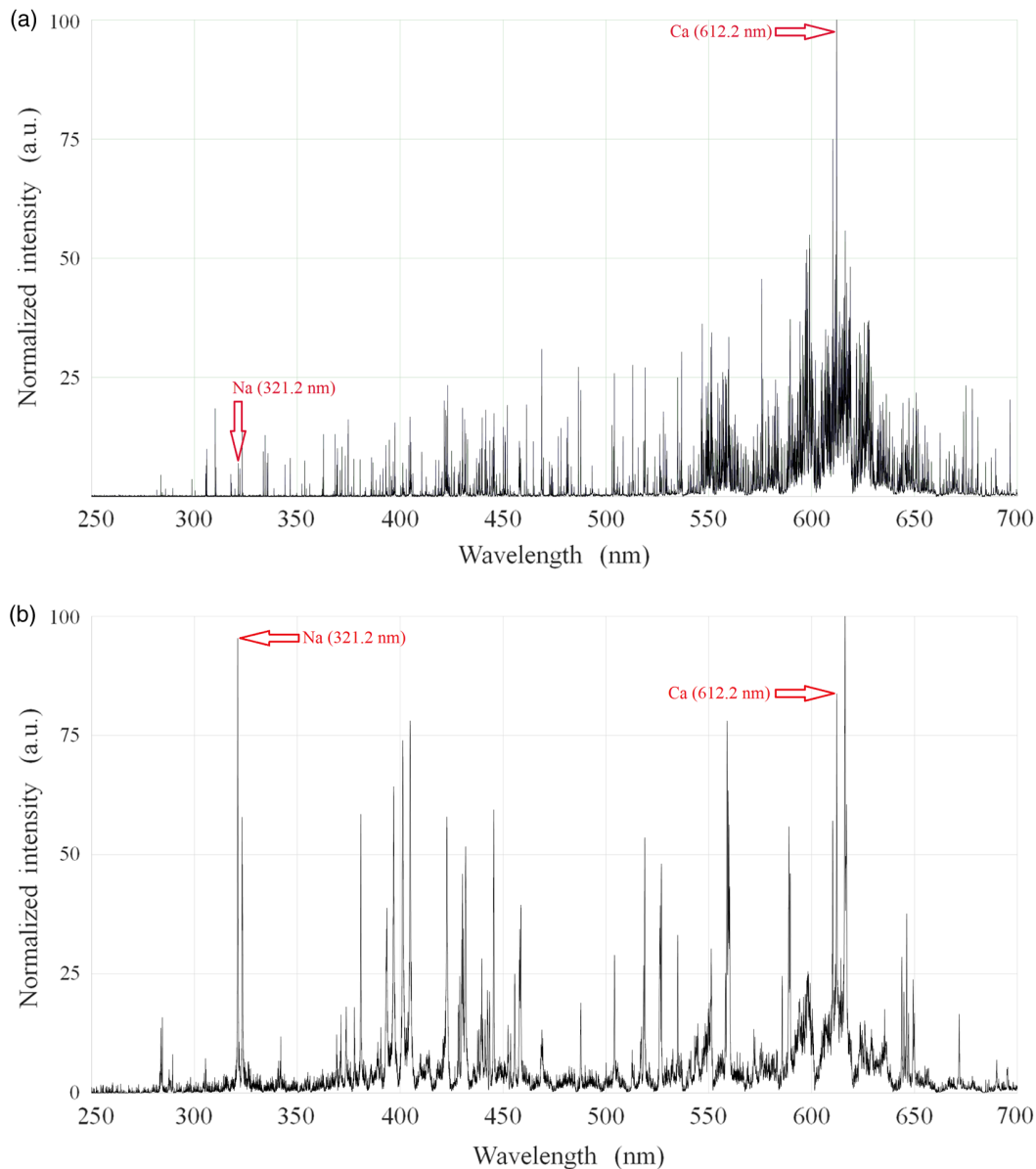


Fig. 3 LIBS spectra of (a) normal and (b) carbonized bone sample showing selected peak pairs.

the sodium-to-calcium intensity ratio for all samples. The first 50 data points were obtained from sample 1, the second 50 data points from sample 2, and so on, until the last 50 data points from sample 5.

As shown in Fig. 4, most of the ratios related to normal bone are below the threshold line, and most of the ratios related to carbonized bone are above the threshold line. The threshold line was selected in a way to maximize the accuracy of the classifier. Statistical parameters of the classifier, including true positive rate (sensitivity), true negative rate (specificity), positive predictive value (precision), negative predictive value, and accuracy, are shown in Table 1.

As written in the last column of Table 1, all statistical parameters (obtained from 500 spectra) are above 92%. The ROC curve was also plotted, and the area under curve (AUC) was calculated to confirm the performance of the classifier. Figure 5 shows the ROC curve. The AUC of the curve was over 98%.

4 Discussion

In this paper, LIBS showed reliable result (accuracy of more than 95%) for carbonization detection in *ex vivo* condition. *Ex vivo* performance of LIBS for detecting carbonized bone seems reliable even with simple ratio-threshold-based methods. Thus, the *ex vivo* results are very likely to transfer also to *in vivo* experiments. However, the achieved accuracy from the *ex vivo* condition is likely to decrease for future *in vivo* experiments, where bone is not so well-prepared. Possible reasons could be the influence of the superficial contamination of the probing surfaces with blood or any rinsing solutions, such as saline or cooling water during the clinical procedures. A possible solution could be employing a double-pulse LIBS system. In double-pulse LIBS, the first pulse can remove the liquid on the focal point; then the second pulse quickly reaches the target surface before the target area is refilled with liquid. From a machine learning point of view, to further increase detection accuracy,

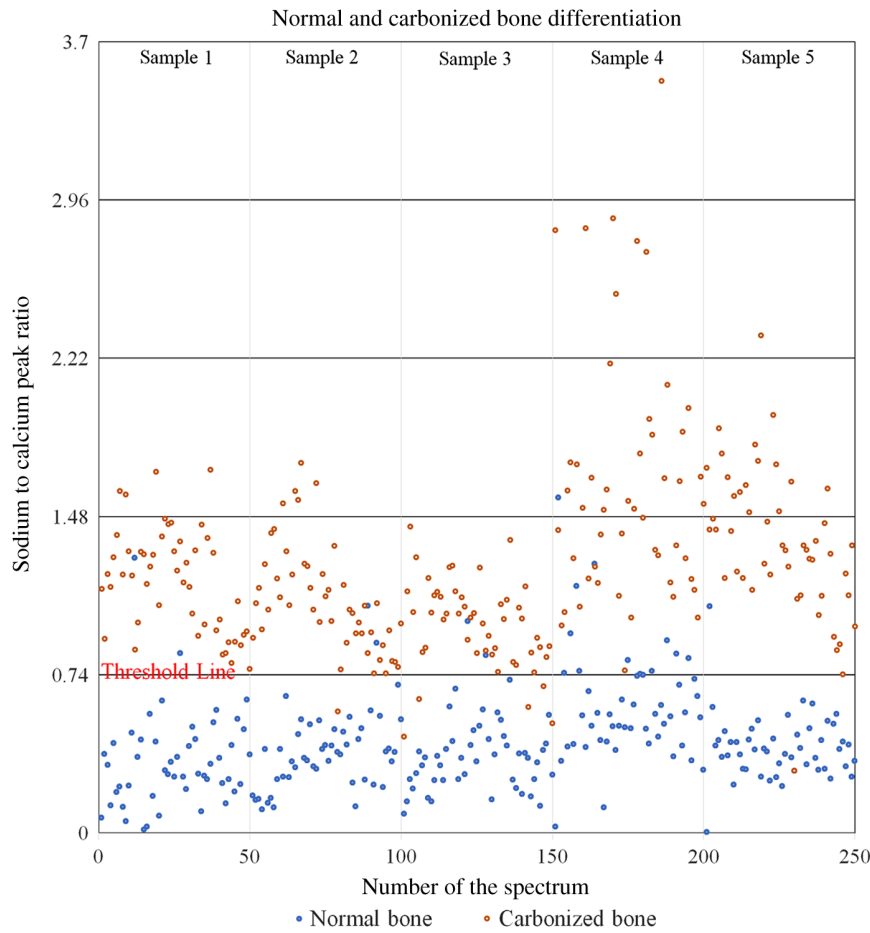


Fig. 4 Sodium-to-calcium intensity ratio for all samples.

Table 1 Statistical parameters of the classifier.

	Sample 1	Sample 2	Sample 3	Sample 4	Sample 5	Total
True positive	50	49	45	50	49	243
False positive	2	2	2	12	1	19
True negative	48	48	48	38	49	231
False negative	0	1	5	0	1	7
True positive rate (sensitivity) (%)	100	98	90	100	98	97
True negative rate (specificity) (%)	96	96	96	76	98	92
Positive predictive value (precision) (%)	96	96	96	81	98	93
Negative predictive value (%)	100	98	91	100	98	97
Accuracy (%)	98	97	93	88	98	95

more complex classifiers could be used that, e.g., also involve additional intensities of other elements. While the number of false positives in this experiment was very low (19 out of 500), but false positives are not a real issue in this case. From a safety point of view, it is better to assume that carbonization has occurred and increases irrigation to avoid future

carbonization at the cost of a reduced cutting speed. In the current experiment, the soft tissue was carefully removed from the surface of the bone using a surgical scalpel, but it is suggested to consider the first initial shots as a cleaning shot. Although it has been reported that the type of nutrition and also age may influence the elemental composition of the tissues, this will not

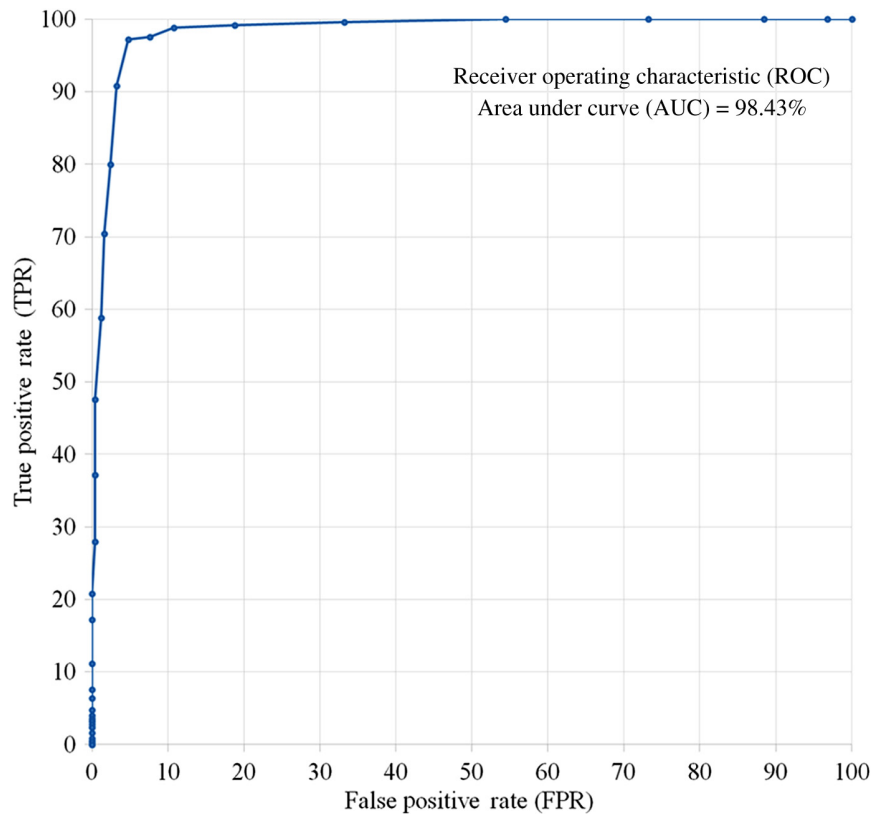


Fig. 5 ROC curve.

significantly influence the differentiation performance in this study because only the most prominent emission lines were considered for classification.^{33,39} However, the differentiation performance could be improved by considering the average of multiple spectra for the analysis, but using multiple spectra in a real-time application is time-consuming both for collection and also data analysis. Moreover, it should be considered that using multiple spectra is a trade-off between the damage caused during the collection/calculation time and the increase in differentiation accuracy. Finally, it is worth noting that in this pilot study, a well-carbonized bone was used as a sample; therefore, in the further studies, the performance of the technique should also be evaluated with less carbonized samples to confirm the applicability of the proposed method.

5 Conclusion

The preliminary results of this study demonstrate that LIBS is a powerful technique for autcarbonization detection under *ex vivo* conditions by monitoring the plasma plumes occurring during laserosteotomy procedures. Based on the previous reports, the elements detected during the ablation were in agreement with those expected to be found in the elemental composition of bone. The intensity ratio of sodium and calcium enabled successful differentiation of carbonized bone from noncarbonized bone with high accuracy. Sensitivity and specificity of 97% and 92% were achieved, respectively. Therefore, this suggests that carbonization monitoring during laserosteotomy could be successfully achieved using an LIBS-based detection system. However, further research will be needed to confirm the potential *in vivo* clinical applicability of the proposed method.

Disclosures

The authors have no potential conflicts of interest to declare in this paper.

Acknowledgments

The authors gratefully acknowledge funding of the Werner Siemens Foundation through the Minimally Invasive Robot-Assisted Computer-Guided Laserosteotomy (MIRACLE) project. Moreover, the authors are particularly appreciative of the assistance given by Ms. Shohreh Khatami.

References

1. G. R. Gunaratne et al., "A review of the physiological and histological effects of laser osteotomy," *J. Med. Eng. Technol.* **41**(1), 1–12 (2017).
2. K.-W. Baek et al., "A comparative investigation of bone surface after cutting with mechanical tools and Er:YAG laser," *Lasers Surg. Med.* **47**(5), 426–432 (2015).
3. K.-W. Baek et al., "Clinical applicability of robot-guided contact-free laser osteotomy in cranio-maxillo-facial surgery: in-vitro simulation and in-vivo surgery in minipig mandibles," *Br. J. Oral Maxillofac. Surg.* **53**(10), 976–981 (2015).
4. N. Jowett et al., "Bone ablation without thermal or acoustic mechanical injury via a novel picosecond infrared laser (PIRL)," *Otolaryngology* **150**(3), 385–393 (2014).
5. C.-A. Tulea et al., "Highly efficient nonthermal ablation of bone under bulk water with a frequency-doubled Nd:YVO₄ picosecond laser," *Proc. SPIE* **8565**, 85656E (2013).
6. C.-A. Tulea et al., "Laser cutting of bone tissue under bulk water with a pulsed ps-laser at 532 nm," *J. Biomed. Opt.* **20**(10), 105007 (2015).
7. A. Pourzarandian et al., "Histological and TEM examination of early stages of bone healing after Er:YAG laser irradiation," *Photomed. Laser Ther.* **22**(4), 342–350 (2004).

8. L. Beltrán et al., "Effect of laser pulse duration on ablation efficiency of hard bone in microseconds regime," *Proc. SPIE* **10453**, 104531S (2017).
9. J. T. Walsh, T. J. Flotte, and T. F. Deutsch, "Er:YAG laser ablation of tissue: effect of pulse duration and tissue type on thermal damage," *Lasers Surg. Med.* **9**(4), 314–326 (1989).
10. Y.-M. Lee et al., "Average-power mediated ultrafast laser osteotomy using a mode-locked Nd:YVO₄ laser oscillator," *J. Biomed. Opt.* **12**(6), 060505 (2007).
11. D. Kundrat et al., "Endoluminal non-contact soft tissue ablation using fiber-based Er:YAG laser delivery," *Proc. SPIE* **9702**, 97020E (2016).
12. Y. Zhang et al., "Dependence of ablation depth on angle of incidence for hard tissue ablation using pulsed CO₂ laser," in *European Conf. on Biomedical Optics*, Paper No. 809216 (2011).
13. Y. Liu and M. Niemi, "Ablation of femoral bone with femtosecond laser pulses—a feasibility study," *Lasers Med. Sci.* **22**(3), 171–174 (2007).
14. H. Kang, I. Rizoiu, and A. Welch, "Hard tissue ablation with a spray-assisted mid-IR laser," *Phys. Med. Biol.* **52**(24), 7243–7259 (2007).
15. H. Abbasi et al., "Effect of cooling water on ablation in Er:YAG laser-osteotomy of hard bone," *Proc. SPIE* **10453**, 10453II (2017).
16. S. A. Boppart et al., "High-resolution optical coherence tomography-guided laser ablation of surgical tissue," *J. Surg. Res.* **82**(2), 275–284 (1999).
17. A. V. Shakhov et al., "Optical coherence tomography monitoring for laser surgery of laryngeal carcinoma," *J. Surg. Oncol.* **77**(4), 253–258 (2001).
18. R. Kanawade et al., "Pilot study of laser induced breakdown spectroscopy for tissue differentiation by monitoring the plume created during laser surgery—an approach on a feedback laser control mechanism," *Spectrochim. Acta Part B* **87**, 175–181 (2013).
19. H. K. Nguendon et al., "Characterization of ablated porcine bone and muscle using laser-induced acoustic wave method for tissue differentiation," *Proc. SPIE* **10417**, 104170N (2017).
20. E. Bay, A. Douplik, and D. Razansky, "Optoacoustic monitoring of cutting efficiency and thermal damage during laser ablation," *Lasers Med. Sci.* **29**(3), 1029–1035 (2014).
21. F. Stelzle et al., "In vivo optical tissue differentiation by diffuse reflectance spectroscopy: preliminary results for tissue-specific laser surgery," *Surg. Innov.* **19**(4), 385–393 (2012).
22. F. Stelzle et al., "Diffuse reflectance spectroscopy for optical soft tissue differentiation as remote feedback control for tissue-specific laser surgery," *Lasers Surg. Med.* **42**(4), 319–325 (2010).
23. F.-Y. Yueh et al., "Preliminary evaluation of laser-induced breakdown spectroscopy for tissue classification," *Spectrochim. Acta Part B* **64**(10), 1059–1067 (2009).
24. D. C. Jeong, P. S. Tsai, and D. Kleinfeld, "Prospect for feedback guided surgery with ultra-short pulsed laser light," *Curr. Opin. Neurobiol.* **22**(1), 24–33 (2012).
25. K. Henn et al., "A spectroscopic approach to monitor the cut processing in pulsed laser osteotomy," *Lasers Med. Sci.* **28**(1), 87–92 (2013).
26. L. A. Reisner et al., "A prototype biosensor-integrated image-guided surgery system," *Int. J. Med. Rob. Comput. Assisted Surg.* **3**(1), 82–88 (2007).
27. P. C. Ashok et al., "A Raman spectroscopy bio-sensor for tissue discrimination in surgical robotics," *J. Biophotonics* **7**(1–2), 103–109 (2014).
28. A. Douplik et al., "Limitations of cancer margin delineation by means of autofluorescence imaging under conditions of laser surgery," *J. Innovative Opt. Health Sci.* **3**(1), 45–51 (2010).
29. F. Krause et al., "Evaluation of selective calculus removal by a fluorescence feedback-controlled Er:YAG laser in vitro," *J. Clin. Periodontol.* **34**(1), 66–71 (2007).
30. F. Mehari et al., "Laser induced breakdown spectroscopy for bone and cartilage differentiation-ex vivo study as a prospect for a laser surgery feedback mechanism," *Biomed. Opt. Express* **5**(11), 4013–4023 (2014).
31. F. Mehari et al., "Investigation of laser induced breakdown spectroscopy (LIBS) for the differentiation of nerve and gland tissue—a possible application for a laser surgery feedback control mechanism," *Plasma Sci. Technol.* **18**(6), 654–660 (2016).
32. F. Mehari et al., "Investigation of the differentiation of ex vivo nerve and fat tissues using laser-induced breakdown spectroscopy (LIBS): prospects for tissue-specific laser surgery," *J. Biophotonics* **9**(10), 1021–1032 (2016).
33. M. Rohde et al., "The differentiation of oral soft-and hard tissues using laser induced breakdown spectroscopy—a prospect for tissue specific laser surgery," *J. Biophotonics* **10**, 1250–1261 (2017).
34. F. Scholkmann et al., "A review on continuous wave functional near-infrared spectroscopy and imaging instrumentation and methodology," *NeuroImage* **85**, 6–27 (2014).
35. M. Nazeri et al., "Laser-induced breakdown spectroscopy via the spatially resolved technique using non-gated detector," *J. Russ. Laser Res.* **37**(2), 164–171 (2016).
36. J. E. Sansonetti and W. C. Martin, "Handbook of basic atomic spectroscopic data," *J. Phys. Chem. Ref. Data* **34**(4), 1559–2259 (2005).
37. R. K. Gill et al., "Preliminary fsLIBS study on bone tumors," *Biomed. Opt. Express* **6**(12), 4850–4858 (2015).
38. O. Samek et al., "Quantitative laser-induced breakdown spectroscopy analysis of calcified tissue samples," *Spectrochim. Acta Part B* **56**(6), 865–875 (2001).
39. M. Tofanelli et al., "Spectroscopic analysis of bones for forensic studies," *Spectrochim. Acta Part B* **99**, 70–75 (2014).
40. R. K. Gill et al., "The effects of laser repetition rate on femtosecond laser ablation of dry bone: a thermal and LIBS study," *J. Biophotonics* **9**(1–2), 171–180 (2016).
41. J. H. Han et al., "Differentiation of cutaneous melanoma from surrounding skin using laser-induced breakdown spectroscopy," *Biomed. Opt. Express* **7**(1), 57–66 (2016).
42. H. Huang et al., "Smart surgical tool," *J. Biomed. Opt.* **20**(2), 028001 (2015).
43. M. Kasem et al., "Effect of the wavelength on laser induced breakdown spectrometric analysis of archaeological bone," *Spectrochim. Acta Part B* **101**, 26–31 (2014).
44. D. Santos et al., "Evaluation of femtosecond laser-induced breakdown spectroscopy for analysis of animal tissues," *Appl. Spectrosc.* **62**(10), 1137–1143 (2008).
45. B. D. Mistry, *A Handbook of Spectroscopic Data, Chemistry (UV, IR, PMR, CNMR and Mass Spectroscopy)*, Oxford Book Company, Jaipur (2009).
46. Z. Movasaghi et al., "Raman spectroscopy of biological tissues," *Appl. Spectrosc. Rev.* **42**(5), 493–541 (2007).
47. K. Kochan et al., "Pathological changes in the biochemical profile of the liver in atherosclerosis and diabetes assessed by Raman spectroscopy," *Analyst* **138**(14), 3885–3890 (2013).
48. M. D. Morris et al., "Recent developments in Raman and infrared spectroscopy and imaging of bone tissue," *Spectroscopy* **18**(2), 155–159 (2004).
49. M. D. Morris et al., "Raman assessment of bone quality," *Clin. Orthop. Relat. Res.* **469**(8), 2160–2169 (2011).
50. P. Meksiarun et al., "Comparison of multivariate analysis methods for extracting the paraffin component from the paraffin-embedded cancer tissue spectra for Raman imaging," *Sci. Rep.* **7**, 44890 (2017).
51. E. P. Paschalis et al., "Vibrational spectroscopic techniques to assess bone quality," *Osteoporosis Int.* **28**(8), 2275–2291 (2017).
52. J. W. Ager et al., "Deep-ultraviolet Raman spectroscopy study of the effect of aging on human cortical bone," *J. Biomed. Opt.* **10**(3), 034012 (2005).
53. M. D. Morris et al., "Kerr-gated time-resolved Raman spectroscopy of equine cortical bone tissue," *J. Biomed. Opt.* **10**(1), 014014 (2005).

Biographies for the authors are not available.

4.3. Pilot ex vivo study of laser-induced breakdown spectroscopy to detect bone dehydration: An approach for irrigation feedback in laserosteotomy

In Section 4.2, we showed that feedback on carbonization could help stop further carbonization in laserosteotomy; however, successful feedback on dehydration could help prevent carbonization in the first place, as dehydration is the precursory stage of carbonization. Therefore, we studied the ability of LIBS to detect self-dehydration over time. Assuming that the dehydration caused by gradual evaporation on the dehydrated bone happens in a similar fashion to laser-induced dehydration, this detection approach could be transferred to the real-time feedback systems of laserosteotomes. The result of this study was published as a conference proceeding.

Publication: Abbasi, H., Sugiarto, I., Rauter, G., Guzman, R., Cattin, P. and Zam, A., 2018. Pilot Ex Vivo Study of Laser-Induced Breakdown Spectroscopy to Detect Bone Dehydration: An Approach for Irrigation Feedback in Laserosteotomy. In *2018 International Conference on Electrical Engineering and Computer Science (ICEECS)*. <https://doi.org/10.5281/zenodo.3514693>

Pilot *Ex Vivo* Study of Laser-Induced Breakdown Spectroscopy to Detect Bone Dehydration: An Approach for Irrigation Feedback in Laserosteotomy

Hamed Abbasi
*Biomedical Laser and Optics Group,
 Department of Biomedical Engineering
 University of Basel*
 Allschwil, Switzerland
 hamed.abbasi@unibas.ch

Raphael Guzman
*Department of Neurosurgery
 University Hospital Basel*
 Basel, Switzerland
 raphael.guzman@unibas.ch

Irena Sugiarto
*Department of Biomedical Engineering
 Swiss German University, Tangerang,
 Indonesia, and
 University of Basel*
 Allschwil, Switzerland
 irena.sugiarto@student.sgu.ac.id

Philippe C. Cattin
*Center for medical Image Analysis and
 Navigation, Department of Biomedical
 Engineering,
 University of Basel*
 Allschwil, Switzerland
 philippe.cattin@unibas.ch

Georg Rauter
*Bio-Inspired ROBots for MEDicine-
 Lab, Department of Biomedical
 Engineering,
 University of Basel*
 Allschwil, Switzerland
 georg.rauter@unibas.ch

Azhar Zam
*Biomedical Laser and Optics Group,
 Department of Biomedical Engineering
 University of Basel*
 Allschwil, Switzerland
 azhar.zam@unibas.ch

Abstract— A successful laserosteotome should cut the bone without inducing thermal damage to the surrounding tissue, otherwise the healing process will be prolonged. To avoid such thermal damage, laserosteotomes typically employ an irrigation system with a pre-defined flow rate of cooling water. If this pre-defined flow rate is insufficient, for any reason, the laser beam will induce thermal damage by first dehydrating and then carbonizing the tissue. On the other hand, a too high water flow rate will result in lower ablation rates since the laser beam first needs to ablate the extra water before cutting bone, especially with lasers that water has a high absorption peak in their wavelengths, like Er:YAG and CO₂. While a feedback mechanism detecting carbonization has been demonstrated in literature already, it would be desirable to detect possible dehydration at an earlier stage (underirrigation) where the tissue damage is still negligible. This pilot study evaluates the applicability of laser-induced breakdown spectroscopy (LIBS) to detect bone dehydration already at its onset. The results confirmed a good accuracy of over 89 % (cross-validated) in classifying normal and dehydrated bone.

Keywords— LIBS, plasma spectroscopy, bone dehydration, minimally invasive surgery, laserosteotome

I. INTRODUCTION

In order to replace conventional bone cutting tools with laserosteotomes, laser systems have to cut the bone in a fast and safe manner without inducing any thermal damage to the surrounding tissue. Therefore, the beam of the laser needs to be complemented with an irrigation system to avoid thermal damage [1-6]. The flow rate of the water in the irrigation system should be set optimally as too little water causes carbonization of the bone or too much water reduces the cutting speed and achievable maximum cutting depth [7, 8]. Without any irrigation, the bone dehydrates after only a few laser pulses and then starts to carbonize [7, 8]. A feedback mechanism on dehydration would thus be suitable to control

the flow rate of the irrigation system. Laser-induced breakdown spectroscopy (LIBS) has been reported to be a fast and accurate analytical technique for detecting the type and properties of the tissues [9-20]; therefore, this method looks as a promising candidate to detect dehydration as well. Moreover, the authors have shown that laser-induced bone carbonization is detectable through a LIBS-based feedback mechanism [21]. Feedback on carbonization could help to stop further carbonization in laserosteotomy, while successful feedback on dehydration could help preventing carbonization in the first place, as dehydration is the precursory stage of carbonization. This pilot study examines the applicability of LIBS to discriminate fresh from dehydrated bone. A porcine femur bone bought from a local slaughterhouse (kept in the freezer before the experiment), was used as the non-dehydrated sample, henceforth called “fresh sample”. Also, a bone which was left open under room temperature conditions for 10 days was used as a “dehydrated sample”. We assumed that crystallization of water content of the bone in the freezer has not any significant effect on our result. A total of 50 laser shots from each sample were measured. Assuming that the dehydration caused by gradual evaporation on the dehydrated bone happens in a similar fashion to laser-induced dehydration and there is no major chemical decomposition over these 10 days, this detection approach could be transferred to the real-time feedback system of laserosteotomes.

II. MATERIALS AND METHODS

A. Bone Preparation

Two bisected porcine femur bone samples were used in this study. One bone was kept in room temperature for ten days, after removing the surrounding soft tissues (the dehydrated sample). The other bone sample was kept in a freezer to keep the water content stable (the fresh sample). The freezer temperature was set to -18°C . Four hours prior to the experiment the specimen was moved from the freezer

to the refrigerator with a temperature of +4° C. Later on, the surrounding soft tissues were removed from the surface of the bone with the help of a surgical scalpel. The experiments were carried out at room temperature.

B. Ethics Committee Approval

Since the used bone samples were commercially available as regular food obtained from the local slaughterhouse, ethics committee approval was not necessary.

C. Laser Source

The second harmonic beam line of a flashlamp-pumped Q-switched Nd:YAG laser (Q-smart 450, Quantel, France) at 532 nm was used to perform plasma-mediated ablation in both groups of samples. The laser emitted a pulsed beam with a duration of 5.2 ns and linewidth (FWHM) of fewer than 0.7 cm⁻¹. The energy and repetition rate of the laser were set to 108 mJ and 1 Hz, respectively. More information about the generation, separation, and blocking of the harmonics of the laser setup is explained in our previous work [11, 21]. The frequency-doubled output beam of the laser with 6.5 mm diameter was horizontally directed to an uncoated Calcium Fluoride plano-convex lens (LA5458, Thorlabs, USA) with a focal length of 80 mm which was placed perpendicular to the laser line and optical table. The high focusability of the employed laser (M-squared of less than 2), provided a high power density at the focal point. The focused light was guided to the surface of the bone samples from the side to generate a microplasma at the surface of the specimens.

D. Spectroscopy Setup

Due to the need for both, a high power resolution combined with a large bandwidth, an Echelle spectrometer was chosen to be used in this study for analyzing the emitted light from the laser-induced microplasma. The employed Echelle spectrometer resolved the input light with the resolving power of better than 4000 [a.u.] in the interval of 200 to 975 nm (aperture F/7). In total, the input light was separated into more than 28000 different wavelengths. A 16-bit intensified CCD (ICCD) with a built-in delay generator was used as the detector of the spectrometer. The spectrometer was synchronized with the Q-switch of the laser using a TTL 5 pulse to apply the desired time delay (Q-switch as a master and the spectrometer as a slave). The gate delay of 5 μs was applied to avoid collecting continuum radiation which could hide the atomic and molecular lines of the generated microplasma [22, 23]. In order to increase the signal to noise ratio (SNR), the ICCD was cooled down to -30° C to minimize the background noise (during the calibration and also the experiment). The experiments were run at the same temperature that was employed during calibration of the spectrometer (+25° C) in order to avoid misalignment caused by thermal expansion/contraction of the system. A UV-NIR light collector with an F-number of 2 connected to a fiber optic with a 50 μm core was used to collect the plasma emission light and deliver it to the spectrometer. No polarization/spatial-resolved technique was employed. All spectra were recorded in a time-resolved manner. Figure 1 shows the schematic of the employed time-resolved LIBS setup. As has been shown in the figure the

plasma light was collected at 45° in reference to the incident beam.

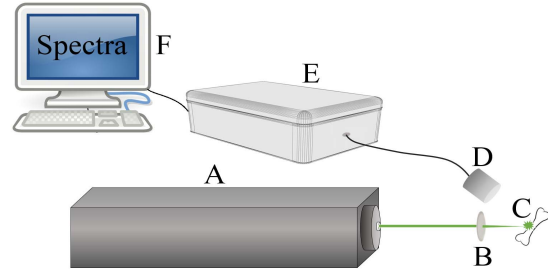


Fig. 1. The schematics of the LIBS setup. A: Laser (frequency-doubled Nd:YAG), B: Focusing lens, C: Generated plasma at the surface of the bone, D: Optical fiber and light collector, E: Echelle spectrometer, F: Computer.

E. Data Analysis

A total of 50 shots from the fresh sample and 50 shots from the dehydrated sample were taken, resulting in 100 spectra. After finding common peaks in both groups of samples which were in good agreement with those represented in the literature, 10 reproducible peaks among the whole spectra were chosen. Later on, 45 different ratios (all possible combinations) between the 10 chosen peak intensities were generated, using permutation without repetition. Canonical discriminant function analysis, as a well-known method in LIBS data processing [16, 24-26], was applied to these 45 peak intensity ratios to discriminate the fresh from the dehydrated bone. Lastly, the accuracy of the applied classifier was measured using a covariance matrix in both separate-groups and within-groups modes. In the within-groups mode, one-fold cross-validation was applied where each spectrum is classified by the function derived from the remaining ones.

III. RESULTS

A. Original Grouped Cases

The observed atomic lines in the bone samples through LIBS were identified as calcium (Ca), sodium (Na), potassium (K), hydrogen (H), nitrogen (N), iron (Fe), and zinc (Zn). The observed atomic lines were in agreement with those described in the literature [9-18]. Figure 2 shows the classification result of the original grouped cases, dehydrated (dry) bone as group type 1 (upper histogram), and fresh bone as group type 2 (lower histogram). As is clear from the histograms shown in Fig. 2, the distribution of the dehydrated bone measurements (type 1) has a mean value of 2.77 (with a standard deviation of 1.035) while the fresh bone cases have the mean value of -2.77 (with a standard deviation of 0.964).

By employing the covariance matrix in separate-groups mode (original grouped cases), all of the 50 dehydrated cases were classified correctly as dehydrated bone (100 % accuracy), and 49 out of the 50 fresh cases as a fresh bone (98 % accuracy). Therefore, by employing the generated canonical discriminant function, in total 99 % of original grouped cases were classified correctly.

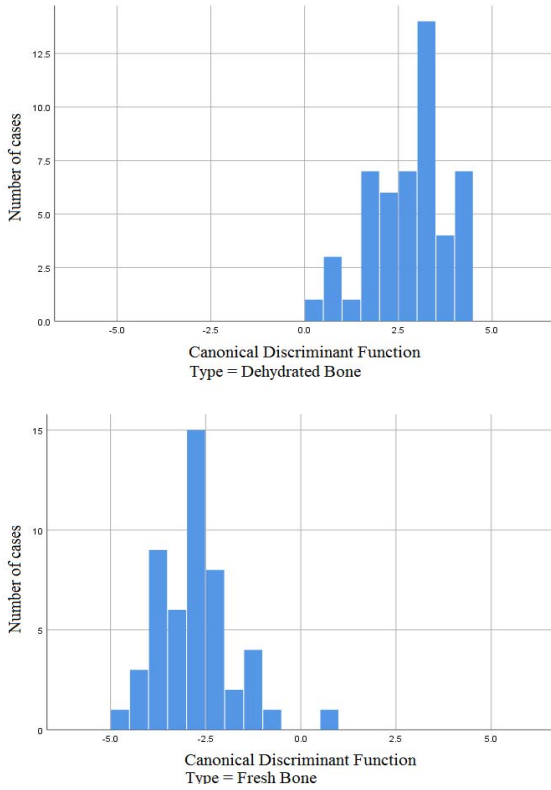


Fig. 2. Histogram graph of the group samples, dehydrated bone (upper), and fresh bone (lower). Unstandardized canonical discriminant functions evaluated at group centroid are +2.768 and -2.768 for dehydrated and fresh bone samples, respectively.

B. Cross-Validated Grouped Cases

In addition to the original grouped cases method, the validation method has been applied to make sure that the classifier is not overtrained. In the cross-validated mode, each case is classified by the function derived from the remaining cases. In within-groups mode (cross-validated grouped cases), 86 % of dehydrated cases, i.e. 43 out of 50, and 92 % of fresh cases, i.e. 46 out of 50, (89 % on average) were classified correctly. Since the accuracy in validation mode is also high, the classifier does not appear to be overtrained. Table 1 shows the predicted group membership in both original grouped cases and cross-validated grouped cases.

TABLE I. PREDICTED GROUP MEMBERSHIP

		Predicated Group Membership		
		Count (Percentage)		
		Dehydrated	Fresh	Total
Original	Dehydrated	50 (100 %)	0 (0 %)	50 (100 %)
	Fresh	1 (2 %)	49 (98 %)	50 (100 %)
Cross-validated	Dehydrated	43 (86 %)	7 (14 %)	50 (100 %)
	Fresh	4 (8 %)	46 (92 %)	50 (100 %)

C. ROC Analysis

In addition, Receiver Operating Characteristic (ROC) analysis was also performed to confirm the performance of the proposed classifier. Figure 3. shows the result of the ROC analysis of the classifier. Sensitivity is shown in the vertical axis, and fall-out (1-specificity) on the horizontal axis. As it is clear from the figure, most of the area under the curve (AUC) is filled (more than 99 %), which is an indicator for the performance of the employed classifier to differentiate dehydrated from fresh bone.

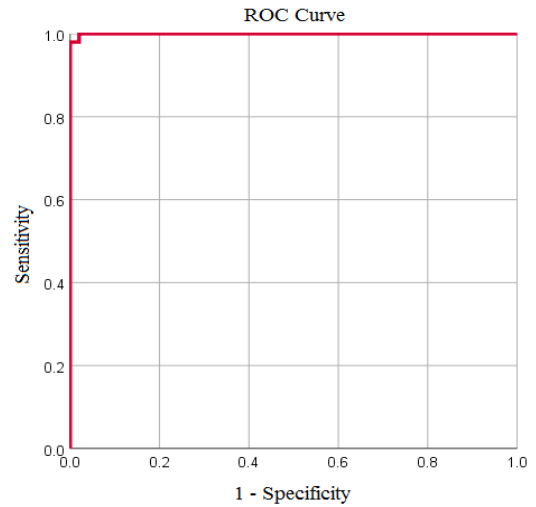


Fig. 3. ROC curve of the employed classifier. The area under the curve is more than 99 %.

IV. DISCUSSIONS

The preliminary results of this study confirmed the idea of bone dehydration detection through LIBS with an accuracy of 89 % in cross-validation mode. Regarding the high accuracy of validation, the classifier does not seem to be overfitting, even though only 45 ratios between intensities of 10 selected peaks were used as an input of the classifier. This pilot study was done with the assumption that the laser-induced dehydration process is similar to self-dehydration over time. Also, we applied the assumption that freezing keeps the original bone structure intact like in fresh bone. Further studies should be carried out to confirm these assumptions and also with a higher number of samples, before transferring the proposed method to the laserosteotomy system.

V. CONCLUSIONS

In conclusion, LIBS showed its potential to detect dehydration in bone with good accuracy in an *ex vivo* set-up. Although this pilot study was done with self-dehydration as compared to laser-induced dehydration, the results pave the way to the future work on real-time detection of laser-induced dehydration. Moreover, it should be mentioned that the future work needs to be performed with higher number of samples, to be able to add this feedback mechanism to laserosteotomes. In an experiment with a bigger number of samples, adding more inputs (peak intensities or ratios) to the classifier, the less likely the classifier will overfit, which could help to build a more robust discriminant function.

Also, a significant improvement for the further studies would be the ability to detect gradation in the degree of dehydration, instead of a yes/no decision.

REFERENCES

- [1] Q. T. Le, R. Vilar, and C. Bertrand. "Influence of external cooling on the femtosecond laser ablation of dentin," *Lasers Med. Sci.*, vol. 32, pp. 1943-1951, 2017.
- [2] L. T. Canguero, and R. Vilar. "Influence of the pulse frequency and water cooling on the femtosecond laser ablation of bovine cortical bone," *Appl. Surf. Sci.*, vol. 283, pp. 1012-1017, 2013.
- [3] L. Kuscer, and J. Diaci, "Measurements of erbium laser-ablation efficiency in hard dental tissues under different water cooling conditions," *J. Biomed. Opt.*, vol. 18, p. 108002, 2013.
- [4] M. Augello, W. Deibel, K. Nuss, P. Cattin, P. and P. Jürgens, "Comparative microstructural analysis of bone osteotomies after cutting by computer-assisted robot-guided laser osteotome and piezoelectric osteotome: an in vivo animal study," *Lasers Med. Sci.*, vol. 33, pp. 1-8, 2018.
- [5] K-W. Baek, W. Deibel, D. Marinov, M. Griessen, A. Bruno, et al., "Clinical applicability of robot-guided contact-free laser osteotomy in cranio-maxillo-facial surgery: in-vitro simulation and in-vivo surgery in minipig mandibles," *Br. J. Oral Maxillofac. Surg.*, vol. 53, pp. 976-981, 2015.
- [6] D. G. Panduric, I. B. Juric, S. Music, K. Molcanov, M. Susic, et al., "Morphological and ultrastructural comparative analysis of bone tissue after Er: YAG laser and surgical drill osteotomy," *Photomed. Laser Surg.*, vol. 32, pp. 401-408, 2014.
- [7] H. Abbasi, L. Beltrán, G. Rauter, R. Guzman, P. C. Cattin, et al., "Effect of cooling water on ablation in Er: YAG laserosteotome of hard bone," *Proc. SPIE.*, vol. 10453, 2017.
- [8] L. M. B. Bernal, G. Shayeganrad, G. Kosa, M. Zelechowski, G. Rauter, et al., "Performance of Er: YAG laser ablation of hard bone under different irrigation water cooling conditions," *Proc. SPIE.*, vol. 10492, 2018.
- [9] R. Kanawade, F. Mahari, F. Klämpfl, M. Rohde, C. Knipfer, et al., "Qualitative tissue differentiation by analysing the intensity ratios of atomic emission lines using laser induced breakdown spectroscopy (LIBS): prospects for a feedback mechanism for surgical laser systems," *J. Biophotonics*, vol. 8, pp. 153-161, 2015.
- [10] M. Rohde, F. Mehari, F. Klämpfl, W. Adler, F-W. Neukam, et al., "The differentiation of oral soft - and hard tissues using laser induced breakdown spectroscopy-a prospect for tissue specific laser surgery," *J. Biophotonics*, vol. 10, pp. 1250-1261, 2017.
- [11] H. Abbasi, G. Rauter, R. Guzman, P. C. Cattin, and A. Zam, "Differentiation of femur bone from surrounding soft tissue using laser induced breakdown spectroscopy as a feedback system for smart laserosteotomy," *Proc. SPIE.*, vol. 10685, 2018.
- [12] M. Youngmin, J. H. Han, S. Shin, Y.-C. Kim, and S. Jeong, "Elemental analysis of tissue pellets for the differentiation of epidermal lesion and normal skin by laser-induced breakdown spectroscopy," *Biomed. Opt. Express*, vol. 7, pp. 1626-1636, 2016.
- [13] F. Ghasemi, P. Parvin, N. S. H. Motlagh, A. Amjadi, and S. Abachi, "Laser induced breakdown spectroscopy and acoustic response techniques to discriminate healthy and cancerous breast tissues," *Appl. Optics*, vol. 55, pp. 8227-8235, 2016.
- [14] B. Busser, S. Moncayo, J.-L. Coll, L. Sancey, and V. Motto-Ros, "Elemental imaging using laser-induced breakdown spectroscopy: A new and promising approach for biological and medical applications," *Coord. Chem. Rev.*, vol. 358, pp. 70-79, 2018.
- [15] S. A. Davari, S. Masjedi, Z. Ferdous, and D. Mukherjee, "In - vitro analysis of early calcification in aortic valvular interstitial cells using Laser - Induced Breakdown Spectroscopy (LIBS)," *J. Biophotonics*, vol. 11, p. e201600288, 2018.
- [16] M. Bahreini, B. Ashrafkhani, and S. H. Tavassoli, "Discrimination of patients with diabetes mellitus and healthy subjects based on laser-induced breakdown spectroscopy of their fingernails," *J. Biomed. Opt.*, vol. 18, p. 107006, 2013.
- [17] R. K. Gill, F. Knorr, Z. J. Smith, M. Kahraman, D. Madsen, et al., "Characterization of femtosecond laser-induced breakdown spectroscopy (fsLIBS) and applications for biological samples," *Appl. Spectrosc.*, vol. 68, pp. 949-954, 2014.
- [18] R. K. Gill, Z. J. Smith, R. R. Panchal, J. W. Bishop, R. Gandour-Edwards, et al., "Preliminary fsLIBS study on bone tumors," *Biomed. Opt. Express*, vol. 6, pp. 4850-4858, 2015.
- [19] Y. Moon, J. H. Han, J.-h. Choi, S. Shin, Y.-C. Kim, et al., "Mapping of cutaneous melanoma by femtosecond laser-induced breakdown spectroscopy," *J. Biomed. Opt.*, vol. 24, p. 031011, 2018.
- [20] X. Li, S. Yang, R. Fan, X. Yu, and D. Chen, "Discrimination of soft tissues using laser-induced breakdown spectroscopy in combination with k nearest neighbors (kNN) and support vector machine (SVM) classifiers," *Opt. Laser Technol.*, vol. 120, pp. 233-239, 2018.
- [21] H. Abbasi, G. Rauter, R. Guzman, P. C. Cattin, and A. Zam, "Laser-induced breakdown spectroscopy as a potential tool for autocarbonization detection in laserosteotomy," *J. Biomed. Opt.*, vol. 23, p. 071206, 2018.
- [22] H. Abbasi, G. Rauter, R. Guzman, P. C. Cattin, and A. Zam, "Plasma plume expansion dynamics in nanosecond Nd: YAG laserosteotome," *Proc. SPIE.*, vol. 10505, 2018.
- [23] M. Nazeri, A. E. Majd, R. Massudi, S. H. Tavassoli, A. Mesbahinia, et al., "Laser-induced breakdown spectroscopy via the spatially resolved technique using non-gated detector," *J. Russ. Laser Res.*, vol. 37, pp. 164-171, 2016.
- [24] C. Cocozzelli, "Understanding canonical discriminant function analysis: Testing typological hypotheses," *J. Soc. Serv. Res.*, vol. 11, pp.93-117, 1988.
- [25] Z. Hosseinimakarem, and S. H. Tavassoli, "Analysis of human nails by laser-induced breakdown spectroscopy," *J. Biomed. Opt.*, vol. 16, p.057002, 2011.
- [26] M. Bahreini, B. Ashrafkhani, S. H. and Tavassoli, "Elemental analysis of fingernail of alcoholic and doping subjects by laser-induced breakdown spectroscopy," *Appl. Phys. B*, vol. 114, pp.439-447, 2014.

Chapter 5:
Real-time closed-loop tissue-specific laserosteotomy

5.1. Combined Nd:YAG and Er:YAG lasers for real-time closed-loop tissue-specific laser osteotomy

Chapters 3 and 4 showed experiments that were performed in an offline mode, meaning that the data was collected and stored on a PC and analyzed afterward. This section presents a peer-reviewed journal publication describing the combination of two lasers, a low energy Nd:YAG for tissue differentiation and high energy Er:YAG for providing efficient ablation. Tissue differentiation was performed in a real-time and closed-loop manner, i.e., a mechanical shutter blocked the Er:YAG beam when it encountered a tissue meant to be preserved. In this study, the energy of the Nd:YAG laser was reduced to avoid ablating non-target tissue; the method introduced here, laser-induced breakdown thresholding, provided non-destructive, real-time, closed-loop tissue differentiation.

Publication: Hamed Abbasi, Lina M. Beltrán Bernal, Arsham Hamidi, Antoine Droneau, Ferda Canbaz, Raphael Guzman, Steven L. Jacques, Philippe C. Cattin, and Azhar Zam, "Combined Nd:YAG and Er:YAG lasers for real-time closed-loop tissue-specific laser osteotomy," *Biomed. Opt. Express* 11, 1790-1807 (2020). <https://doi.org/10.1364/BOE.385862>

Copyright notice: © 2020 Optical Society of America under the terms of the [OSA Open Access Publishing Agreement](#)



Combined Nd:YAG and Er:YAG lasers for real-time closed-loop tissue-specific laser osteotomy

HAMED ABBASI,^{1,6}  LINA M. BELTRÁN BERNAL,¹  ARSHAM HAMIDI,¹  ANTOINE DRONEAU,^{1,2}  FERDA CANBAZ,¹  RAPHAEL GUZMAN,³ STEVEN L. JACQUES,⁴  PHILIPPE C. CATTIN,⁵  AND AZHAR ZAM^{1,7} 

¹*Biomedical Laser and Optics Group (BLOG), Department of Biomedical Engineering, University of Basel, CH-4123 Allschwil, Switzerland*

²*Grenoble INP, Grenoble Alpes University, Phelma, France*

³*Department of Neurosurgery, University Hospital Basel, CH-4056 Basel, Switzerland*

⁴*Department of Bioengineering, University of Washington, Seattle, Washington 98195, USA*

⁵*Center for medical Image Analysis and Navigation (CIAN), Department of Biomedical Engineering, University of Basel, CH-4123 Allschwil, Switzerland*

⁶*hamed.abbasi@unibas.ch*

⁷*azhar.zam@unibas.ch*

Abstract: A novel real-time and non-destructive method for differentiating soft from hard tissue in laser osteotomy has been introduced and tested in a closed-loop fashion. Two laser beams were combined: a low energy frequency-doubled nanosecond Nd:YAG for detecting the type of tissue, and a high energy microsecond Er:YAG for ablating bone. The working principle is based on adjusting the energy of the Nd:YAG laser until it is low enough to create a microplasma in the hard tissue only (different energies are required to create plasma in different tissue types). Analyzing the light emitted from the generated microplasma enables real-time feedback to a shutter that prevents the Er:YAG laser from ablating the soft tissue.

© 2020 Optical Society of America under the terms of the [OSA Open Access Publishing Agreement](#)

1. Introduction

Due to the many side effects of the traditional osteotomy tools, e.g., poor surface evenness, mechanical vibrations, high amount of heat production, limited cutting geometry, high material loss, and potential contamination, alternative solutions are sought. Lasers seem to be a perfect candidate for replacing conventional saws and drills in osteotomy procedures [1–11]. However, lasers pose the risk of collateral damage to the neighboring tissue if feedback about the type of tissue is not provided. In order to preserve the adjacent soft tissue, several approaches to such differentiation have been developed using the optical properties of the ablated tissues. These methods include optical coherence tomography (OCT) [12,13], Raman spectroscopy [14–17], autofluorescence spectroscopy [18,19], diffuse reflectance spectroscopy (DRS) [20–23], ablative optoacoustic techniques [24–29], random lasing [30], laser-induced breakdown spectroscopy (LIBS) [31–42], and combustion/pyrolysis light analysis [43,44]. However, many of these methods have not been tested in combination with an ablating laser; studies have focused on tissue differentiation only. In addition to the work carried out in the area of tissue-specific surgery, several studies have used similar approaches for detecting cancer borders during surgery [45–51]. Each method has its own advantages and disadvantages. Some of them, like OCT and Raman, use a low power continuous wave (CW) laser, where the diagnostic beam does not involve ablation. Other methods, like ablative optoacoustic techniques, require high energy pulsed lasers to produce a measurable acoustic wave. However, the required energy levels can create damage

to sensitive tissues with just one pulse. LIBS also has the potential to differentiate tissue types (not only between hard and soft tissues, but also between different soft tissues) and, additionally, to provide feedback regarding laser-induced thermal damage (dehydration [39] and carbonization [38]). However, during surgery, at least a single shot of the laser (around tens of millijoules using nanosecond pulses) needs to be applied to the tissue in order to detect its type. Therefore, in both LIBS and acoustic methods, the applied energy could ablate a small amount of the tissue. Raman spectroscopy, another advanced optical technique, can provide information regarding the molecular bonds of the tissue. However, due to its low cross-section, a few seconds of integration of the measured signal are required [14,15], which makes it unsuitable as a real-time feedback sensor. Photodiode-based pyrolysis analysis (also known as combustion analysis) is yet another method to achieve tissue-specific cutting during microsecond Er:YAG osteotomy [43,44]. Here,

Table 1. A comparison of optical sensor-based laser ablation published works for tissue-specific cutting

Work	method	Ablating laser	Diagnostic light source	Ablation-free detection ^a	Real-time ^b	Closed-loop ^c
[12]	OCT	N.A. ^d	Swept source (1060 nm)	✓	✗	✗
[14–17]	Raman	N.A.	CW (785 nm)	✓	✗	✗
[18]	Autofluorescence	N.A.	mercury lamp	✓	✗	✗
[20–23]	Diffuse Reflectance	N.A.	Pulsed Xenon/ Halogen lamp	✓	✗	✗
[24–26]	Shockwave (speckle-analysis)	ns-Nd:YAG (1064 nm)	CW Nd:YAG (532 nm) ^e	✗	✗	✗
[27,28]	Shockwave (Mach-Zehnder)	ns-Nd:YAG (532 nm)	Same as ablating one	✗	✗	✗
[29]	Ablative optoacoustic (FBG)	ms-fiber laser (1070 nm)	Same as ablating one	✗	✗	✗
[30]	Random lasing	ns-Nd:YAG (532 nm)	Lasing by the tissue ^f	✗	✗	✗
[31–39]	ns-LIBS	ns-Nd:YAG /Excimer (1064/532/193 nm)	Same as ablating one	✗	✗	✗
[40]	Double-pulse LIBS	μs-Er:YAG (2940 nm)	ns-Nd:YAG (532 nm)	✗	✗	✗
[41]	CO ₂ -LIBS	Pulsed CO ₂ (10.6 μm)	Same as ablating one	✗	✓	✗
[42]	fs-LIBS	fs-mode-locked (1030 nm)	Same as ablating one	✗	✓	✗
[43,44]	Photodiode-based pyrolysis analysis	μs-Er:YAG (2940 nm)	Same as ablating one	✗	✓	✓

^aThis column shows whether detection can be provided without ablating the tissue which meant to be preserved.

^bReal-time here means diagnosis within millisecond range. Some works with near-real-time analysis (more than a second processing time) were not marked as real-time in this table.

^cOnly those works in which the feedback from the dedicated sensor was sent to the ablating laser/shutter (in order to stop cutting) were marked as closed-loop, here. Works with closed-loop ability without testing or a concept as a future plan were not marked in this table.

^dN.A. in this column means that in the published work, only the ability of the method for tissue differentiation was examined and it was not combined with any ablating laser.

^eIn speckle analysis, the ablation caused during the procedure required to determine the type of tissue is caused by the high energy laser used to generate shockwave at the tissue.

^fIn random lasing, the ablation caused during the procedure required to determine the type of tissue is caused by the high energy laser used to pump the tissue for lasing.

a photodiode is used to observe the light emitted from the pyrolysis created in the ablation zone. The pyrolysis light is observable only at high energy densities. In this setup, no additional laser is utilized. Employing a single laser to both ablate and differentiate tissue offers a simpler optical setup. However, if the laser beam reaches a tissue that should be preserved, the laser beam would be stopped, as a result, the tissue-type diagnosis cannot be continued (i.e., no ablation beam, no diagnosis beam).

Table 1 provides a summary comparing studies where different methods were used to differentiate tissues. The last three columns of the table are dedicated to comparing three important features of a feedback mechanism that are required for an applicable system. These are having a non-ablating diagnostic laser, functioning in real-time, and tested together within a closed-loop setup. Each feature is more precisely defined in the table's footnote. The middle column shows whether two different lasers are used for ablation and differentiation or not. Table 1 covers all studies, to the best of our knowledge, related to tissue-specific surgeries. However, the table does not cover works that have used a similar feedback mechanism for detecting cancer margins [45–51] in the tissues.

As shown in Table 1, previously conducted works could not completely fulfill the requirement for a closed-loop smart laser osteotomy. Therefore, the current study is intended to fulfill all requirements. The current study introduces a different approach, whereby ablation is performed in hard tissues only, and no ablation occurs in soft tissue. We tested this approach in a real-time closed-loop scenario. Two laser beams were combined: a high energy Er:YAG for ablating the bone and a low energy Nd:YAG for detecting the type of tissue. Therefore, when the beam encounters soft tissue, only the Er:YAG beam is blocked (using a fast mechanical shutter), and tissue-type differentiation can continue. The energy of the Nd:YAG laser required is low enough to be delivered using fiber optics, making it more suitable for miniaturization for minimally-invasive surgery (MIS).

2. Methodology

2.1. Hard tissue ablation process

Bone ablation can be performed in different ways, e.g., by photothermal or electro-mechanical means. Photothermal ablation has shown excellent results. It is based on the high absorption of water and mineral components (e.g., hydroxyapatite) at mid-infrared wavelengths, like 3 μm and 10 μm , for lasers working in the microsecond regime [2,3,52–55]. Once the microsecond laser pulse strikes the bone surface, it heats up the water molecules accumulated in the interstitial walls of the bone. High pressure (hundreds of bars) is created inside the bone structure, leading to explosive evaporation of the tissue [55]. The most common lasers used for tissue ablation are Ho:YAG at 2.1 μm , Er,Cr:YSGG at 2.79 μm , Er:YAG at 2.94 μm and CO₂ at 9.3, 9.6, and 10.6 μm [56–58]. The Er:YAG laser causes minimal damage to the bone surroundings [59,60]. To ensure efficient tissue ablation with less collateral damage and faster healing time, the stability of the laser pulses [61] and the highest degree of absorption are desirable. In this study, a flashlamp-pumped Er:YAG laser (LiteTouch by Syneron) with microsecond-long pulses was used to ablate the bone.

2.2. Tissue differentiation working principle

Depending on the applied energy and pulse duration of a laser, several different phenomena may occur when the laser interacts with biological tissues [62–64]. When tissue interacts with pulsed lasers, there might be a nonlinear absorption of the light, thus, the type of interaction can be changed quickly by changing the parameters of the laser [65]. A laser-tissue interaction map can explain the underlying principle of the work. The laser-tissue interaction map was initially depicted by Boulnois in 1986 [66]. Later, the map was reproduced and modified on different

occasions by other researchers [55,67–69]. Due to limited access to ultra-short laser pulses, the initial map included four main phenomena: (I) photochemical (mainly only for CW lasers), (II) thermal (including coagulation, vaporization, carbonization, and melting), (III) photoablative, and (IV) electro-mechanical. Basically, the different phenomena are the result of laser energy converting to different kinds of energy: chemical, thermal, or mechanical [70]. In most of the recently reproduced maps, the electro-mechanical part (using short and ultra-short laser pulses only) is divided into two different sections: photodisruption and plasma-induced ablation (there is no consensus for that, and other terms are also used). However, in both cases (photodisruption and plasma-induced ablation), the tissue is ionized and a localized plasma is produced at the ablation zone (breakdown). The difference is the higher impact of mechanical effects in photodisruption (the term disruption originates from the Latin word *ruptus*, meaning ruptured) [69]. Mechanical effects produce shockwaves (high pressure gradients moving at supersonic speed at the shock front) in all tissues, cavitation (explosive vaporization involving negative tensile waves that disrupt a material, causing successive expansion and collapse due to strong compression of water and carbon oxides) in soft tissues, and jet formation (only in fluids) near a solid boundary during collapse from cavitation [71,72]. Figure 1 shows a representation of the laser-interaction map from [69].

Which interaction mechanism tissue undergoes depends on multiple laser parameters; these include pulse duration and applied power density as the two main parameters as used in the two-dimensional map. Moreover, tissue properties like transmission, reflection, scattering, absorption (function of laser wavelength), tissue density, heat conduction and heat capacity also determine the type of interaction. A variety of optical and mechanical properties of different kinds of tissue widen the borders shown in Fig. 1. This means that a specific laser parameter can lead to two different interactions for different tissues. The optical breakdown formed by nanosecond pulses is always associated with a shock wave (for both hard and soft tissues) and cavitation (only for soft tissues) even at the very threshold. In electro-mechanical ablation relatively powerful thermoelastic tensile pressure is generated, which can produce cavitation inside the irradiated medium; its amplitude is a function of the absorption coefficient of the medium and the power density of the applied laser beam [73]. Considering all the differences between the mechanical and physical properties of hard and soft tissues, the fact that cavitation (negative tensile pressure disruption) occurs only in soft tissues, and that up to one fourth of the applied energy will be consumed in cavitation [69], at specific pulse durations, higher energy is required to start the breakdown at soft tissues (different required dosimetry based on the tissue optics [74]). The critical point determined in Fig. 1 (the single red dot) shows the starting point or threshold of bone ablation for a nanosecond Nd:YAG laser.

Due to the complexity of all involved parameters, no complete model has been formulated to describe the ablation process. However, two simplified models are useful for describing the working principle utilized in the current study: “steady-state” and “blow-off”. The former is normally used to describe longer pulses (typically in the microsecond regime) as compared to the later one (typically shorter than 100 ns) [62]. Both models seek an ablation threshold, $\Phi_{\text{threshold}}$ [J/cm²], in which only an energy density (radiant exposure) higher than the ablation threshold can onset the ablation. Molecular dynamic simulations have confirmed that lower energy density will result in heating the tissue without material ejection; this has been confirmed by some experiments as well [75].

The steady-state model is based on the assumption of having constant ablation enthalpy (also known as the heat of ablation), H [J/kg]. In this model, the ablation efficiency, η [kg/J], i.e., the amount of mass removed per unit energy, is related to the applied energy density, Φ_{applied} [J/cm²], using the following equation:

$$\eta = \frac{\Phi_{\text{applied}} - \Phi_{\text{threshold}}}{H\Phi_{\text{applied}}} \quad (1)$$

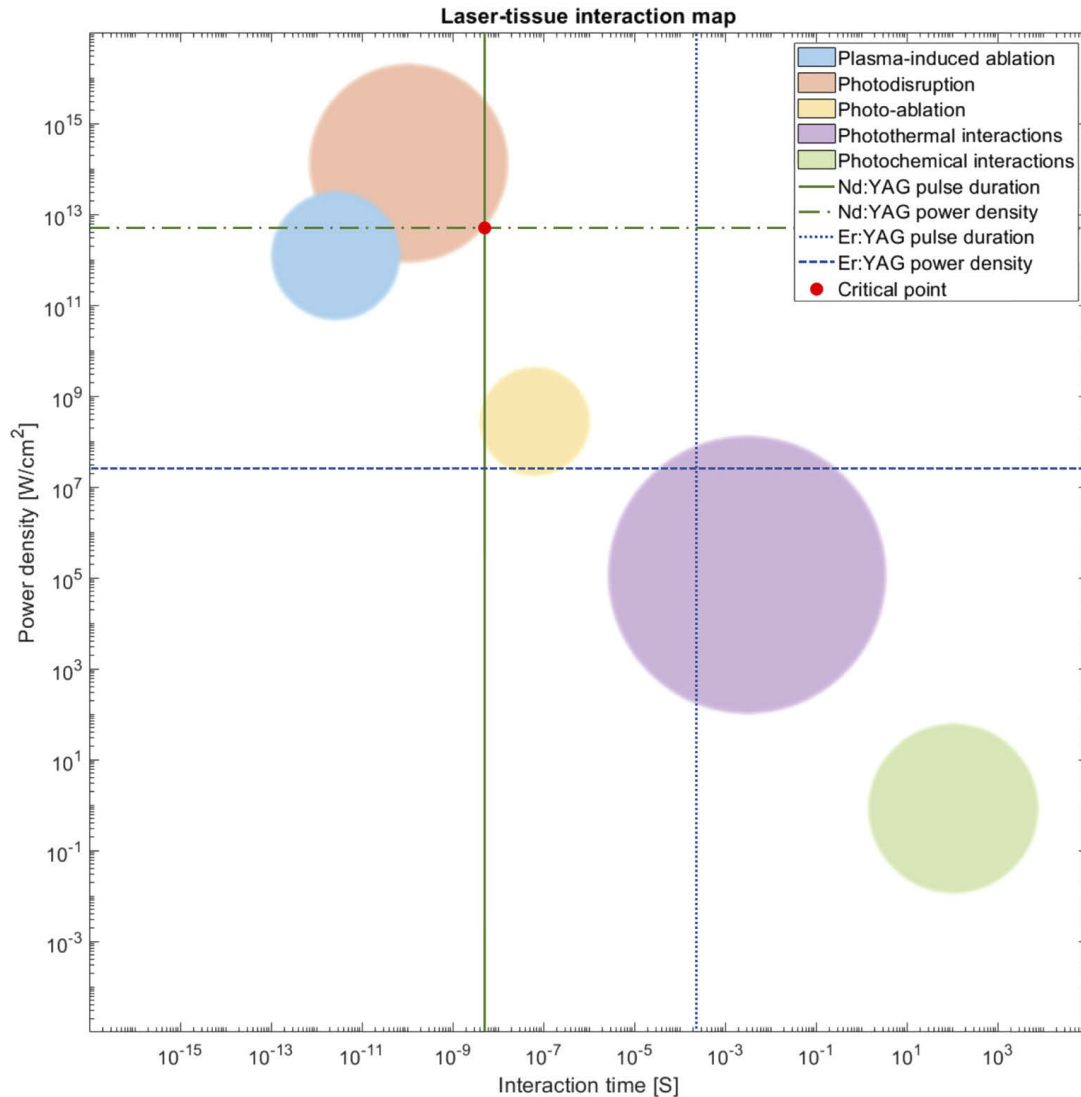


Fig. 1. Laser-tissue interaction map. The vertical blue dotted and the horizontal blue dashed lines show the pulse duration and power density of the Er:YAG laser that were used in the experiments. The red dot on the map (critical point) shows where the vertical green solid (Nd:YAG pulse duration), and horizontal green dash-dotted (Nd:YAG power density) lines meet. This critical point is the starting point of ablation, which varies from hard to soft tissues.

The blow-off model, which is based on the satisfaction of the Beer-Lambert law for the spatial distribution of the absorbed energy, can be described by the following equation:

$$\eta = \frac{\rho}{\mu\Phi_{applied}} \ln \left(\frac{\Phi_{applied}}{\Phi_{threshold}} \right) \quad (2)$$

where ρ [kg/m³] is tissue density, and μ [cm⁻¹] is the absorption coefficient of tissue at the applied wavelength. In both models, the ablation efficiency would be zero (no ablation) if the applied energy density does not exceed the ablation threshold ($\Phi_{applied} \leq \Phi_{threshold}$).

2.3. Specimens

In this experiment, five different bisected pig femur slices were bought from a local supermarket; two of them were used to train the shutter, and the rest were used for testing. All specimens were washed using tap water right before the experiment, in order to remove possible pollution at the surface of the specimens. Both sides of each bisected slice were used, therefore, four series of data were recorded to train the shutter, and six experiments were carried out for testing. Each specimen consisted of four different kinds of tissue: the hard tissue bone and the soft tissues bone marrow, muscle and fat. By moving the specimens using a motorized translation stage, the laser beam encountered different tissue types on each trip. Since the specimens used were available as food-based material, ethical committee approval was not required.

2.4. Experimental setup

Two laser beams were combined to perform ablation and tissue differentiation, a microsecond Er:YAG and a nanosecond Nd:YAG, respectively. The Er:YAG laser energy was 226 mJ (measured by PE50-DIF-ER-C pyroelectric energy meter, Ophir, USA), with a pulse duration of 106.4 μ s (measured by PDA20H-EC - PbSe fixed gain pre-amplified detector, Thorlabs, USA, connected to an IR bandpass filter, FB3000-500, Thorlabs, USA), and Fluke 190-504 scope meter, Fluke Corporation, USA), and emitting a 2940 nm Mid-Infrared (MIR) beam. Note that lower energies could also be used for performing photothermal bone ablation; however, it might result in lower ablation efficiency. Also, it is worth mentioning that shorter pulse durations matching thermal relaxation time of bone (typically below 80 μ s [76]) would be desirable, if accessible. The frequency-doubled Q-switched Nd:YAG laser energy was 4.10 mJ (measured by EnergyMax-USB J-50MB-YAG Energy Sensor, Coherent, USA), with a pulse duration of 5 ns, and emitting a 532 nm green beam (numbers provided by the manufacturing company, Quantel, France). The energy of both lasers was measured after the beams passed through all optical components. The experimental setup is shown in Fig. 2. The Er:YAG laser is placed out of the frame at the left side and its beam path is depicted in red. The Er:YAG beam was divided into two unequal parts using a microscope slide (part (a) in Fig. 2). Around 4% of the light reflected to the photodiode (part (b) in Fig. 2) was used for synchronization while the rest of the light was transmitted through the microscope slide and then directed to the specimen. The Nd:YAG laser is also placed out of the frame in Fig. 2 on the right, and its path beam is depicted in green. Two beams were combined using a dichroic mirror (Er:YAG in reflection mode, and Nd:YAG in transmission mode), shown as (d) in Fig. 2. The combined beam was passed through a broadband convex lens with a focal length of 2 cm (part (e) in Fig. 2) in order to focus the beam at the surface of the specimens. It is worth mentioning that during tissue ablation (especially for soft tissues) with such a short focal length lens, the lens can become dirty with debris (water and small fatty particles ablated from the soft tissue) hitting the lens surface. If the focal length were longer, different laser beams could focus on two different points, especially if the wavelength and quality of the beams are not similar.

To calculate the focal spot size of each laser beam at the specimen's surface, Gaussian optics were used, taking into account the initial beam size and the beam quality factor, M-squared (M^2), also known as the focusability factor. This parameter allows us to determine the extent of beam divergence compared to an ideal Gaussian beam, which has the same beam size but $M^2=1$. Therefore, beam divergence (θ) for a real Gaussian beam is defined as

$$\theta = M^2 \frac{\lambda}{\pi w_0}. \quad (3)$$

Here, w_0 and λ indicate the beam radius of the laser at its waist position and the center wavelength of the laser, respectively. The M^2 of the beam allows one to determine the beam propagation of the real Gaussian and, therefore, the actual beam size at any position in its trajectory. In our case,

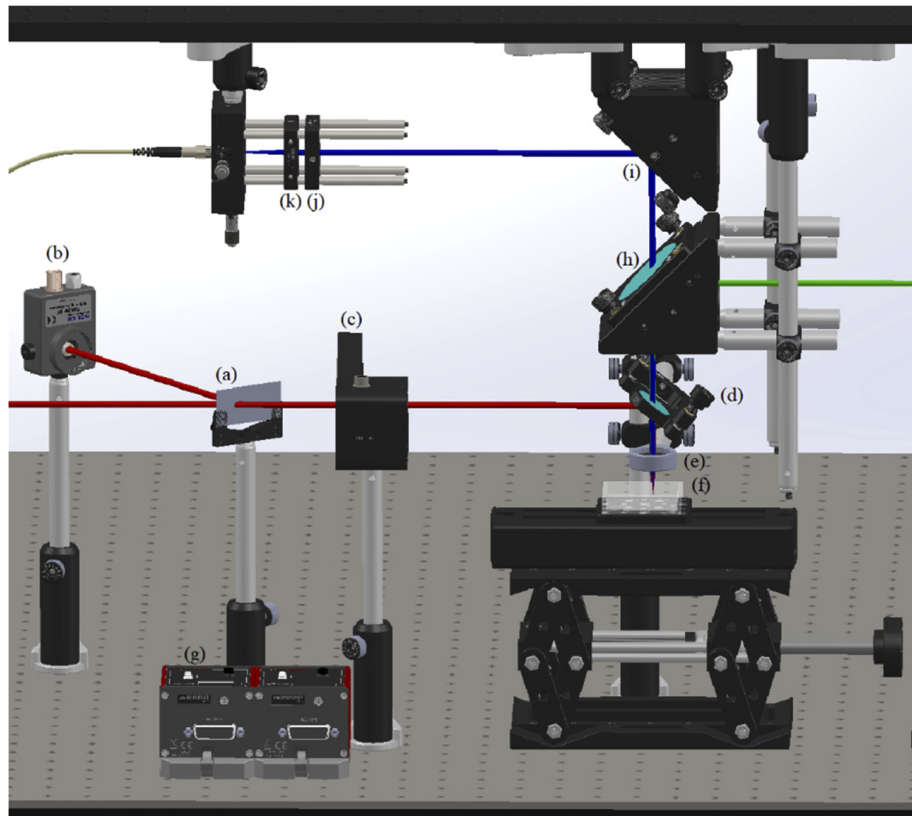


Fig. 2. The CAD design of the experimental setup (performed in SolidWorks 2017). (a): microscope slide as beam splitter, (b): photodiode, (c): shutter, (d): 1st dichroic mirror, (e): focusing lens, (f): sample holder and translation stage, (g): controller of shutter and translation stage, (h): 2nd dichroic mirror, (i): broadband mirror, (j): notch filter, (k): focusing lens. The path of Er:YAG, Nd:YAG, and collected plasma light is depicted in red, green, and dark blue, respectively. The yellow optical fiber depicted in the left side of the figure, guides the light to the camera. The wires for connecting the photodiode, translation stage, shutter, lasers and camera were removed from the figure, intentionally, to avoid a crowded design.

we are interested in knowing the beam size at the focal point, where the tissues are positioned for ablation. The initial beam size and M^2 of the Nd:YAG laser were provided by the manufacturing company as 6.5 mm and ≤ 2 , respectively. We experimentally measured initial beam size and M^2 of the Er:YAG laser. The beam size was estimated by using the knife-edge method, in which the beam is cut axially at different positions. We started covering the beam slowly in the axial plane so that the power went from maximum to minimum as we covered almost all of the beam with the blade. Afterwards, we applied the equations explained in [77] to fit the power function. Then, we obtained the beam size at the focal plane. Since the laser beam can also ablate the blade at the focus point, we did not put the blade there. Instead, we used a lens to focus the beam slowly so that we performed the knife-edge method at approximately ten different positions along the propagation direction. Therefore, we determined the beam size at any position of its trajectory, including the focal plane. With information about all beam sizes along its propagation, the beam diameter (d) can be fitted as a function of the propagation direction (z) by using a hyperbolic function [78]

$$d(z) = \sqrt{A + Bz + Cz^2} \quad (4)$$

where A, B, and C are the fitting parameters. Accordingly, M^2 can be determined from

$$M^2 = \frac{\pi}{8\lambda} \sqrt{4AC - B^2}. \quad (5)$$

We evaluated the beam quality factor of the Er:YAG laser to be ~ 22 . Using this information, we estimated the beam size at the surface of the tissue to be $\theta_{Er:YAG} = 103.35 \mu\text{m}$ and $\theta_{Nd:YAG} = 4.17 \mu\text{m}$. The variation between the calculated spot sizes is due to the difference between the M^2 of the lasers as well as their wavelengths. The actual spot sizes might be slightly different as compared to the estimated ones, due to any possible imperfection in the utilized focusing system. In the experiments, the Er:YAG and the Nd:YAG lasers operated at 20 Hz and 4 Hz, respectively, to ablate and determine the type of tissue. In other words, after every five Er:YAG pulses applied to the specimens, the tissue type was determined by an Nd:YAG laser pulse. The sample was located on top of a motorized translation stage connected to a direct-drive servo motor with a 50 mm travel range (DDSM50/M, Thorlabs, USA). The translation stage (part (f) in Fig. 2) moved at a speed of 1 mm/s for 7 runs for each specimen. At this speed, specimens were subject to one Er:YAG pulse every 50 μm and one Nd:YAG shot every 250 μm (see Fig. 3). This speed leads to one Er:YAG shot every 50 μm , and one Nd:YAG shot every 250 μm (see Fig. 3). As mentioned above, the Nd:YAG laser generated a localized low-energy microplasma at the surface of the bone. The microplasma was collected using the same lens used for focusing and, then, passed through a dichroic mirror reflecting 532 nm and transmitting almost the rest of the visible spectrum towards the collection part (parts (i), (j) and (k) in Fig. 2). The path of the collected plasma light is depicted in Fig. 2 with a dark blue line. After passing the dichroic mirror, the collected light is transmitted through the second dichroic mirror (part (h) in Fig. 2) that was used to reflect the Nd:YAG beam. Then, the collected light is directed (by part (i) in Fig. 2) to the multi-mode optical fiber for delivery to the camera.

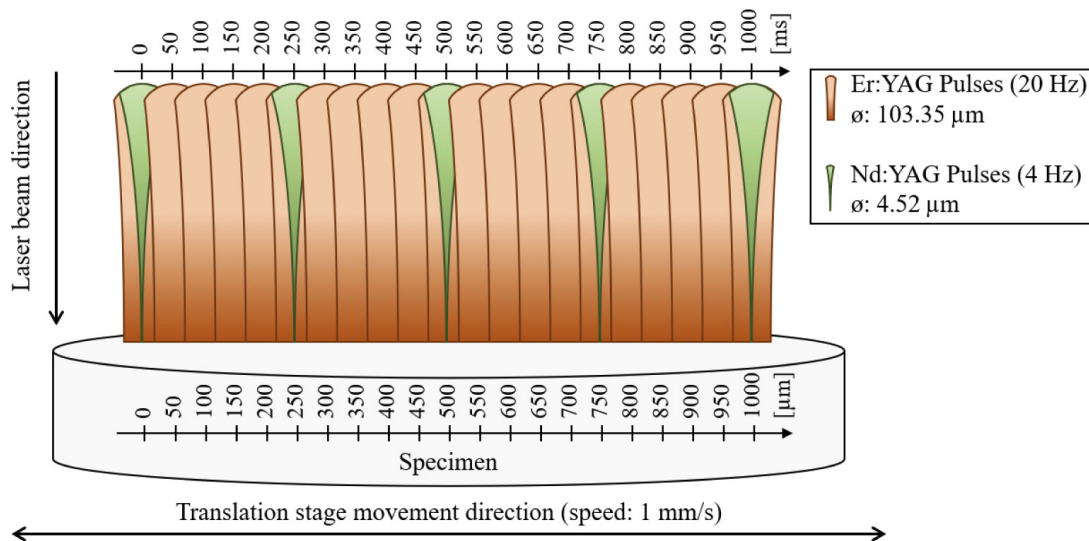


Fig. 3. Schematic of Er:YAG and Nd:YAG beam scales on the surface of the specimens. Time and space scales are positioned at the top and the bottom, respectively. It shows the relative frequency and distance of the ablation (Er:YAG laser) and tissue differentiation (Nd:YAG laser).

The collection part includes a notch filter with an optical density of 7 to avoid collecting reflections from the specimen; a collector lens; and an optical fiber (parts (j) and (k) in Fig. 2). The optical fiber directed the light to the camera (PI-MAX 4, Princeton Instruments, USA). A motorized shutter (SH1/M, Thorlabs, USA) can be seen in part (c) in Fig. 2, in the path of the

Er:YAG laser, which was commanded by the feedback signal received from the camera in a closed-loop and in a way to prevent cutting soft tissues. The Er:YAG laser used in the experiment could not be triggered externally, therefore, the first Er:YAG laser shots were blocked by the shutter as the shutter was programmed to start in closed mode only. In this way, first the Nd:YAG beam (tissue differentiation beam) probes the specimen, then the Er:YAG beam (cutting beam). In the end, an in-house swept-source OCT (SS-OCT) system was employed to observe the width and depth of the cuts. The SS-OCT system operated at a central wavelength of 1060 nm, a bandwidth of 100 nm, and a sweep rate of 100 kHz. The utilized SS-OCT system could provide 3 volumes per second with sizes up to 15.6 mm × 15.6 mm × 3.6 mm. The corresponding lateral and axial resolutions were 44 μm and 10 μm, respectively.

3. Results

3.1. Synchronization

To ensure sequential pulses for tissue differentiation and cutting, respectively, two laser beams and the camera were synchronized using TTL trigger pulses. Figure 4 shows the synchronization diagram of the connected devices. Synchronization started with the Er:YAG laser, as it could not be triggered externally. However, the first pulses of the Er:YAG were blocked to allow the Nd:YAG beam to reach the specimen first. When the photodiode receives a small portion of the Er:YAG beam, the photodiode generates a TTL trigger pulse (rise time (0 - 63%) equal to 35 μs), which is sent to the flash lamp input of the Nd:YAG laser. The flash lamp of the Nd:YAG laser (with a duration of 171.2 μs) excites the crystal rod of the laser, allowing the laser's Q-switch to open based on a pre-defined delay set by the user; the longer the delay, the lower the energy. Then, the Q-switch produces a TTL trigger pulse (with a duration of 25.6 μs), which is sent to the camera. The camera was controlled using LabVIEW. The translation stage started to move after the first trigger pulse from the Nd:YAG's Q-switch was received by the camera, and it stopped moving after 3.5 round trips (each round trip was equal to 100 mm). Around 80 ns after opening the Q-switch (information was provided by the manufacturing company), the Nd:YAG emits a pulse lasting 5 ns. Based on the applied energy and also the targeted material, the plasma expansion dynamics can vary [79,80]. Since the plasma generated in the current study had very low energy (4.1 mJ), it quenched quickly. Therefore, a short delay was applied to open the camera gate (200 ns after Q-switch triggering signal was received, i.e., 120 ns after lasing). The camera gate remained open for 4 ms and then closed before the next laser pulse arrived.

3.2. Training the shutter

As mentioned in Section 2.3, two of the five specimens were dedicated to training the shutter. Figure 5 shows the results of the training. One hundred data samples were recorded on each side of the training specimens for each tissue type in order to define a threshold for determining if ablation had occurred or not. The results confirmed that no ablation occurred at soft tissues.

3.3. Closed-loop results

After using two specimens to train the shutter to close upon reaching soft tissue, the experiment was carried out on the remaining three test specimens. Both sides of each specimen were subjected to the ablation setup developed, including and excluding the tissue differentiation setup. Figure 6 shows the results of the closed-loop experiment. The line cuts with the tissue differentiation setup in the loop are marked with a green box and those without tissue differentiation feedback are indicated with a red box. Figure 6(a)–(f) clearly shows that soft tissues were ablated only when tissue differentiation was shut off whereas bone was always ablated. The localized collateral thermal damages seen in some sections of the ablated bone samples are because the current

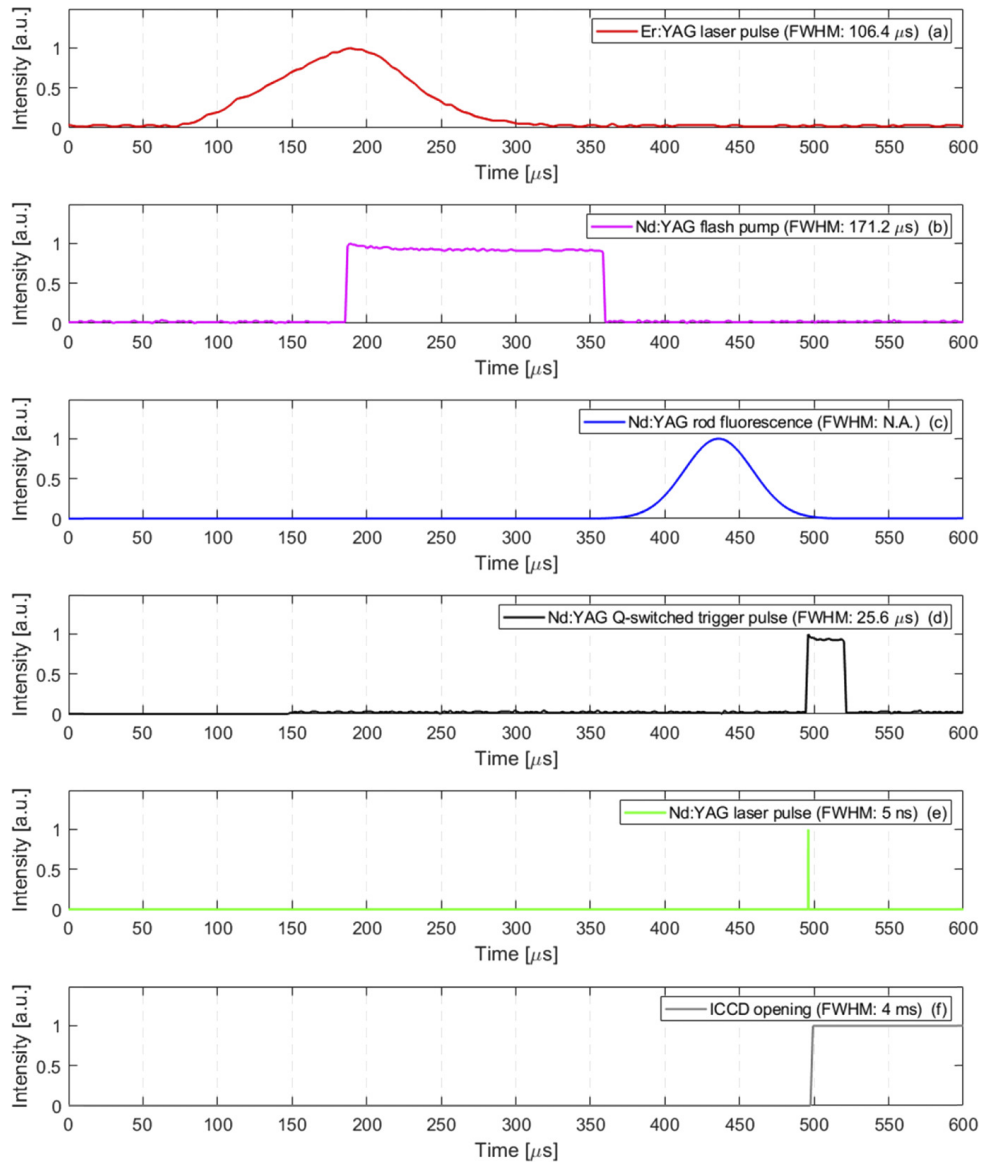


Fig. 4. The synchronization diagram of the connected devices in chronological order. Parts (a), (b), and (d) were recorded by a digital oscilloscope; parts (c), (e), and (f) were depicted by the authors based on the data received from the manufacturing companies. Based on the data provided by the camera, the shutter can be opened or closed (rising/falling time: 10 ms).

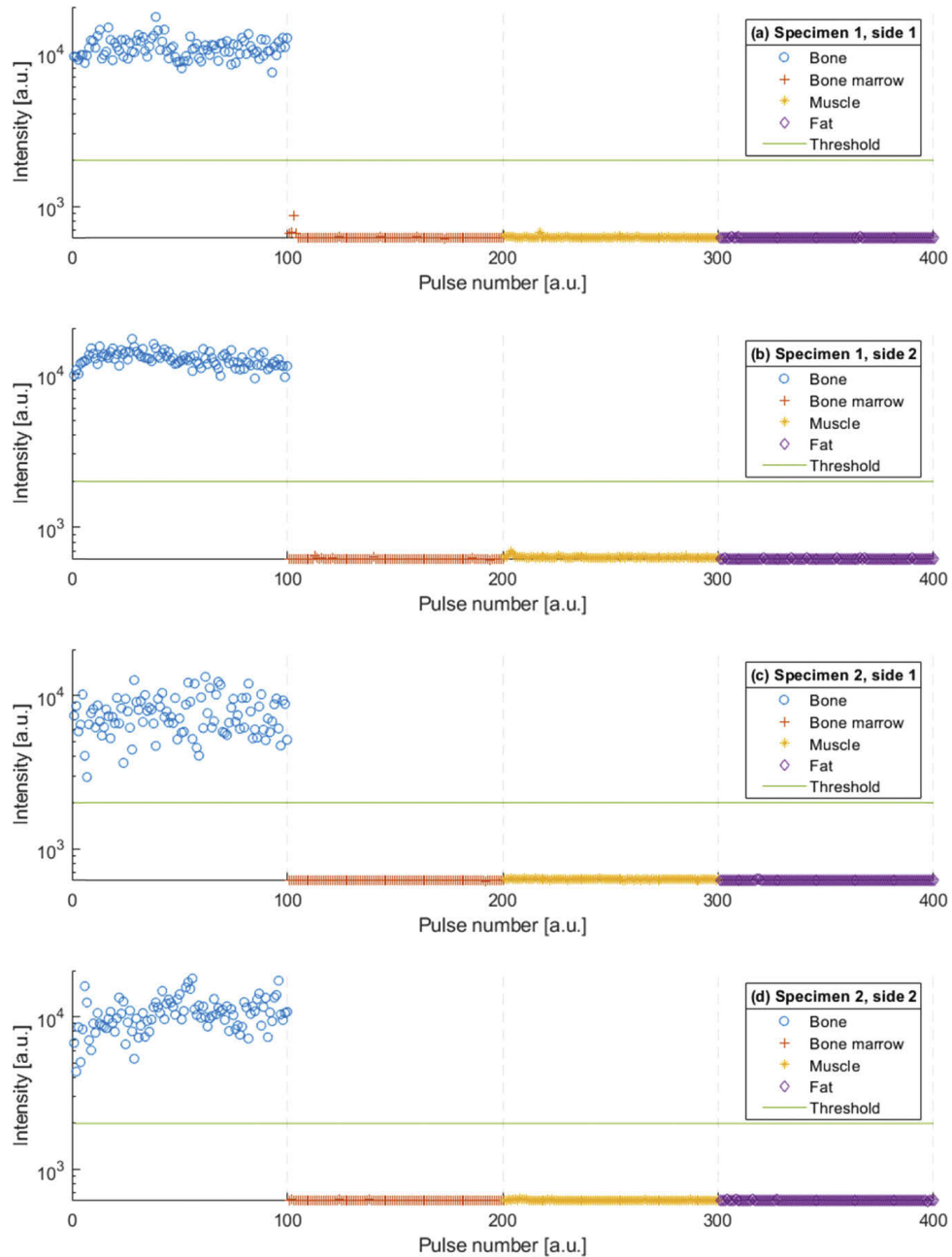


Fig. 5. Results from the training of the shutter. One hundred data points were recorded per tissue type, per specimen, per side (in total, four hundred times per tissue type). The result clearly confirms that ablation occurred only at hard tissue.

study did not use any irrigation; therefore, an irrigation system needs to be added to the current experimental setup to avoid carbonization [81,82].

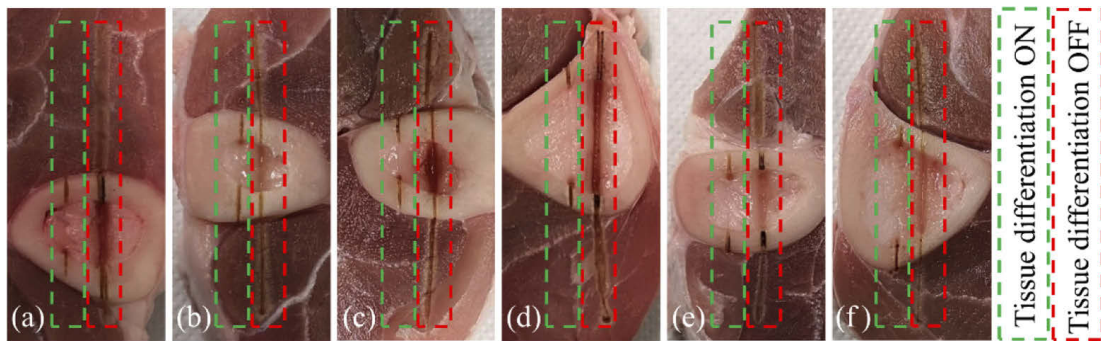


Fig. 6. (a)–(f) The results of the closed-loop experiment. All types of soft tissues were preserved when the real-time feedback system was ON. The photographs were taken after the experiment when the tissues were no longer fresh; this accounts for the observable detachment between bone and muscle in the figures.

3.4. OCT measurement

After the ablation experiments, the SS-OCT system was used to observe the profile of the cuts with and without the tissue differentiation system. Figure 7 shows the OCT images of the first specimen. The top view (en-face) is shown in Fig. 7(a); the three horizontal lines in bone marrow, bone, and muscle areas are marked as dashed lines in the image. A cross-section image (B-scan) of bone marrow, bone, and muscle are shown in Figs. 7(b), (c), and (d), respectively. In Figs. 7(b) and (d), where the tissue was supposed to be preserved, no cut is observable when the tissue differentiation system was ON (green box). In the red box (tissue differentiation OFF), the bone marrow was cut to a depth of 2.40 mm, and a width of 1.28 mm; muscle was cut to a depth and width of 0.62 mm and 1.21 mm, respectively. The widths were measured at the full width at half maximum (FWHM) of the cut. The data shows a higher ablation rate for the bone marrow as compared to muscle. In Fig. 7(c), the cut profile of bone in both scenarios (ON and OFF) is visible. In ON mode, the bone was cut to a depth and width of 1.47 mm and 0.28 mm, respectively; in OFF mode the bone was cut to a similar width (0.27 mm), but to a lower depth of 0.66 mm. In ON mode, where the Er:YAG beam ablated only the hard tissue, no debris from soft tissue was created. In OFF mode, where the beam ablated both hard and soft tissue, a high degree of debris was scattered (sprayed) on the lens surface. Such debris can pollute the focusing lens surface, especially if the lens is close to the sample surface (2 cm distance in our experiment). This debris can absorb some of the lasers' energy, especially that of the Er:YAG laser, which has a high absorption rate in water. Therefore, lower ablation efficiency was achieved in OFF mode, when the lens was covered by a superficial layer of watery/fatty particles. To avoid this, either a higher focal length should be chosen for the focusing lens or a hydrophobic protecting window should be added to the setup.

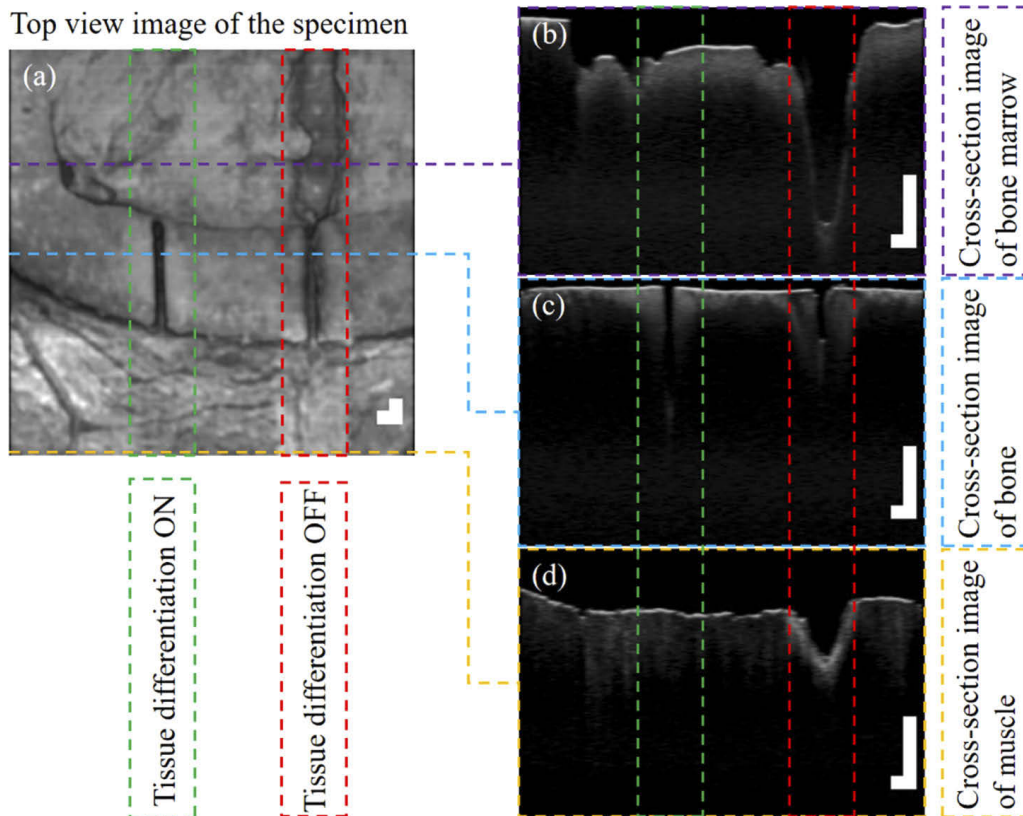


Fig. 7. OCT image of the first specimen with and without tissue differentiation in the loop. (a): top view of the cut (en-face). (b), (c), and (d): cross-section images (B-scan) of lines in bone marrow, bone, and muscle, respectively. The scale bar shown on the lower right side of each image is 1 mm in both vertical and horizontal planes. The non-symmetry of the scale bar in cross-section images is due to the difference between the lateral and axial resolution of the employed OCT system. OCT images were analyzed by ImageJ software.

4. Discussion

4.1. Advantage and disadvantage of the introduced method

Compared to other methods developed for tissue differentiation in laser surgery, the proposed method has several advantages. Similar to LIBS and laser-induced shockwave measurement methods, the procedure is based on generating plasma at the local spot of the tissue. However, in our method, the laser energy applied (4.10 mJ) is much lower than that used for LIBS (38 mJ for ns-Excimer laser [32,33], 73–108 mJ for ns-Nd:YAG laser [31,34–38], and 75–200 mJ for CO₂-LIBS [41]) or shockwave measurements (200 mJ for ns-Nd:YAG [27,28], and 0.75–15 J for ms-fiber laser [29]). Also, the energy applied is well below the reported energy required to pump the tissue for random lasing (100 mJ for ns-Nd:YAG [30]), and pyrolysis analysis (300–2000 mJ for μ s-Er:YAG [43,44]), which occurs inside the ablation zone in the laser-tissue interaction map. Differentiating tissue using a low energy (non-ablating) laser beam has two main advantages. First, it does not ablate the tissue that needs to be preserved (no probed ablation in soft tissues). Second, the diagnostic laser is more likely to be miniaturized for minimally invasive surgery (MIS). In MIS, the laser light should be delivered through an optical fiber (a small bending radius and core size are required) inside the narrow channel of an endoscope, which is not an easy task if the peak energy is high. In addition, since it is not an imaging-based method, unlike OCT, a single optical fiber can be used to collect the data. No scanning part (like MEMS mirror)

is required, thus, less space needs to be dedicated to the detecting system in the endoscope. Moreover, imaging methods are more likely to diminish in performance in-vivo, as increased debris reduces the quality of the image. Compared to spectroscopic methods (LIBS, Raman, DRS, autofluorescence, and random lasing), the spectrometer is not required, and the delivering optical fiber is connected directly to the camera. Thus, the cost of the final setup could be less, without the need for the expensive, high-resolution spectrometer typically used in such setups [83]. Our method does not require a full-frame reading, meaning that the sampling rate (frame per second) can be higher and the time dedicated to signal processing (for classification) is much less in the proposed method. The processing time depends on both, the integration time and the time required for computation. For example, in Raman spectroscopy, where the cross-section of the signal is low, the tissue should be exposed to the light for a long time (e.g., 10 s [14], or 5 s [15]) in order to get the spectra; therefore it can only be applied in a near-real-time scenario. There are few studies that have reported tissue differentiation methods in real-time [41–44]; to the best of our knowledge, all of them have used a single laser for ablation and tissue-type detection. In cases where a single laser is used for both ablation and detection, the diagnostic laser stops together with the ablation laser once the laser reaches a tissue that should be preserved. Therefore, a closed-loop scenario cannot be repeated, meaning that the ablation can start with the tissue that needs to be ablated, and will stop once the laser beam reaches other tissue types, after which, neither ablation nor tissue type detection can be continued.

The main drawback of the proposed method is the absence of tissue differentiation among soft tissues. Most of the other methods have been explored for their ability to differentiate between hard and soft tissues as well as among different soft tissues. Additionally, some tissue properties, like dehydration and carbonization, are detectable through other methods [38,39]. The current method is most useful for surgeries in which the soft tissues must be preserved. It is worth mentioning that the ablation threshold can also be slightly different among similar tissues (e.g., among retinal pigment epithelial (RPE) melanosome, and melanin compared to cutaneous melanosome [84,85]). Note that the threshold is also a function of tissue temperature [86,87]. Therefore, with more stabilized laser energy and deep-cooled detector (and also constant tissue temperature), differentiation between soft tissues could also be possible. However, the current setup has multiple applications, and all green checkmarks in Table 1 can be given to it.

4.2. Outlook

The current system can be improved by integrating the OCT system in the loop, which was conducted offline in this study. As the OCT provides complementary information, both, the information about the type of tissue and information about the depth of cut can be used in a closed-loop system. We also plan to deliver both lasers using a fiber-based system. In this way, the system will be ready to be fitted inside the channel of an endoscope for MIS applications. Currently, only the collection fiber is suitable for an endoscope; the rest of the setup is in free-space. As mentioned above, by employing nanosecond lasers, ablation will be based on photodisruption, whereby all the associated phenomena take place together even at the very threshold. Therefore, one alternative to the current camera-based detection system is to use a microphone to detect whether ablation has occurred or not, based on shockwave detection. Also, a simpler camera or a photomultiplier/photodetector can replace the current ICCD, in order to reduce the final cost of the system. Another possible improvement could be to increase the frequency of diagnostic pulses for more precise tissue border detection than achievable at the current setup of every 250 μ s (it corresponds to every 250 μ m, with 1 mm/s moving speed). In the current setup, a lateral error of maximum ± 250 μ m could occur when determining tissue border. Finally, an optimized control of the irrigation system needs to be added to avoid thermal damage to the surrounding tissue [81,82]; for this, the effect of water spray on efficiency of the current system should be investigated.

5. Conclusion

A novel method for differentiating hard from soft tissue was proposed and tested in a closed-loop real-time system. A short overview of other similar methods, together with relevant advantages and disadvantages of each as compared to the proposed method, was provided. We concluded that the proposed method could be less costly, since no spectrometer is required, and that the experiment could be performed with a higher sampling rate (no full-frame recording, no heavy signal processing required). Given that the ablation took place in the hard tissue only, the soft tissue was preserved even after several round trips of the laser beam. Because the proposed method is a non-imaging setup with a low energy pulse, it is very likely to be miniaturized to be fitted inside the narrow channel of an endoscope. The setup, for now, can be used for free-space ablation; however, a future fiber-based setup for MIS is planned. Likewise, an OCT system will be integrated into the current setup for full control of cutting depth and for detecting the type of tissue during surgery, in the real-time.

Funding

Werner Siemens Foundation through the Minimally Invasive Robot-Assisted Computer-guided Laserosteotomy (MIRACLE) project.

Acknowledgments

The authors gratefully acknowledge the assistance given by Prof. Georg Rauter and his team.

Disclosures

The authors declare no conflicts of interest.

References

1. D. G. Panduric, I. B. Juric, S. Music, K. Molcanov, M. Susic, and I. Anic, "Morphological and ultrastructural comparative analysis of bone tissue after Er:YAG laser and surgical drill osteotomy," *Photomed. Laser Surg.* **32**(7), 401–408 (2014).
2. N. Jowett, W. Wöllmer, R. Reimer, J. Zustin, U. Schumacher, P. W. Wiseman, A. M. Mlynarek, A. Böttcher, C. V. Dalchow, B. B. Lörinz, R. Knecht, and R. J. D. Miller, "Bone Ablation without Thermal or Acoustic Mechanical Injury via a Novel Picosecond Infrared Laser (PIRL)," *Otolaryngol.–Head Neck Surg.* **150**(3), 385–393 (2014).
3. S. Stübinger, "Advances in bone surgery: the Er:YAG laser in oral surgery and implant dentistry," *Clin., Cosmet. Invest. Dent.* **2**, 47–62 (2010).
4. Y.-M. Lee, R. Y. Tu, A. Chiang, and Y.-C. Huang, "Average-power mediated ultrafast laser osteotomy using a mode-locked Nd:YVO₄ laser oscillator," *J. Biomed. Opt.* **12**(6), 060505 (2007).
5. B. Girard, K. Franjic, M. Cloutier, D. Wilson, C. M. L. Cloke, B. C. Wilson, and R. J. Dwayne Miller, *Bone surgery with femtosecond laser compared to mechanical instruments: healing studies*, High-Power Laser Ablation 2006 (SPIE, 2006), Vol. 6261.
6. M. Ivanenko, M. Werner, S. Afilal, M. Klasing, and P. Hering, "Ablation of hard bone tissue with pulsed CO₂ lasers," *Med. Laser Appl.* **20**(1), 13–23 (2005).
7. L. Beltrán, H. Abbasi, G. Rauter, N. Friederich, P. Cattin, and A. Zam, *Effect of laser pulse duration on ablation efficiency of hard bone in microseconds regime*, Third International Conference on Applications of Optics and Photonics (SPIE, 2017), Vol. 10453.
8. H. Abbasi, L. Beltrán, G. Rauter, R. Guzman, P. C. Cattin, and A. Zam, *Effect of cooling water on ablation in Er:YAG laserosteotomy of hard bone*, Third International Conference on Applications of Optics and Photonics (SPIE, 2017), Vol. 10453.
9. R. Mauceri, V. Panzarella, L. Maniscalco, A. Bedogni, M. E. Licata, A. Albanese, F. Toia, E. M. G. Cumbo, G. Mazzola, O. Di Fedè, and G. Campisi, "Conservative Surgical Treatment of Bisphosphonate-Related Osteonecrosis of the Jaw with Er,Cr:YSGG Laser and Platelet-Rich Plasma: A Longitudinal Study," *BioMed Res. Int.* **2018**, 1–10 (2018).
10. Y. Ohsugi, A. Aoki, K. Mizutani, S. Katagiri, M. Komaki, M. Noda, T. Takagi, S. Kakizaki, W. Meinzer, and Y. Izumi, "Evaluation of bone healing following Er:YAG laser ablation in rat calvaria compared with bur drilling," *J. Biophotonics* **12**(3), e201800245 (2019).
11. M. Augello, C. Baetscher, M. Segesser, H.-F. Zeilhofer, P. Cattin, and P. Juergens, "Performing partial mandibular resection, fibula free flap reconstruction and midfacial osteotomies with a cold ablation and robot-guided Er:YAG

- laser osteotome (CARLO®) – A study on applicability and effectiveness in human cadavers,” *J. Cranio Maxill Surg.* **46**(10), 1850–1855 (2018).
12. Y. A. Bayhaqi, A. Navarini, G. Rauter, P. C. Cattin, and A. Zam, *Neural network in tissue characterization of Optical Coherence Tomography (OCT) image for smart laser surgery: preliminary study*, Third International Seminar on Photonics, Optics, and Its Applications (ISPhOA 2018) (SPIE, 2019), Vol. 11044.
 13. Y. A. Bayhaqi, G. Router, A. Navarini, P. C. Cattin, and A. Zam, *Fast optical coherence tomography image enhancement using deep learning for smart laser surgery: preliminary study in bone tissue*, IV International Conference on Applications of Optics and Photonics (AOP 2019) (SPIE, 2019), Vol. 11207.
 14. T. Minamikawa, Y. Harada, and T. Takamatsu, *Raman spectroscopic detection of peripheral nerves towards nerve-sparing surgery*, SPIE BiOS (SPIE, 2017), Vol. 10054.
 15. L. A. Reisner, B. W. King, M. D. Klein, G. W. Auner, and A. K. Pandya, “A prototype biosensor-integrated image-guided surgery system,” *Int. J. Med. Robotics Comput. Assist. Surg.* **3**(1), 82–88 (2007).
 16. P. C. Ashok, N. Krstajić, M. E. Giardini, K. Dholakia, and W. Sibbett, “Raman Spectroscopy Sensor for Surgical Robotics – Instrumentation and Tissue Differentiation Algorithm,” in *Biomedical Optics and 3-D Imaging*, OSA Technical Digest (Optical Society of America, 2012), JM3A.26.
 17. P. C. Ashok, M. E. Giardini, K. Dholakia, and W. Sibbett, “A Raman spectroscopy bio-sensor for tissue discrimination in surgical robotics,” *J. Biophotonics* **7**(1-2), 103–109 (2014).
 18. F. Stelzle, C. Knipfer, W. Adler, M. Rohde, N. Oetter, E. Nkenke, M. Schmidt, and K. Tangermann-Gerk, “Tissue Discrimination by Uncorrected Autofluorescence Spectra: A Proof-of-Principle Study for Tissue-Specific Laser Surgery,” *Sensors* **13**(10), 13717–13731 (2013).
 19. A. Zam, “Optical Tissue Differentiation for Sensor-Controlled Tissue-Specific Laser Surgery,” (2011).
 20. R. Gunaratne, I. Monteath, J. Goncalves, R. Sheh, C. N. Ironside, M. Kapfer, R. Chipper, B. Robertson, R. Khan, and D. Fick, “Machine learning classification of human joint tissue from diffuse reflectance spectroscopy data,” *Biomed. Opt. Express* **10**(8), 3889–3898 (2019).
 21. A. Zam, F. Stelzle, K. Tangermann-Gerk, W. Adler, E. Nkenke, F. W. Neukam, M. Schmidt, and A. Douplik, “In vivo soft tissue differentiation by diffuse reflectance spectroscopy: preliminary results,” *Phys. Procedia* **5**, 655–658 (2010).
 22. F. Stelzle, A. Zam, W. Adler, K. Tangermann-Gerk, A. Douplik, E. Nkenke, and M. Schmidt, “Optical Nerve Detection by Diffuse Reflectance Spectroscopy for Feedback Controlled Oral and Maxillofacial Laser Surgery,” *J. Transl. Med.* **9**(1), 20 (2011).
 23. F. Stelzle, K. Tangermann-Gerk, W. Adler, A. Zam, M. Schmidt, A. Douplik, and E. Nkenke, “Diffuse reflectance spectroscopy for optical soft tissue differentiation as remote feedback control for tissue-specific laser surgery,” *Lasers Surg. Med.* **42**(4), 319–325 (2010).
 24. B. Lengenfelder, K. Schwarzkopf, N. Oetter, F. Mehari, E. Eschner, F. Klämpfl, F. Stelzle, M. Kesting, Z. Zalevsky, and M. Schmidt, *Acoustic differentiation of dental soft and hard tissues using remote speckle-analysis during Er:YAG ablation*, European Conferences on Biomedical Optics (SPIE, 2019), Vol. 11077.
 25. B. Lengenfelder, F. Mehari, M. Hohmann, M. Heinlein, E. Chelales, M. J. Waldner, F. Klämpfl, Z. Zalevsky, and M. Schmidt, “Remote photoacoustic sensing using speckle-analysis,” *Sci. Rep.* **9**(1), 1057 (2019).
 26. B. Lengenfelder, F. Mehari, M. Hohmann, C. Löhr, M. J. Waldner, M. Schmidt, Z. Zalevsky, and F. Klämpfl, “Contact-free endoscopic photoacoustic sensing using speckle-analysis,” *J. Biophotonics* **12**(12), e201900130 (2019).
 27. H. N. Kenhagho, G. Rauter, R. Guzman, P. Cattin, and A. Zam, “Optoacoustic Tissue Differentiation Using a Mach-Zehnder Interferometer: Preliminary Results,” in *2018 IEEE International Ultrasonics Symposium (IUS)*, 2018, 1–9.
 28. H. N. Kenhagho, G. Rauter, R. Guzman, P. C. Cattin, and A. Zam, “Optoacoustic Tissue Differentiation Using a Mach-Zehnder Interferometer,” *IEEE Trans. Ultrason., Ferroelect., Freq. Contr.* **66**(9), 1435–1443 (2019).
 29. H. Nguendon Kenhagho, S. Shevchik, F. Saeidi, N. Faivre, B. Meylan, G. Rauter, R. Guzman, P. Cattin, K. Wasmer, and A. Zam, “Characterization of Ablated Bone and Muscle for Long-Pulsed Laser Ablation in Dry and Wet Conditions,” *Materials* **12**(8), 1338 (2019).
 30. M. Hohmann, D. Dörner, F. Mehari, C. Chen, M. Späth, S. Müller, H. Albrecht, F. Klämpfl, and M. Schmidt, “Investigation of random lasing as a feedback mechanism for tissue differentiation during laser surgery,” *Biomed. Opt. Express* **10**(2), 807–816 (2019).
 31. H. Abbasi, G. Rauter, R. Guzman, P. C. Cattin, and A. Zam, *Differentiation of femur bone from surrounding soft tissue using laser-induced breakdown spectroscopy as a feedback system for smart laserosteotomy*, SPIE Photonics Europe (SPIE, 2018), Vol. 10685.
 32. R. Kanawade, F. Mehari, C. Knipfer, M. Rohde, K. Tangermann-Gerk, M. Schmidt, and F. Stelzle, “Pilot study of laser induced breakdown spectroscopy for tissue differentiation by monitoring the plume created during laser surgery — An approach on a feedback Laser control mechanism,” *Spectrochim. Acta, Part B* **87**, 175–181 (2013).
 33. R. Kanawade, F. Mahari, F. Klämpfl, M. Rohde, C. Knipfer, K. Tangermann-Gerk, W. Adler, M. Schmidt, and F. Stelzle, “Qualitative tissue differentiation by analysing the intensity ratios of atomic emission lines using laser induced breakdown spectroscopy (LIBS): prospects for a feedback mechanism for surgical laser systems,” *J. Biophotonics* **8**(1-2), 153–161 (2015).
 34. F. Mehari, M. Rohde, C. Knipfer, R. Kanawade, F. Klämpfl, W. Adler, F. Stelzle, and M. Schmidt, “Laser induced breakdown spectroscopy for bone and cartilage differentiation - ex vivo study as a prospect for a laser surgery feedback mechanism,” *Biomed. Opt. Express* **5**(11), 4013–4023 (2014).

35. F. Mehari, M. Rohde, R. Kanawade, C. Knipfer, W. Adler, F. Klämpfl, F. Stelzle, and M. Schmidt, "Investigation of the differentiation of ex vivo nerve and fat tissues using laser-induced breakdown spectroscopy (LIBS): Prospects for tissue-specific laser surgery," *J. Biophotonics* **9**(10), 1021–1032 (2016).
36. M. Rohde, F. Mehari, F. Klämpfl, W. Adler, F.-W. Neukam, M. Schmidt, and F. Stelzle, "The differentiation of oral soft- and hard tissues using laser induced breakdown spectroscopy – a prospect for tissue specific laser surgery," *J. Biophotonics* **10**(10), 1250–1261 (2017).
37. X. Li, S. Yang, R. Fan, X. Yu, and D. Chen, "Discrimination of soft tissues using laser-induced breakdown spectroscopy in combination with k nearest neighbors (kNN) and support vector machine (SVM) classifiers," *Opt. Laser Technol.* **102**, 233–239 (2018).
38. H. Abbasi, G. Rauter, R. Guzman, P. C. Cattin, and A. Zam, "Laser-induced breakdown spectroscopy as a potential tool for autocarbonization detection in laserosteotomy," *J. Biomed. Opt.* **23**(7), 1–7 (2018).
39. H. Abbasi, I. Sugiarto, G. Rauter, R. Guzman, P. C. Cattin, and A. Zam, "Pilot Ex Vivo Study of Laser-Induced Breakdown Spectroscopy to Detect Bone Dehydration: An Approach for Irrigation Feedback in Laserosteotomy," in *International Conference on Electrical Engineering & Computer Science (ICEECS 2018)*, (Bali, Indonesia, 2018).
40. F. Mehari, B. Lengenfelder, R. Figura, F. Klämpfl, and M. Schmidt, "LIBS based Tissue Differentiation for Er: YAG Surgical Laser," *Proceedings of the 6th International Conference on Photonics, Optics and Laser Technology - Volume 1: PHOTOPTICS*, 5 (2018).
41. K. Henn, G. G. Gubaidullin, J. Bongartz, J. Wahrburg, H. Roth, and M. Kunkel, "A spectroscopic approach to monitor the cut processing in pulsed laser osteotomy," *Lasers Med. Sci.* **28**(1), 87–92 (2013).
42. H. Huang, L.-M. Yang, S. Bai, and J. Liu, "Smart surgical tool," *J. Biomed. Opt.* **20**(07), 1–7 (2015).
43. S. Rupprecht, K. Tangermann, P. Kessler, F. W. Neukam, and J. Wiltfang, "Er:YAG laser osteotomy directed by sensor controlled systems," *J. Cranio Maxill Surg.* **31**(6), 337–342 (2003).
44. S. Rupprecht, K. Tangermann-Gerk, J. Wiltfang, F. W. Neukam, and A. Schlegel, "Sensor-based laser ablation for tissue specific cutting: an experimental study," *Lasers Med. Sci.* **19**(2), 81–88 (2004).
45. A. Seifalinezhad, M. Bahreini, M. M. Hassani Matin, and S. H. Tavassoli, "Feasibility Study on Discrimination of Neo-plastic and Non-Neoplastic Gastric Tissues Using Spark Discharge Assisted Laser Induced Breakdown Spectroscopy," *J. Lasers Med. Sci.* **10**(1), 64–69 (2018).
46. J. H. Han, Y. Moon, J. J. Lee, S. Choi, Y.-C. Kim, and S. Jeong, "Differentiation of cutaneous melanoma from surrounding skin using laser-induced breakdown spectroscopy," *Biomed. Opt. Express* **7**(1), 57–66 (2016).
47. Y. Moon, J. H. Han, S. Shin, Y.-C. Kim, and S. Jeong, "Elemental analysis of tissue pellets for the differentiation of epidermal lesion and normal skin by laser-induced breakdown spectroscopy," *Biomed. Opt. Express* **7**(5), 1626–1636 (2016).
48. X. Chen, X. Li, S. Yang, X. Yu, and A. Liu, "Discrimination of lymphoma using laser-induced breakdown spectroscopy conducted on whole blood samples," *Biomed. Opt. Express* **9**(3), 1057–1068 (2018).
49. A. V. DSouza, H. Lin, E. R. Henderson, K. S. Samkoe, and B. W. Pogue, "Review of fluorescence guided surgery systems: identification of key performance capabilities beyond indocyanine green imaging," *J. Biomed. Opt.* **21**(8), 080901 (2016).
50. A. L. Lazarides, M. J. Whitley, D. B. Strasfeld, D. M. Cardona, J. M. Ferrer, J. L. Mueller, H. L. Fu, S. Bartholf DeWitt, B. E. Brigman, N. Ramanujam, D. G. Kirsch, and W. C. Eward, "A Fluorescence-Guided Laser Ablation System for Removal of Residual Cancer in a Mouse Model of Soft Tissue Sarcoma," *Theranostics* **6**(2), 155–166 (2016).
51. J. Odenthal, P. Friedl, and R. P. Takes, "Compatibility of CO₂ laser surgery and fluorescence detection in head and neck cancer cells," *Head & Neck* **41**(5), 1253–1259 (2019).
52. S. R. Visuri, J. T. Walsh Jr., and H. A. Wigdor, "Erbium laser ablation of dental hard tissue: Effect of water cooling," *Lasers Surg. Med.* **18**(3), 294–300 (1996).
53. M. Papadaki, A. Doukas, W. A. Farinelli, L. Kaban, and M. Troulis, "Vertical ramus osteotomy with Er:YAG laser: a feasibility study," *Int. J. Oral Maxillofac. Surg.* **36**(12), 1193–1197 (2007).
54. L. Kuscer and J. Diaci, "Measurements of erbium laser-ablation efficiency in hard dental tissues under different water cooling conditions," *J. Biomed. Opt.* **18**(10), 108002 (2013).
55. V. Tuchin, "Tissue optics and photonics: Light-tissue interaction II," *J. Biomed. Photonics Eng.* **2**(3), 030201 (2016).
56. N. M. Fried and D. Fried, "Comparison of Er:YAG and 9.6- μ m TE CO₂ lasers for ablation of skull tissue," *Lasers Surg. Med.* **28**(4), 335–343 (2001).
57. N. Fried and D. Fried, *Laser ablation of skull tissue using transverse excited 9.6-um CO₂ lasers with pulse durations of 1-100 us*, BiOS 2000 The International Symposium on Biomedical Optics (SPIE, 2000), Vol. 3914.
58. K. Chan, N. Fried, and D. Fried, *Selective ablation of carious lesions using an integrated multispectral near-IR imaging system and a novel 9.3- μ m CO₂ laser*, SPIE BiOS (SPIE, 2018), Vol. 10473.
59. A. Charlton, M. R. Dickinson, T. A. King, and A. J. Freemont, "Erbium-YAG and holmium-YAG laser ablation of bone," *Lasers Med. Sci.* **5**(4), 365–373 (1990).
60. M. Buchelt, H.-P. Kutschera, T. Katterschafka, H. Kiss, S. Lang, R. Beer, and U. Losert, "Erb:YAG and Hol:YAG Laser Osteotomy: The Effect of Laser Ablation on Bone Healing," *Lasers Surg. Med.* **15**(4), 373–381 (1994).
61. J. T. Walsh Jr. and T. F. Deutsch, "Er:YAG laser ablation of tissue: Measurement of ablation rates," *Lasers Surg. Med.* **9**(4), 327–337 (1989).

62. A. Vogel and V. Venugopalan, "Mechanisms of Pulsed Laser Ablation of Biological Tissues," *Chem. Rev.* **103**(2), 577–644 (2003).
63. J. Noack, D. X. Hammer, G. D. Noojin, B. A. Rockwell, and A. Vogel, "Influence of pulse duration on mechanical effects after laser-induced breakdown in water," *J. Appl. Phys.* **83**(12), 7488–7495 (1998).
64. N. Linz, S. Freidank, X.-X. Liang, and A. Vogel, "Wavelength dependence of femtosecond laser-induced breakdown in water and implications for laser surgery," *Phys. Rev. B* **94**(2), 024113 (2016).
65. A. Vogel, "Nonlinear absorption: intraocular microsurgery and laser lithotripsy," *Phys. Med. Biol.* **42**(5), 895–912 (1997).
66. J.-L. Boulnois, "Photophysical processes in recent medical laser developments: A review," *Lasers Med. Sci.* **1**(1), 47–66 (1986).
67. F. Reza, K. A. Katayoun, A. Farzaneh, and T. Nikoo, "Laser in orthodontics," in *Principles in Contemporary Orthodontics* (IntechOpen, 2011).
68. Z. Qin and J. C. Bischof, "Thermophysical and biological responses of gold nanoparticle laser heating," *Chem. Soc. Rev.* **41**(3), 1191–1217 (2012).
69. M. H. Niemz, *Laser-tissue interactions* (Springer, 2007).
70. S. L. Jacques, "Laser-Tissue Interactions: Photochemical, Photothermal, and Photomechanical," *Surg. Clin. North Am.* **72**(3), 531–558 (1992).
71. A. Vogel, W. Lauterborn, and R. Timm, "Optical and acoustic investigations of the dynamics of laser-produced cavitation bubbles near a solid boundary," *J. Fluid Mech.* **206**, 299–338 (1989).
72. A. Vogel, S. Busch, K. Jungnickel, and R. Birngruber, "Mechanisms of intraocular photodisruption with picosecond and nanosecond laser pulses," *Lasers Surg. Med.* **15**(1), 32–43 (1994).
73. R. O. Esenaliev, A. A. Oraevsky, S. L. Jacques, and F. K. Tittel, *Effect of tensile stress amplitude and temporal characteristics on threshold of cavitation-driven ablation*, Photonics West '96 (SPIE, 1996), Vol. 2681.
74. S. L. Jacques, *How tissue optics affect dosimetry for photochemical, photothermal, and photomechanical mechanisms of laser-tissue interaction*, Recent Advances in the Uses of Light in Physics, Chemistry, Engineering, and Medicine (SPIE, 1992), Vol. 1599.
75. A. Vogel and V. Venugopalan, "Pulsed laser ablation of soft biological tissues," in *Optical-Thermal Response of Laser-Irradiated Tissue* (Springer, 2010), pp. 551–615.
76. A. Gholami, M. Baradaran-Ghahfarokhi, M. Ebrahimi, and M. Baradaran-Ghahfarokhi, "Thermal effects of laser-osteotomy on bone: mathematical computation using maple," *J. Med. Signals Sens.* **3**(4), 262 (2013).
77. Y. Suzaki and A. Tachibana, "Measurement of the μm sized radius of Gaussian laser beam using the scanning knife-edge," *Appl. Opt.* **14**(12), 2809–2810 (1975).
78. I. Standard, "11146, "Test methods for laser beam widths, divergence angles and beam propagation ratios"(2005)."
79. M. Nazeri, A. E. Majd, R. Massudi, S. H. Tavassoli, A. Mesbahinia, and H. Abbasi, "Laser-Induced Breakdown Spectroscopy Via the Spatially Resolved Technique Using Non-Gated Detector," *J. Russ. Laser Res.* **37**(2), 164–171 (2016).
80. H. Abbasi, G. Rauter, R. Guzman, P. C. Cattin, and A. Zam, *Plasma plume expansion dynamics in nanosecond Nd:YAG laserosteotome*, SPIE BiOS (SPIE, 2018), Vol. 10505.
81. L. M. B. Bernal, G. Shayeganrad, G. Kosa, M. Zelechowski, G. Rauter, N. Friederich, P. C. Cattin, and A. Zam, *Performance of Er:YAG laser ablation of hard bone under different irrigation water cooling conditions*, SPIE BiOS (SPIE, 2018), Vol. 10492.
82. M. Beltran Bernal Lina, T. Schmidt Iris, N. Vulin, J. Widmer, G. Snedeker Jess, C. Cattin Philippe, A. Zam, and G. Rauter, "Optimizing controlled laser cutting of hard tissue (bone)," in *at - Automatisierungstechnik*, (2018), p. 1072.
83. H. Abbasi, G. Rauter, R. Guzman, P. C. Cattin, and A. Zam, *Design and implementation of a compact high-throughput echelle spectrometer using off-the-shelf off-axis parabolic mirrors for analysis of biological samples by LIBS (Conference Presentation)*, SPIE Optical Metrology (SPIE, 2019), Vol. 11060.
84. S. L. Jacques, R. D. Glickman, and J. A. Schwartz, *Internal absorption coefficient and threshold for pulsed laser disruption of melanosomes isolated from retinal pigment epithelium*, Photonics West '96 (SPIE, 1996), Vol. 2681.
85. S. L. Jacques, A. A. Oraevsky, C. R. Thompson, and B. S. Gerstman, *Working theory and experiments on photomechanical disruption of melanosomes to explain the threshold for minimal visible retinal lesions for sub-nl laser pulses*, OE/LASE '94 (SPIE, 1994), Vol. 2134.
86. S. L. Jacques and D. J. McAuliffe, "The melanosome: threshold temperature for explosive vaporization and internal absorption coefficient during pulsed laser irradiation," *Photochem. Photobiol.* **53**(6), 769–775 (1991).
87. S. L. Jacques, "Optical properties of biological tissues: a review," *Phys. Med. Biol.* **58**(11), R37–R61 (2013).

5.2. A simple acoustic-cased method for lens-to-sample distance adjustment in μ LIBS

The research presented in the previous section describes a few challenges we faced. One of the challenges was adjusting the distance between the focusing lens and the sample. This was a difficult and time-consuming task to perform manually, due to the fact that the focal length of the lens provided a short Rayleigh length. Later, we developed a method to help the researcher adjust this distance with the help of an acoustic sensor. This section presents a short publication from a conference proceeding that introduces a method for lens-to-sample distance adjustment, while using a low-energy Nd:YAG laser for plasma formation.

Publication: H. Abbasi, P. C. Cattin and A. Zam, "A Simple Acoustic-Based Method for Lens-to Sample Distance Adjustment in μ LIBS," *2020 Photonics North (PN)*, 2020, pp. 1-1, doi: 10.1109/PN50013.2020.9167018. [<https://doi.org/10.1109/PN50013.2020.9167018>]

Copyright notice: © 2020, IEEE. Reprinted, with permission, from H. Abbasi, P. C. Cattin and A. Zam, A Simple Acoustic-Based Method for Lens-to Sample Distance Adjustment in μ LIBS, IEEE 2020 Photonics North (PN), May 2020.

A Simple Acoustic-Based Method for Lens-to-Sample Distance Adjustment in μ LIBS

Hamed Abbasi, Philippe C. Cattin, Azhar Zam

Department of Biomedical Engineering, University of Basel, CH-4123 Allschwil, Switzerland

hamed.abbasi@unibas.ch; azhar.zam@unibas.ch

Abstract—A cost-effective method employing a smartphone sensor to measure the laser-induced sound pressure level (SPL) has been introduced for lens-to-sample distance (LTSD) adjustment in micro laser-induced breakdown spectroscopy (μ LIBS).

Keywords—LIBS; focusing control; repeatability improvement

I. INTRODUCTION

LIBS is a powerful analytical technique with numerous applications in industry and medicine. The authors have recently introduced a novel real-time method for tissue-specific laserosteotomy based on μ LIBS [1]. In μ LIBS, a low energy laser beam with a high spatial resolution is utilized to investigate materials in a nearly non-destructive manner. To minimize the fluctuations in laser fluence (J cm^{-2}) caused by LTSD mismatch, a supplementary method to adjust LTSD is advantageous. For this purpose, several approaches have been investigated so far. They are mainly based on additional lasers and/or a camera [2-5]. Moreover, Peret et al. restored the autofocus capability of the ChemCam instrument onboard NASA's Curiosity rover that landed on Mars [6]. This paper presented a simple method based on monitoring the laser-induced SPL using a smartphone to adjust the LTSD.

II. MATERIALS AND METHODS

A. μ LIBS setup

The μ LIBS setup consists of a Q-switched Nd:YAG (532 nm, 1 Hz), a lab-made Echelle spectrometer [7], and a few optics including mirrors, and a convex lens ($f=20$ mm).

B. SPL measurement

SPLs have been measured using a smartphone (Huawei P20 Pro) and Phyphox application (an application dedicated to measurements using implemented physical sensors of smartphones, developed in RWTH Aachen University [8]). The sample, a porcine femur bone attached to a motorized translation stage (Standa, speed = $10 \mu\text{m/s}$), was located 6 cm above the smartphone while the laser was directed to it from the side. Every ten microns, new data has been collected. Alternatively, the focusing lens could be moved instead.

III. RESULTS AND CONCLUSIONS

Figure 1 shows the collected SPL around the focal spot (± 2 mm) at three energies: (a) 2.3 mJ, (b) 4.8 mJ, (c) 6.6 mJ. At

lower energies, the signal intensity was almost at noise level (with the employed sensor); at higher energies due to plasma creation in the air, an overlapping signal appeared when the LTSD was longer than it should be.

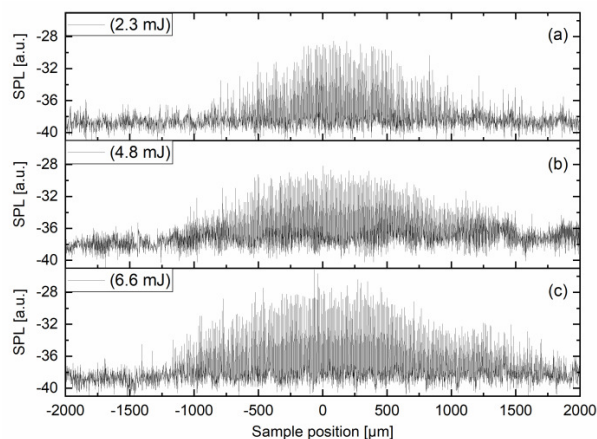


Fig. 1. Collected SPL signals around the focal spot (± 2 mm). The best LTSDs are located at high amplitudes. The shallower slope on the right side of the signal is due to micro ablation (mass removal) that occurred during the measurements (400 s for each energy); therefore, the LTSD changed slightly.

At low energies, the working range is more limited since the ablation is threshold-based [1]. By considering a threshold for the amplitude of SPL, points close to the Rayleigh length can be identified. The proposed method provides a simple and cost-effective way to improve the repeatability of μ LIBS analysis, especially outside the laboratory. For further studies, the setup can be utilized in a closed-loop fashion to adjust the LTSD, automatically. Miniaturized acoustic sensors [9] can also be employed for potential endoscopic applications.

REFERENCE:

- [1] H. Abbasi, et al., Biomed. Opt. Express 11.4 (2020).
- [2] B. Ashrafkhani et al., Opt. Spectrosc. 118.5 (2015).
- [3] J. Cortez et al., Appl. Spectrosc. 71.4 (2017).
- [4] P. Zhang et al., Anal. Chem. 90.7 (2018).
- [5] W. Wang et al., Plasma Sci. Technol. 21.3 (2019).
- [6] L. Peret et al., SpaceOps Conf. (2016).
- [7] H. Abbasi, et al., Proc. SPIE 11060 (2019).
- [8] C. Stampfer et al., Nat. Rev. Mater. 5 (2020).
- [9] H. Nguendon et al., IEEE Sens. Conf. (2019).

Chapter 6:
**Development of miniaturized laser-induced breakdown
spectroscopy (mini-LIBS) probe for endoscopic smart
laserosteotomy**

6.1. Simulation of Echellogram using Zemax OpticStudio and Matlab for LIBS

In an FO-LIBS system, the plasma plume created is less luminous than that of a free-space LIBS plasma. Additionally, if a small lens at the fiber tip is used for light collection, only a small portion of plasma light is collected. Therefore, to compensate for the low optical collection of plasma emissions in a miniaturized FO-LIBS, we custom-made an Echelle spectrometer with higher optical throughput (low F-number) than those commercially available on the market. This section presents a publication from a conference proceeding that introduces a methodology for simulating an Echellogram. This simulation was later used to develop a high optical throughput Echelle spectrometer.

Publication: Abbasi H., Sahraei N., Canbaz F., Cattin P.C., Zam A. (2021) Simulation of Echellogram Using Zemax OpticStudio and Matlab for LIBS. In: Rauter G., Cattin P.C., Zam A., Riener R., Carbone G., Pisla D. (eds) *New Trends in Medical and Service Robotics. MESROB 2020. Mechanisms and Machine Science*, vol 93. Springer, Cham. https://doi.org/10.1007/978-3-030-58104-6_24

Copyright notice: Reprinted/adapted by permission from Springer Nature Customer Service Centre GmbH: Springer, Cham, *New Trends in Medical and Service Robotics, MESROB 2020*, Editors: Rauter, G., Cattin, P.C., Zam, A., Riener, R., Carbone, G., Pisla, D. (Eds.) COPYRIGHT 2021.

Simulation of Echellogram Using Zemax OpticStudio and Matlab for LIBS

Hamed Abbasi¹, Negin Sahraei², Ferda Canbaz¹, Philippe C. Cattin², Azhar Zam¹

¹ Biomedical Laser and Optics Group (BLOG), Department of Biomedical Engineering, University of Basel, CH-4123 Allschwil, Switzerland

hamed.abbasi@unibas.ch

² Center for medical Image Analysis and Navigation (CIAN), Department of Biomedical Engineering, University of Basel, CH-4123 Allschwil, Switzerland

Abstract. Echelle spectrometers offer high-resolution (ca. one Angstrom or higher) and wide range (ca. half a micron or wider), simultaneously, without having a mechanical moving part. However, they require a complicated optical set-up as compared to conventional one-dimensional-dispersion/diffraction spectrometers, e.g., Czerny-Turner. Therefore, the simulation of the Echellogram is required before building the spectrometer. This paper aims to develop an application for visualizing the Echellogram using MATLAB App Designer followed by simulation of the optical aberrations by Zemax OpticStudio to optimize the spectrometer parameters. The developed application provides an interactive graphical interface with a user-friendly dashboard to control and monitor the required parameters. This spectrometer is being used in laser-induced breakdown spectroscopy (LIBS) system application used for robot-guided laser ablation of biological tissues.

Keywords: Echelle Spectrometer, Simulation, Zemax OpticStudio, Matlab, Diffraction Grating.

1 Introduction

Echelle spectrometers are widely used in observatories [1-3] and Laser-Induced Breakdown Spectroscopy (LIBS) experiments [4-6]. The ones used in observatories are typically up to several meters to have the highest possible resolving power [7-9]. The ones used in LIBS utilize rather small designs to make the system portable (trade-off between size and resolving power) [10, 11]. However, in both cases, the Free Spectral Range (FSR) and optical throughput are required to be wide and high enough, respectively, complicated due to low light intensity (in observatories) [12] and low exposure time (time-resolved measurements in LIBS) [13]. Unlike conventional prism- [14] or grating-based [15] monochromators/spectrometers with one-

dimensional-dispersion/diffraction, Echelle spectrometers have dispersion/diffraction in two dimensions, one caused by the Echelle grating and the other caused by the cross-dispenser to separate the different order of diffractions from each other. Therefore, without employing any mechanical moving part, a large number of pixels in the camera can be used to separate wavelengths from each other, to achieve a high resolving power, without reducing FSR. Although designing an Echelle spectrometer has its challenges, the performance (etendue, resolution, bandwidth, etc.) can still be improved by utilizing an application-oriented design [16, 17]. Therefore, several toolboxes, based on different platforms, have been developed to simulate the Echellogram (frequency-separated image of the slit in the camera plane) focusing mainly on astronomical application [18-23]. To overcome the design challenges of Echelle spectrometers for LIBS application, a user-friendly simulation approach can foster the design, by reducing the final cost and designing time. In this work, therefore, an application for simulating Echellograms has been developed. This application allows rapid calculation of the properties of an Echelle spectrometer, primarily with LIBS application in mind. This design-aid tool can quickly simulate the images seen by the camera. However, the widening of the slit image in the Echellogram due to optical aberrations is not considered; therefore, the simulation is followed by a secondary simulation by Zemax OpticStudio to consider the effect of induced aberration on its resolution. The final step includes combining these two simulation platforms to develop a user-friendly designing tool for Echelle spectrometer in LIBS systems.

2 Spectrometer Design

We previously performed some initial experiments on LIBS measurements of biological tissues [24-26] employing a commercially available Echelle spectrometer. In these experiments, we aimed to find the most important atomic and molecular lines for differentiation of tissue types to be used as feedback for smart laser surgery. Based on these preliminary experimental results, the design requirements were obtained. A bandwidth from 330 to 830 nm and resolution of ca. one Angstrom has been selected for the design with an emphasis on maximizing the optical throughput as compared to the commercially available Echelle spectrometers [6]. Therefore, we set up our spectrometer using off-axis parabolic mirrors with 2-inch diameter to reduce the F-number and consequently increasing the optical throughput. Figure 1 shows a CAD representation of the spectrometer set-up. The input fiber (A) delivers light to the first collimator (B), which reflects the parallel light to the Echelle grating positioned at the Littrow angle at point C. After being reflected back to point B, due to a small off-axis angle induced to the Echelle grating, the light passes slightly above the fiber and goes to the second collimator (D) which reflects the light to the second diffraction grating (E) for separating the Echelle orders (cross-dispenser). Separated orders are imaged to the camera through the imaging lens (F). Note that, since both collimators have the same properties (size, focal length, etc.), the design can also be simulated considering only a single collimator.

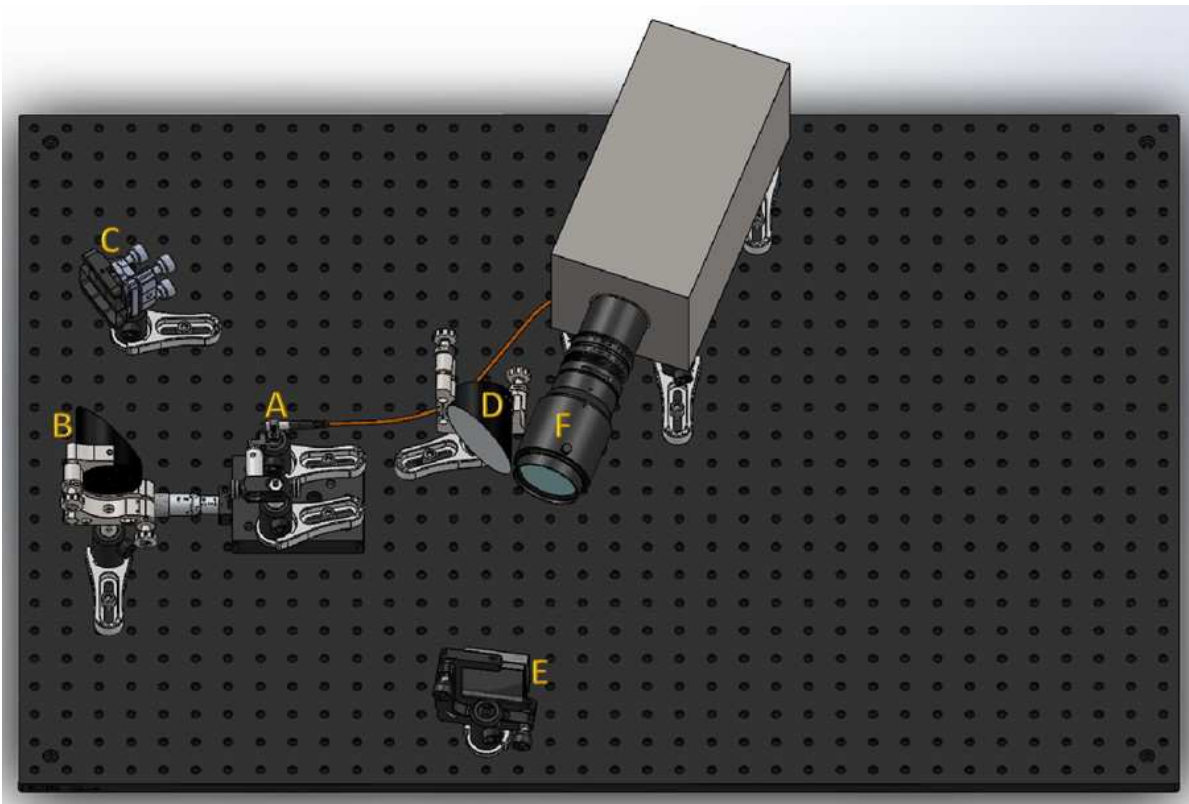


Fig. 1. CAD representation of the spectrometer set-up (A: input fiber, B: first collimating mirror, C: Echelle grating, D: second collimating mirror, E: cross-disperser grating, F: imaging lens). The light pass starts from point A, goes to B, and C, comes back to B, passes above point A, goes to D, E, F, and Camera, accordingly. The optical base plate is 90×60 cm. The size of the set-up without considering the camera and its lens is 44 (l) \times 36 (w) \times 13 (h) cm³. The camera should be located outside of the spectrometer in order to not obstruct the camera cooling fan. The CAD representation was designed using SolidWorks 2017.

3 Echellogram Simulator

Echellogram simulator application was developed using MATLAB app designer (R2018b) to simulate the grating cross-dispense Echelle spectrometers. The developed application provides an interactive graphical user interface (GUI) with a user-friendly control panel. It asks the user to enter the required 22 design parameters and returns 27 calculated output parameters plus the depicted Echellogram. Figure 2 shows the user interface of the developed application. In the user interface, the required input and output parameters are shown in dark blue and black, respectively. The suggested pixel width/height is given according to the Nyquist criterion to avoid “under-sampling” i.e. aliasing [12]. Smaller pixels fulfill the Nyquist–Shannon sampling theorem as well and will offer more points for peak fitting; however, it does not narrow down the FWHM of the peaks. The offered tilt angle for the camera helps to align the pixels with the order rows to be able to do binning (to increase the frame rate). The suggested input slit width/height shows the counterproductive limit, i.e., smaller slits would not result in improved resolution but only reduce the intensity of the entered light [27]. To evaluate the performance of the developed application, the results for

modified OPTIMA (commercially available Echelle spectrometer) simulation have been compared by the one simulated with “SimEchelle” [12]. SimEchelle is an excel-based simulator without a GUI. The results from both simulators were in agreement. The developed application provides some additional useful information (including requirements for a matching camera sensor and its placement angle) for designing an Echelle spectrometer as compared to similar previously developed software. The input numbers shown in the application interface after starting the application (default numbers) are those from the modified OPTIMA simulation, as shown in Figure 2.

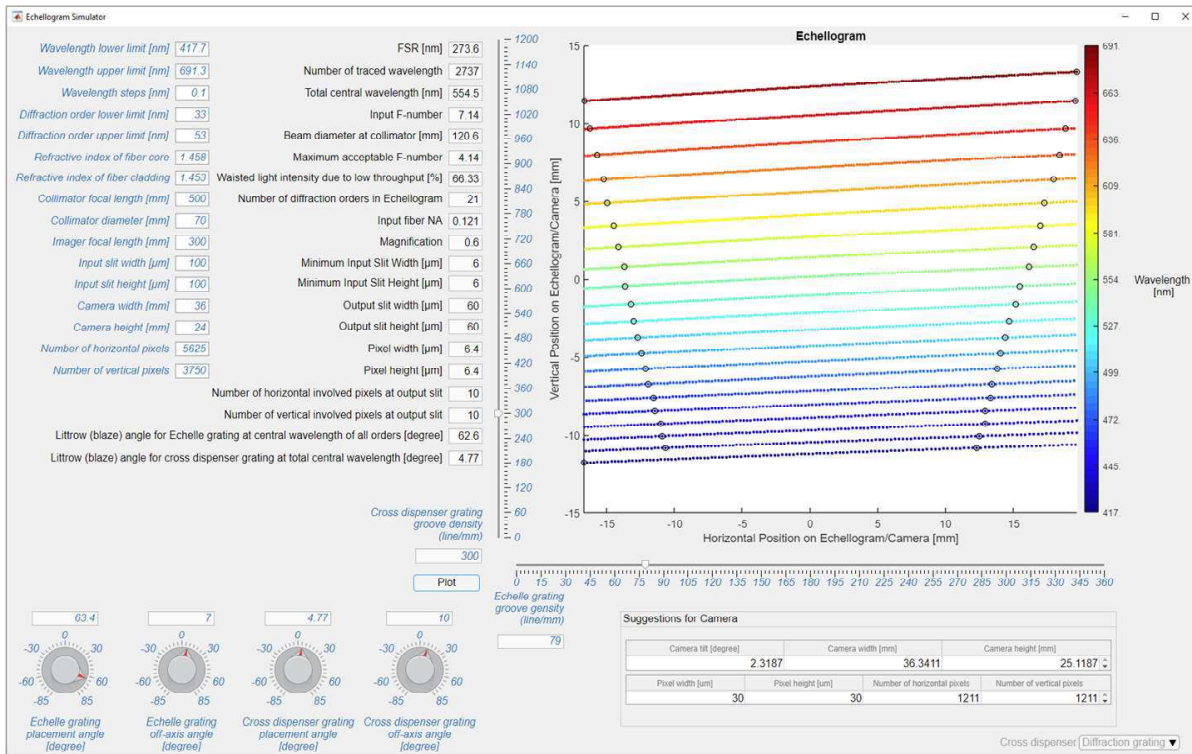


Fig. 2. The user interface of the developed application. The required input parameters are entered in the dark blue boxes, knobs, and sliders. The output parameters are shown in black; the simulated Echellogram is depicted once the plot button is pressed. Positions on the Echellogram are in reference to the diffracted light at Littrow configuration for both gratings. The black circles on the sides of each order show the overlapping border.

Besides the inserted figure in the application, some additional pop-up figures additionally are shown by the application, e.g., diffraction orders vs. diffraction angle/wavelength (with or without spatial filtering). Figure 3 shows the pop-up figures for the spectrometer designed to cover 330 to 830 nm for the analysis of biological samples by LIBS.

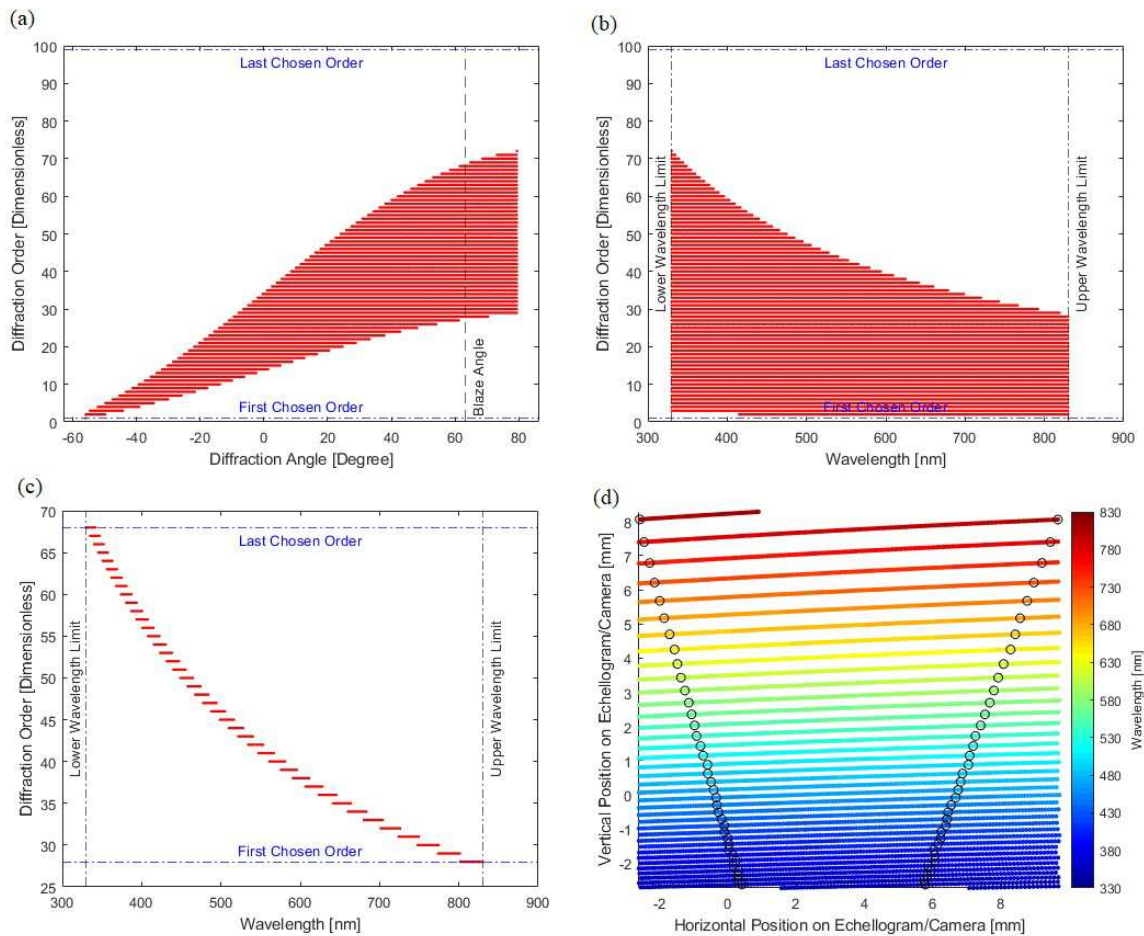


Fig. 3. Auxiliary pop-up figures created by the developed application. Part (a) shows all possible diffraction orders without spatial filtering. Part (b) shows all diffractable wavelengths at each diffraction order. Part (c) is the same as (a) with spatial filtering. Part (d) is the Echellogram. By holding the mouse cursor on each point, its properties will be shown to the user.

4 Zemax OpticStudio Simulation

The Echellogram simulator application showed the position of the exit slit on the camera plane, which can be used to define the required camera properties for the desired FSR based on the chosen grating and lenses/mirrors. However, induced optical aberrations were not considered. Therefore, an additional simulation step is required to show the effect of aberrations on the resolution of the system. Optical aberrations can reduce the resolution of the system and potentially cause crosstalk between the orders. Zemax OpticStudio is the most commonly used software for spectrometer aberration simulation [28, 29]. Figure 4 shows the simulation of the designed spectrometer by Zemax OpticStudio for the exemplary sodium (Na) doublets. The sodium doublets are the closest peaks we expect important for differentiating tissues [24]. A clear separation can be observed in the spot diagram for the chosen parameters.

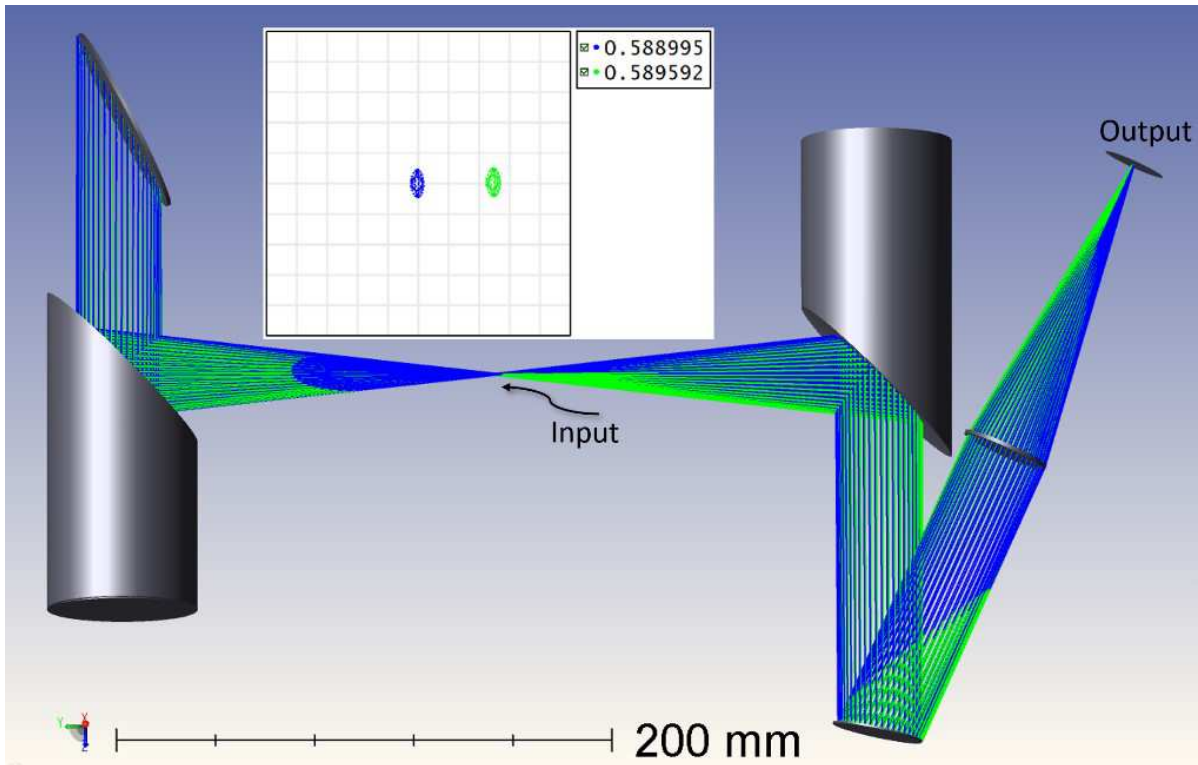


Fig. 4. Simulation of the designed spectrometer using Zemax OpticStudio 16.5 standard edition. The spot diagram shows the separation of doublet of sodium (Na) with 5.97 Angstrom distance (from 5889.95 to 5895.92 Angstrom). An astigmatism aberration is visible in the spot diagram; however, it did not reduce the required resolution.

5 Conclusions

A simulator application for quick calculation of Echellograms (image seen by the camera) properties has been developed. According to user input parameters such as groove density, placement angles of gratings, focal length, and sizes of lenses/mirrors, the Echellogram simulator application returns the requirements for a matching camera sensor, including the size and number of required pixels as well as camera tilt angle. Secondary, simulation has also been conducted to determine that the induced aberrations do not result in insufficient resolution. The result of both simulations showed that the designed spectrometer with high optical throughput had the potential to be used in the desired spectral range with enough resolving power based on the previous experimental data for differentiating tissues using LIBS. Future work might be combining both simulator platforms into a single software application.

Acknowledgments The authors gratefully acknowledge funding of the Werner Siemens Foundation through the Minimally Invasive Robot-Assisted Computer-guided Laserosteotomy (MIRACLE) project. Moreover, the authors acknowledge the assistance given by Mr. Arsham Hamidi and Mr. Yakub Bayhaqi.

References

1. J. H. Telting, G. Avila, L. Buchhave, S. Frandsen, D. Gandolfi, B. Lindberg, H. C. Stempels, t. N. staff, and S. Prins, "FIES: The high-resolution Fiber-fed Echelle Spectrograph at the Nordic Optical Telescope," *Astronomische Nachrichten* 335, 41-45 (2014).
2. F. Pepe, S. Cristiani, R. Rebolo Lopez, N. Santos, A. Amorim, et al., ESPRESSO: the Echelle spectrograph for rocky exoplanets and stable spectroscopic observations, *SPIE Astronomical Telescopes + Instrumentation* (SPIE, 2010), Vol. 7735.
3. M. Tala , P. Heeren, M. Grill, R. Harris, J. Stürmer, C. Schwab, et al., A high-resolution spectrograph for the 72cm Waltz Telescope at Landessternwarte, Heidelberg, *SPIE Astronomical Telescopes + Instrumentation* (SPIE, 2016), Vol. 9908.
4. M. Sabsabi, V. Detalle, M. A. Harith, W. Tawfik, and H. Imam, "Comparative study of two new commercial echelle spectrometers equipped with intensified CCD for analysis of laser-induced breakdown spectroscopy," *Appl. Opt.* 42, 6094-6098 (2003).
5. P. Fichet, D. Menut, R. Brennetot, E. Vors, and A. Rivoallan, "Analysis by laser-induced breakdown spectroscopy of complex solids, liquids, and powders with an echelle spectrometer," *Appl. Opt.* 42, 6029-6035 (2003).
6. H. Abbasi, G. Rauter, R. Guzman, P. C. Cattin, and A. Zam, Design and implementation of a compact high-throughput echelle spectrometer using off-the-shelf off-axis parabolic mirrors for analysis of biological samples by LIBS (Conference Presentation), *SPIE Optical Metrology* (SPIE, 2019), Vol. 11060.
7. C. Schwab, A. Rakich, Q. Gong, S. Mahadevan, S. Halverson, A. Roy, R. Terrien, et al. Design of NEID, an extreme precision Doppler spectrograph for WIYN, *SPIE Astronomical Telescopes + Instrumentation* (SPIE, 2016), Vol. 9908.
8. N. Lentini, B. Kuo Tiong, L. DuBois, T. Feger, D. Coutts, C. Fallscheer, and C. Schwab, A high resolution echelle spectrograph for exoplanet searches with small aperture telescopes, *SPIE Astronomical Telescopes + Instrumentation* (SPIE, 2018), Vol. 10702.
9. A. Chakraborty, S. Mahadevan, A. Roy, V. Dixit, E. Harvey Richardson, V. Dongre, et al. "The PRL Stabilized High-Resolution Echelle Fiber-fed Spectrograph: Instrument Description and First Radial Velocity Results," *Publications of the Astronomical Society of the Pacific* 126, 133-147 (2014).
10. X. Fu, F. Duan, J. Jiang, T. Huang, L. Ma, and C. Lv, "Astigmatism-corrected echelle spectrometer using an off-the-shelf cylindrical lens," *Appl. Opt.* 56, 7861-7868 (2017).
11. W. T. Y. Mohamed, "Study of the matrix effect on the plasma characterization of six elements in aluminum alloys using LIBS with a portable Echelle spectrometer," *Progress in physics* 2, 42-49 (2007).
12. T. Eversberg and K. Vollmann, *Spectroscopic instrumentation* (Springer, 2015).
13. H. Abbasi, G. Rauter, R. Guzman, P. C. Cattin, and A. Zam, Plasma plume expansion dynamics in nanosecond Nd:YAG laserosteotome, *SPIE BiOS* (SPIE, 2018), Vol. 10505.
14. H. Abbasi, M. Nazeri, and S. A. Mireei, "Design and development of a LabVIEW-based LED-induced fluorescence spectroscopy system with applications in non-destructive quality assessment of agricultural products," *Journal of Physics: Conference Series* 672, 012010 (2016).
15. M. Nazeri, A. E. Majd, R. Massudi, S. H. Tavassoli, A. Mesbahinia, et al., "Laser-Induced Breakdown Spectroscopy Via the Spatially Resolved Technique Using Non-Gated Detector," *Journal of Russian Laser Research* 37, 164-171 (2016).

16. R. A. Probst, T. Steinmetz, Y. Wu, F. Grupp, T. Udem, and R. Holzwarth, "A compact echelle spectrograph for characterization of astro-combs," *Applied Physics B* 123, 76 (2017).
17. S. V. Bykov, B. Sharma, and S. A. Asher, "High-Throughput, High-Resolution Echelle Deep-UV Raman Spectrometer," *Applied Spectroscopy* 67, 873-883 (2013).
18. A. A. Dantzler, "Echelle spectrograph software design aid," *Appl. Opt.* 24, 4504-4508 (1985).
19. S. Barnes, "The design and performance of high resolution échelle spectrographs in astronomy," (2004).
20. S. Barnes, *EchMod: a MATLAB toolbox for modeling high resolution échelle spectrographs*, SPIE Optical Systems Design (SPIE, 2012), Vol. 8550.
21. T. Eversberg and K. Vollmann, "Considerations for Designing an Echelle Spectrometer," in *Spectroscopic Instrumentation: Fundamentals and Guidelines for Astronomers* (Springer Berlin Heidelberg, Berlin, Heidelberg, 2015), pp. 229-279.
22. J. Stürmer, A. Seifahrt, Z. Robertson, C. Schwab, and J. L. Bean, "Echelle++, a Fast Generic Spectrum Simulator," *Publications of the Astronomical Society of the Pacific* 131, 024502 (2018).
23. D. P. Sablowski and K. Vollmann, "SILENT: Spectrograph simulation and emulation tool," *New Astronomy* 75, 101303 (2020).
24. H. Abbasi, G. Rauter, R. Guzman, P. C. Cattin, and A. Zam, "Differentiation of femur bone from surrounding soft tissue using laser-induced breakdown spectroscopy as a feedback system for smart laserosteotomy," *SPIE Photonics Europe* (SPIE, 2018), Vol. 10685.
25. H. Abbasi, G. Rauter, R. Guzman, P. C. Cattin, and A. Zam, "Laser-induced breakdown spectroscopy as a potential tool for autocarbonization detection in laserosteotomy," *Journal of Biomedical Optics* 23, 1-7, 7 (2018).
26. H. Abbasi, I. Sugiarto, G. Rauter, R. Guzman, P. C. Cattin, and A. Zam, "Pilot Ex Vivo Study of Laser-Induced Breakdown Spectroscopy to Detect Bone Dehydration: An Approach for Irrigation Feedback in Laserosteotomy," in *International Conference on Electrical Engineering & Computer Science (ICEECS 2018)*, (Bali, Indonesia, 2018).
27. W. Demtröder, *Laser spectroscopy 1: basic principles* (Springer, 2014).
28. V. Bagusat, M. Kraus, E. Förster, D. Thomae, T. Hönle, R. Brüning, H. Hillmer, and R. Brunner, "Concept and optical design of a compact cross-grating spectrometer," *J. Opt. Soc. Am. A* 36, 345-352 (2019).
29. A. Scheeline, "How to Design a Spectrometer," *Applied Spectroscopy* 71, 2237-2252 (2017).

6.2. Highly flexible fiber delivery of high peak power nanosecond Nd:YAG laser beam for flexiscopic applications

This section presents the development of a flexible bend-insensitive fiber bundle for use in an FO-LIBS system. A custom-made fused-end bundle of 800 fibers was used to deliver high-peak power from a nanosecond Nd:YAG laser pulse. The results demonstrate, to the best of our knowledge, the highest peak power (>20MW) delivered through a flexible fiber (tested bending radius of 15mm), for a frequency-doubled Q-switched Nd:YAG laser. The result of this work was published in Biomedical Optics Express (OSA).

Publication: Hamed Abbasi, Ferda Canbaz, Raphael Guzman, Philippe C. Cattin, and Azhar Zam, "Highly flexible fiber delivery of a high peak power nanosecond Nd:YAG laser beam for flexiscopic applications," *Biomed. Opt. Express* 12, 444-461 (2021). <https://doi.org/10.1364/BOE.405825> [Editors' Pick]

Copyright notice: © 2020 Optical Society of America under the terms of the [OSA Open Access Publishing Agreement](#)



Highly flexible fiber delivery of a high peak power nanosecond Nd:YAG laser beam for flexiscopic applications

HAMED ABBASI,^{1,4}  FERDA CANBAZ,¹  RAPHAEL GUZMAN,²
PHILIPPE C. CATTIN,³  AND AZHAR ZAM^{1,5} 

¹*Biomedical Laser and Optics Group (BLOG), Department of Biomedical Engineering, University of Basel, CH-4123 Allschwil, Switzerland*

²*Department of Neurosurgery, University Hospital Basel, CH-4056 Basel, Switzerland*

³*Center for medical Image Analysis and Navigation (CIAN), Department of Biomedical Engineering, University of Basel, CH-4123 Allschwil, Switzerland*

⁴*hamed.abbasi@unibas.ch*

⁵*azhar.zam@unibas.ch*

Abstract: Minimally invasive laser surgeries that require the use of a flexible endoscope (flexiscope) could benefit from high-energy nanosecond laser pulses delivered through fibers for real-time tissue characterization and phenotyping. The damage threshold of the fiber's glass material limits the maximum amount of deliverable peak power. To transmit high-energy pulses without damaging the fiber material, large-diameter fibers are typically used, leading to a limited bending radius. Moreover, in a large-core fiber, self-focusing can damage the fiber even if the tip remains intact. In this work, we tested a fused-end fiber bundle combined with a beam shaper capable of delivering more than 20 MW (>100 mJ/5 ns). The fiber bundle was tested over more than eight hours of operation, with different bending radiuses down to 15 mm. The results demonstrate, to the best of our knowledge, the highest peak power delivered through a flexible fiber, for a frequency-doubled Q-switched Nd:YAG laser.

© 2020 Optical Society of America under the terms of the [OSA Open Access Publishing Agreement](#)

1. Introduction

Q-switched Nd:YAG lasers have been used in industry and medicine for a wide array of applications, including hard and soft tissue ablation [1–4], laser-based diagnosis [5,6], laser-induced breakdown spectroscopy (LIBS) [7–9], laser-induced shockwave measurement [10–12], photoacoustic imaging/tomography [13,14], particle image velocimetry (PIV) [15], nanoparticle synthesis [16–18], laser shock processing [19], spark generation (laser ignition) [20,21] as a feedback mechanism for tissue-specific laser surgery [22–24]. Q-switched Nd:YAG lasers can emit nanosecond pulses at a center wavelength of 1064 nm, with harmonics of 532, 355, 266, and 213 nm. These lasers are also widely used to pump optical parametric oscillators (OPOs) to reach different wavelength regions. For example, photoacoustic imaging/tomography applications could require wavelengths in the 600 to 800 nm region [13,14]. In such applications, laser line mirrors and prisms are typically used to deliver the laser beam to the point of interest. However, this type of free-space delivery is not applicable to remote, standoff, or endoscopic applications. For standoff applications, telescopes are used to deliver and collect light over a long-distance, while remote and endoscopic applications depend on optical fibers for the same purpose. Compared to continuous wave (CW) and pulsed lasers with long pulse durations (milliseconds to microseconds), nanosecond pulses are more challenging to deliver through optical fibers due to their high peak power (the shorter the pulse duration, the higher the peak power). The nanosecond pulses induce more damage caused by laser-driven shockwaves (a result of higher peak energy levels), compared to ultra-short laser pulses (picoseconds to femtoseconds) [25]. The generated shockwaves can

easily crack the fiber material (glass) [26]. Considering the high peak power of Q-switched lasers ($\text{mJ/ns} = \text{MW}$) and the small diameter (cross-section) of optical fibers (10^{-3} – 10^{-6} cm^2), the fiber optic often faces a peak power density (GW/cm^2 – TW/cm^2) that exceeds the laser-induced damage threshold (LIDT) of the glass material. To overcome these challenges, a number of alternatives have been proposed. Sapphire fibers, for example, have a higher LIDT than silica glass fibers. They are, however, more expensive, with a limited choice of length and core size on the market. Additionally, the minimum bending radius (mBR) of a sapphire fiber is much higher than that of a silica fiber with an equal outer diameter. Hollow-core fibers present another possible solution, but they are more suitable for infrared (IR) wavelengths due to the limited smoothness (fineness) of the coating material on the internal surface of the capillary [27]. Other limiting factors of hollow-core fibers include a dramatic increase in attenuation (loss) as it bends [27–29] and optical breakdown (air plasma creation) inside the capillary (bore). To overcome the latter, researchers have experimented with blowing an inert gas with a higher plasma generation threshold into the capillary, and reducing the air pressure by creating a vacuum [29]. While the results showed an improved LIDT, the setup was highly complex (requiring a rotary pump and pressure gage) and bulky, especially at the tip of the fibers, making the technique unsuitable for endoscopic applications.

In glass fibers, damage typically occurs at the facet where air and glass interface. The LIDT of the air-glass interface depends heavily on the polishing quality; therefore, a cleaved fiber is often preferred over polished fiber, especially when a high-quality polishing machine is not accessible [19,30]. The most frequently used method for increasing the LIDT at the air-glass interface is to taper the tip of the fiber and apply an end-cap [31,32]. Applying pressurized air to the fiber tip also helps to remove dust particles that may lead to plasma generation. Placing the coupling optic inside a vacuumed box can also prevent plasma generation, although it increases the complexity of the setup [29]. Another possible means to increase the LIDT is to use large-core optical fibers, up to $1500 \mu\text{m}$ (the bigger the fiber cross-section, the lesser the need to use a high irradiance, tightly-focused beam for coupling). Different fiber diameters, mBRs, and delivered peak power levels are listed in Table 1. while Table 1 shows that delivering high peak power levels is possible with large core diameter fibers (a potential candidate for remote applications), large core fibers are not suitable for endoscopic applications, where flexibility is imperative. More specifically, increasing the cross-section of the fiber core increases the fiber's tolerance for power; however, it reduces the mBR of the fiber. Therefore, large core fibers cannot be inserted into flexible endoscopes (flexiscopes). An alternative approach would be to bundle fibers with a cross-section large enough to prevent the use of tightly focused beams for coupling, and a combined fiber diameter small enough to maintain bending capabilities. Fiber bundle diameters can be adjusted depending on the needs. A few studies have shown that delivering nanosecond pulses with thick fiber bundles (up to 5, 8, or 9 mm diameter) is possible [13,33–35]. Another benefit of using fiber bundles is that light cannot travel between the fibers within a bundle, thereby preventing self-focusing.

In general, the output intensity profile of a laser has a Gaussian intensity distribution. In the case of fiber coupling, the Gaussian profile of the laser can induce a hot spot a few millimeters after the fiber facet mainly due to the high intensity of the reflected beam at the center of the fiber [15]. Therefore, to avoid related damages, it is necessary to homogenize the laser beam profile. Homogenization can be achieved using a lenslet array (spherical/cylindrical) or a diffractive optical element (DOE). A homogenized beam (ideally top-hat-shaped) can prevent self/re-focusing (also known as self/re-imaging) inside the fibers. It is worth mentioning that the distribution of a Gaussian input beam might be altered at the bundle's output for non-ordered bundles, while this is not the case for top-hat beams. For this reason, large-core fibers are mostly used in combination with a beam homogenizer [14,19,49]. Beam shaping can also help to obtain a uniform ablation crater, which is required for some applications. The crater produced by the

Table 1. Delivered peak power and estimated mBR for different fiber diameters^a.

λ [nm]	Type	Core	$r_{\text{core/clad/bundle}}$ [μm]	Estimated mBR [mm]	Power [MW] (E/ τ) [mJ/ns]	Assisted by	Work
1064	single	solid	100/-/-	10–31	0.5 (3/6)	-	[36]
			100/120/-	12–36	2.3 (16/7)	DOE	[37]
			200/-/-	21–62	2.5 (15/6)	-	[36]
			275/-/-	28–85	3.3 (30/9)	-	[30]
			300/-/-	31–93	4.7 (70/15)	taper	[31]
				15 (120/8)	taper	[32]	
			400/-/-	41–124	3.5 (35/10)	-	[38,39]
				5.3 (80/15)	taper	[31]	
			470/-/-	48–145	7.5 (45/6)	-	[36]
	500/-/-	52–155	2.1 (12.5/6)	vacuum box	[40]		
	hollow	350/-/-	36–108	2.9 (21.5/7.5)	-	[41]	
			5.9 (47/8)	He	[20]		
		500/750/-	75–225	4.3 (30/7)	-	[27]	
		500/-/-	52–155	5 (30/6)	-	[21]	
			8.3 (50/6)	He	[42]		
			9.8 (142/14.5)	-	[28]		
			17.6 (158/9)	vacuum cell	[29]		
20 (100/5)		-	[43]				
bundle	solid	-/-/4500	-	16 (80/5)	-	[13]	
	hollow	350/430/2750	45–131	24 (145/6)	-	[44]	
				33 (200/6)	N ₂	[45]	
532	single	solid	500/517.5/-	52–155	1.3 (12.8/10)	-	[46]
			500/-/-	52–155	3.4 (24/7)	-	[47]
					4.1 (29/7)	-	[48]
			750/-/-	77–232	20 (100/5)	lens array, N ₂	[19,49]
	hollow	500/-/-	52–155	10 (50/5)	-	[43]	
				10.7 (75/7)	He	[50]	
				17.5 (105/6)	N ₂	[45]	
bundle	solid	100/110/550	11–33	3.1 (25/8)	DOE	[15]	
	hollow	350/430/2750	45–131	10 (70/7)	-	[51]	
355	single	hollow	500/-/-	52–155	0.29 (2/7)	He	[50]
266	single	hollow	500/-/-	52–155	0.14 (1/7)	He	[50]
					3 (15/5)	-	[43]
OPO	single	solid	500/517.5/-	52–155	12 (48/4)	lens array	[14]
			750/775/-	78–233	15 (60/4)	lens array	[14]
	bundle	solid	92.5/100/4000	14.3–34.3	6.4 (32/5)	-	[35]

^aA hyphen (-) indicates that a parameter is not applicable or was not mentioned in a study. Estimated mBR ranges derived based on the method described in Sections 2.2 and 2.3 (for unknown cladding radiuses, the radius of the core plus 3 % has been used for calculations). The method for estimating mBR is more accurate for solid core fibers than for hollow-core fibers.

top-hat laser beam is much smoother and flatter than that produced by the traditional Gaussian beam. Besides, it has recently been shown that using a homogenized beam for LIBS reduces the plasma shielding and matrix effect, improves the signal intensity and repeatability due to uniform beam energy distribution, and results in less unwanted heating [52,53]. When using a Gaussian beam for launching fiber bundles, fibers located in the central part of the bundle encounter more power than those located in the outer part. Therefore, while centrally located fibers might incur damage, the outer fibers can still deliver power. In this study, we report on the use of a fiber bundle in combination with a top-hat beam shaper for flexible delivery of second harmonic pulses of a Q-switched Nd:YAG laser beam.

2. Materials and methods

2.1. Fiber material

In our experiments, we used an incoherent silica fiber bundle. Silica is the most widely-used material for optical fibers, mainly because of its flexibility and availability and because it costs less than other fiber materials. Moreover, as compared to other glass materials, e.g., borosilicate glass (BK7), fused silica does not demonstrate any correlation between the number of shots and LIDT, due to its short lifetime decay from the conduction band to the valance band [54,55]. Low OH silica (below one ppm) was selected as the fiber's core material (CeramOptec GmbH, Bonn, Germany). Fluorine-doped (F-doped) silica made up the cladding material. No buffer was provided. Four different jacket materials were available, each with different operating temperatures: polyimide (−190 to +350 °C), ethylene tetrafluoroethylene (also known as ETFE) (−40 to +150 °C), nylon (−40 to +100 °C), and acrylate (−40 to +85 °C). Of these, polyimide was selected due to its higher operating temperature.

2.2. Bending radius

Glass fibers have a limited bending radius. Under a tight bend, the inner and outer surfaces of the fiber experience high compression and strong tension, respectively. Strong tension on the glass' surface causes crack growth and, subsequently, fracture. To avoid this problem, a minimum bending radius (mBR) is defined to determine the bending limit of a fiber. Bending the fiber below this limit might result in a broken fiber. The bending limit or mBR is determined by fiber specific parameters:

$$mBR = k.r \quad (1)$$

where, k is a specific fiber material parameter and r is the outer radius of the cladding. Here, k is defined as a ratio as follows:

$$k = \frac{Y}{\sigma} \quad (2)$$

where Y is the Young's modulus of the fiber material, and σ is the highest amount of tension that the fiber experiences at the outer surface of the bend [56,57]. Young's modulus for silica-based glass is equal to 72 GPa (=10,440 kpsi). The fiber material used in this study has a standard proof test of 70 kpsi (measured by the manufacturing company). Therefore, parameter k was calculated to be 149.14. However, the fiber might survive for a short period with a bending radius below this limit. Even so, the breaking radius is larger while the fiber is run with lasers, especially with high-power lasers. For instance, Sun et al., found that the strength of their fiber diminished by approximately 2 to 3 times after applying a high-power laser. For silica-based fibers, the parameter k typically ranges between 80 and 110 for short-term mBR, and between 160 and 300 for long-term mBR; the higher the applied power, the higher the k parameter (indicating a decrease in strength). The short-term bending radius is defined as a mechanical stress limit, meaning that the fiber might be irreversibly damaged or even broken if subjected to a bending radius lower than the one defined. Likewise, fibers should not be held at the short-term mBR

limit for more than 60 seconds. Long-term mBR is defined as the limit before causing damage to the fiber; however, bending loss may be high as the fiber approaches the long-term mBR. For the purchased silica fiber, the manufacturer determined that $k=100$ and $k=300$ for short-term and long-term mBR (while working with high-power lasers), respectively.

2.3. Fiber bundle

Like a stranded wire that can be bent more easily than a solid wire with the same diameter, a fiber bundle has a much smaller mBR than a single fiber with the same diameter. To estimate the mBR of a fiber bundle, the following equation can be used:

$$mBR' = mBR + r' - r \quad (3)$$

where mBR' and mBR represents the mBR of the fiber bundle and that of the individual fibers used to develop the bundle, respectively; r' and r represents the radius of the fiber bundle and of the individual fiber, respectively. As shown in Eq. (3), adding several individual fibers beside each other do not add up to the mBR more than the bundle radius. Figure 1 illustrates the difference between the mBR of an individual fiber versus that of the fiber bundle.

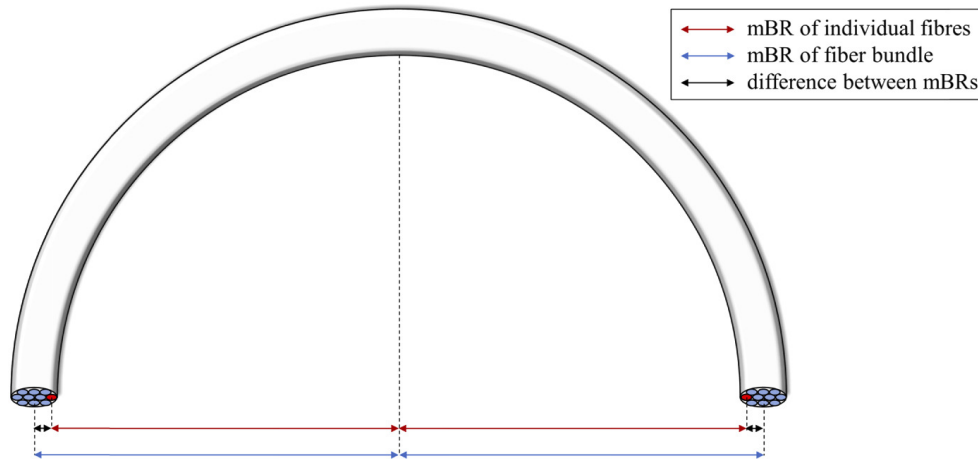


Fig. 1. The difference (black arrow) between the mBR of a single fiber (red arrow) and that of a fiber bundle (blue arrow).

As shown in Fig. 1, the difference between the mBR of a single fiber and that of a fiber bundle is less than the radius of the bundle. Therefore, by utilizing a fiber bundle, the cross-section of the fiber can be increased while keeping the mBR short. To find the ratio between the mBR of a fiber bundle and the mBR of a single fiber with the same radius as the fiber bundle, irrespective of the radius of the fibers in the bundle, a packing problem must be solved. In mathematics, the packing problem is used to determine how many circles (with the same radius) can fit into a bigger circle by minimizing the space between the circles. In other words, solving the packing problem finds the most compact arrangement for a defined number of neighboring circles of the same size, for which the geometry of that group of circles is similar to another big circle. There is no unique equation that can determine the ratio between the radius of packed circles and that of the surrounding circle; there is only a conjectured upper bound, as introduced by David W. Cantrell [58]. Employing Cantrell's upper bound, we have:

$$f_n = \frac{r}{r'} \leq \frac{4\rho}{4\rho - 1 + (16\rho^2 + (16n - 24)\rho + 1)^{1/2}} \quad (4)$$

where f_n is the fraction describing the ratio of the surrounded circle to the surrounding circle, n is the number of individual fibers used to develop the bundle, and ρ is the density of an infinite

hexagonal packing of circles:

$$\rho = \frac{\pi}{2(3)^{1/2}} \approx 0.91 \quad (5)$$

However, for a few n , Cantrell's conjectured upper bound has been violated [58]. Since 1967 [59], the packing problem for n number of surrounded circles has been solved and improved upon by different research groups [60,61]. A database hosted by Otto von Guericke University Magdeburg provides answers to packing problems up to $N=2600$ [58]. By using the best-known packings of equal-sized circles within a circle as given by the database, a fraction of surrounded circle radius to the surrounding circles radius, f_n , can be assessed.

Combining Eqs. (1), (3), and (4) we derive:

$$\frac{mBR''}{mBR} = k(f_n(k-1) + 1)^{-1} \quad (6)$$

Here, mBR'' represents the minimum bending radius of a fiber that has the same radius as a bundle with a minimum bending radius of mBR . Employing Eq. (6) improvement of mBR by using n number of individual fibers in a bundle is calculatable, irrespective of the radius of fiber or bundle. Figure 2 shows the improvement in mBR for $k=100$ (short-term) and $k=300$ (long-term) for different numbers of individual fibers in a bundle.

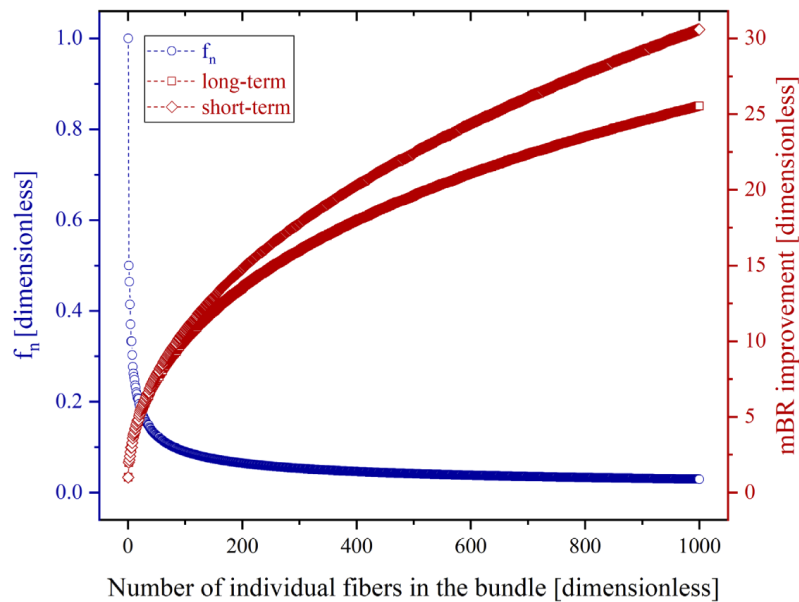


Fig. 2. The fraction of individual fiber radius to bundle radius (f_n), and mBR improvement (long-term and short-term) for a bundle of n individual fibers.

In this study, an 800 m long multimode fiber was divided into 800 pieces of 1 m long fiber pieces to make the bundle. Both ends were polished to $0.3 \mu\text{m}$ specification (performed by the manufacturing company). Therefore, as shown in Fig. 2, the short- and long-term mBR s were 24 and 28 times smaller, respectively, than a single fiber of the same radius as the bundle.

Even though the use of fiber bundles over single large-diameter fibers is highly advantageous in terms of mBR , the coupling efficiency (i.e., that ratio of the coupled energy to the incident energy) of a fiber bundle is less than that of a single fiber. Two main reasons account for the reduced coupling efficiency. First, in a single fiber, the light is focused on the core area, while in a fiber bundle, the light faces both the core and cladding area of individual fibers in the bundle. At the tip of the bundle, plastic/polymer parts, like the jacket, are detachable, but the cladding is made of glass and cannot be separated from the core before fusing. Therefore, thin cladding

is desirable to reduce the cross-section of cladding at the tip of the bundle. In this study, the individual fibers used to develop the bundle had a core and cladding radius of 50 μm and 53 μm , respectively. Second, the gap between the fibers also reduces coupling efficiency. The ratio of the glass area to the gap area in the tip of a bundle is called density or fill factor. Based on the number of individual fibers in the bundle, the density may differ. To reach a higher filling factor, the number of fibers can be increased. However, based on the number of individual fibers in the bundle, a few loose fibers are to be expected. Without loose fibers, wrapping the individual fibers would be enough to fix the position of the fibers in the bundle. For instance, Stephens et al. developed a bundle of 19 fibers, and managed to fix the fibers by mechanically holding them in a close-fitting tapered glass capillary tube [15]. However, in most cases, a few loose fibers are likely. Figure 3 shows the density and number of loose fibers based on the number of individual fibers in the bundle. A horizontal line, demonstrating the density limit, acquired from Eq. (5), is depicted in Fig. 3 as well.

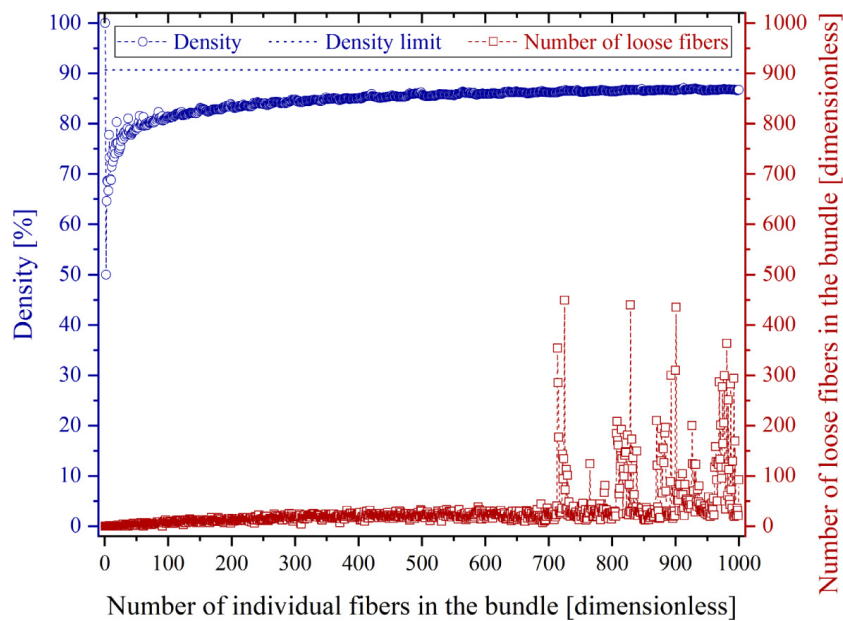


Fig. 3. Theoretical density and number of loose fibers for packing of n individual fibers.

Since light cannot travel over a long distance in the cladding, and also considering the limitation of a fiber bundle's density, the following equation can be used to estimate the coupling efficiency of the bundle:

$$\text{Bundle coupling efficiency} \leq \rho \left(\frac{r_{\text{core}}}{r_{\text{clad}}} \right)^2 \quad (7)$$

where ρ , r_{core} , and r_{clad} represent the density, the radius of the core, and the radius of the cladding, respectively. Since the light will be sent through the central part of the fiber bundle and because gaps exist in the outer part of the bundle, we can consider the maximum density of a hexagonal packing of circles [Eq. (5)]. Equation (7) determines a coupling efficiency of approximately 81% or less from our fiber bundle. Figure 4 represents a simulation of a bundle of 800 fibers, packed with the most compact known geometry. In this configuration, the fibers have 1,746 contacts, 95 of which have contact with the container (the outer circle); however, 23 loose fibers exist, and are depicted in gray in Fig. 4. The density of this configuration is 0.86, and it has an f_n value of 0.033 [58].

Due to the existence of loose fibers (fibers that still have a degree of freedom for movement inside the container; so-called rattlers) in the bundle, holding the 95 boundary fibers would not

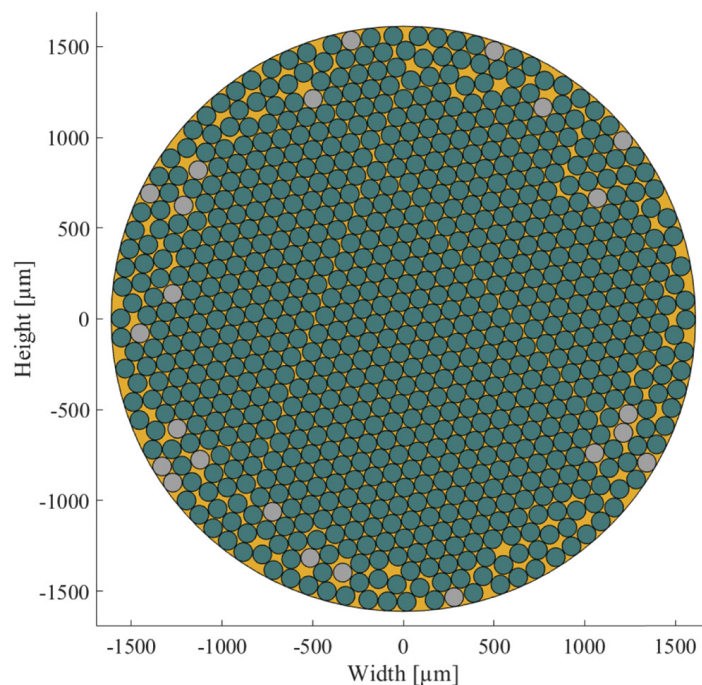


Fig. 4. Simulation of packing 800 individual fibers with a radius of $53\ \mu\text{m}$ (r_{clad}) in a circle (capillary container). The fibers with a degree of freedom for movement are colored in gray. The yellow zone shows the wasted areas (approximately 14% without fusion).

be enough to fix them. At the output facet, the fibers could be glued to each other, but this would not work for the input facet (subjected to high peak power pulses), due to the low LIDT of glues. Therefore, at the input facet, fibers were fused to each other (jackets removed). Fusing the fibers also served to increase the density by filling the gaps between fibers. During the fusing process (performed by the manufacturing company), the fibers attained a hexagonal shape. Filling the gaps reduced the outer diameter of the bundle as well.

2.4. Output energy measurement

To measure laser energy, a high damage threshold energy meter (EnergyMax-USB J-50MB-YAG, Coherent Inc., United States), was used, depicted as EM in Fig. 5. The delivered energy was measured directly by placing the EM in front of the fiber bundle.

2.5. LIDT measurement

To determine the bundle's LIDT, we utilized the second harmonic of a Q-switched flashlamp-pumped Nd:YAG laser (Q-Smart 450, Quantel, France) with a pulse duration of 5 ns providing a Gaussian beam output (M^2 below 2). For this part of the experiment, a single convex lens (indicated as FL in Fig. 5) was used for focusing (i.e., no beam shaper (BS) or aperture (A) was used). The laser's energy was gradually increased by reducing the delay between the flashlamp and Q-switch until damage was observed. A longwave infrared (LWIR) thermal camera (FLIR A655sc, FLIR Systems AB, Sweden) was initially used (depicted as TC in Fig. 5) in the setup; however, it was later removed as it failed to record any temperature change when damage occurred. This thermal camera shows the average recorded thermal radiation (accumulated heat) over each frame (tens of ms), while damage occurs within the range of laser pulse duration (ns), hence temperature change at the moment of damage could not be recorded. By obtaining the LIDT for a specific beam parameter, LIDT for another beam specification (close to the original one) can be

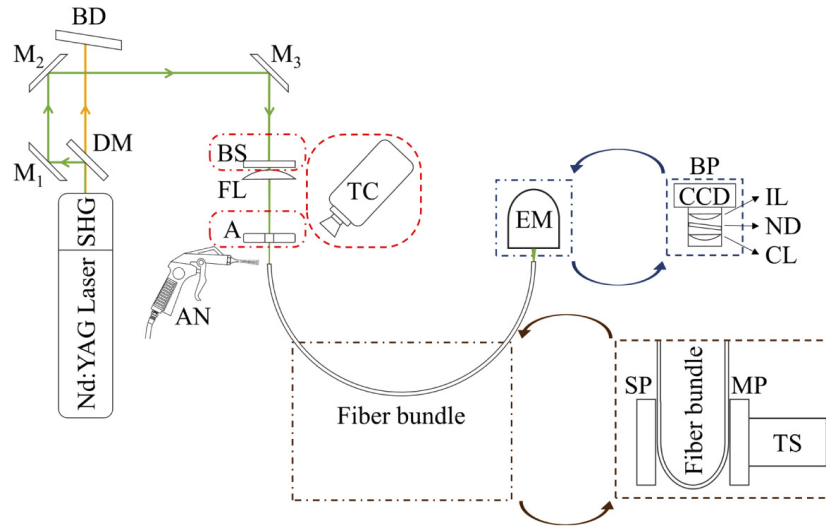


Fig. 5. Schematic of the experimental setup. Parts inside dash-dotted rectangles have been replaced with parts inside dashed rectangles of the same color during different parts of the experiment. Components inside red rectangles with rounded corners were present in some parts of the experiment only. SHG: Second Harmonic Generator, DM: Dichroic Mirror, M: Mirror, BD: Beam Dump, BS: Beam Shaper, FL: Focusing Lens, A: Aperture, AN: Air Nozzle, TC: Thermal Camera, SP: Stationary Plate, MP: Moving Plate, TS: Translation Stage, EM: Energy Meter, BP: Beam Profiler, CCD: Charge-Coupled Device, IL: Imaging Lens, ND: Natural Density filter, CL: Collimating Lens.

estimated using the following equation:

$$LIDT_{(\lambda_2, \tau_2, PF_2)} \left[\frac{J}{cm^2} \right] \approx LIDT_{(\lambda_1, \tau_1, PF_1)} \left[\frac{J}{cm^2} \right] \times \left(\frac{\lambda_2}{\lambda_1} \right)^{j_\lambda} \times \left(\frac{\tau_2}{\tau_1} \right)^{j_\tau} \times \left(\frac{PF_2}{PF_1} \right) \quad (8)$$

where λ is the wavelength, τ is pulse duration, and PF is the profile factor. In most cases, j_λ and j_τ can be approximated as 1 and $1/2$, respectively; however, a few studies have reported different numbers [26,54,62,63]. PF represents the homogeneity of the beam profile. As a rule of thumb, a top-hat-shaped laser beam has a PF approximately two times better than that of a typical laser with a Gaussian intensity distribution. In a Gaussian distribution, the percentage of photons within a band around the mean, four standard deviations wide (2σ on either side of the mean), is around 95%. Assuming a rectangular top hat (in a two-dimensional plane), a top-hat beam with the same width (2σ from either side of the mean) and only half the height of the Gaussian distribution would encompass the same number of photons (assuming 5% loss for top-hat beam shaper) as the Gaussian beam. Therefore, individual fibers at the center of a bundle illuminated with a Gaussian laser beam have a two times higher chance (than average) of being damaged. Contrastingly, with top-hat illumination, most of the individual fibers tolerate the same amount of energy. In sum, by converting the laser beam from Gaussian to top-hat, we can expect a two-fold increase in the bundle's ability to handle power.

2.6. Beam shaping

We used a high damage threshold top-hat beam shaper, GTH-5-250-4-532 (TOPAG Lasertechnik GmbH, Darmstadt, Germany), with an antireflection coating at 532 nm. The beam shaper had an integrated lens with a 250 mm focal length. It required an input beam with a diameter ($1/e^2$) of approximately 5.0 ± 0.15 mm, TEM_{00} .

The beam shaper's free-form surface redistributed a top-hat square beam with beam homogeneity of $\pm 5\%$ (in reference to the average intensity within the top-hat beam) and a size of

$4 \times 4 \text{ mm}^2$ (scalable with an additional lens) at its focal length. Since the top-hat size created exceeded the diameter of the fiber bundle, an additional lens with a 500 mm focal length was placed after the beam shaper to adjust the size of the top-hat beam. The beam shaper has been shown as BS in Fig. 5. The following equations show the working distance and top-hat beam size of the beam shaper in combination with an additional lens.

$$\text{working distance} \approx \frac{f_i f_a}{f_i + f_a} \quad (9)$$

$$\text{top hat size [mm]} \approx 4 \frac{\text{working distance}}{f_i} = 4 \frac{f_a}{f_i + f_a} \quad (10)$$

In Eqs. (9) and (10), f_i is the integrated focal length (250 mm), and f_a is the focal length of the additional lens (500 mm). However, using an input beam with a larger diameter results in a larger top-hat output at a slightly shorter working distance, with rounded corners/edges. A round diaphragm was used to aperture and change the profile of the beam from square to round before entering the fiber bundle.

Another benefit of using a beam shaper to couple the light into the fiber (compared to a single-lens setup) is that it enters the fiber with a very low numerical aperture (NA). Launching a fiber with a low NA (low incidence angle) results in filling the fiber with low-order modes, also known as an underfilled launch condition. Low-order modes are less sensitive to bending than high-order modes as the total internal reflection (TIR) angle is not close to the critical angle of the fiber. Therefore, by changing the critical angle of the fiber during bending, the TIR condition is still fulfilled. More information is provided in Section 2.8.

2.7. Beam profiling

A custom beam profiler was used to observe the profile of the laser at the fiber output. The setup consisted of a collimating lens, a natural density filter, an imaging lens, and a megapixel CCD. The setup of the beam profiler is shown as BP in the delineated experimental setup shown in Fig. 5. The beam profiler, depicted in a blue dashed rectangle, was replaced with the energy meter (EM), shown inside the dash-dotted blue rectangle, after the profiling experiments.

2.8. Durability and bending loss measurement

To maximize the repeatability of any laser experiment, keeping the laser power constant throughout the experiment is vital. Therefore, for potential flexiscopic applications, the power of the laser is required to remain constant while the fiber is under different bending radiuses. Thus, we simulated whether the developed fiber is bend-sensitive or bend-insensitive. Next, the simulation has consequently been supported by the experiment.

Light delivery inside solid core waveguides is based on total internal reflection, thus, bending loss occurs only if the light inside the fiber core cannot be reflected back from the cladding to the core. Based on the refractive index of the core and cladding, a critical angle is defined for guidance. Hence, the fiber can deliver light rays propagated into the core below the critical angle, which limits the incidence angle of the light entering the fiber. The critical threshold for the incidence angle is called the acceptance angle (see Fig. 6). Alternatively, NA can also be used to assess the acceptance angle. The critical angle (θ_{crit}), acceptance angle (θ_{acc}), and NA of fibers are related to the refractive index of the core (n_{core}) and of the cladding (n_{clad}), according to the following equations:

$$\theta_{crit} = \sin^{-1} \left(\frac{n_{clad}}{n_{core}} \right), \quad NA = n_{out} \sin \theta_{acc} = (n_{core}^2 - n_{clad}^2)^{\frac{1}{2}} \quad (11)$$

where n_{out} is the refractive index of the fiber's outside environment. Figure 6 illustrates the definition of θ_{crit} and θ_{acc} .

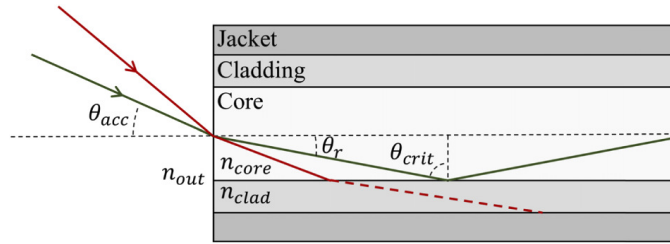


Fig. 6. A beam entering the fiber with an angle equal to or below θ_{acc} refracts at angle θ_r , and reflects from the core-cladding interface with an angle equal to or greater than θ_{crit} (complementary angle of θ_r). Beams outside of these boundary limits (e.g., red beam in the figure) would not be able to follow TIR and will be absorbed by the jacket (if the fiber has one).

Since all parameters mentioned in Eq. (11) are wavelength-dependent, they need to be known for the wavelength of the employed laser (532 nm). The fiber core and cladding were silica glass (also known as silicon dioxide, SiO_2), and F-doped silica, with refractive indexes of 1.457 and 1.440 (at 632.8 nm), respectively. The NA was 0.22 at the standard helium-neon (He-Ne) laser wavelength (632.8 nm). The Sellmeier dispersion equation [64] can be used to model the refractive index of silica at the center wavelength of the laser (532 nm):

$$n(\lambda) = \left(1 + \sum_{i=1}^M \frac{B_i \lambda^2}{\lambda^2 - C_i} \right)^{\frac{1}{2}}, \begin{pmatrix} B_1 & C_1 \\ B_2 & C_2 \\ B_3 & C_3 \end{pmatrix}_{silica} = \begin{pmatrix} 0.6961663 & 0.0684043^2 \\ 0.4079426 & 0.1162414^2 \\ 0.8974794 & 9.8961610^2 \end{pmatrix} \quad (12)$$

where λ [μm] is the wavelength, and B_i [dimensionless] and C_i [μm^2] are experimentally measured Sellmeier coefficients; the three-term ($M=3$) equation yields an absolute residual in the order of 10^{-6} at 20°C [65]. Employing Eq. (6), n_{core} at 532 nm was calculated to be 1.460. A next step was to estimate n_{clad} at 532 nm. Based on the percentage of the doped fluorine, the refractive index varies from the pure silica; the higher the dopant percentage, the lower the refractive index [66]. The percentage of fluorine dopant can be estimated through the following equation, with an accuracy greater than 10^{-4} [67]:

$$d_F(\lambda) = \frac{n_{silica}(\lambda) - n_F(\lambda)}{4.665 \cdot 10^{-3}} \quad (13)$$

where $d_F(\lambda)$ is expressed in [Mol %]. By solving Eq. (7), with refractive index data for the He-Ne wavelength, and subsequently with the achieved dopant percentage and core refractive index for the frequency-doubled Nd:YAG wavelength, the cladding refractive index at 532 nm was estimated to be 1.443. The next step was to find the change in the refractive index while the fiber bends. The refractive index of a fiber core/cladding under a certain bending radius (BR) can be determined by the following equation [68–70]:

$$n_{bent} = n_{straight} \left(1 + (1 + \chi) \frac{x}{BR} \right) \quad (14)$$

where χ is an elasto-optic parameter equal to -0.22 [dimensionless] for silica material [68–70], and x [expressed in the same dimension as BR] is the transversal distance from the center of the core cross-section, positive outwards and negative towards the center of curvature. Figure 7 shows the acceptable NA (upper limit), θ_{acc} (upper limit), and θ_{crit} (lower limit) for different BRs.

According to the simulation depicted in Fig. 7, at long-term BR ($k=300$) incident beams with NAs greater than 0.20 (incident angle greater than 11.5 degrees) would not be guided through the

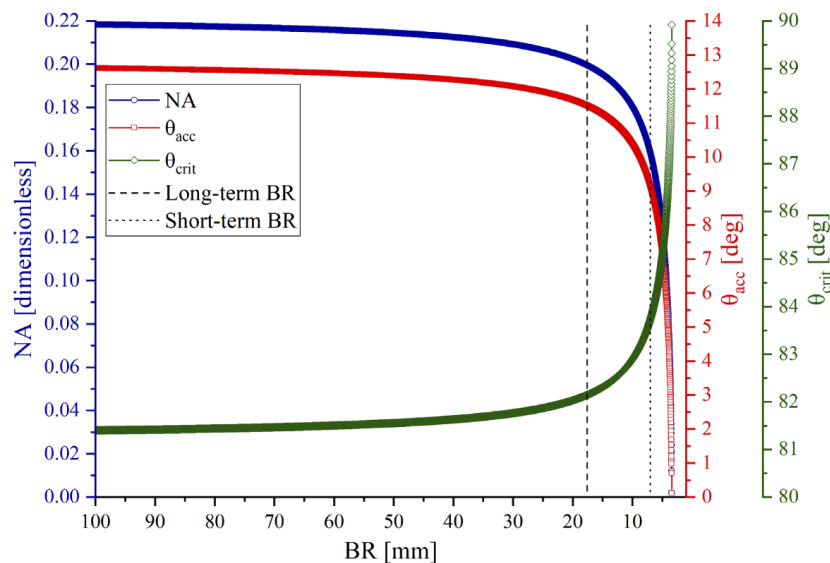


Fig. 7. Acceptable NA (upper limit), θ_{acc} (upper limit), and θ_{crit} (lower limit) for different BRs, including long-term ($k=300$) and short-term ($k=100$) BRs.

bent fiber due to increased θ_{crit} (82.1 degrees). Similarly, for short-term BR ($k=100$) the limiting NA is 0.16 and also the limiting incident and critical angles are 9.2 and 83.7 degrees, respectively. Figure 7 clearly shows that the bending loss depends strongly on the launch condition. Due to the very low NA launch condition employed in this study, no bending loss was expected.

To evaluate the durability of the fiber bundle, the laser operated for one hour at 1 Hz (3600 pulses) while the fiber was bent into a half-circle. Each pulse of delivered energy was recorded with the energy meter connected to a computer. The above-mentioned durability evaluation experiment was repeated three times.

To measure the bending loss, the fiber bundle was placed between two plates; the first plate was attached to the optical table, and the second one was attached to a motorized stage (8MT167S-25LS, Standa Ltd., Lithuania) moving with a step size of 100 μm (dashed brown box in Fig. 5). The following procedure was repeated three times: first, the fiber bundle was configured to the long-term mBR (17.6 mm) and kept at the same position while the laser operated at 1 Hz for 1 hour (3600 pulse measurements). Then, as the BR was adjusted from 17.6 to 15.0 mm, with a step size of 100 μm , 100 pulses were delivered through the fiber bundle at each step. A bending radius of around 15 mm has been reported as a necessary bending radius for endoscopic applications [71]. Each pulse of delivered energy was recorded with the energy meter connected to a computer.

3. Results and discussion

3.1. Fiber bundle

Figure 8 shows the fiber bundle input cross-section as captured by a fiber inspection scope (FS201, Thorlabs Inc., United States) manually connected to a cellphone camera.

Filling the gaps (during the fusion process) between the individual fibers increased the density and, consequently the coupling efficiency. Likewise, the profile (cross-section shape) was changed from circular to semi-hexagonal, particularly for the fibers far from the center of the bundle.

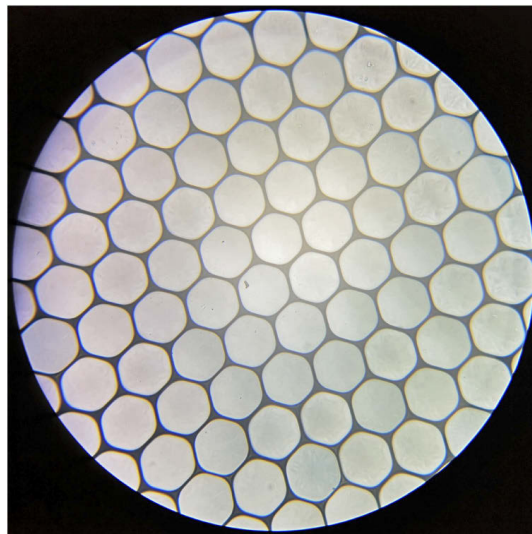


Fig. 8. Image of fiber bundle input cross-section as captured by a fiber microscope, with a field of view (FoV) of approximately 600 μm .

3.2. LIDT measurement

Our first attempt to examine the fiber bundle made use of a single convex lens focusing (FL in Fig. 5) setup, while the fiber was bent into a half-circle (brown dash-dotted box in Fig. 5) with a BR=318.3 mm. To avoid laser-induced air breakdown, a long focal length lens ($f=75$ cm) was utilized (the higher the focal length, the bigger the focal spot). To increase the beam size at the fiber input, the fiber tip was placed 18.8 cm after the focal spot, filling approximately half of the fiber bundle end face. While an air nozzle was applied to the tip of the fiber input and a thermal camera monitored the tip, the energy of the laser was gradually increased until damage was observed. The damage occurred at an input peak power of 15.52 MW (77.6 mJ/5 ns), while the output power was 12 MW (60 mJ/5 ns), with a Gaussian beam profile. These numbers correspond to a delivery efficiency of 77.3 %. Using the beam spot size at the fiber input, the damage threshold was calculated to be 0.87 GW/cm² (Gaussian, 532 nm, 5 ns). Given the slightly lower LIDT of F-doped silica, compared to pure silica [72], we assume that the damage originated from the cladding. Figure 9 shows the fiber input after being damaged.

The bundle was sent back to the manufacturer for repair, the thermal camera was removed from the setup (as it did not record any temperature change), and last but not least, a beam shaper (to homogenize the beam profile) and an aperture (to change the beam profile from square to round) was added to the setup. The fiber bundle was 5 cm shorter after repair. Therefore, the remaining experiments were carried out using a 95 cm fiber bundle.

3.3. Beam profiling

To profile the beam at fiber output, a custom-made beam profiler (BP in Fig. 5) replaced the energy meter (EM in Fig. 5) in the experimental setup. Beam profiling was performed with low energy to avoid ablating the CCD while the fiber was bent (BR=302.2 mm) into a half-circle (brown dash-dotted box in Fig. 5). Figure 10 shows the difference between the profile of the fiber bundle output beam without and with using a top-hat beam shaping setup placed before the fiber bundle.

As evident in Fig. 10, no hot zone was captured when the top-hat beam shaper was employed.

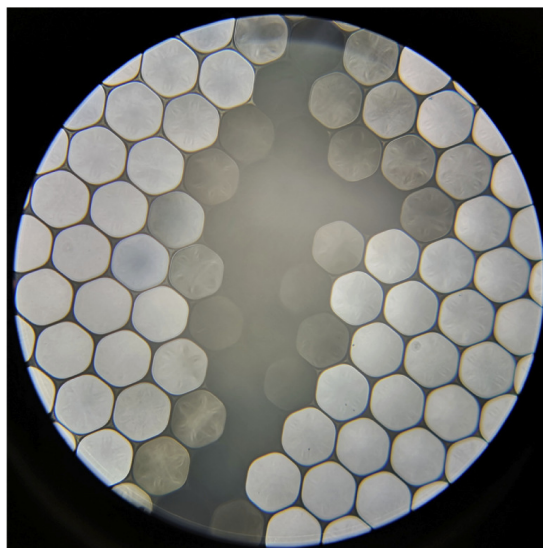


Fig. 9. Image of the fiber input after being damaged ($\text{FoV} \approx 600 \mu\text{m}$).

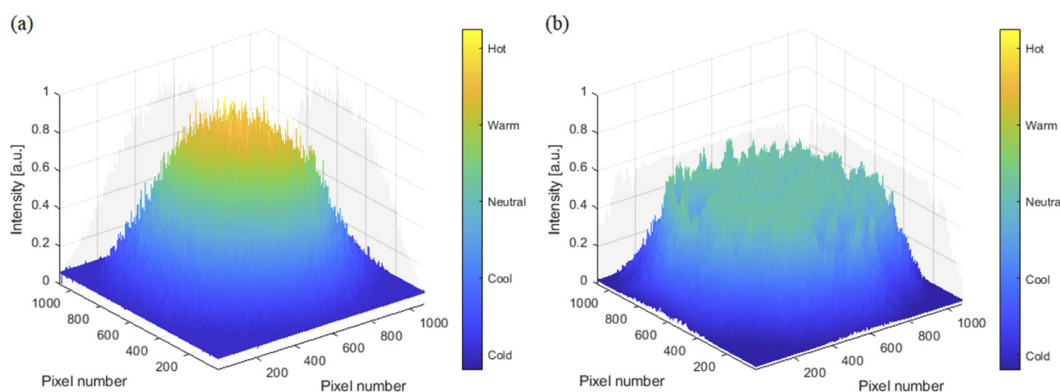


Fig. 10. Profile of fiber output beam without (a) and with (b) top-hat beam shaper. For each beam profile, ten different measurements were averaged. The Gaussian and top-hat beam measurements had a relative standard deviation of 8.3% and 5.8%, respectively.

3.4. Durability and bending loss measurement

Figure 11 shows the durability and bending loss measurements for three consecutive measurements (a, b, and c).

For each repetition, while the bending radius was reduced from 302.2 mm (first hour) to 17.6 mm (second hour), no significant reduction in the delivered power was observed. The average energy \pm standard deviation (SD) measured for the half-circle BR was 102.6 ± 3 mJ. This output energy was achieved while the input energy to the bundle was 133 mJ (coupling efficiency of 77.1%). Note that many laser parameters (e.g., beam profile, beam NA, and beam size at the bundle input) and also bundle properties (e.g., acceptable NA, gaps between fibers, reflection properties) can affect the coupling efficiency. An antireflection coating at the input facet of the fiber bundle could further improve the coupling efficiency. The average energy \pm SD measured for the long-term mBR was 100.2 ± 3.1 mJ, and lastly the average energy \pm SD measured for BRs smaller than the long-term mBR was 97.6 ± 3 mJ.

Considering the fluctuations in the output energy of the laser, the repeatability of the energy meter and consequently the high uncertainty of the measurements, no precise relation between

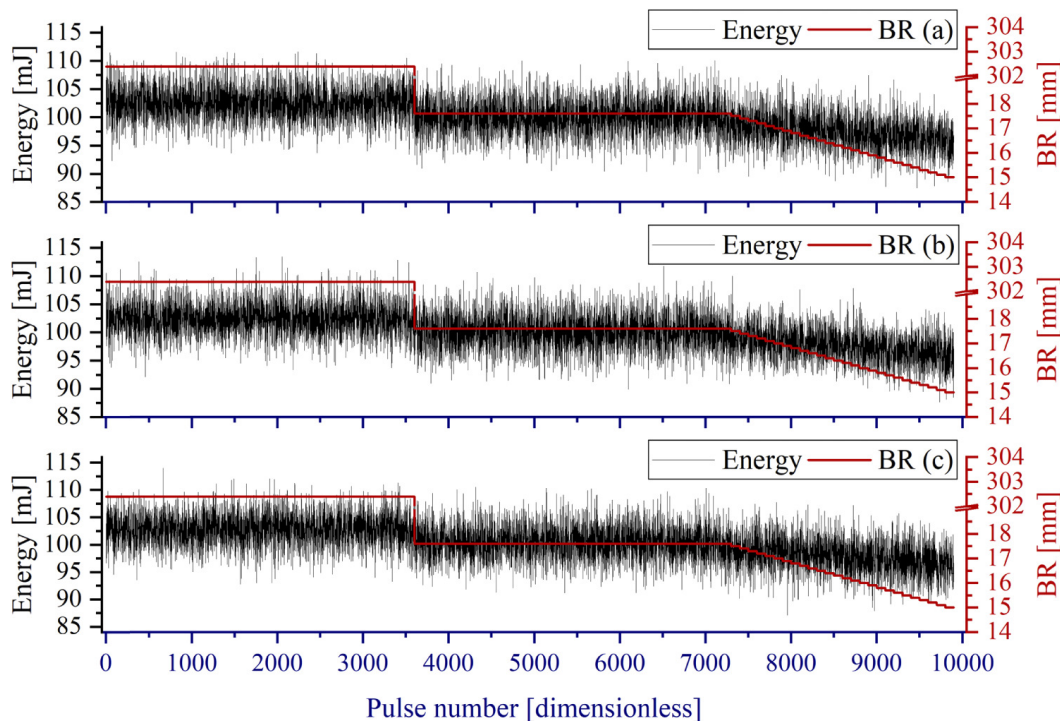


Fig. 11. Three repeated (a, b, and c) output energy measurements. The measured energy for each delivered pulse has been shown in black (associated with the left vertical axis), and the bending radius at each measurement has been shown in red (associated with the right vertical axis). For each repetition, the delivered energy was measured for one hour at half-circle, one hour at the long-term mBR, and 45 minutes below the long-term mBR.

the transmission efficiency and bending radius can be derived. Nevertheless, the transmission efficiency was estimated to be 2% less for the long-term mBR. This small change might be related to mode mixing (coupling to higher-order modes), which occurred because of microbends (imperfectly smooth core-cladding interface) [73]. Observing a higher output NA (approximately 0.1) can confirm the presence of mode mixing the bundle due to microbending. However, even such a small change in the transmitted energy can be calibrated based on feedback from the bending radius. Different sensing methodologies have been internally developed, capable of providing feedback on the bending radius [74–76].

By performing beam shaping in this work, as compared to other studies using similar fused-end fiber bundles [33–35], higher peak energy (102.6 mJ, as compared to 32 mJ/68 mJ) and peak power (20.52 MW, as compared to 6.4 MW/13.6 MW) was delivered through a fused-end fiber bundle with smaller active radius (1.5 mm as compared to 4 mm/2.5 mm) and smaller estimated long-term mBR (17.6 mm as compared to 34.3 mm/30.1 mm).

4. Conclusion

A fused-end bundle of 800 fibers with high flexibility was introduced to deliver high peak power Q-switched nanosecond Nd:YAG laser pulses at 532 nm. The fiber bundle was tested for more than 8 hours (approximately 30,000 pulses) at different bending radiuses, down to 15 mm. Given the low NA of the launch condition, the fiber bundle showed almost bend-insensitive behavior and was capable of delivering pulses with peak power of more than 20 MW (>100 mJ/5 ns), even at the defined long-term mBR. The maximum applicable peak power of the employed laser was tested in this study. The fiber bundle, however, has the potential to deliver higher peak power

levels. Due to homogenizing the laser beam profile using a top-hat beam shaper, all the fibers in the bundle delivered the same energy level, providing high LIDT compared to that of the Gaussian beam. To the best of our knowledge, this is the most flexible fiber delivery system capable of delivering high peak power Q-switched laser pulses at 532 nm. The delivery system developed has the potential for use in flexoscopic applications.

Funding

Werner Siemens Foundation through the Minimally Invasive Robot-Assisted Computer-guided Laserosteotomy (MIRACLE) project.

Disclosures

The authors declare no conflicts of interest.

References

1. L. M. B. Bernal, H. Abbasi, and A. Zam, "Laser in bone surgery," in *Lasers in Oral and Maxillofacial Surgery*, S. Stübinger, F. Klämpfl, M. Schmidt, and H. Zeilhofer, eds. (Springer, 2020), pp. 99–109.
2. K. Hyun Wook, L. Ho. C. Shaochen, and A. J. Welch, "Enhancement of bovine bone ablation assisted by a transparent liquid Layer on a target surface," *IEEE J. Quantum Electron.* **42**(7), 633–642 (2006).
3. A. Vogel, P. Schweiger, A. Frieser, M. N. Asiyu, and R. Birngruber, "Intraocular Nd:YAG laser surgery: laser-tissue interaction, damage range, and reduction of collateral effects," *IEEE J. Quantum Electron.* **26**(12), 2240–2260 (1990).
4. C. Duverney, H. Abbasi, L. M. Beltran Bernal, T. Stauber, J. G. Snedeker, P. C. Cattin, A. Zam, and G. Rauter, "Robot- and laser-assisted bio-sample preparation: development of an integrated, intuitive system," in *MESROB*, (Springer, 2020).
5. M. Bahreini, B. Ashrafkhani, and S. H. Tavassoli, "Discrimination of patients with diabetes mellitus and healthy subjects based on laser-induced breakdown spectroscopy of their fingernails," *J. Biomed. Opt.* **18**(10), 107006 (2013).
6. M. Bahreini, Z. Hosseinimakarem, and S. H. Tavassoli, "A study of association between fingernail elements and osteoporosis by laser-induced breakdown spectroscopy," *J. Appl. Phys.* **112**(5), 054701 (2012).
7. M. Nazeri, A. E. Majd, R. Massudi, S. H. Tavassoli, A. Mesbahinia, and H. Abbasi, "Laser-induced breakdown spectroscopy via the spatially resolved technique using non-gated detector," *J. Russ. Laser Res.* **37**(2), 164–171 (2016).
8. H. Abbasi, G. Rauter, R. Guzman, P. Cattin, and A. Zam, "Laser-induced breakdown spectroscopy as a potential tool for autcarbonization detection in laserosteotomy," *J. Biomed. Opt.* **23**(07), 1 (2018).
9. H. Abbasi, P. C. Cattin, and A. Zam, "A simple acoustic-based method for lens-to-sample distance adjustment in μ LIBS," in *Photonics North*, (IEEE, 2020).
10. H. N. Kenhagho, I. Sugiarto, R. Guzman, P. Cattin, and A. Zam, "Contact-free crater depth monitoring using measured acoustic shock waves for smart laser surgery applications: preliminary result," in *2019 International Conference on Radar, Antenna, Microwave, Electronics, and Telecommunications (ICRAMET)*, 2019), 118–121.
11. H. Nguendon Kenhagho, G. Rauter, R. Guzman, P. C. Cattin, and A. Zam, Comparison of acoustic shock waves generated by micro and nanosecond lasers for a smart laser surgery system, *SPIE BiOS* (SPIE, 2018), Vol. 10484.
12. H. Nguendon Kenhagho, F. Canbaz, T. E. Gomez Alvarez-Arenas, R. Guzman, P. Cattin, and A. Zam, "Machine learning-based optoacoustic tissue classification method for laser osteotomes using an air-coupled transducer," *Lasers in Surgery and Medicine* (2020).
13. W. Xia, D. Piras, M. K. Singh, J. C. van Hespren, T. G. van Leeuwen, W. Steenbergen, and S. Manohar, "Design and evaluation of a laboratory prototype system for 3D photoacoustic full breast tomography," *Biomed. Opt. Express* **4**(11), 2555–2569 (2013).
14. M. Ai, W. Shu, T. Salcudean, R. Rohling, P. Abolmaesumi, and S. Tang, "Design of high energy laser pulse delivery in a multimode fiber for photoacoustic tomography," *Opt. Express* **25**(15), 17713–17726 (2017).
15. T. J. Stephens, M. J. Haste, D. P. Towers, M. J. Thomson, M. R. Taghizadeh, J. D. C. Jones, and D. P. Hand, "Fiber-optic delivery of high-peak-power Q-switched laser pulses for in-cylinder flow measurement," *Appl. Opt.* **42**(21), 4307–4314 (2003).
16. A. Mehrani, D. Dorrnian, and E. Solati, "Properties of Au/ZnO nanocomposite prepared by laser irradiation of the mixture of individual colloids," *J. Cluster Sci.* **26**(5), 1743–1754 (2015).
17. A. G. Rad, H. Abbasi, and K. Golyari, "Fabrication and nonlinear refractive index measurement of colloidal silver nanoparticles," *Int. J. Appl. Phys. Math.* **2**, 135–139 (2012).
18. P. Nasiri, D. Dorrnian, and A. H. Sari, "Synthesis of Au/Si nanocomposite using laser ablation method," *Opt. Laser Technol.* **113**, 217–224 (2019).
19. T. Schmidt-Uhlig, P. Karlitschek, M. Yoda, Y. Sano, and G. Marowsky, "Laser shock processing with 20 MW laser pulses delivered by optical fibers," *Eur. Phys. J.: Appl. Phys.* **9**(3), 235–238 (2000).

20. A. P. Yalin, M. DeFoort, B. Willson, Y. Matsuura, and M. Miyagi, "Use of hollow-core fibers to deliver nanosecond Nd:YAG laser pulses to form sparks in gases," *Opt. Lett.* **30**(16), 2083–2085 (2005).
21. C. Dumitrescu, P. Puzinauskas, S. Olcmen, S. G. Buckley, S. Joshi, and A. P. Yalin, "Fiber-optic spark delivery for gas-phase laser-induced breakdown spectroscopy," *Appl. Spectrosc.* **61**(12), 1338–1343 (2007).
22. H. Abbasi, L. M. Beltrán Bernal, A. Hamidi, A. Droneau, F. Canbaz, R. Guzman, S. L. Jacques, P. C. Cattin, and A. Zam, "Combined Nd:YAG and Er:YAG lasers for real-time closed-loop tissue-specific laser osteotomy," *Biomed. Opt. Express* **11**(4), 1790–1807 (2020).
23. H. Abbasi, G. Rauter, R. Guzman, P. Cattin, and A. Zam, Differentiation of femur bone from surrounding soft tissue using laser-induced breakdown spectroscopy as a feedback system for smart laserosteotomy, *SPIE Photonics Europe* (SPIE, 2018), Vol. 10685.
24. H. Abbasi, I. Sugiarto, G. Rauter, R. Guzman, P. Cattin, and A. Zam, "Pilot ex vivo study of laser-induced breakdown spectroscopy to detect bone dehydration: an approach for irrigation feedback in laserosteotomy," in *ICEECS*, (2018).
25. A. Vogel, S. Busch, and U. Parlitz, "Shock wave emission and cavitation bubble generation by picosecond and nanosecond optical breakdown in water," *J. Acoust. Soc. Am.* **100**(1), 148–165 (1996).
26. V. Rastogi, S. Chaurasia, and D. S. Munda, "Laser induced damage studies in borosilicate glass using nanosecond and sub nanosecond pulses," *J. Non-Cryst. Solids* **463**, 138–147 (2017).
27. Y. Matsuura, K. Hanamoto, S. Sato, and M. Miyagi, "Hollow-fiber delivery of high-power pulsed Nd:YAG laser light," *Opt. Lett.* **23**(23), 1858–1860 (1998).
28. S. Sato, H. Ashida, Y.-W. Shi, Y. Matsuura, and M. Miyagi, Hollow-waveguide-based transmission of a Q-switched Nd:YAG laser beam for biological tissue ablation, *BiOS '99 International Biomedical Optics Symposium* (SPIE, 1999), Vol. 3596.
29. S. Sato, H. Ashida, T. Arai, Y.-W. Shi, Y. Matsuura, and M. Miyagi, "Vacuum-cored hollow waveguide for transmission of high-energy, nanosecond Nd:YAG laser pulses and its application to biological tissue ablation," *Opt. Lett.* **25**(1), 49–51 (2000).
30. D. C. S. Beddows, O. Samek, M. Liška, and H. H. Telle, "Single-pulse laser-induced breakdown spectroscopy of samples submerged in water using a single-fibre light delivery system," *Spectrochim. Acta, Part B* **57**(9), 1461–1471 (2002).
31. X. -H. Zhao and Y. Gao, "Use of tapered fibers to deliver nanosecond laser pulses to launch flyer plates," in *International Summer Session: Lasers and Their Applications* (Optical Society of America, 2011), Th27.
32. X. Fan and J. Liu, New simplified coupling system of 15MW Nd:YAG laser pulse with 600um optical fiber by use of a taper fiber, *AOMATT 2008 - 4th International Symposium on Advanced Optical Manufacturing* (SPIE, 2009), Vol. 7282.
33. A. Buehler, E. Herzog, D. Razansky, and V. Ntziachristos, "Video rate optoacoustic tomography of mouse kidney perfusion," *Opt. Lett.* **35**(14), 2475–2477 (2010).
34. D. Razansky, A. Buehler, and V. Ntziachristos, "Volumetric real-time multispectral optoacoustic tomography of biomarkers," *Nat. Protoc.* **6**(8), 1121–1129 (2011).
35. K. Sivasubramanian, V. Periyasamy, K. K. Wen, and M. Pramanik, "Optimizing light delivery through fiber bundle in photoacoustic imaging with clinical ultrasound system: Monte Carlo simulation and experimental validation," *J. Biomed. Opt.* **22**(4), 041008 (2017).
36. H. El-Rabii and G. Gaborel, "Laser ignition of flammable mixtures via a solid core optical fiber," *Appl. Phys. B* **87**(1), 139–144 (2007).
37. R. R. J. Maier, D. P. Hand, A. Kuhn, P. Blair, M. R. Taghizadeh, and J. D. C. Jones, "Fibre optic beam delivery of nano-second Nd:YAG laser pulses for micro-machining," *International Congress on Applications of Lasers & Electro-Optics 1999*, 204–218 (1999).
38. J. Wu, H. Yu, Y. Qiu, Z. Zhang, T. Liu, F. Xue, W. Yu, X. Li, and A. Qiu, "Plasma characteristics and element analysis of steels from a nuclear power plant based on fiber-optic laser-induced breakdown spectroscopy," *J. Phys. D: Appl. Phys.* **52**(1), 014006 (2019).
39. Y. Qiu, J. Wu, X. Li, T. Liu, F. Xue, Z. Yang, Z. Zhang, and H. Yu, "Parametric study of fiber-optic laser-induced breakdown spectroscopy for elemental analysis of Z3CN20-09M steel from nuclear power plants," *Spectrochim. Acta, Part B* **149**, 48–56 (2018).
40. A. Matsumoto, H. Ohba, M. Toshimitsu, K. Akaoka, A. Ruas, T. Sakka, and I. Wakaida, "Fiber-optic laser-induced breakdown spectroscopy of zirconium metal in air: Special features of the plasma produced by a long-pulse laser," *Spectrochim. Acta, Part B* **142**, 37–49 (2018).
41. S. Sasazawa, S. Kakino, and Y. Matsuura, "Optical-fiber-based laser-induced breakdown spectroscopy for detection of early caries," *J. Biomed. Opt.* **20**(6), 065002 (2015).
42. C. E. Dumitrescu, P. V. Puzinauskas, and S. Olcmen, "Movable fiber probe for gas-phase laser-induced breakdown spectroscopy," *Appl. Opt.* **47**(31), G88–G98 (2008).
43. Y. Matsuura, A. Tsuchiuchi, H. Noguchi, and M. Miyagi, "Hollow fiber optics with improved durability for high-peak-power pulses of Q-switched Nd:YAG lasers," *Appl. Opt.* **46**(8), 1279–1282 (2007).
44. Y. Matsuura, Y. Ozgur, and M. Miyagi, Bundled hollow-optical fiber for delivery of 30-MW peak power Nd:YAG laser pulses, *SPIE BiOS* (SPIE, 2006), Vol. 6083.
45. O. Yilmaz, M. Miyagi, and Y. Matsuura, "Bundled hollow optical fibers for transmission of high-peak-power Q-switched Nd:YAG laser pulses," *Appl. Opt.* **45**(27), 7174–7178 (2006).

46. X. Xiao, "Sensitive Quantification of Chlorine on Steel Surfaces Via Fiber-optic Laser-induced Breakdown Spectroscopy," (The Pennsylvania State University, 2017).
47. Q. Zeng, L. Guo, X. Li, C. He, M. Shen, K. Li, J. Duan, X. Zeng, and Y. Lu, "Laser-induced breakdown spectroscopy using laser pulses delivered by optical fibers for analyzing Mn and Ti elements in pig iron," *J. Anal. At. Spectrom.* **30**(2), 403–409 (2015).
48. Q. Zeng, F. Deng, Z. Zhu, Y. Tang, B. Wang, Y. Xiao, L. Xiong, H. Yu, L. Guo, and X. Li, "Portable fiber-optic laser-induced breakdown spectroscopy system for the quantitative analysis of minor elements in steel," *Plasma Sci. Technol.* **21**(3), 034006 (2019).
49. T. Schmidt-Uhlig, P. Karlitschek, G. Marowsky, and Y. Sano, "New simplified coupling scheme for the delivery of 20 MW Nd:YAG laser pulses by large core optical fibers," *Appl. Phys. B* **72**(2), 183–186 (2001).
50. Y. Matsuura, G. Takada, T. Yamamoto, Y.-W. Shi, and M. Miyagi, "Hollow fibers for delivery of harmonic pulses of Q-switched Nd:YAG lasers," *Appl. Opt.* **41**(3), 442–445 (2002).
51. O. Yilmaz, Y. Matsuura, and M. Miyagi, "Delivery of 10-MW Nd:YAG laser pulses by bundled hollow fibers," in *2005 Pacific Rim Conference on Lasers & Electro-Optics*, (2005), 553–554.
52. J. Jia, H. Fu, Z. Hou, H. Wang, Z. Wang, F. Dong, Z. Ni, and Z. Zhang, "Effect of laser beam shaping on the determination of manganese and chromium elements in steel samples using laser-induced breakdown spectroscopy," *Spectrochim. Acta, Part B* **163**, 105747 (2020).
53. Z. Hou, M. S. Afgan, S. Sheta, J. Liu, and Z. Wang, "Plasma modulation effect of beam shaping to improve signal quality of laser induced breakdown spectroscopy," *J. Anal. At. Spectrom.* (2020).
54. A. V. Smith and B. T. Do, "Bulk and surface laser damage of silica by picosecond and nanosecond pulses at 1064 nm," *Appl. Opt.* **47**(26), 4812–4832 (2008).
55. M. Kimmel, B. Do, and A. Smith, Deterministic single shot and multiple shot bulk laser damage thresholds of borosilicate glass at 1.064 micron, *SPIE Laser Damage* (SPIE, 2011), Vol. 8190.
56. X. Sun, J. Li, A. Hokansson, D. Whelan, and M. Clancy, Study of laser-induced damage to large core silica fiber by Nd:YAG and Alexandrite lasers, *SPIE BiOS* (SPIE, 2009), Vol. 7173.
57. X. Sun and J. Li, Laser-induced damage to large core optical fiber by high peak power laser, *SPIE BiOS* (SPIE, 2013), Vol. 8576.
58. E. Specht, (2014), retrieved <http://hydra.nat.uni-magdeburg.de/packing/cci/cci.html>.
59. S. Kravitz, "Packing Cylinders into Cylindrical Containers," *Mathematics Mag.* **40**(2), 65–71 (1967).
60. N. Mladenović, F. Plastria, and D. Urošević, "Formulation space search for circle packing problems," in *International Workshop on Engineering Stochastic Local Search Algorithms*, (Springer, 2007), 212–216.
61. C. O. López and J. E. Beasley, "A heuristic for the circle packing problem with a variety of containers," *Eur. J. Oper. Res.* **214**(3), 512–525 (2011).
62. M. Niemz, "Threshold dependence of laser-induced optical breakdown on pulse duration," *Appl. Phys. Lett.* **66**(10), 1181–1183 (1995).
63. C. Carr, H. Radousky, and S. Demos, "Wavelength dependence of laser-induced damage: determining the damage initiation mechanisms," *Phys. Rev. Lett.* **91**(12), 127402 (2003).
64. W. Sellmeier, "Ueber die durch die Aetherschwingungen erregten Mitschwingungen der Körpertheilchen und deren Rückwirkung auf die ersteren, besonders zur Erklärung der Dispersion und ihrer Anomalien," *Ann. Phys.* **223**(11), 386–403 (1872).
65. I. H. Malitson, "Interspecimen comparison of the refractive index of fused silica," *J. Opt. Soc. Am.* **55**(10), 1205–1209 (1965).
66. J. W. Fleming and D. L. Wood, "Refractive index dispersion and related properties in fluorine doped silica," *Appl. Opt.* **22**(19), 3102–3104 (1983).
67. V. Brückner, Elements of optical networking: basics and practice of optical data communication; with 13 tables and 93 exercises (Vieweg+ Teubner, 2011).
68. H. Taylor, "Bending effects in optical fibers," *J. Lightwave Technol.* **2**(5), 617–628 (1984).
69. L. Yao, T. A. Birks, and J. C. Knight, "Low bend loss in tightly-bent fibers through adiabatic bend transitions," *Opt. Express* **17**(4), 2962–2967 (2009).
70. K. Naeem, Y. Kwon, Y. Chung, and I. Kwon, "Bend-loss-free distributed sensor based on Rayleigh backscattering in Ge-doped-core PCF," *IEEE Sens. J.* **18**(5), 1903–1910 (2018).
71. K. Iwai, H. Takaku, M. Miyagi, Y.-W. Shi, and Y. Matsuura, "Fabrication of shatter-proof metal hollow-core optical fibers for endoscopic mid-infrared laser applications," *Fibers* **6**(2), 24 (2018).
72. G. Mann and J. Krüger, Nanosecond laser damage of optical multimode fibers, *Pacific Rim Laser Damage 2016: Optical Materials for High Power Lasers* (SPIE, 2016), Vol. 9983.
73. L. Jeunhomme and J. P. Pocholle, "Mode coupling in a multimode optical fiber with microbends," *Appl. Opt.* **14**(10), 2400–2405 (1975).
74. S. Manavi, L. Witthauer, L. Iafolla, A. Zam, G. Rauter, and P. C. Cattin, "Temperature-compensated FBG-based 3D shape sensor using single-mode fibers," in *Advanced Photonics 2018 (BGPP, IPR, NP, NOMA, Sensors, Networks, SPPCom, SOF)*, OSA Technical Digest (online) (Optical Society of America, 2018), JTu6C.1.
75. L. Iafolla, L. Witthauer, A. Zam, G. Rauter, and P. C. Cattin, "Proof of principle of a novel angular sensor concept for tracking systems," *Sens. Actuators, A* **280**, 390–398 (2018).
76. L. Iafolla, L. Witthauer, S. Freund, L. Fasel, A. Zam, G. Rauter, and P. C. Cattin, "Preliminary Tests of the Miniaturization of a Novel Concept of Angular Sensors," in *2019 IEEE SENSORS*, (2019), 1–4.

6.3. All-fiber-optic LIBS system for tissue differentiation: A prospect for endoscopic smart laser surgery

In this study, a portable high optical throughput Echelle spectrometer was developed following the simulation presented in Section 6.1. The fiber delivery system developed in Section 6.2., in combination with a small half-ball lens, can both deliver high peak power to the sample site and collect the plasma plume emission to direct towards the custom-made Echelle spectrometer for analysis. Therefore, the setup, in combination with an advanced chemometric, was used for tissue differentiation. The results demonstrated high accuracy for differentiating bone, muscle, fat, and bone marrow. This miniaturized flexible FO-LIBS system can be inserted into a flexible endoscope for providing feedback during minimally-invasive surgeries. The result of this work was published in *Optics and Lasers in Engineering* (Elsevier).

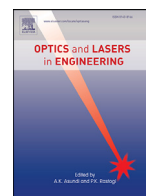
Publication: Hamed Abbasi, Raphael Guzman, Philippe C. Cattin, Azhar Zam, All-fiber-optic LIBS system for tissue differentiation: A prospect for endoscopic smart laser osteotomy, *Optics and Lasers in Engineering*, Volume 148, 2022, 106765, ISSN 0143-8166, <https://doi.org/10.1016/j.optlaseng.2021.106765>

Copyright notice: © 2021 The Author(s). Published by Elsevier Ltd. Under a Creative Commons [license](#).



Contents lists available at ScienceDirect

Optics and Lasers in Engineering

journal homepage: www.elsevier.com/locate/optlaseng

All-fiber-optic LIBS system for tissue differentiation: A prospect for endoscopic smart laser osteotomy

Hamed Abbasi^{a,*}, Raphael Guzman^b, Philippe C. Cattin^c, Azhar Zam^{a,*}

^a Biomedical Laser and Optics Group (BLOG), Department of Biomedical Engineering, University of Basel, CH-4123 Allschwil, Switzerland

^b Department of Neurosurgery, University Hospital Basel, CH-4056 Basel, Switzerland

^c Center for medical Image Analysis and Navigation (CIAN), Department of Biomedical Engineering, University of Basel, CH-4123 Allschwil, Switzerland

ARTICLE INFO

Keywords:

FO-LIBS
Miniaturization
High throughput
Echelle spectrometer
Tissue characterization

ABSTRACT

Minimally-invasive laser surgeries could benefit from a fiber-optic laser-induced breakdown spectroscopy (FO-LIBS) setup for real-time tissue characterization. In FO-LIBS, the sample receives limited light irradiance due to the fiber's low damage threshold and diminished laser beam quality. Therefore, the plasma created with FO-LIBS is less luminant than that of free-space LIBS. Furthermore, only a small portion of plasma emission can be collected, as the lens's size at the fiber tip is restricted to fit inside the narrow channel of an endoscope. A high optical throughput Echelle spectrometer was developed to compensate for low-intensity light collection with FO-LIBS. The Echelle spectrometer was tested for tissue differentiation when combined with a flexible fiber bundle delivery setup and a small lens at the bundle's tip. The customized FO-LIBS setup, coupled with multivariate data analysis, successfully differentiated bone from surrounding soft tissue (muscle, fat, and bone marrow) with 100% cross-validated (CV) sensitivity and specificity. The CV sensitivity and specificity for differentiation between all tissues were 90.2% and 96.7%, respectively. The results demonstrate, to the best of our knowledge, the first flexible FO-LIBS system, which may provide a further step towards the development of a smart endoscopic laser scalpel.

1. Introduction

Traditional mechanical tools (e.g., saws, drills, chisels) used for bone cutting — the gold standard in osteotomy for thousands of years — require a certain degree of mechanical force (like grinding or hammering) to function [1,2]. The mechanical pressure exerted by saws and drills (contact mode cutting) presents some disadvantages for use as an osteotomy tool, including poor surface evenness, high risk of contamination, substantial material loss, metal abrasion, limited cutting geometry, bone fragmentation, and thermal damage. Moreover, saws and drills can create an amorphous, mineral-rich carbon layer on the bone surface, changing the mineralized matrix, which results in a prolonged healing process [3,4]. Due to the many side effects of using conventional osteotomy tools, alternative solutions are being sought. Some of the lesser-known techniques for osteotomy proposed and examined over the last decades include machining based on microwaves, ion beams, ultrasonic energy, water jets, and lasers [5,6]. Laser beams do not deflect while traveling (unlike water jets) and do not carry momentum. Lasers interact with materials without mechanical interaction forces and thus contactless. Without such mechanical forces, the body movements during surgery are minimized, and consequently, intraoperative image guid-

ance systems can perform with higher accuracy. Several studies have been carried out to compare the performance of laserosteotomy with the conventional mechanical saws and drills as well as piezoelectric cutting tools. Using a laser beam offers a high axial and lateral resolution, allowing for a high degree of freedom when cutting. This freedom provides significant advantages during surgery, particularly oral and maxillofacial surgery, where implants are used to replace parts of the bone. Microstructural analysis, namely micro-computed tomography (CT) and histological examinations, have shown that more new mineralized bone is formed in cuts being performed with a laser rather than a piezo-osteotome (PZE) [7]. Accelerated healing of laserosteotomy is also reported here [8]. Histological and radiological examinations revealed primary gap healing in sheep two months post-laserosteotomy, and almost no visible osteotomy gap after three months [9]. While pre-operative planning can navigate the laser to the required area, a lack of real-time monitoring risks iatrogenic damage due to any possible number of unpredicted errors or body movement. Therefore, real-time feedback is vital to preventing damage to the surrounding soft tissues during laserosteotomy. To avoid such damage, several optical approaches have been developed, including laser-induced breakdown spectroscopy (LIBS), laser-induced breakdown thresholding, diffuse reflectance spec-

* Corresponding authors.

E-mail addresses: hamed.abbasi@unibas.ch (H. Abbasi), azhar.zam@unibas.ch (A. Zam).

<https://doi.org/10.1016/j.optlaseng.2021.106765>

Received 19 February 2021; Received in revised form 18 June 2021; Accepted 27 July 2021

0143-8166/© 2021 The Author(s). Published by Elsevier Ltd. This is an open access article under the CC BY license (<http://creativecommons.org/licenses/by/4.0/>)

troscopy (DRS), Raman spectroscopy, autofluorescence spectroscopy, random lasing, optical coherence tomography (OCT), speckle analysis, shockwave measurement, and combustion/pyrolysis light analysis. A short overview of these feedback methods is provided elsewhere [10]. Of the approaches mentioned above, LIBS is an up-and-coming technique for analyzing biological tissues, especially calcified tissues like bone. It allows for analysis without sample preparation and, with a single shot, reveals the material's chemical composition under the cut in a few milliseconds [11-17]. Multiple studies have shown the potential of using LIBS to differentiate bone from other soft tissues, such as muscle, fat, skin, nerve, mucosa, liver, tendon, as well as cartilage [18-26]. The studies differentiated between the soft tissues surrounding bone, except for bone marrow. Moreover, none of the studies mentioned could simultaneously fulfill the complete set of requirements for a minimally-invasive laserosteotomy feedback system, including the possibility of insertion inside the narrow channel of a flexible endoscope. A delivery system capable of transmitting tens of megawatts of nanosecond pulses of frequency-doubled Nd:YAG (532 nm) was recently developed [27]. The fiber delivery system developed showed high flexibility and bend-insensitive behavior. Flexibility is of high importance for compatibility with flexible endoscopes. This study aims to develop a method capable of providing optical feedback on the type of tissue being cut, namely bone, bone marrow, muscle, and fat (adipose), using the flexible fiber delivery system and a custom-made sensitive Echelle spectrometer dedicated to this application.

2. Materials and methods

While a large body of research on using LIBS for biological tissue analysis exists, most studies utilized free-space beam delivery and fiber-optic light collection [28-35]. In free-space LIBS, sufficient peak power can be delivered to the sample surface by simply using a few mirrors and/or lenses. Moreover, the laser beam maintains focusability, as it does not pass through an optical fiber. Therefore, the beam can be focused onto a relatively small focal spot, allowing for higher irradiance of the sample. Without space limitations, free-space LIBS can use bulky light collectors/collimators to collect more light from the laser-induced plasma. The light collectors/collimators employ wide diameter lenses/mirrors to maximize optical throughput light collection (low F-number). Although this is the most efficient way of performing LIBS analysis, the bulky setup can not be miniaturized for endoscopic applications. Minimally-invasive surgery requires a miniaturized beam delivery setup. In other words, the laser pulse should be delivered to the sample via optical fibers; this limits the amount of deliverable peak power to the sample (due to the limited laser-induced damage threshold (LIDT) of optical fibers) and prevent the use of bulky light collectors/collimators. In such a setup, the plasma emissions cannot be collected with high optical throughput (i.e., the smaller the lens/mirror diameter, the lower the optical throughput). Commercially available Echelle spectrometers typically have a high F-number of 10 or more [36-40], which results in low optical throughput. For this reason, a custom-made Echelle spectrometer was designed and developed with higher optical throughput than those available on the market. For use in minimally-invasive surgery, fiber-optic LIBS (FO-LIBS) must also collect the plasma light using the same fiber employed for laser beam delivery, as space inside the endoscope is limited. For flexible endoscopic applications, the fiber system should be flexible down to a bending radius of approximately 15 mm [41] and operate without bending loss. While a few researchers have used either a fiber laser [21] or a laser coupled to a fiber optic [42,43] for beam delivery during biological tissue analysis with LIBS, none of them achieved the conditions for flexible endoscopic application — namely, a common fiber for both beam delivery and light collection with flexible and bend-insensitive behavior, and small focusing/collection optics at the tip of the fiber.

2.1. Fiber-based laser beam delivery

Due to the limited LIDT of glass, large solid-core fiber or hollow-core fiber are typically used for delivering the high peak powers required for LIBS, typically in the gigawatt (GW) range. Using large-core fibers limits the bending radius, which depends on the fiber's core and cladding thickness. Therefore, a high-power delivery setup was recently developed to achieve bend-insensitive flexible beam delivery. The setup uses a beam shaper and a fused-end fiber bundle of 800 individual fibers (CeramOptec GmbH, Bonn, Germany), with low numerical aperture (NA) launch conditions [27]. A single small half-ball lens focuses the laser beam on the sample and collects the plasma emission. Fig. 1 shows the dimensions of the fiber system.

As shown in Fig. 1, the length of the solid parts inside of the endoscope is 13.5 mm; other parts are flexible with a minimum bending radius of 15 mm (tested) [27]. The diameter of the parts inside the endoscope are small enough to fit inside an endoscope with an internal diameter of 10 mm [44]. At the bundle input, the jackets were removed and individual fibers were fused together, providing a solid structure without gaps between the individual fibers. The length and diameter of the fused part of the bundle were 10 mm and 3 mm, respectively. For other parts of the bundle, the jackets of individual fibers were not removed and the individual fibers remained unattached to maintain flexibility. The diameter of the total bundle was 3.5 mm. At the bundle output, individual fibers were glued to each other. The core, cladding, and jacket diameter of individual fibers were 100 μm , 106 μm , and 112 μm , respectively. Fig. 2 shows the input and output bundle facets.

This study used a pulsed Q-switched Nd:YAG laser (Q-smart 450, Quantel, France) working at its fundamental harmonic (1064 nm), with a pulse duration of 6 ns. A green, low-power continuous wave (CW) diode laser, aligned with the pulsed laser beam, was used to visualize the focal spot. A top-hat beam shaper (GTH-5-250-4-532, TOPAG Lasertechnik GmbH, Darmstadt, Germany) was employed to illuminate all individual fibers within the fiber bundle with equal energy. An air nozzle helped to prevent dust from reaching the surface of the fiber bundle. The bundle exhibited bend-insensitive behavior due to using low-order modes to launch the bundle (tested with different bending radii down to 1.5 cm). More information about the fiber delivery process can be found elsewhere [27]. Fig. 3 (a) and (b) shows the experimental setup for laser beam delivery and plasma emission collection.

The same optical fiber and half-ball lens used to deliver the laser pulses were used to collect the plasma emission. The surface of the half-ball lens was wiped off with a lens cleaning tissue when needed (to clean the surface from the deposited particle due to tissue ablation). An off-axis parabolic (OAP) mirror with a through-hole (the pierced mirror in Fig. 3) allowed the laser beam to pass through while simultaneously directing the plasma emission to the spectrometer's optical fiber.

2.2. Echelle spectrometer

Bandwidth, resolution, and optical throughput are three spectrometer parameters that cannot be maximized simultaneously. Attempts to maximize all parameters at the same time result in either a very bulky setup (not portable and very expensive, like spectrometers designed for observatories), or a spectrometer incapable of snapshot collection (spectrometers with mechanical movable parts), which cannot be used for fast measurements [45]. Two-dimension spectroscopic configurations such as the Echelle designs have helped achieve wider bandwidth without losing resolution. Still, it is not possible to accomplish high-resolution, high-throughput, and wide bandwidth at the same time. Therefore, parameters were optimized according to the application.

The sensitivity of a spectrometer is a function of its optical throughput. The optical throughput, i.e. how much light can pass through the spectrometer, is indicated by its F-number; the lower the F-number, the higher the throughput. High F-numbers can reduce the sensitivity of the spectrometer. The plasma plume created with FO-LIBS is less luminant

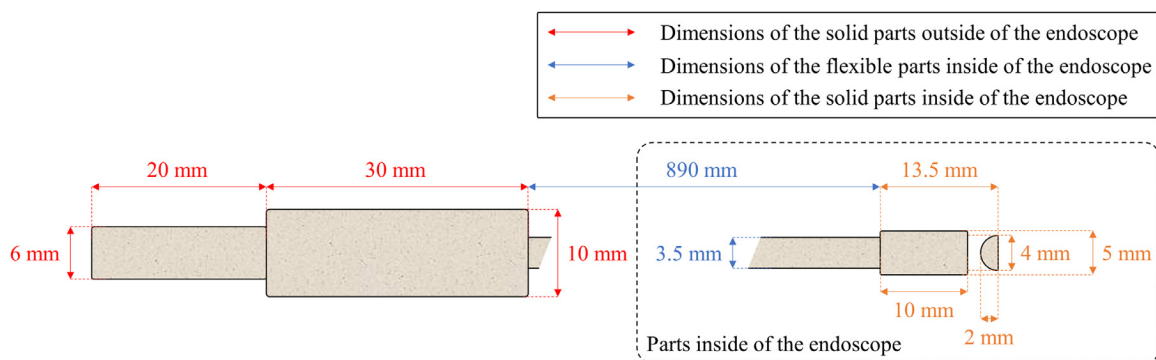


Fig. 1. Dimensions of the developed fiber system (input from the left side, the output from the right side) in relation to endoscopic placement. The half-ball lens shown on the right was used to focus the laser beam and collect the plasma emission simultaneously.

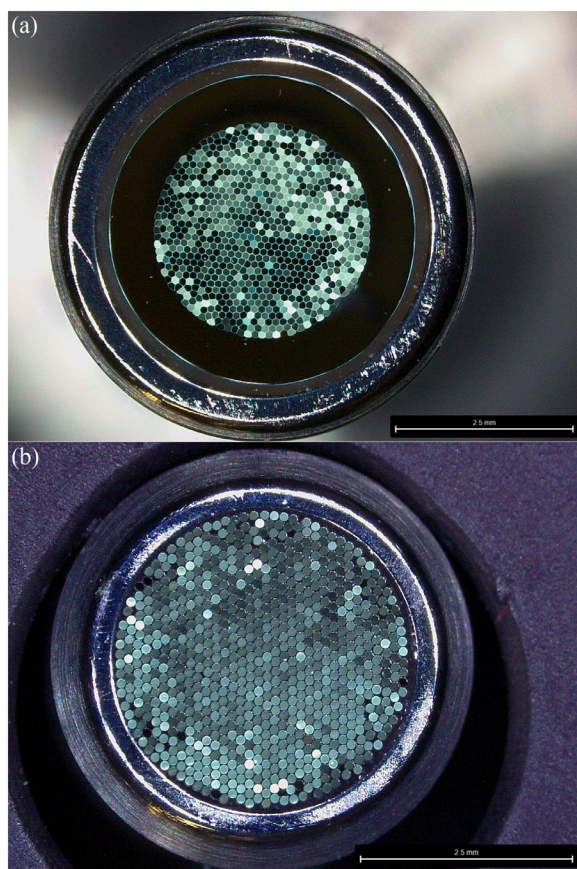


Fig. 2. (a) Input, and (b) output facets of the bundle. The images were captured using a digital microscope (Leica DVM6, Leica Microsystems GmbH, Germany). The scale shown is 2.5 mm in both (a) and (b).

(due to limited deliverable energy and reduced focusability) than that created with free-space LIBS. This fact, along with the small portion of plasma light collected by the small lens at the fiber tip, results in the spectrometer receiving low-intensity light. Therefore, a custom-made Echelle spectrometer was developed to compensate for low throughput light collection. The spectrometer was developed by simulating the mechanical and optical parts in Solidworks, Matlab, and Zemax (OpticStudio) [46], to find the most suitable components and to provide better performance than the previously developed Echelle spectrometer by the authors [45]. Fig. 4 shows the experimental setup of the customized Echelle spectrometer.

Light fed by an optical fiber patch cord (NA=0.12, core diameter=50 μm , acting as input slit) inside the spectrometer travels from the fiber output to the first OPA mirror (with an effective focal length (EFL) of 152.4 mm). After reflecting off of the mirror's surface, the collimated light reaches the Echelle grating in a quasi-Littrow orientation. A Littrow configuration would cause the center of each diffracted order to reflect back exactly on its path, thereby returning the light to the fiber. By tilting the Echelle grating from its initial position (quasi-Littrow configuration), the fiber no longer poses an obstacle to the beam. There are several ways of inducing this kind of off-axis angle in the system. The Echelle grating can be tilted either around its grooves (perpendicular to the optical table) or around the diffraction orientation (perpendicular to grooves). The former displaces the beam laterally, while the latter shifts the beam vertically. Unlike lateral displacement, vertical displacement is the same for all diffracted orders. If displacement is the same for all wavelengths in the interval of the Echellogram, then any defocusing can be corrected by simply adjusting the imaging lens. However, different displacements result in a curved imaging plane that cannot be adjusted easily unless additional optics are used. Another way to induce vertical displacement is to tilt the Echelle grating around its surface normal. Downside vertical displacement is not helpful as it directs the light to the fiber's holder (optical post and post holder). Therefore, the Echelle grating was tilted around its surface normal in a way that yielded an upside displacement. The tilt angle can be determined by gradually tilting the grating until the beam is no longer blocked by the fiber. The beam is collimated by a second OPA mirror with the same EFL as the first OPA mirror, after passing above the fiber. The second OPA mirror was installed in an antiparallel configuration to cancel out the aberration caused by the first one [47]. Both OPA mirrors have an off-axis angle of 90°; this angle was chosen based on its availability on the market. However, a mirror with a lower off-axis angle (e.g., 30°), which was not commercially available through optics catalogs at the time of development, might slightly diminish the aberration [47]. The collimated beam reflected from the second OPA mirror's surface is directed toward a cross-disperser to separate the overlapping Echelle orders. A blazed ruled grating was used here as the cross-disperser. The grooves in the cross-disperser grating were perpendicular to those of the Echelle grating. After the cross-disperser, similar to the beam's situation after being diffracted from the Echelle grating, an off-axis angle is needed to allow the beam to reach the imaging lens without obstruction from the second OPA mirror. The degree of tilt required here is higher than that of the Echelle grating to overcome the larger obstruction of the OPA mirror (compared to the smaller fiber obstruction). A high optical density (OD) longpass filter was used to filter half of the beam's cross-section diffracted from the cross-disperser (also known as ordered sorting). The separated orders are directed to the imaging lens to form the Echellogram on the camera's pixels. The optical base plate is 90 \times 60 cm^2 . The size of the setup without the camera is (l)44 $\text{cm} \times$ (w)36 $\text{cm} \times$ (h)13 cm .

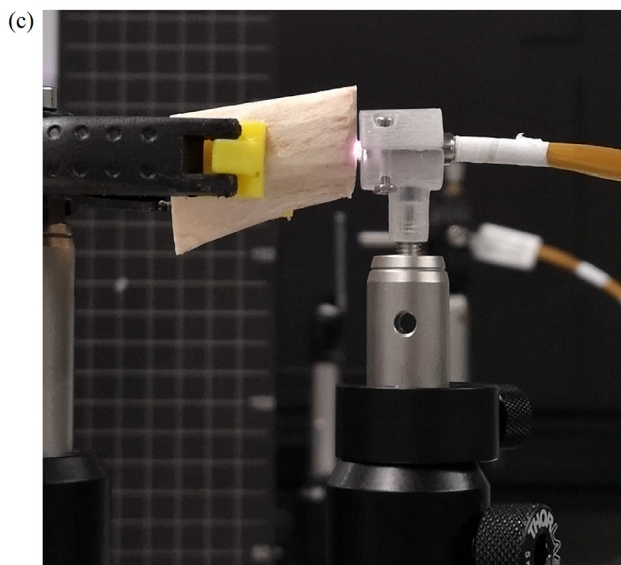
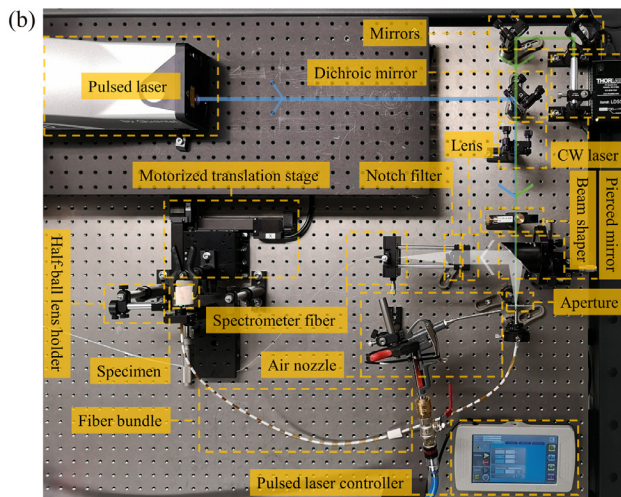
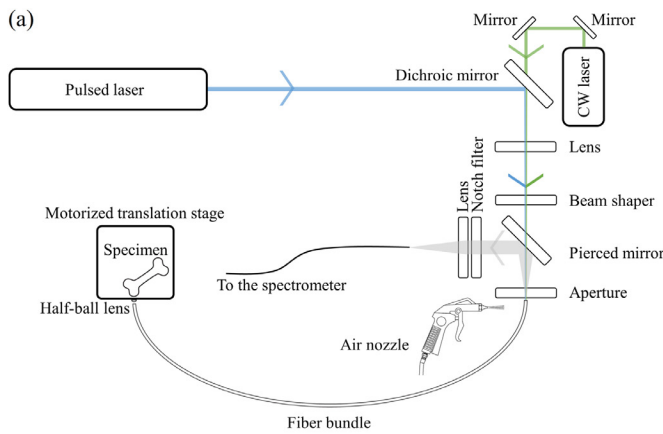


Fig. 3. (a) Schematic and (b) photograph of the experimental setup for laser beam delivery and plasma emission collection. The path of the pulsed laser, CW laser, and plasma emission are indicated by blue, green, and white lines, respectively. Arrows in (a) and (b) show the direction of light propagation. The half-ball lens (not marked in (a) and (b)) was clamped by a holder, 1.5 mm away from the fiber output. (c) Photograph of the bundle's tip.

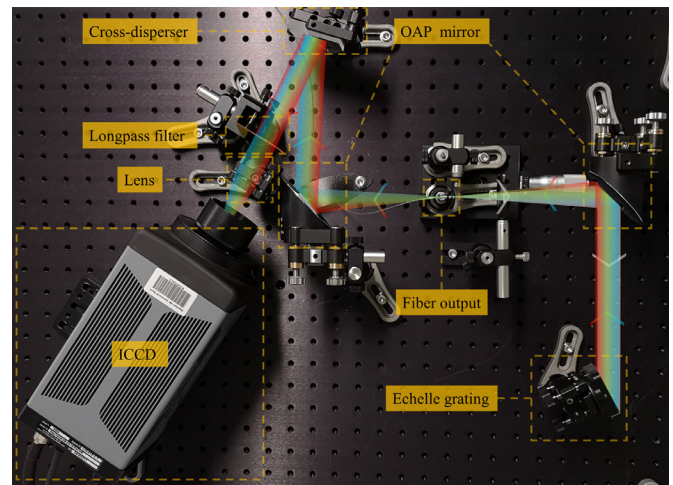


Fig. 4. Experimental setup of the customized Echelle spectrometer. The enclosure box has not been shown intentionally. The path of the light, from the fiber output to the detector, is highlighted. Arrows show the direction of light propagation.

The ICCD camera (PI-MAX 4, Princeton Instruments, USA) was synchronized with the laser Q-switched using TTL trigger pulses to have the proper time window for collecting plasma emission. The customized spectrometer was installed on top of a three-tier utility cart for portability. The middle tier was left empty for this study but could be used for a laser coupling system to achieve a portable LIBS setup. The bottom tier was dedicated to calibration instruments (a NIST traceable balanced Deuterium-Halogen light source for intensity calibration and some gas/vapor spectral lamps, including Mercury-Argon, Argon, Neon, and Krypton for wavelength calibration).

2.3. Specimen

Five bisected femora from porcine specimens (purchased from a local slaughterhouse) were used in this study. Each bisected tissue consisted of bone, bone marrow, fat, and muscle. From each side of each bisected specimen, 50 LIBS data points were collected from each tissue. In total, 2000 data points were collected (5 specimens \times 4 tissue types \times 2 sides \times 50 shots).

2.4. Data analysis

The data collected from the five specimens were divided into five folds (each 400) to train a classifier in cross-validation (CV) mode. Afterward, each spectrum was normalized to its mean. Principal component analysis (PCA) was used to reduce data dimensionality while preserving as much of the data's variation as possible. The output of the PCA was used as input for a quadratic support vector machine (Q-SVM). An SVM with quadratic kernel was selected. It showed slightly better classification accuracy over other kernels. It was subsequently used to train a classifier on the training dataset and test the classifier on each fold's testing dataset. The data were analyzed using Matlab R2019b.

3. Results

Fig. 5 shows the Echellogram of the Deuterium-Halogen (DH) lamp. Fig. 6 shows the measured spectrum of four calibration lamps used for calibrating the spectrometer's wavelength.

The spectrometer's resolution was in the Angstrom range, sufficient for resolving peaks in the LIBS spectra (representing biological tissues) throughout the entire bandwidth. The spectrum of tissues is shown in Fig. 7.

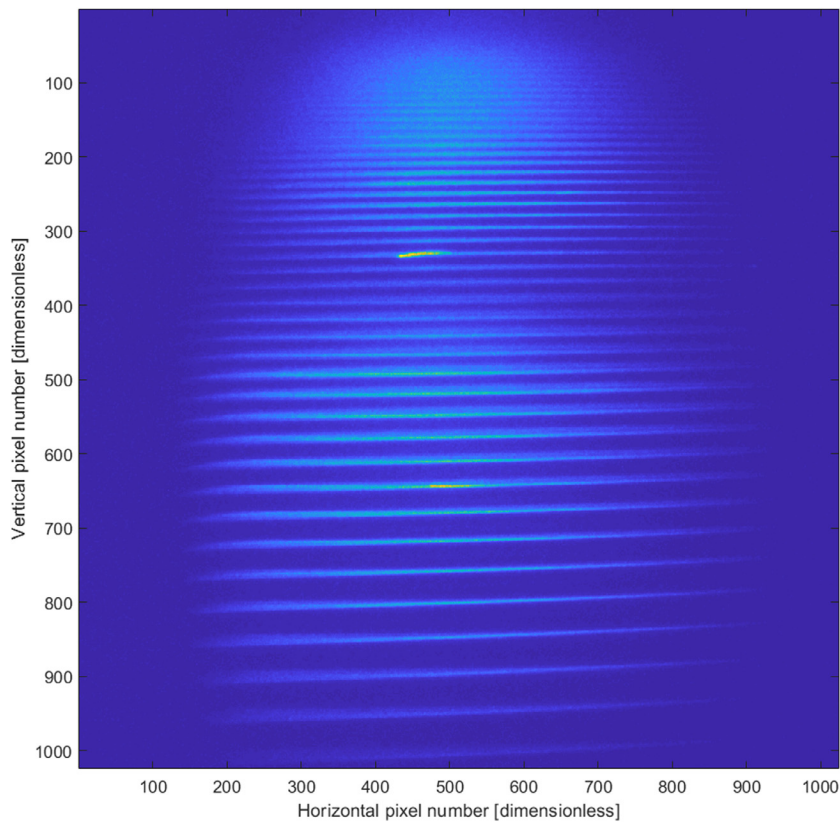


Fig. 5. Echellogram of Deuterium-Halogen (DH) lamp showing Echelle orders.

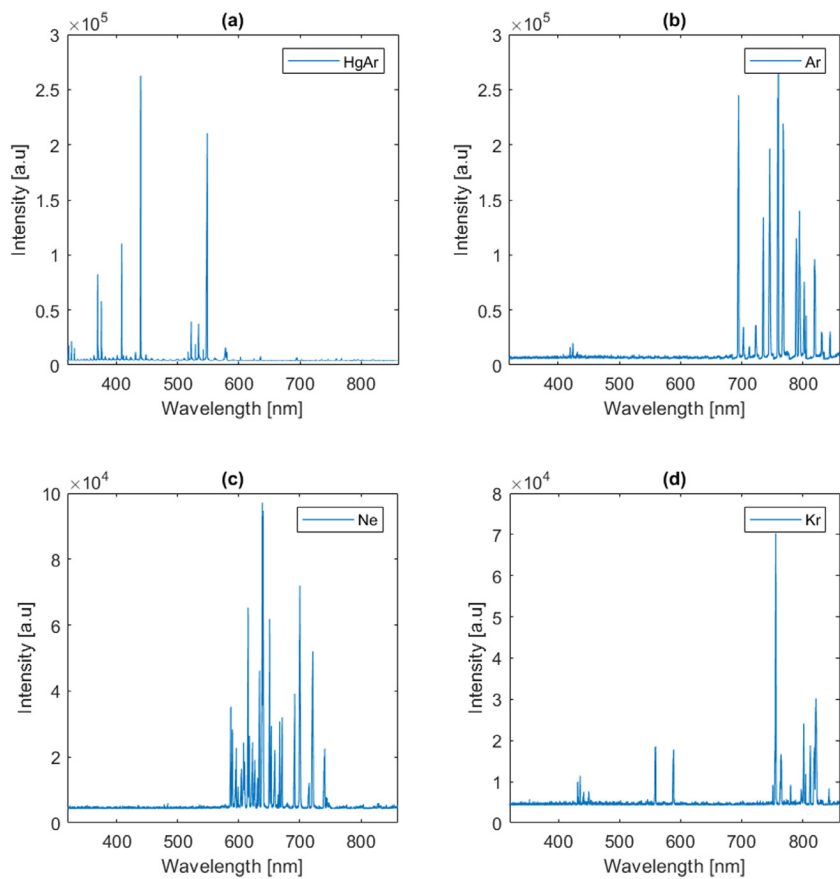


Fig. 6. The measured spectrum of calibration lamps used for calibrating the spectrometer's wavelength: (a) Mercury-Argon, (b) Argon, (c) Neon, and (d) Krypton.

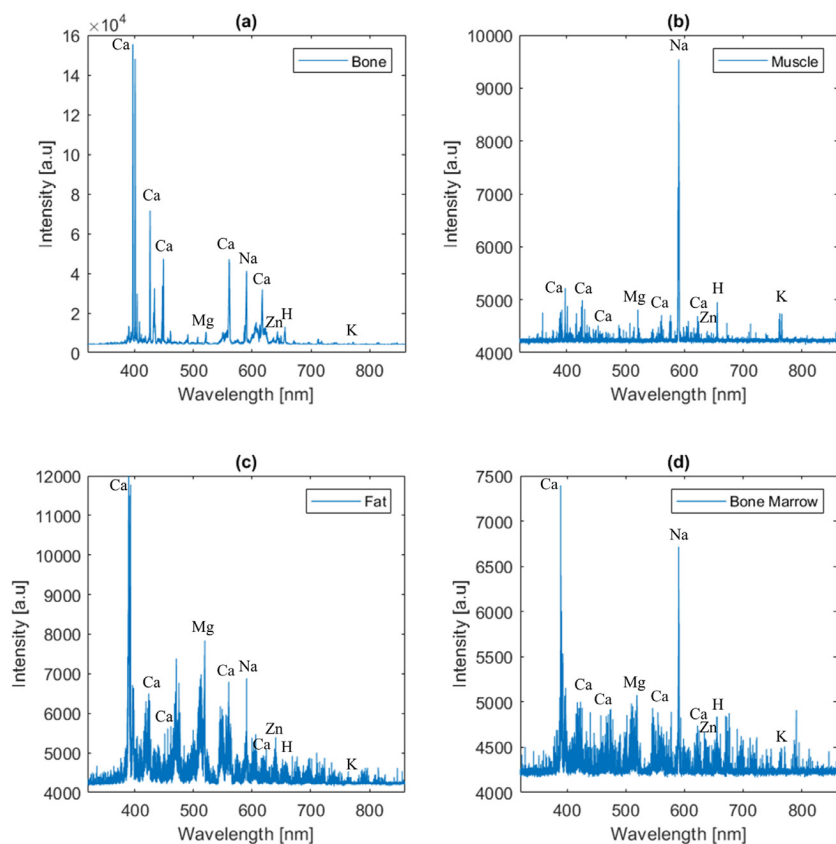


Fig. 7. LIBS spectrum of tissues: (a) bone, (b) muscle, (c) fat, and (d) bone marrow. The wavelength of some elements, including calcium (Ca), magnesium (Mg), sodium (Na), zinc (Zn), hydrogen (H), and potassium (K) are marked in each spectrum.

Table 1
Confusion matrix for the classifier.

		Predicted class				Sensitivity (CV)	Specificity (CV)	AUC
		Tissue	Bone	Muscle	Fat			
Actual class	Bone	500	0	0	0	100%	100%	1.00
	Muscle	0	490	9	1	98%	96.7%	0.99
	Fat	0	20	423	57	84.6%	94.1%	0.96
	Bone marrow	0	30	79	391	78.2%	96.1%	0.95
		Average				90.2%	96.7%	0.98

After reducing the dimensionality of the data through PCA, the first six principal components (PCs) were used to feed the Q-SVM, which could classify bone from other soft tissues with 100% sensitivity and specificity (CV). The muscle was classified from other tissues with very high CV sensitivity (98%) and specificity (96.7%), as well. However, fat and bone marrow were classified with slightly lower CV sensitivity (84.6% and 78.2%) and specificity (94.1% and 96.1%).

Moreover, a receiver operating characteristic (ROC) curve was depicted and the area under the curve (AUC) was calculated (Fig. 8).

Table 1 shows the result of the classification.

4. Discussion

A few FO-LIBS systems had previously been proposed for biological tissue differentiation. However, endoscopic smart laser surgery systems require miniaturization and flexibility, as well. Therefore, a custom-made, bend-insensitive bundle delivery setup with sufficient flexibility was tested, in combination with a tiny half-ball lens at the bundle's tip (please see Section 2.1 for details of fiber delivery setup). The setup's dimensions and flexibility allowed for endoscopic application. Use of a bundle prevents self-focusing, as light does not penetrate between the individual fibers within the bundle. Compared to that of a single fiber,

the larger cross-section of the bundle makes it less sensitive to mechanical movements (more robust setup), offering yet another benefit.

Due to the need to enhance sensitivity in an FO-LIBS setup, a custom-made Echelle spectrometer was developed and optimized for our application (please see Section 2.2 for details of the spectrometer design). We aimed to achieve the following specifications: 500 nm spectral bandwidth from 330 to 830 nm, at least 0.6 nm resolution, high optical throughput (low F-number), and compact size. Astigmatism aberrations in the spectrometer were minimized via off-axis parabolic mirrors. Coma aberrations were quelled by two collimators with an antiparallel configuration. Employing two collimators (first collimator in dual-pass mode) instead of one enabled us to maintain the Echelle grating in a quasi-Littrow configuration, with minimal deviation from the optical axis. Camera tilt compensated for longitudinal chromatic aberrations. Therefore, an appropriate resolving power was achieved within a sufficiently wide spectral bandwidth. Using off-axis mirrors eliminated the need for high focal-length designs. Therefore, we were able to keep the F-number of our design very low (i.e., 3). In the other designs, using a short focal-length necessitated tilting the mirror (producing extensive off-axis aberrations into the system). Mirrors with a 90° degree off-axis were used in this study because of their availability. However, a lower off-axis angle (e.g., 30°) would decrease aberrations in the system [47]. The compact size of the spectrometer made it portable. A portable

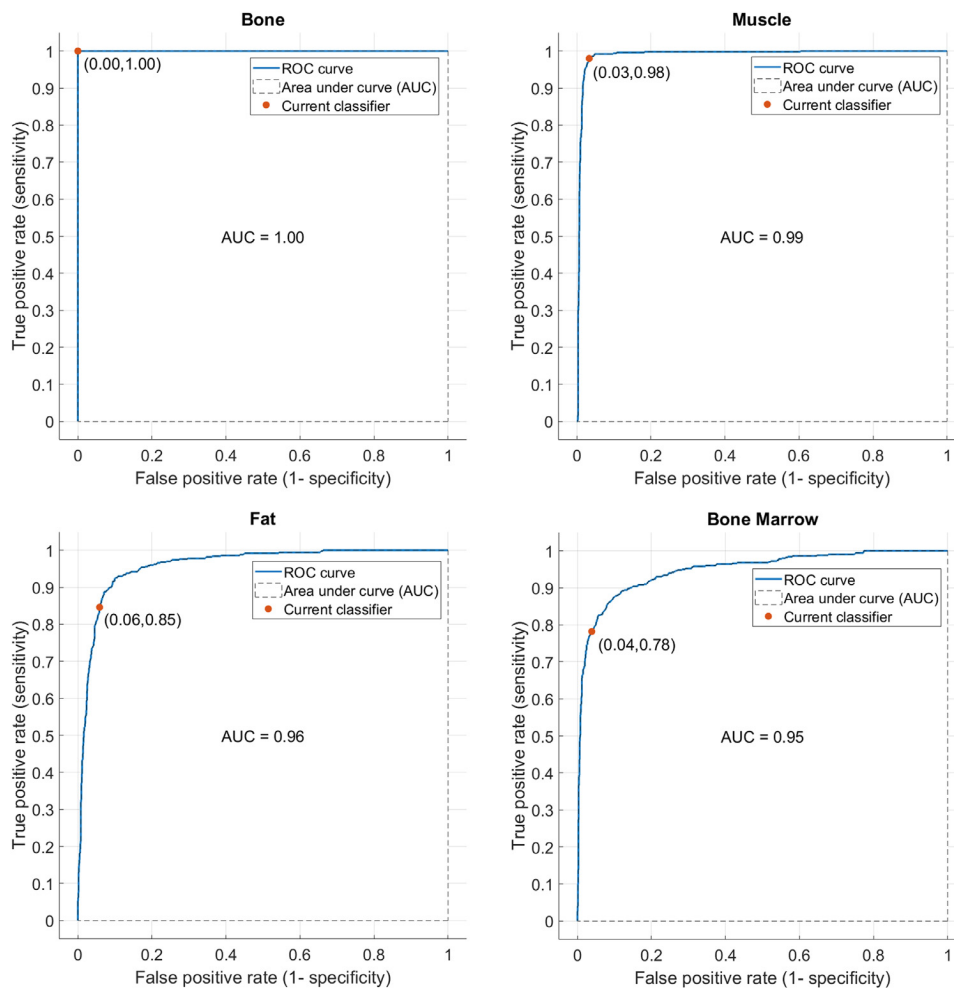


Fig. 8. ROC curve for the classifier for (a) bone, (b) muscle, (c) fat, and (d) bone marrow.

LIBS spectrometer is remarkably valuable for testing and characterizing different biological samples on-site. This is an excellent capability, especially if the target sample is potentially contagious. The customized LIBS setup was tested to differentiate bone from surrounding soft tissues, namely muscle, fat, and bone marrow. It is worth mentioning that since ablation is threshold-based, and plasma can initiate with lower energy in bone than in soft tissues [10], finding an optimum laser and ICCD parameter was challenging. For this study, the ICCD gate was open for 1 ms, after a 1 μ s delay of the laser pulse, while the laser energy applied to specimens was 130 mJ. A higher intensity spectrum could be obtained with higher energies, but it leads to saturation of the ICCD's pixels while collecting the spectrum from the bone specimen. That is why in Fig. 7, the bone specimen yields a more intense signal than the soft tissues. The setup was able to differentiate bone from surrounding soft tissues (the requirement for endoscopic laserosteotomy) with 100% sensitivity and specificity (please see Section 2.3 and 2.4 for the details of the specimen and data analysis, respectively). The overall sensitivity and specificity for differentiating all tissues (the requirement for general endoscopic laser surgery) were 90.2% and 96.7%, respectively. The differentiation between fat and bone marrow accounts for most of the errors, as tissues have a similar chemical composition. An average classification error of 57.7% for differentiating bone marrow was reported after optoacoustic monitoring of Nd:YAG-laser-produced plasma using a Mach-Zehnder Interferometer [48]. However, averaging two subsequent data points might improve accuracy [49]. It should be noted that as bone marrow and fat are not adjacent tissues in the body, differentiating between them is less important than other tissues. The all-fiber-optic LIBS offers a stand-alone setup that does not need an additional laser for

characterization, a common shortcoming of other miniaturized sensors developed for laser surgery monitoring [50].

5. Conclusion

The fiber delivery system proposed herein, including the bundle and the lens, was suitable for endoscopic application thanks to its small size and bend-insensitive flexibility. However, for successful endoscopic LIBS, a proper Echelle spectrometer was required as well. The main feature of most commercially available Echelle spectrometers is the ability to achieve the highest possible resolution and bandwidth at the same time. This meets the demand for a general device that is suitable for most applications. However, since optimizing all of the spectrometer parameters simultaneously is not possible, optical throughput is typically sacrificed to achieve simultaneous high-resolution and bandwidth. Low optical throughput reduces the system's sensitivity, so it does not work correctly in low light conditions (like those of miniaturized systems). The spectrometer was designed based on the spectral interval with most significant number of LIBS peaks for tissue differentiation (330 to 830 nm), and the resolution better than distance between the two closest peaks (0.6 nm) [24]. In our design, we reduced the bandwidth and resolution compared to the levels associated with commercially available Echelle spectrometers. Therefore, we were able to increase the optical throughput of the spectrometer. Our design leads to an F-number of 3, which is a significant improvement over other designs (typically ten or more). At the same time, we achieved the spectral bandwidth required to cover the essential biological LIBS peaks, and the resolution of the system exceeded the initial requirement. The

results show that the customized system was both sensitive and specific (selective) when differentiating tissues, label-free and in a single shot without sample preparation. The proposed setup is thus suitable for minimally-invasive smart laser surgery.

Declaration of Competing Interest

The authors declare that they have no known competing financial interests or personal relationships that could have appeared to influence the work reported in this paper.

CRedit authorship contribution statement

Hamed Abbasi: Conceptualization, Methodology, Software, Validation, Formal analysis, Investigation, Data curation, Writing – original draft, Writing – review & editing, Visualization. **Raphael Guzman:** Writing – review & editing, Supervision. **Philippe C. Cattin:** Writing – review & editing, Supervision, Funding acquisition. **Azhar Zam:** Conceptualization, Methodology, Resources, Writing – review & editing, Supervision, Project administration.

Acknowledgement

The authors gratefully acknowledge funding from the Werner Siemens Foundation through the Minimally Invasive Robot-Assisted Computer-guided Laserosteotomy (MIRACLE) project. Moreover, the assistance given by Dr. Ferda Canbaz is highly appreciated.

References

- [1] Sotsuka Y, Nishimoto S, Tsumano T, Kawai K, Ishise H, Kakibuchi M, et al. The dawn of computer-assisted robotic osteotomy with ytterbium-doped fiber laser. *Lasers Med Sci* 2014;29:1125–9.
- [2] Bernal LMB, Abbasi H, Zam A. Laser in Bone Surgery. In: Stübinger S, Klämpfl F, Schmidt M, Zeilhofer H, editors. *Lasers in Oral and Maxillofacial Surgery*. Springer; 2020. p. 99–109.
- [3] Jowett N, Wöllmer W, Reimer R, Zustin J, Schumacher U, Wiseman PW, Mlynarek AM, Bötcher A, Dalchow CV, Lörincz BB. Bone ablation without thermal or acoustic mechanical injury via a novel picosecond infrared laser (PIRL). *Otolaryngology–head and neck surgery* 2014;150:385–93.
- [4] Giraud JY, Villemin S, Darmana R, Cahuzac JP, Autefage A, Morucci JP. Bone cutting. *Clin Phys Physiol Meas* 1991;12:1–19.
- [5] Pantawane M, Dahotre N. Challenges and advances in osteotomy. *Ann Bone Joint Surg* 2019;2(1):1007–2019.
- [6] Dahotre NB, Joshi S. *Machining of bone and hard tissues*. Springer; 2016.
- [7] Augello M, Deibel W, Nuss K, Cattin P, Jürgens P. Comparative microstructural analysis of bone osteotomies after cutting by computer-assisted robot-guided laser osteotomy and piezoelectric osteotomy: an in vivo animal study. *Lasers Med Sci* 2018;33:1471–8.
- [8] Baek K-w, Dard M, Zeilhofer H-F, Cattin PC, Juergens P. Comparing the Bone Healing After Cold Ablation Robot-Guided Er:YAG Laser Osteotomy and Piezoelectric Osteotomy—A Pilot Study in a Minipig Mandible. *Lasers Surg Med* 2020.
- [9] Stübinger S, Nuss K, Pongratz M, Price J, Sader R, Zeilhofer H-F, et al. Comparison of Er:YAG laser and piezoelectric osteotomy: An animal study in sheep. *Lasers Surg Med* 2010;42:743–51.
- [10] Abbasi H, Beltrán Bernal LM, Hamidi A, Droneau A, Canbaz F, Guzman R, Jacques SL, Cattin PC, Zam A. Combined Nd:YAG and Er:YAG lasers for real-time closed-loop tissue-specific laser osteotomy. *Biomedical Optics Express* 2020;11:1790–807.
- [11] Gaudiuso R, Melikechi N, Abdel-Salam ZA, Harith MA, Palleschi V, Motto-Ros V, et al. Laser-induced breakdown spectroscopy for human and animal health: A review. *Spectrochim Acta, Part B* 2019;152:123–48.
- [12] Kasem MA, Gonzalez JJ, Russo RE, Harith MA. LIBS analysis of artificial calcified tissues matrices. *Talanta* 2013;108:53–8.
- [13] Abdel-Salam ZA, Nanjing Z, Anglos D, Harith MA. Effect of experimental conditions on surface hardness measurements of calcified tissues via LIBS. *Appl Phys B* 2009;94:141–7.
- [14] Abdel-Salam ZA, Galmed AH, Tognoni E, Harith MA. Estimation of calcified tissues hardness via calcium and magnesium ionic to atomic line intensity ratio in laser induced breakdown spectra. *Spectrochim Acta, Part B* 2007;62:1343–7.
- [15] Abdel-Salam ZA, Palleschi V, Harith MA. Study of the feeding effect on recent and ancient bovine bones by nanoparticle-enhanced laser-induced breakdown spectroscopy and chemometrics. *J Adv Res* 2019;17:65–72.
- [16] Kasem MA, Russo RE, Harith MA. Influence of biological degradation and environmental effects on the interpretation of archeological bone samples with laser-induced breakdown spectroscopy. *J Anal At Spectrom* 2011;26:1733–9.
- [17] Tofaneli M, Pardini L, Borriini M, Bartoli F, Bacci A, D'Ulivo A, et al. Spectroscopic analysis of bones for forensic studies. *Spectrochim Acta, Part B* 2014;99:70–5.
- [18] Kanawade R, Mehari F, Knipfer C, Rohde M, Tangermann-Gerk K, Schmidt M, et al. Pilot study of laser induced breakdown spectroscopy for tissue differentiation by monitoring the plume created during laser surgery — An approach on a feedback Laser control mechanism. *Spectrochim Acta, Part B* 2013;87:175–81.
- [19] Mehari F, Rohde M, Knipfer C, Kanawade R, Klämpfl F, Adler W, Stelzle F, Schmidt M. Laser induced breakdown spectroscopy for bone and cartilage differentiation-ex vivo study as a prospect for a laser surgery feedback mechanism. *Biomedical optics express* 2014;5:4013–23.
- [20] Kanawade R, Mahari F, Klämpfl F, Rohde M, Knipfer C, Tangermann-Gerk K, et al. Qualitative tissue differentiation by analysing the intensity ratios of atomic emission lines using laser induced breakdown spectroscopy (LIBS): prospects for a feedback mechanism for surgical laser systems. *J Biophotonics* 2015;8:153–61.
- [21] Huang H, Yang L-M, Bai S, Liu J. Smart surgical tool. *J Biomed Opt* 2015;20:028001.
- [22] Mehari F, Rohde M, Kanawade R, Knipfer C, Adler W, Klämpfl F, et al. Investigation of the differentiation of ex vivo nerve and fat tissues using laser-induced breakdown spectroscopy (LIBS): Prospects for tissue-specific laser surgery. *J Biophotonics* 2016;9:1021–32.
- [23] Rohde M, Mehari F, Klämpfl F, Adler W, Neukam F-W, Schmidt M, et al. The differentiation of oral soft- and hard tissues using laser induced breakdown spectroscopy — a prospect for tissue specific laser surgery. *J Biophotonics* 2017;10:1250–61.
- [24] Abbasi H, Rauter G, Guzman R, Cattin P, Zam A. Differentiation of femur bone from surrounding soft tissue using laser-induced breakdown spectroscopy as a feedback system for smart laserosteotomy. *SPIE*; 2018.
- [25] Abbasi H, Rauter G, Guzman R, Cattin P, Zam A. Laser-induced breakdown spectroscopy as a potential tool for autocarbonization detection in laserosteotomy. *J Biomed Opt* 2018;23:071206.
- [26] Abbasi H, Sugiarto I, Rauter G, Guzman R, Cattin P, Zam A. Pilot Ex Vivo Study of Laser-Induced Breakdown Spectroscopy to Detect Bone Dehydration: An Approach for Irrigation Feedback in Laserosteotomy. *ICEECS*; 2018.
- [27] Abbasi H, Canbaz F, Guzman R, Cattin PC, Zam A. Highly flexible fiber delivery of a high peak power nanosecond Nd:YAG laser beam for flexoscopic applications. *Biomedical Optics Express* 2021;12:444–61.
- [28] Bahreini M, Hosseinimakarem Z, Tavassoli SH. A study of association between fingernail elements and osteoporosis by laser-induced breakdown spectroscopy. *J Appl Phys* 2012;112:054701.
- [29] Bahreini M, Ashrafkhani B, Tavassoli SH. Discrimination of patients with diabetes mellitus and healthy subjects based on laser-induced breakdown spectroscopy of their fingernails. *J Biomed Opt* 2013;18:107006.
- [30] Bahreini M, Ashrafkhani B, Tavassoli SH. Elemental analysis of fingernail of alcoholic and doping subjects by laser-induced breakdown spectroscopy. *Appl Phys B* 2014;114:439–47.
- [31] Gazmeh M, Bahreini M, Tavassoli SH. Discrimination of healthy and carious teeth using laser-induced breakdown spectroscopy and partial least square discriminant analysis. *Appl. Opt.* 2015;54:123–31.
- [32] Henn K, Gubaidullin GG, Bongartz J, Wahrburg J, Roth H, Kunkel M. A spectroscopic approach to monitor the cut processing in pulsed laser osteotomy. *Lasers Med Sci* 2013;28:87–92.
- [33] Abdel-Salam Z, Abdel-Salam SAM, Harith MA. Application of Laser Spectrochemical Analytical Techniques to Follow Up Spoilage of White Meat in Chicken. *Food Anal Methods* 2017;10:2365–72.
- [34] Corsi M, Cristoforetti G, Giuffrida M, Hidalgo M, Legnaioli S, Palleschi V, Salvetti A, Tognoni E, Vallebona C. Analysis of biological tissues by laser induced breakdown spectroscopy technique. *International Congress on Applications of Lasers & Electro-Optics* 2003;2003:404.
- [35] Corsi M, Cristoforetti G, Hidalgo M, Legnaioli S, Palleschi V, Salvetti A, Tognoni E, Vallebona C. Application of laser-induced breakdown spectroscopy technique to hair tissue mineral analysis. *Appl. Opt.* 2003;42:6133–7.
- [36] Farsad M. A design cycle for echelle spectrometers. *SPIE*; 2017.
- [37] Hoehse M, Mory D, Florek S, Weritz F, Gornushkin I, Panne U. A combined laser-induced breakdown and Raman spectroscopy Echelle system for elemental and molecular microanalysis. *Spectrochim Acta, Part B* 2009;64:1219–27.
- [38] Sabsabi M, Detalle V, Harith MA, Tawfik W, Imam H. Comparative study of two new commercial echelle spectrometers equipped with intensified CCD for analysis of laser-induced breakdown spectroscopy. *Appl. Opt.* 2003;42:6094–8.
- [39] Florek S, Haisch C, Okrus M, Becker-Ross H. A new, versatile echelle spectrometer relevant to laser induced plasma applications. *Spectrochim Acta, Part B* 2001;56:1027–34.
- [40] Haisch C, Panne U, Niessner R. Combination of an intensified charge coupled device with an echelle spectrograph for analysis of colloidal material by laser-induced plasma spectroscopy. *Spectrochim Acta, Part B* 1998;53:1657–67.
- [41] Iwai K, Takaku H, Miyagi M, Shi Y-W, Matsuura Y. Fabrication of Shatter-Proof Metal Hollow-Core Optical Fibers for Endoscopic Mid-Infrared Laser Applications. *Fibers* 2018;6:24.
- [42] Sasazawa S, Kakino S, Matsuura Y. Optical-fiber-based laser-induced breakdown spectroscopy for detection of early caries. *J Biomed Opt* 2015;20:065002.
- [43] Samek O, Telle HH, Beddows DCS. Laser-induced breakdown spectroscopy: a tool for real-time, in vitro and in vivo identification of carious teeth. *BMC Oral Health* 2001;1:1.
- [44] Ahmadi M, Hassani RH, Kosa G, Zam A, Guzman R, Cattin PC, Rauter G. EndoCAT: An EtherCAT-based Articulated Rear View Endoscope for Single Port Surgery. In: 2018 7th IEEE International Conference on Biomedical Robotics and Biomechatronics (Biorob); 2018. p. 1070–5.
- [45] Abbasi H, Rauter G, Guzman R, Cattin P, Zam A. Design and implementation of a compact high-throughput echelle spectrometer using off-the-shelf off-axis parabolic mirrors for analysis of biological samples by LIBS (Conference Presentation). *SPIE*; 2019.

- [46] Abbasi H, Sahraei N, Canbaz F, Cattin PC, Zam A. Simulation of Echellogram Using Zemax OpticStudio and Matlab for LIBS. Cham: Springer International Publishing; 2021. p. 211–18.
- [47] Probst RA, Steinmetz T, Wu Y, Grupp F, Udem T, Holzwarth R. A compact echelle spectrograph for characterization of astro-combs. *Appl Phys B* 2017;123:76.
- [48] Kenhagho HN, Rauter G, Guzman R, Cattin PC, Zam A. Optoacoustic Tissue Differentiation Using a Mach–Zehnder Interferometer. *IEEE Trans Ultrason Ferroelectr Freq Control* 2019;66:1435–43.
- [49] Nguendon Kenhagho H, Canbaz F, Gomez Alvarez-Arenas TE, Guzman R, Cattin P, Zam A. Machine Learning-Based Optoacoustic Tissue Classification Method for Laser Osteotomes Using an Air-Coupled Transducer. *Lasers Surg Med* 2020.
- [50] Kenhagho HN, Canbaz F, Rauter G, Guzman R, Cattin P, Zam A. A First Approach to Miniaturized Optoacoustic Feedback Sensor for Smart Laser Osteotome : Fiber-Coupled Fabry-Pérot Etalon Sensor, 2019 2019:1–4.

Chapter 7: Discussion and conclusion

7.1 Discussion

It was the goal to develop a method for optically monitoring the type and characteristics of the tissue being ablated in laserosteotomy. The method had to differentiate bone from surrounding soft tissue and detect laser-induced thermal damages (e.g., carbonization) in real-time. Moreover, the method had to have the potential for miniaturization for endoscopic applications. Therefore, in the framework of the current thesis project, the following research was carried out.

Chapter 3: Initially, we explored the dynamics of a laser-produced plasma plume over time. By observing the plasma expansion dynamics, we were able to experimentally determine the best time frame for gating the camera during LIBS for bone. The goals were to block the continuum emission at the beginning of plasma formation and to achieve high SNR. Afterward, based on the results obtained, a time-resolved LIBS experiment was carried out to differentiate bone from muscle and fat in free-space. We observed 21 reproducible atomic emission lines, including calcium (Ca), sodium (Na), potassium (K), zinc (Zn), hydrogen (H), iron (Fe), oxygen (O), chlorine (Cl), and nitrogen (N). Additionally, a molecular line of carbon to nitrogen bonding (CN) was detected in the captured spectra. Later, we applied a DFA algorithm to the data and differentiated tissues from each other with high accuracy.

Chapter 4: We experimentally demonstrated that bone under long-pulse Er:YAG (currently, the most efficient laser used for advanced laserosteotomy) irradiation can survive for only a few pulses without irrigation. We also showed that an Er:YAG beam cannot pass through a layer of water beyond approximately 1 mm (energy-dependent). After showing the importance of an irrigation system, we demonstrated that LIBS can automatically detect carbonization in a laser-irradiated bone. The same experimental setup used in Chapter 3 was used here, as well. A possible error in the irrigation system can cause carbonization; therefore, such feedback can stop further carbonization. However, successful feedback on dehydration could help prevent carbonization in the first place, as dehydration is the precursory stage of carbonization. Therefore, we studied the ability of LIBS to detect self-dehydration over time. Assuming that the dehydration caused by gradual evaporation on the dehydrated bone happens in a fashion similar to that of laser-induced dehydration, this approach could be used for tuning an irrigation system in a laserosteotome.

Chapter 5: The research presented in chapters 3 and 4 showed experiments conducted in an offline mode, i.e., the data was collected and stored on a PC and analyzed afterward. Afterward, we combined two lasers, a low energy Nd:YAG for tissue differentiation and a high energy Er:YAG for efficient ablation. Tissue differentiation was performed in a real-time and closed-loop manner. A mechanical shutter blocked the Er:YAG beam when it encountered a tissue meant to be preserved. In the study, the energy of the Nd:YAG laser was reduced to avoid ablating non-target tissue; the method introduced, laser-induced breakdown thresholding, provided non-destructive, real-time, closed-loop tissue differentiation. However, as it was a challenging and time-consuming task to adjust the distance between the focusing lens and the sample, later, we developed a method to help the researcher adjust this distance with the help of an acoustic sensor

Chapter 6: For use in minimally-invasive endoscopic applications, the setup has to be miniaturized. Therefore, we developed a fiber optic LIBS (FO-LIBS) setup. Compared to free-space LIBS, FO-LIBS limits the amount of deliverable peak power due to higher peak power density (irradiance) produced when the laser beam is focused on an optical fiber (the smaller the focal spot, the higher the irradiance). Also, the laser beam typically loses its focusability after passing through an optical fiber. Therefore, the plasma plume created at the sample surface is weakly luminous. On top of these limitations, the use of a small lens at the tip of the fiber limits the amount of collectible plasma emission (the smaller the lens diameter, the lower the optical throughput). As a result, the spectrometer receives very low-intensity plasma emissions. To compensate for such low optical throughput in plasma emission collection in a miniaturized FO-LIBS setup, we custom-made an Echelle spectrometer with higher optical throughput (low F-number) than those commercially available on the market. Moreover, we used a custom-made fiber bundle, in which the individual fibers were fused to each other at the input facet, but not at its other parts. Consequently, the fiber bundle was able to deliver high peak power without losing its flexibility. The custom fiber delivery system showed bend-insensitive behavior, as well. Flexibility is required if the fiber is to be inserted in a flexible endoscope. In the end, the miniaturized FO-LIBS system in combination with an advanced chemometric, was used for tissue differentiation. The results demonstrated high accuracy for differentiating bone, muscle, fat, and bone marrow.

7.2 Future Work

While studying the dynamics of plasma expansion, we observed that the expansion dynamic is quite different based on the type of material under the laser beam. This observation suggests that plasma expansion-dynamic monitoring might be another approach for tissue differentiation. However, more experiments are needed to confirm the hypothesis.

Moreover, we were interested in examining the performance of different machine learning methods (to compare the required training and testing time, and also the accuracy). We performed a few preliminary tests, though the results were never published. Some of the results were presented at ICBE 2018, Marrakech, Morocco (please refer to Appendix I) [238]. However, many other approaches remain unexplored. This is a fascinating topic to engage with as a separate thesis work. Advanced deep learning based on convolutional neural networks (CNN) might perform better than classical approaches, either 1D-CNN for analyzing the spectrum or 2D-CNN for analyzing the Echellogram, directly. Other advanced chemometrics, like calibration-free LIBS (CF-LIBS), would be interesting to explore as well.

We showed that detecting dehydration and carbonization is possible through LIBS. Later, we tried to find a regression model to determine the number of Er:YAG pulses that had been sent to the bone without irrigation. Such information can further be used as a feedback mechanism for fine-tuning the irrigation system in laserosteotomy (real-time, closed-loop operation). This preliminary result was presented at EMSLIBS 2019, Brno, Czech Republic (please refer to Appendix II) [239]. The intention of performing this experiment was to provide a baseline for future work.

As mentioned in the previous section, we faced some challenges performing closed-loop real-time experiments with the combination Nd:YAG / Er:YAG lasers. One challenge was solved (lens-to-sample distance adjustment). Another challenge was running both lasers with the same repetition rate, due to some synchronization difficulties. However, with the help of another Ph.D. student, we managed to solve this problem as well [240]. The problem was solved by controlling all devices using a central electronic cabinet. The only remaining challenge was keeping the focusing lens clean during the whole experiment. Since the focal length was short, the debris generated during the ablation soiled the surface of the lens. An unclean lens surface might result in reduced transmission, both of the laser beam and plasma light. After each round of the experiment, we had to clean the lens. In the real-scenario application, more difficulties could occur if the debris accumulates over time during long periods of ablation. Adding a protective window with some hydrophobic coating could help to solve the issue. Additionally, an automatic cleaning mechanism using airflow (to prevent debris from catching on the lens/window surface) or water (to clean the lens/window surface) might be helpful. However, additional experiments are required to confirm the effectiveness of such an approach.

Another interesting topic to pursue is how best to utilize the new spectroscopic system for tumor margin detection in cancer surgery, during a complete tumor resection, for example. A few preliminary spectroscopic examinations of formalin-fixed paraffin-embedded (FFPE) bone tumor samples showed very promising results. Combining different optical modalities might also improve classification accuracy for such a challenging task.

All experiments in this thesis study were performed *ex vivo* with fresh porcine tissues. To employ the new system *in vivo* during surgery on humans, the device would need to be retrained due to the higher percentage of blood and water and some possible minor difference between the chemical matrix of porcine tissue and human tissue.

7.3 Conclusion

In conclusion, we developed an optical feedback mechanism capable of monitoring the type and characteristics of tissue being cut during laserosteotomy. The feedback mechanism was integrated into an efficient Er:YAG ablation setup and functioned in a closed-loop, real-time manner. In the end, the setup was miniaturized using a custom-made fiber bundle delivery system with high flexibility and bend-insensitive behavior and a tiny lens at the tip. The miniaturized laser delivery system was used in combination with a tailor-made high optical throughput Echelle spectrometer coupled to multivariate spectrochemical analysis, and successfully differentiated tissues.

Appendix I:

We were interested in examining the performance of different machine learning methods (to compare the required training and testing time, and also the accuracy). We performed a few preliminary tests, though the results were never published. Part of the results were presented at a conference (ICBE 2018, abstract on the next pages). Bagged decision trees appeared to provide the best accuracy among the methods examined. However, many other approaches remain unexplored. This is a fascinating topic to engage with as a separate thesis work. Advanced deep learning based on convolutional neural networks (CNN) might perform better than classical approaches.

Publication: Abbasi, Hamed, Georg Rauter, Raphael Guzman, Philippe C. Cattin, and Azhar Zam. (2018, October 5). Toward finding the best machine learning classifier for LIBS-based tissue differentiation. *Book of Abstracts of the First International Conference on Biomedical Engineering (ICBE)*, Marrakech, Morocco. <https://doi.org/10.5281/zenodo.4393614>

ICBE 2018

**Marrakech, Morocco
October 05-06, 2018**

***Book of Abstracts
of the First International Conference on
Biomedical Engineering
ICBE 2018***

***Under the theme
"BIOMEDICAL IMAGING : TECHNIQUES AND
INNOVATIONS"***

**Organized by:
The Moroccan Society for Biomedical Engineering**

TOWARD FINDING THE BEST MACHINE LEARNING CLASSIFIER FOR LIBS-BASED TISSUE DIFFERENTIATION

Hamed Abbasi¹, Georg Rauter², Raphael Guzman³, Philippe C. Cattin⁴, Azhar Zam¹

1 Biomedical Laser and Optics Group, Department of Biomedical Engineering, University of Basel, CH-4123 Allschwil, Switzerland

2 Bio-Inspired RObots for MEDicine-Lab, Department of Biomedical Engineering, University of Basel, CH-4123 Allschwil, Switzerland

3 Department of Neurosurgery, University Hospital Basel, CH-4056 Basel, Switzerland

4 Center for medical Image Analysis and Navigation, Department of Biomedical Engineering, University of Basel, CH-4123 Allschwil, Switzerland

azhar.zam@unibas.ch

Keywords: Laser-induced breakdown spectroscopy; Decision tree; KNN; SVM; Classifier.

Abstract:

Lasers have become generally accepted devices in surgical applications, especially as a cutting tool, for cutting both soft and hard tissues including bone (laserosteotomy). It has been shown that applying lasers in osteotomy have important advantages over mechanical tools, including faster healing, more precise cut and functional cutting geometries as well as less trauma [1, 2]. However, the ability of detecting the type of tissue that being cut during surgery can extend the application and safety of laserosteotomes in practice. As a result, the laser could be stopped automatically in case of cutting a tissue that should be preserved. Authors have previously demonstrated that laser-induced breakdown spectroscopy (LIBS) is a potential candidate to differentiate surrounding soft tissue from the bone in *ex vivo* condition [3]. In the current study, different machine learning classifiers were examined to find the best possible method to differentiate bone from soft tissues based on LIBS data. These methods include decision tree, K Nearest Neighbor (KNN), linear and quadratic Support Vector Machine (SVM) as well as linear and quadratic discriminant analysis. All classifiers were applied on LIBS data obtained from bone, muscle, and fat tissues using an Nd:YAG laser and an Echelle spectrometer. Confusion matrix and Receiver Operating Characteristic (ROC) curve were obtained for each classifier afterwards. Moreover, in order to estimate the model's performance on new data and also to protect the model against overfitting, cross-validation was applied. All mentioned examinations were performed with MATLAB (R2017b).

Acknowledgement: The authors gratefully acknowledge funding of the Werner Siemens Foundation through the Minimally Invasive Robot-Assisted Computer-guided Laserosteotomy (MIRACLE) project.

References:

- [1] D.G. Panduric, I.B. Juric, S. Music, K. Molcanov, M. Susic, I. Anic, Morphological and Ultrastructural Comparative Analysis of Bone Tissue After Er:YAG Laser and Surgical Drill Osteotomy, *Photomedicine and Laser Surgery*, 32, 401 (2014).
- [2] C.-A. Tulea, J. Caron, N. Gehlich, A. Lenenbach, R. Noll, P. Loosen, Laser cutting of bone tissue under bulk water with a pulsed ps-laser at 532 nm, *Journal of Biomedical Optics*, 20, 105007 (2015).
- [3] H. Abbasi, G. Rauter, R. Guzman, P.C. Cattin, A. Zam, Differentiation of femur bone from surrounding soft tissue using laser-induced breakdown spectroscopy as a feedback system for smart laserosteotomy, *Proc. SPIE*, 10685 (2018).

Appendix II:

Previously, we showed that detecting dehydration and carbonization is possible through LIBS. Here, we tried to find a regression model to determine the number of Er:YAG pulses that had been sent to the bone without irrigation. The intention of performing this experiment was to provide a baseline for future work. Such information can further be used as a feedback mechanism for fine-tuning the irrigation system in laserosteotomy (real-time, closed-loop operation). This preliminary result was presented (abstract on the next pages) at the 10th Euro-Mediterranean Symposium on Laser-Induced Breakdown Spectroscopy, 8 – 13th September 2019, Brno, Czech Republic.

Publication: Hamed Abbasi, Georg Rauter, Raphael Guzman, Philippe C. Cattin, & Azhar Zam. (2019, September 8). LIBS for real-time monitoring of laser-induced thermal damage in laserosteotomy: from dehydration to full carbonization. *Book of Abstracts of the 10th Euro-Mediterranean Symposium on Laser-Induced Breakdown Spectroscopy (EMSLIB 2019)*, Brno, Czech Republic. <https://doi.org/10.5281/zenodo.5032264>

LIBS for real-time monitoring of laser-induced thermal damage in laserosteotomy: from dehydration to full carbonization

Hamed Abbasi¹, Georg Rauter², Raphael Guzman³, Philippe C. Cattin⁴, Azhar Zam¹

1. Biomedical Laser and Optics Group (BLOG), Department of Biomedical Engineering, University of Basel, CH-4123 Allschwil, Switzerland
2. Bio-Inspired RObots for MEDicine-Lab (BIROMED-Lab), Department of Biomedical Engineering, University of Basel, CH-4123 Allschwil, Switzerland
3. Department of Neurosurgery, University Hospital Basel, CH-4056 Basel, Switzerland
4. Center for medical Image Analysis and Navigation (CIAN), Department of Biomedical Engineering, University of Basel, CH-4123 Allschwil, Switzerland

E-mail: hamed.abbasi@unibas.ch

Laserosteotomes will only be clinically applied if they do not carbonize the tissue. This can only be ensured with an irrigation system with correctly tuned water and air flow rate. Well-designed irrigation helps avoiding thermal damage, increases ablation speed, and accelerates healing while too little water leads to bone carbonization, and too much water decreases the ablation efficiency [1]. State-of-the-art for determining the irrigation parameters is to apply water and air flow rates based on pre-performed experiments without monitoring the bone surface in real-time. The lack of real-time monitoring of the laser-induced thermal damage can thus result in carbonization, caused by either a malfunction in the irrigation system or by unexpected changes in the properties of the tissues from patient-to-patient (or even point-to-point due to an inhomogeneous structure). Authors recently demonstrated that LIBS can classify fully carbonized bone from not carbonized one [2]. While such a classification can avoid further carbonization, even localized carbonization on the surface of the bone can still prolong the healing process. There are several stages before full carbonization occurs, such as dehydration and early carbonization. The detection of these early signs makes prospective carbonization prediction possible. This study aims at finding a regression between all steps of laser-induced thermal damage. Therefore, the spectrum of localized plasma generated in the ablation spot, together with the number of shots sent to the bone without irrigation was recorded using an in-house fiber-coupled Echelle spectrometer. Later on, based on the recorded spectra, regression models were trained. The model used were regression tree (single tree and also an ensemble of several trees), support vector machine, and a convolutional neural network. Finally, we calculated the root mean square error of each model and applied the trained models to the data collected afterwards in real-time.

References

- [1] H. Abbasi, et al., "Effect of cooling water on ablation in Er:YAG laserosteotome of hard bone", Proc. SPIE 10453 (2017).

- [2] H. Abbasi, et al., "Laser-induced breakdown spectroscopy as a potential tool for autcarbonization detection in laserosteotomy", J. Biomed. Opt. 23 (2018).

Acknowledgement

The authors gratefully acknowledge funding of the Werner Siemens Foundation through the Minimally Invasive Robot-Assisted Computer-guided Laserosteotomy (MIRACLE) project.

List of peer-reviewed publications and presentations on the Ph.D. topic

Journal papers:

1. **H. Abbasi**, R. Guzman, P. C. Cattin, A. Zam, “All-fiber-optic LIBS system for tissue differentiation, a prospect for endoscopic smart laser surgery”, *Optics and Lasers in Engineering (Elsevier)*, Vol. 148, 106765 (2022).
2. **H. Abbasi**, F. Canbaz, R. Guzman, P. C. Cattin, A. Zam, “Highly flexible fiber delivery of high peak power nanosecond Nd:YAG laser beam for flexiscopic applications”, *Biomedical Optics Express (OSA)*, Vol. 12, No. 1 (2021). [Editors' Pick]
3. C. Duverney, **H. Abbasi**, M. Berkelaar, K. Pelttari, P. C. Cattin, A. Barbero, A. Zam, G. Rauter, “Sterile Tissue Ablation Using Laser Light—System Design, Experimental Validation, and Outlook on Clinical Applicability”, *Journal of Medical Devices (Transactions of the ASME)*, Vol. 15, No. 1 (2021).
4. **H. Abbasi**, L. Beltrán, A. Hamidi, A. Droneau, F. Canbaz, R. Guzman, S. Jacques, P. Cattin, A. Zam, “Combined Nd:YAG and Er:YAG lasers for real-time closed-loop tissue-specific laser osteotomy”, *Biomedical Optics Express (OSA)*, Vol. 11, No. 4 (2020).
5. **H. Abbasi**, G. Rauter, R. Guzman, P. C. Cattin, A. Zam, “Laser-induced breakdown spectroscopy as a potential tool for autocarbonization detection in laserosteotomy”, *Journal of Biomedical Optics (SPIE)*, Vol. 23, No. 7, p. 071206 (2018).

Full-length conference proceedings:

6. F. Canbaz, **H. Abbasi**, Y. A. Bayhaqi, P. C. Cattin, A. Zam, “Laser-induced breakdown spectroscopy combined with artificial neural network for pre-carbonization detection in laserosteotomy”, *Accepted to be published in MESROB Conf. book, Springer* (2021). [Best Application Paper Bronze Award]
7. **H. Abbasi**, N. Sahraei, F. Canbaz, P. C. Cattin, A. Zam, “Simulation of Echellogram Using Zemax OpticStudio and Matlab for LIBS”, *MESROB Conf. book, Springer* (2020).
8. C. Duverney, **H. Abbasi**, L. Beltrán, T. Stauber, J. G. Snedeker, P. C. Cattin, A. Zam, G. Rauter, “Robot- and Laser-Assisted Bio-Sample Preparation: Development of an Integrated, Intuitive System”, *MESROB Conf. book, Springer* (2020).
9. **H. Abbasi**, P. C. Cattin, A. Zam, “A Simple Acoustic-Based Method for Lens-to-Sample Distance Adjustment in micro-LIBS”, *in IEEE Photonics North* (2020).
10. **H. Abbasi**, I. Sugiarto, G. Rauter, R. Guzman, P. C. Cattin, A. Zam, “Pilot Ex Vivo Study of Laser-Induced Breakdown Spectroscopy to Detect Bone Dehydration: An Approach for Irrigation Feedback in Laserosteotomy”, *Proc. ICEECS* (2019).

11. **H. Abbasi**, G. Rauter, R. Guzman, P. C. Cattin, A. Zam, “[Differentiation of femur bone from surrounding soft tissue using laser-induced breakdown spectroscopy as a feedback system for tissue-specific laser surgery](#)”, *Proc. SPIE*, Vol. 10685, in *Photonics Europe* (2018).
12. **H. Abbasi**, G. Rauter, R. Guzman, P. C. Cattin, A. Zam, “[Plasma plume expansion dynamics in nanosecond Nd:YAG laserosteotome](#)”, *Proc. SPIE*, Vol. 10505, in *Photonics West: BIOS* (2018).
13. **H. Abbasi**, L. Beltrán, G. Rauter, R. Guzman, P. C. Cattin, A. Zam, “[Effect of cooling water on ablation in Er:YAG laserosteotome of hard bone](#)”, *Proc. SPIE*, Vol. 10453 in *AOP* (2017).
14. L. Beltrán, **H. Abbasi**, G. Rauter, N. Friederich, P. C. Cattin, A. Zam, “[Effect of laser pulse duration on ablation efficiency of hard bone in microseconds regime](#)”, *Proc. SPIE*, Vol. 10453, in *AOP* (2017).
15. **H. Abbasi**, and A. Zam, "Pilot ex vivo study of laser induced breakdown spectroscopy for hard and soft tissue differentiation as a feedback system for tissue-specific laser surgery", *Proc. Biophotonics '17* (2017).

Book chapter:

16. L. Beltrán, **H. Abbasi**, A. Zam, “[Laser in Bone Surgery](#)”, in *Lasers in Oral and Maxillofacial Surgery*, S. Stübinger, F. Klämpfl, M. Schmidt, H.-F. Zeilhofer (Eds.), Springer, (2020). ISBN: 978-3-030-29604-9.

Abstracts:

17. **H. Abbasi**, G. Rauter, R. Guzman, P. C. Cattin, A. Zam, “[LIBS for Real-Time Monitoring of Laser-Induced Thermal Damage in Laserosteotomy: from Dehydration to Full Carbonization](#)”, in *EMSLIBS Book of Abstracts* (2019).
18. **H. Abbasi**, G. Rauter, R. Guzman, P. C. Cattin, A. Zam, “[Toward finding the best machine learning classifier for LIBS-based tissue differentiation](#)” in *ICBE Book of Abstracts* (2018).

Invited Talk:

19. **H. Abbasi**, “[Spectroscopy-Based Optical Feedback for Minimally Invasive Robotic Laser Surgery](#)”, Department of Physics, University of Kashan, Kashan, Iran, 30 December 2019.

Oral Presentations:

20. **H. Abbasi**, P. C. Cattin, A. Zam, “[A Simple Acoustic-Based Method for Lens-to-Sample Distance Adjustment in micro-LIBS](#)”, in *IEEE Photonics North*, Online, 27 May 2020.
21. **H. Abbasi**, R. Guzman, P. C. Cattin, A. Zam, “[Real-time optical feedback for smart laserosteotomy: miniaturization and closed-loop operation](#)”, in *6th DBE Research Day*, Zentrum für Lehre und Forschung, Basel, Switzerland, 8 September 2020.

22. **H. Abbasi**, A. Zam, "[Optical Feedback Mechanism for Minimally Invasive Laserosteotome](#)", in *Yearly meeting of the Biomedical Photonics Network (BMPN), Progress in Biomedical Photonics*, University of Bern, Switzerland, 10 December 2019.
23. **H. Abbasi**, G. Rauter, R. Guzman, P. C. Cattin, A. Zam, "[Design and Implementation of a Compact High-Throughput Echelle Spectrometer Using Off-the-Shelf Off-Axis Parabolic Mirrors for Analysis of Biological Samples by LIBS](#)", in *SPIE Optical Metrology*, Munich, Germany, 24-27 June 2019.
24. **H. Abbasi**, G. Rauter, R. Guzman, P. C. Cattin, A. Zam, "[All Fiber-Based LIBS Feedback System for Endoscopic Laser Surgery](#)", in *41st Colloquium Spectroscopicum Internationale (CSI-XLI)*, Mexico City, Mexico, 09 - 14 June 2019.
25. **H. Abbasi**, G. Rauter, R. Guzman, P. C. Cattin, A. Zam, "Spectroscopic Feedback System for Smart Laser Osteotome", in *Eucor-GRACE Crossborder Networking Event, La Bresse, France*, 29-30 April 2019.
26. **H. Abbasi**, H. Nguendon, G. Rauter, R. Guzman, P. C. Cattin, and A. Zam, "[Feedback System for a Laserosteotome: Optical and Acoustical Approaches](#)" in *4th DBE Research Day*, Zentrum für Lehre und Forschung, Basel, Switzerland, 05 September 2018.
27. **H. Abbasi**, G. Rauter, R. Guzman, P. C. Cattin, and A. Zam, "Optical Feedback System for Smart Laserosteotome: Main Challenges" in *3rd DBE Summer School (More than just surgery: laser, robots, intuitive navigation, and smart implant technologies)*, Zschokke-Haus, Engelberg, Switzerland, 03 - 08 June 2018.
28. **H. Abbasi**, G. Rauter, R. Guzman, P. C. Cattin, A. Zam, "[Differentiation of femur bone from surrounding soft tissue using laser-induced breakdown spectroscopy as a feedback system for tissue-specific laser surgery](#)", in *Photonics Europe*, Strasbourg, France 25 April 2018.
29. **H. Abbasi** and A. Zam, "Optical Feedback System for Smart Laserosteotome", in *MIRACLE Retreat*, Zschokke-Haus, Engelberg, Switzerland, 09-11 December 2017.
30. **H. Abbasi** and A. Zam, "[Laser-induced breakdown spectroscopy as a potential tool for auto carbonization detection in laserosteotome](#)" in *3rd DBE Research Day*, Zentrum für Lehre und Forschung, Basel, Switzerland, 23 August 2017 (speed pitch).
31. **H. Abbasi**, L. Beltrán, G. Rauter, R. Guzman, P. C. Cattin, A. Zam, "[Effect of cooling water on ablation in Er:YAG laserosteotome of hard bone](#)", in *Third International Conference on Applications of Optics and Photonics (AOP)*, Faro, Portugal, 10 May 2017.

Poster Presentations:

32. **H. Abbasi**, G. Rauter, R. Guzman, P. C. Cattin, A. Zam, "[LIBS for Real-Time Monitoring of Laser-Induced Thermal Damage in Laserosteotomy: from Dehydration to Full Carbonization](#)", in *10th Euro-Mediterranean Symposium on Laser-Induced Breakdown Spectroscopy (EMSLIBS)*, Brno, Czech Republic, 08-13 September 2019.

33. **H. Abbasi**, G. Rauter, R. Guzman, P. C. Cattin, A. Zam, "LIBS for Smart Laserosteotomy", in *5th DBE Research Day*, Zentrum für Lehre und Forschung, Basel, Switzerland, 28 August 2019.
34. **H. Abbasi**, G. Rauter, R. Guzman, P. C. Cattin, A. Zam, "Laser-Induced Breakdown Spectroscopy for Smart Laserosteotomy", in *Eucor-GRACE Crossborder Networking Event*, La Bresse, France, 29-30 April 2019.
35. **H. Abbasi**, G. Rauter, R. Guzman, P. C. Cattin, and A. Zam, "Laser-induced breakdown spectroscopy for smart laserosteotomy" in *4th DBE Research Day*, Zentrum für Lehre und Forschung, Basel, Switzerland, 05 September 2018.
36. **H. Abbasi**, G. Rauter, R. Guzman, P. C. Cattin, and A. Zam, "Laser-induced breakdown spectroscopy for smart laserosteotomy" in *3rd DBE Summer School (More than just surgery: laser, robots, intuitive navigation, and smart implant technologies)*, Zschokke-Haus, Engelberg, Switzerland, 03 - 08 June 2018.
37. **H. Abbasi**, and A. Zam, "[LIBS for Smart Laserosteotomy](#)" in *International Conference on BioMedical Photonics*, Montpellier, France, 16 - 17 March 2018.
38. **H. Abbasi** and A. Zam, "Pilot ex vivo study of laser-induced breakdown spectroscopy for hard and soft tissue differentiation as a feedback system for tissue-specific laser surgery" in *3rd DBE Research Day*, Zentrum für Lehre und Forschung, Basel, Switzerland, 23 August 2017.
39. **H. Abbasi**, and A. Zam, "[Pilot ex vivo study of laser induced breakdown spectroscopy for hard and soft tissue differentiation as a feedback system for tissue-specific laser surgery](#)" in *8th International Graduate Summer School on Biophotonics*, Ven, Sweden, 10-17 June 2017.

Curriculum Vitae

Personal Data and Contact Information:

- ❖ **Name:** Hamed Abbasi
- ❖ **Date of Birth:** 26 June 1989
- ❖ **Languages:** English (Fluent), Persian (Native), German (Basic), Arabic (Basic)
- ❖ **Address:** Gewerbestr. 14 (DBE), 4123 Allschwil, Switzerland (office)
- ❖ **Email:** hamed.abbasi@unibas.ch ; hamedabbasi@gmail.com
- ❖ **Phone:** +41 61 207 54 67 (office)



CV update: Dec. 2020

Research Interests/skills:

- ❖ Optical Sensing/Metrology (Instrumentation/Application), Spectrometer Engineering (Echelle, Grating/Prism-Based), Analytical Spectroscopy (LIBS, Raman, Fluorescence), Laser Ablation, Hyperspectral Imaging, Bio-photonics, Laser Surgery, Laser Diagnostic, Material Identification, Spectra Treatment, Plasma Characterization, Tunable Lasers, Machine Learning, Data Analysis.

Education:

- ❖ **Ph.D., Biomedical Engineering** (Sep. 2016 – Dec. 2020)
Biomedical Laser and Optics Group, Dept. of Biomedical Engineering, University of Basel, Switzerland
(<http://www.blog.dbe.unibas.ch>)
Doctoral Dissertation: Optical Feedback System for Smart Laserosteotome (**Magna Cum laude**)
part of MIRACLE Project (Minimally Invasive Robot-Assisted Computer-guided Laserosteotome)
(<http://www.miracle.dbe.unibas.ch>)
Supervisors: Prof. Azhar Zam, Prof. Philippe C. Cattin, Prof. Raphael Guzman
Courses/Training: Principles of Medical Imaging, Advanced Laser & Optics in Medicine, Materials & Technologies in Dentistry, Medical Terminology: Basics in Human Medicine, Rapid Prototyping (for measurement, automation, control, artificial intelligence, and virtual reality), Nanoscience for Human Health, Optical Coherence Tomography in Medicine (ETH), Laser Safety, Project Management, Patenting & Spin-Off, Entrepreneurship.
- ❖ **M. Sc., Photonics** (Sep. 2012- Sep. 2014)
Dept. of Photonics, Faculty of Physics, University of Kashan, Kashan, Iran
Master Thesis: Design and Development of a Laser-Induced Fluorescence Spectroscopy System for Non-Destructive Quality Assessment of Agricultural Products (**Grade 19.71/20**)
Courses: Theory & Technology of Making Optical Elements, Advanced Laser Physics, Advanced Quantum Mechanics, Electrodynamics, Optical Electronics, Laser Spectroscopy.
- ❖ **B. Sc., Engineering Physics, Laser and Optics** (Sep. 2007- Sep. 2012)
Plasma Physics Research Center (PPRC), Science and Research Branch, Azad University, Tehran, Iran
Bachelor Project: Synthesizing of Gold and Silver Nanoparticles by Laser Ablation: Characterizing and Studying Its Novel Applications in Recent Years (**Grade 20/20**)

Bibliography

1. F. Ramirez Rozzi and A. Froment, "Earliest Animal Cranial Surgery: from Cow to Man in the Neolithic," *Scientific Reports* **8**, 5536 (2018).
2. R. J. Wallace, "A comparison of past, present and future bone surgery tools," *International Journal of Orthopaedics* **2**, 266-269 (2015).
3. M. Pantawane and N. Dahotre, "Challenges and advances in osteotomy," *Ann Bone Joint Surg.* 2019; 2 (1) **1007**(2019).
4. G. D. Rajitha Gunaratne, R. Khan, D. Fick, B. Robertson, N. Dahotre, and C. Ironside, "A review of the physiological and histological effects of laser osteotomy," *Journal of Medical Engineering & Technology* **41**, 1-12 (2017).
5. L. M. B. Bernal, H. Abbasi, and A. Zam, "Laser in Bone Surgery," in *Lasers in Oral and Maxillofacial Surgery*, S. Stübinger, F. Klämpfl, M. Schmidt, and H. Zeilhofer, eds. (Springer, 2020), pp. 99-109.
6. S. Stübinger, "Advances in bone surgery: the Er: YAG laser in oral surgery and implant dentistry," *Clinical, Cosmetic and Investigational Dentistry* **2**, 47 (2010).
7. D. G. Panduric, I. B. Juric, S. Music, K. Molčanov, M. Sušić, and I. Anić, "Morphological and ultrastructural comparative analysis of bone tissue after Er: YAG laser and surgical drill osteotomy," *Photomedicine and laser surgery* **32**, 401-408 (2014).
8. M. Augello, C. Baetscher, M. Segesser, H.-F. Zeilhofer, P. Cattin, and P. Juergens, "Performing partial mandibular resection, fibula free flap reconstruction and midfacial osteotomies with a cold ablation and robot-guided Er:YAG laser osteotome (CARLO®) – A study on applicability and effectiveness in human cadavers," *Journal of Cranio-Maxillofacial Surgery* **46**, 1850-1855 (2018).
9. B.-I. Berg, M. Peyer, L. Kuske, M. Augello, A. Schötzau, M. Steineck, W. Deibel, D. Mathys, P. Jürgens, C. Kunz, and D. Goldblum, "Comparison of an Er: YAG laser osteotome versus a conventional drill for the use in osteo- odonto-keratoprosthesis (OOKP)," *Lasers in Surgery and Medicine* **51**, 531-537 (2019).
10. Y. Ohsugi, A. Aoki, K. Mizutani, S. Katagiri, M. Komaki, M. Noda, T. Takagi, S. Kakizaki, W. Meinzer, and Y. Izumi, "Evaluation of bone healing following Er:YAG laser ablation in rat calvaria compared with bur drilling," *Journal of Biophotonics* **12**, e201800245 (2019).
11. J. Zeitouni, B. Clough, S. Zeitouni, M. Saleem, K. Al Aisami, and C. Gregory, "The effects of the Er: YAG laser on trabecular bone micro-architecture: Comparison with conventional dental drilling by micro-computed tomographic and histological techniques," *F1000Research* **6**(2017).
12. D. G. Pandurić, I. Bago, D. Katanec, J. Žabkar, I. Miletić, and I. Anić, "Comparison of Er:YAG Laser and Surgical Drill for Osteotomy in Oral Surgery: An Experimental Study," *Journal of Oral and Maxillofacial Surgery* **70**, 2515-2521 (2012).
13. B. Girard, K. Franjic, M. Cloutier, D. Wilson, C. Clokie, B. Wilson, and R. J. D. Miller, *Bone surgery with femtosecond laser compared to mechanical instruments: healing studies*, High-Power Laser Ablation 2006 (SPIE, 2006), Vol. 6261.
14. K.-w. Baek, M. Dard, H.-F. Zeilhofer, P. C. Cattin, and P. Juergens, "Comparing the Bone Healing After Cold Ablation Robot-Guided Er:YAG Laser Osteotomy and Piezoelectric Osteotomy—A Pilot Study in a Minipig Mandible," *Lasers in Surgery and Medicine* (2020).
15. K.-w. Baek, W. Deibel, D. Marinov, M. Griessen, M. Dard, A. Bruno, H.-F. Zeilhofer, P. Cattin, and P. Juergens, "A comparative investigation of bone surface after cutting with mechanical tools and Er:YAG laser," *Lasers in Surgery and Medicine* **47**, 426-432 (2015).
16. K. W. Baek, M. Dard, W. Deibel, D. Marinov, M. Griessen, P. Cattin, H. F. Zeilhofer, and P. Juergens, "Clinical applicability of robot guided contact-free laser osteotomy—a comparative study in minipigs," *International Journal of Oral and Maxillofacial Surgery* **42**, 1301 (2013).

17. M. Augello, W. Deibel, K. Nuss, P. Cattin, and P. Jürgens, "Comparative microstructural analysis of bone osteotomies after cutting by computer-assisted robot-guided laser osteotome and piezoelectric osteotome: an in vivo animal study," *Lasers in Medical Science* **33**, 1471-1478 (2018).
18. S. Stübinger, K. Nuss, M. Pongratz, J. Price, R. Sader, H.-F. Zeilhofer, and B. von Rechenberg, "Comparison of Er:YAG laser and piezoelectric osteotomy: An animal study in sheep," *Lasers in Surgery and Medicine* **42**, 743-751 (2010).
19. F. Canbaz, H. Abbasi, Y. Bayhaqi, P. Cattin, and A. Zam, "Laser-induced breakdown spectroscopy combined with artificial neural network for pre-carbonization detection in laserosteotomy," in *New Trends in Medical and Service Robotics* (Springer International Publishing, 2021).
20. R. Kanawade, F. Mehari, C. Knipfer, M. Rohde, K. Tangermann-Gerk, M. Schmidt, and F. Stelzle, "Pilot study of laser induced breakdown spectroscopy for tissue differentiation by monitoring the plume created during laser surgery — An approach on a feedback Laser control mechanism," *Spectrochimica Acta Part B: Atomic Spectroscopy* **87**, 175-181 (2013).
21. F. Mehari, M. Rohde, C. Knipfer, R. Kanawade, F. Klämpfl, W. Adler, F. Stelzle, and M. Schmidt, "Laser induced breakdown spectroscopy for bone and cartilage differentiation-ex vivo study as a prospect for a laser surgery feedback mechanism," *Biomedical optics express* **5**, 4013-4023 (2014).
22. R. Kanawade, F. Mahari, F. Klämpfl, M. Rohde, C. Knipfer, K. Tangermann-Gerk, W. Adler, M. Schmidt, and F. Stelzle, "Qualitative tissue differentiation by analysing the intensity ratios of atomic emission lines using laser induced breakdown spectroscopy (LIBS): prospects for a feedback mechanism for surgical laser systems," *Journal of Biophotonics* **8**, 153-161 (2015).
23. H. Huang, L.-M. Yang, S. Bai, and J. Liu, "Smart surgical tool," *Journal of Biomedical Optics* **20**, 028001 (2015).
24. F. Mehari, M. Rohde, R. Kanawade, C. Knipfer, W. Adler, F. Klämpfl, F. Stelzle, and M. Schmidt, "Investigation of the differentiation of ex vivo nerve and fat tissues using laser-induced breakdown spectroscopy (LIBS): Prospects for tissue-specific laser surgery," *Journal of Biophotonics* **9**, 1021-1032 (2016).
25. M. Rohde, F. Mehari, F. Klämpfl, W. Adler, F.-W. Neukam, M. Schmidt, and F. Stelzle, "The differentiation of oral soft- and hard tissues using laser induced breakdown spectroscopy – a prospect for tissue specific laser surgery," *Journal of Biophotonics* **10**, 1250-1261 (2017).
26. X. Li, S. Yang, R. Fan, X. Yu, and D. Chen, "Discrimination of soft tissues using laser-induced breakdown spectroscopy in combination with k nearest neighbors (kNN) and support vector machine (SVM) classifiers," *Optics & Laser Technology* **102**, 233-239 (2018).
27. R. Gunaratne, I. Monteath, J. Goncalves, R. Sheh, C. N. Ironside, M. Kapfer, R. Chipper, B. Robertson, R. Khan, and D. Fick, "Machine learning classification of human joint tissue from diffuse reflectance spectroscopy data," *Biomedical optics express* **10**, 3889-3898 (2019).
28. F. Stelzle, W. Adler, A. Zam, K. Tangermann-Gerk, C. Knipfer, A. Douplik, M. Schmidt, and E. Nkenke, "In Vivo Optical Tissue Differentiation by Diffuse Reflectance Spectroscopy:Preliminary Results for Tissue-Specific Laser Surgery," *Surgical Innovation* **19**, 385-393 (2012).
29. F. Stelzle, A. Zam, W. Adler, K. Tangermann-Gerk, A. Douplik, E. Nkenke, and M. Schmidt, "Optical Nerve Detection by Diffuse Reflectance Spectroscopy for Feedback Controlled Oral and Maxillofacial Laser Surgery," *Journal of Translational Medicine* **9**, 20 (2011).
30. E. J. M. Baltussen, S. G. Brouwer de Koning, J. Sanders, A. G. J. Aalbers, N. F. M. Kok, G. L. Beets, B. H. W. Hendriks, H. J. C. M. Sterenborg, K. F. D. Kuhlmann, and T. J. M. Ruers, "Using Diffuse Reflectance Spectroscopy to Distinguish Tumor Tissue From Fibrosis in Rectal Cancer Patients as a Guide to Surgery," *Lasers in Surgery and Medicine* **52**, 604-611 (2020).
31. E. J. M. Baltussen, S. G. Brouwer de Koning, J. Sanders, A. G. J. Aalbers, N. F. M. Kok, G. L. Beets, B. H. W. Hendriks, H. J. C. M. Sterenborg, K. F. D. Kuhlmann, and T. J. M. Ruers, "Tissue diagnosis during colorectal cancer surgery using optical sensing: an in vivo study," *Journal of Translational Medicine* **17**, 333 (2019).

32. L. Kreiß, M. Hohmann, F. Klämpfl, S. Schürmann, F. Dehghani, M. Schmidt, O. Friedrich, and L. Büchler, "Diffuse reflectance spectroscopy and Raman spectroscopy for label-free molecular characterization and automated detection of human cartilage and subchondral bone," *Sensors and Actuators B: Chemical* **301**, 127121 (2019).
33. L. A. Reisner, B. W. King, M. D. Klein, G. W. Auner, and A. K. Pandya, "A prototype biosensor-integrated image-guided surgery system," *The International Journal of Medical Robotics and Computer Assisted Surgery* **3**, 82-88 (2007).
34. P. C. Ashok, N. Krstajić, M. E. Giardini, K. Dholakia, and W. Sibbett, "Raman Spectroscopy Sensor for Surgical Robotics—Instrumentation and Tissue Differentiation Algorithm," in *Digital Holography and Three-Dimensional Imaging*, (Optical Society of America, 2012), JM3A. 26.
35. P. C. Ashok, M. E. Giardini, K. Dholakia, and W. Sibbett, "A Raman spectroscopy bio-sensor for tissue discrimination in surgical robotics," *Journal of Biophotonics* **7**, 103-109 (2014).
36. T. Minamikawa, Y. Harada, and T. Takamatsu, *Raman spectroscopic detection of peripheral nerves towards nerve-sparing surgery*, SPIE BiOS (SPIE, 2017), Vol. 10054.
37. A. Zam, "Optical Tissue Differentiation for Sensor-Controlled Tissue-Specific Laser Surgery," (2011).
38. F. Stelzle, C. Knipfer, W. Adler, M. Rohde, N. Oetter, E. Nkenke, M. Schmidt, and K. Tangermann-Gerk, "Tissue discrimination by uncorrected autofluorescence spectra: a proof-of-principle study for tissue-specific laser surgery," *Sensors* **13**, 13717-13731 (2013).
39. Y. A. Bayhaqi, G. Rauter, A. Navarini, P. C. Cattin, and A. Zam, *Fast optical coherence tomography image enhancement using deep learning for smart laser surgery: preliminary study in bone tissue*, IV International Conference on Applications of Optics and Photonics (AOP 2019) (SPIE, 2019), Vol. 11207.
40. Y. Bayhaqi, A. Navarini, G. Rauter, P. Cattin, and A. Zam, *Neural network in tissue characterization of Optical Coherence Tomography (OCT) image for smart laser surgery: preliminary study*, Third International Seminar on Photonics, Optics, and Its Applications (ISPhOA 2018) (SPIE, 2019), Vol. 11044.
41. B. Lengenfelder, K. Schwarzkopf, N. Oetter, F. Mehari, E. Eschner, F. Klämpfl, F. Stelzle, M. Kesting, Z. Zalevsky, and M. Schmidt, "Acoustic differentiation of dental soft-and hard tissues using remote speckle-analysis during Er: YAG ablation," in *European Conference on Biomedical Optics*, (Optical Society of America, 2019), 11077_11057.
42. B. Lengenfelder, F. Mehari, M. Hohmann, M. Heinlein, E. Chelales, M. J. Waldner, F. Klämpfl, Z. Zalevsky, and M. Schmidt, "Remote photoacoustic sensing using speckle-analysis," *Scientific Reports* **9**, 1057 (2019).
43. B. Lengenfelder, F. Mehari, M. Hohmann, C. Löhr, M. J. Waldner, M. Schmidt, Z. Zalevsky, and F. Klämpfl, "Contact-free endoscopic photoacoustic sensing using speckle analysis," *Journal of Biophotonics* **12**, e201900130 (2019).
44. H. N. Kenhagho, F. Canbaz, G. Rauter, R. Guzman, P. Cattin, and A. Zam, "A First Approach to Miniaturized Optoacoustic Feedback Sensor for Smart Laser Osteotome : Fiber-Coupled Fabry-Pérot Etalon Sensor," in *2019 IEEE SENSORS*, (2019), 1-4.
45. H. N. Kenhagho, G. Rauter, R. Guzman, P. C. Cattin, and A. Zam, "Optoacoustic Tissue Differentiation Using a Mach-Zehnder Interferometer," *IEEE Transactions on Ultrasonics, Ferroelectrics, and Frequency Control* **66**, 1435-1443 (2019).
46. S. Rupprecht, K. Tangermann, P. Kessler, F. W. Neukam, and J. Wiltfang, "Er:YAG laser osteotomy directed by sensor controlled systems," *Journal of Cranio-Maxillofacial Surgery* **31**, 337-342 (2003).
47. S. Rupprecht, K. Tangermann-Gerk, J. Wiltfang, F. W. Neukam, and A. Schlegel, "Sensor-based laser ablation for tissue specific cutting: an experimental study," *Lasers in Medical Science* **19**, 81-88 (2004).

48. K. Tangermann, S. Roth, D. Muller, H. Tragler, J. Uller, and S. Rupprecht, *Sensor-controlled laser processes for medical applications*, Laser Florence 2002: A Window on the Laser Medicine World (SPIE, 2003), Vol. 5287.
49. M. Hohmann, D. Dörner, F. Mehari, C. Chen, M. Späth, S. Müller, H. Albrecht, F. Klämpfl, and M. Schmidt, "Investigation of random lasing as a feedback mechanism for tissue differentiation during laser surgery," *Biomedical optics express* **10**, 807-816 (2019).
50. H. Abbasi, G. Rauter, R. Guzman, P. Cattin, and A. Zam, *Plasma plume expansion dynamics in nanosecond Nd:YAG laserosteotome*, SPIE BiOS (SPIE, 2018), Vol. 10505.
51. H. Abbasi, G. Rauter, R. Guzman, P. Cattin, and A. Zam, *Differentiation of femur bone from surrounding soft tissue using laser-induced breakdown spectroscopy as a feedback system for smart laserosteotomy*, SPIE Photonics Europe (SPIE, 2018), Vol. 10685.
52. H. Abbasi, L. Beltrán, G. Rauter, R. Guzman, P. Cattin, and A. Zam, *Effect of cooling water on ablation in Er:YAG laserosteotome of hard bone*, Third International Conference on Applications of Optics and Photonics (SPIE, 2017), Vol. 10453.
53. H. Abbasi, G. Rauter, R. Guzman, P. Cattin, and A. Zam, "Laser-induced breakdown spectroscopy as a potential tool for autocarbonization detection in laserosteotomy," *Journal of Biomedical Optics* **23**, 071206 (2018).
54. H. Abbasi, I. Sugiarto, G. Rauter, R. Guzman, P. Cattin, and A. Zam, "Pilot Ex Vivo Study of Laser-Induced Breakdown Spectroscopy to Detect Bone Dehydration: An Approach for Irrigation Feedback in Laserosteotomy," in *ICEECS*, 2018).
55. H. Abbasi, L. M. Beltrán Bernal, A. Hamidi, A. Droneau, F. Canbaz, R. Guzman, S. L. Jacques, P. C. Cattin, and A. Zam, "Combined Nd:YAG and Er:YAG lasers for real-time closed-loop tissue-specific laser osteotomy," *Biomedical Optics Express* **11**, 1790-1807 (2020).
56. H. Abbasi, P. C. Cattin, and A. Zam, "A Simple Acoustic-Based Method for Lens-to-Sample Distance Adjustment in μ LIBS," in *Photonics North*, (IEEE, 2020).
57. H. Abbasi, R. Guzman, P. C. Cattin, and A. Zam, "All-fiber-optic LIBS system for tissue differentiation: A prospect for endoscopic smart laser osteotomy," *Optics and Lasers in Engineering* **148**, 106765 (2022).
58. H. Abbasi, F. Canbaz, R. Guzman, P. C. Cattin, and A. Zam, "Highly flexible fiber delivery of a high peak power nanosecond Nd:YAG laser beam for flexiscopic applications," *Biomedical Optics Express* **12**, 444-461 (2021).
59. H. Abbasi, N. Sahraei, F. Canbaz, P. C. Cattin, and A. Zam, "Simulation of Echellogram Using Zemax OpticStudio and Matlab for LIBS," in *New Trends in Medical and Service Robotics* (Springer International Publishing, 2021), 211-218.
60. X. Feng, "Chemical and Biochemical Basis of Cell-Bone Matrix Interaction in Health and Disease," *Curr Chem Biol* **3**, 189-196 (2009).
61. M. Forrer, M. Frenz, V. Romano, H. J. Altermatt, H. P. Weber, A. Silenok, M. Istomyn, and V. I. Konov, "Bone-ablation mechanism using CO₂ lasers of different pulse duration and wavelength," *Applied Physics B* **56**, 104-112 (1993).
62. N. B. Dahotre and S. Joshi, *Machining of bone and hard tissues* (Springer, 2016).
63. K. R. Senior, *Bone and Muscle: Structure, Force, and Motion* (The Rosen Publishing Group, Inc, 2010).
64. A. B. Matos, C. S. de Azevedo, P. A. da Ana, S. B. Botta, and D. M. Zezell, "Laser technology for caries removal," *Contemporary Approach to Dental Caries* **1**(2012).
65. Y. Sotsuka, S. Nishimoto, T. Tsumano, K. Kawai, H. Ishise, M. Kakibuchi, R. Shimokita, T. Yamauchi, and S.-i. Okihara, "The dawn of computer-assisted robotic osteotomy with ytterbium-doped fiber laser," *Lasers in Medical Science* **29**, 1125-1129 (2014).
66. N. Jowett, W. Wöllmer, R. Reimer, J. Zustin, U. Schumacher, P. W. Wiseman, A. M. Mlynarek, A. Böttcher, C. V. Dalchow, and B. B. Lörincz, "Bone ablation without thermal or acoustic mechanical

- injury via a novel picosecond infrared laser (PIRL)," *Otolaryngology–head and neck surgery* **150**, 385-393 (2014).
67. J. Y. Giraud, S. Villemin, R. Darmana, J. P. Cahuzac, A. Autefage, and J. P. Morucci, "Bone cutting," *Clinical Physics and Physiological Measurement* **12**, 1-19 (1991).
 68. K. Schwieger, V. Carrero, R. Rentzsch, A. Becker, N. Bishop, E. Hille, H. Louis, M. Morlock, and M. Honl, "Abrasive water jet cutting as a new procedure for cutting cancellous bone—In vitro testing in comparison with the oscillating saw," *Journal of Biomedical Materials Research Part B: Applied Biomaterials* **71B**, 223-228 (2004).
 69. G. Rauter, "19 The MIRACLE," *Lasers in Oral and Maxillofacial Surgery*, 247 (2020).
 70. A. Einstein, "Zur quantentheorie der strahlung," *Phys. Z.* **18**, 124 (1917).
 71. T. H. Maiman, "Stimulated Optical Radiation in Ruby," *Nature* **187**, 493-494 (1960).
 72. M. M. Zaret, G. M. Breinin, H. Schmidt, H. Ripps, I. M. Siegel, and L. R. Solon, "Ocular Lesions Produced by an Optical Maser (Laser)," *Science* **134**, 1525-1526 (1961).
 73. A. Zam, "Laser–Tissue Interaction," in *Lasers in Oral and Maxillofacial Surgery*, S. Stübinger, F. Klämpfl, M. Schmidt, and H.-F. Zeilhofer, eds. (Springer International Publishing, Cham, 2020), pp. 25-34.
 74. A. Vogel and V. Venugopalan, "Mechanisms of Pulsed Laser Ablation of Biological Tissues," *Chemical Reviews* **103**, 577-644 (2003).
 75. C. Duverney, H. Abbasi, M. Berkelaar, K. Pelttari, P. C. Cattin, A. Barbero, A. Zam, and G. Rauter, "Sterile Tissue Ablation Using Laser Light—System Design, Experimental Validation, and Outlook on Clinical Applicability," *Journal of Medical Devices* **15**(2021).
 76. A. Vogel, "Nonlinear absorption: intraocular microsurgery and laser lithotripsy," *Physics in Medicine and Biology* **42**, 895-912 (1997).
 77. J.-L. Boulnois, "Photophysical processes in recent medical laser developments: a review," *Lasers in medical science* **1**, 47-66 (1986).
 78. V. Tuchin, "Tissue optics and photonics: Light-tissue interaction II," *Journal of Biomedical Photonics and Engineering* **2**, 030201 (2016).
 79. M. H. Niemz, "Matter Acting on Light," in *Laser-Tissue Interactions: Fundamentals and Applications* (Springer International Publishing, Cham, 2019), pp. 9-44.
 80. S. L. Jacques, "Laser-tissue interactions. Photochemical, photothermal, and photomechanical," *Surg Clin North Am* **72**, 531-558 (1992).
 81. A. Vogel, S. Busch, K. Jungnickel, and R. Birngruber, "Mechanisms of intraocular photodisruption with picosecond and nanosecond laser pulses," *Lasers in Surgery and Medicine* **15**, 32-43 (1994).
 82. A. Vogel, W. Lauterborn, and R. Timm, "Optical and acoustic investigations of the dynamics of laser-produced cavitation bubbles near a solid boundary," *Journal of Fluid Mechanics* **206**, 299-338 (1989).
 83. R. Esenaliev, A. Oraevsky, S. Jacques, and F. Tittel, *Effect of tensile stress amplitude and temporal characteristics on threshold of cavitation-driven ablation*, Photonics West '96 (SPIE, 1996), Vol. 2681.
 84. S. Jacques, *How tissue optics affect dosimetry for photochemical, photothermal, and photomechanical mechanisms of laser-tissue interaction*, Recent Advances in the Uses of Light in Physics, Chemistry, Engineering, and Medicine (SPIE, 1992), Vol. 1599.
 85. L. Beltrán, H. Abbasi, G. Rauter, N. Friederich, P. Cattin, and A. Zam, *Effect of laser pulse duration on ablation efficiency of hard bone in microseconds regime*, Third International Conference on Applications of Optics and Photonics (SPIE, 2017), Vol. 10453.
 86. A. Gholami, M. Baradaran-Ghahfarokhi, M. Ebrahimi, and M. Baradaran-Ghahfarokhi, "Thermal effects of laser-osteotomy on bone: mathematical computation using maple," *Journal of medical signals and sensors* **3**, 262 (2013).

87. C. Plötz, F. Schelle, C. Bourauel, M. Frentzen, and J. Meister, "Ablation of porcine bone tissue with an ultrashort pulsed laser (USPL) system," *Lasers in Medical Science* **30**, 977-983 (2015).
88. H. Petersen, A. Gliese, Y. Stober, S. Maier, N.-O. Hansen, S. Kruber, D. Eggert, M. Tóth, T. Gosau, and H. Schlüter, "Picosecond Infrared Laser (PIRL) Application in Stapes Surgery—First Experience in Human Temporal Bones," *Otology & Neurotology* **39**, e224 (2018).
89. F. Aljekhedab, W. Zhang, H. K. Haugen, G. R. Wohl, M. M. El-Desouki, and Q. Fang, "Influence of environmental conditions in bovine bone ablation by ultrafast laser," *Journal of Biophotonics* **12**, e201800293 (2019).
90. S. A. Ashforth, R. N. Oosterbeek, O. L. Bodley, C. Mohr, C. Agueraray, and M. C. Simpson, "Femtosecond lasers for high-precision orthopedic surgery," *Lasers in Medical Science*, 1-8 (2019).
91. N. Fried and D. Fried, *Laser ablation of skull tissue using transverse excited 9.6-um CO2 lasers with pulse durations of 1-100 us*, BiOS 2000 The International Symposium on Biomedical Optics (SPIE, 2000), Vol. 3914.
92. L. Beltrán Bernal, G. Shayeganrad, G. Kosa, M. Zelechowski, G. Rauter, N. Friederich, P. Cattin, and A. Zam, *Performance of Er:YAG laser ablation of hard bone under different irrigation water cooling conditions*, SPIE BiOS (SPIE, 2018), Vol. 10492.
93. L. M. B. Bernal, I. T. Schmidt, N. Vulin, J. Widmer, J. G. Snedeker, P. C. Cattin, A. Zam, and G. Rauter, "Optimizing controlled laser cutting of hard tissue (bone)," *at - Automatisierungstechnik* **66**, 1072 (2018).
94. I.-M. Rizoiu and G. Levy, *Efficiency of bone ablation with a Nd:Yag laser beam delivered with a cooling spray: an in-vitro study*, OE/LASE'93: Optics, Electro-Optics, and Laser Applications in Science and Engineering (SPIE, 1993), Vol. 1882.
95. L. Kuscer and J. Diaci, "Measurements of erbium laser-ablation efficiency in hard dental tissues under different water cooling conditions," *Journal of Biomedical Optics* **18**, 108002 (2013).
96. K. Hyun Wook, L. Ho, C. Shaochen, and A. J. Welch, "Enhancement of bovine bone ablation assisted by a transparent liquid layer on a target surface," *IEEE Journal of Quantum Electronics* **42**, 633-642 (2006).
97. Y.-M. Lee, R. Y. Tu, A. Chiang, and Y.-C. Huang, "Average-power mediated ultrafast laser osteotomy using a mode-locked Nd:YVO₄ laser oscillator," *Journal of Biomedical Optics* **12**, 060505 (2007).
98. M. Strassl, V. Wiegner, D. Brodoceanu, F. Beer, A. Moritz, and E. Wintner, *Ultra-short pulse laser ablation of biological hard tissue and biocompatibles* (na, 2008).
99. C. Tulea, J. Caron, H. Wahab, N. Gehlich, M. Hofer, D. Esser, B. Jungbluth, A. Lenenbach, and R. Noll, *Highly efficient nonthermal ablation of bone under bulk water with a frequency-doubled Nd:YVO₄ picosecond laser*, SPIE BiOS (SPIE, 2013), Vol. 8565.
100. C.-A. Tulea, J. Caron, N. Gehlich, A. Lenenbach, R. Noll, and P. Loosen, "Laser cutting of bone tissue under bulk water with a pulsed ps-laser at 532 nm," *Journal of Biomedical Optics* **20**, 105007 (2015).
101. J. Jivraj, C. Chen, Y. Huang, J. Ramjani, Y. Lu, B. Vuong, X. Gu, and V. X. Yang, "Smart laser osteotomy: integrating a pulsed 1064nm fiber laser into the sample arm of a fiber optic 1310nm OCT system for ablation monitoring," *Biomedical optics express* **9**, 6374-6387 (2018).
102. J. Jivraj, C. Chen, D. Barrows, X. Gu, and V. X. D. Yang, "Optimization of laser osteotomy at 1064 nm using a graphite topical absorber and a nitrogen assist gas jet," *Biomedical Optics Express* **10**, 3114-3123 (2019).
103. B. Emigh, J. Hayward, R. An, E. Hsu, T. Crawford, H. Haugen, G. Wohl, and Q. Fang, "Porcine cortical bone ablation by ultrashort pulsed laser irradiation," *Journal of Biomedical Optics* **17**, 028001 (2012).
104. D. D. Lo, M. A. Mackanos, M. T. Chung, J. S. Hyun, D. T. Montoro, M. Grova, C. Liu, J. Wang, D. Palanker, A. J. Connolly, M. T. Longaker, C. H. Contag, and D. C. Wan, "Femtosecond plasma

- mediated laser ablation has advantages over mechanical osteotomy of cranial bone," *Lasers in Surgery and Medicine* **44**, 805-814 (2012).
105. S. Ashforth, M. Simpson, O. Bodley, and R. Oosterbeek, *Ultrashort pulse laser interactions with cortical bone tissue for applications in orthopaedic surgery*, SPIE LASE (SPIE, 2015), Vol. 9355.
 106. B. Girard, D. Yu, M. R. Armstrong, B. C. Wilson, C. M. L. Clokie, and R. J. D. Miller, "Effects of femtosecond laser irradiation on osseous tissues," *Lasers in Surgery and Medicine* **39**, 273-285 (2007).
 107. J. Neev, L. B. D. Silva, M. D. Feit, M. D. Perry, A. M. Rubenchik, and B. C. Stuart, "Ultrashort pulse lasers for hard tissue ablation," *IEEE Journal of Selected Topics in Quantum Electronics* **2**, 790-800 (1996).
 108. L. Canguero, R. Mário Correia da Silva Vilar, A. Botelho do Rego, and V. S. Muralha, "Femtosecond laser ablation of bovine cortical bone," *Journal of Biomedical Optics* **17**, 125005 (2012).
 109. L. T. Canguero and R. Vilar, "Influence of the pulse frequency and water cooling on the femtosecond laser ablation of bovine cortical bone," *Applied Surface Science* **283**, 1012-1017 (2013).
 110. R. S. Marjoribanks, C. Dille, J. E. Schoenly, L. McKinney, A. Mordovanakis, P. Kaifosh, P. Forrester, Z. Qian, A. Covarrubias, Y. Feng, and L. Lilge, "Ablation and thermal effects in treatment of hard and soft materials and biotissues using ultrafast-laser pulse-train bursts," *Photonics & Lasers in Medicine* **1**, 155 (2012).
 111. V. Wieger, S. Zoppel, and E. Wintner, "Ultrashort pulse laser osteotomy," *Laser Physics* **17**, 438-442 (2007).
 112. Y. Song and Y. Guan, *Magnetic-field-assisted femtosecond laser drilling of bone in ambient environment*, Applied Optics and Photonics China (AOPC2019) (SPIE, 2019), Vol. 11333.
 113. A. Charlton, M. R. Dickinson, T. A. King, and A. J. Freemont, "Erbium-YAG and holmium-YAG laser ablation of bone," *Lasers in Medical Science* **5**, 365-373 (1990).
 114. M. Buchelt, H.-P. Kutschera, T. Katterschafka, H. Kiss, S. Lang, R. Beer, and U. Losert, "Erb:YAG and Hol:YAG Laser Osteotomy: The Effect of Laser Ablation on Bone Healing," *Lasers in Surgery and Medicine* **15**, 373-381 (1994).
 115. T. Bilici, S. Mutlu, H. Kalaycioglu, A. Kurt, A. Sennaroglu, and M. Gulsoy, "Development of a thulium (Tm:YAP) laser system for brain tissue ablation," *Lasers in Medical Science* **26**, 699-706 (2011).
 116. H. Alagha and M. Gülsoy, "Photothermal ablation of liver tissue with 1940-nm thulium fiber laser: an *in vivo* study on lamb liver," *Journal of Biomedical Optics* **21**, 015007 (2016).
 117. L. Gholami, S. A. Moghaddam, M. A. Rigi Ladiz, Z. Molai Manesh, H. Hashemzahi, A. Fallah, and N. Gutknecht, "Comparison of gingival depigmentation with Er,Cr:YSGG laser and surgical stripping, a 12-month follow-up," *Lasers in Medical Science* **33**, 1647-1656 (2018).
 118. J. C. Esteves, A. P. de Souza Faloni, P. D. Macedo, P. B. Nakata, R. A. Chierici Marcantonio, G. Intini, and E. Marcantonio Jr., "Effects on Bone Repair of Osteotomy With Drills or With Erbium, Chromium: Yttrium-Scandium-Gallium-Garnet Laser: Histomorphometric and Immunohistochemical Study," *Journal of Periodontology* **87**, 452-460 (2016).
 119. K. Shinkai, M. Takada, S. Kawashima, M. Suzuki, and S. Suzuki, "Effects of the percentage of air/water in spray on the efficiency of tooth ablation with erbium, chromium: yttrium-scandium-gallium-garnet (Er, Cr: YSGG) laser irradiation," *Lasers in Medical Science* **34**, 99-105 (2019).
 120. K. Shinkai, M. Suzuki, and S. Suzuki, "Effects of intensity and frequency of erbium, chromium:yttrium-scandium-gallium-garnet (Er,Cr:YSGG) laser irradiation on tooth ablation," *Lasers in Dental Science* **4**, 123-129 (2020).
 121. J.-I. Youn, P. Sweet, and G. M. Peavy, "A comparison of mass removal, thermal injury, and crater morphology of cortical bone ablation using wavelengths 2.79, 2.9, 6.1, and 6.45 μm ," *Lasers in Surgery and Medicine* **39**, 332-340 (2007).

122. K. Henn, G. G. Gubaidullin, J. Bongartz, J. Wahrburg, H. Roth, and M. Kunkel, "A spectroscopic approach to monitor the cut processing in pulsed laser osteotomy," *Lasers in Medical Science* **28**, 87-92 (2013).
123. N. M. Fried and D. Fried, "Comparison of Er:YAG and 9.6- μ m TE CO₂ lasers for ablation of skull tissue," *Lasers in Surgery and Medicine* **28**, 335-343 (2001).
124. K. Chan, N. Fried, and D. Fried, *Selective ablation of carious lesions using an integrated multispectral near-IR imaging system and a novel 9.3- μ m CO₂ laser*, SPIE BiOS (SPIE, 2018), Vol. 10473.
125. M. Ivanenko, M. Werner, S. Afilal, M. Klasing, and P. Hering, "Ablation of hard bone tissue with pulsed CO₂ lasers," *Medical Laser Application* **20**, 13-23 (2005).
126. A. G. Rad, H. Abbasi, and K. Golyari, "Fabrication and nonlinear refractive index measurement of colloidal silver nanoparticles," *International Journal of Applied Physics and Mathematics* **2**, 135 (2012).
127. H. Abbasi and A. Zam, "Optical Feedback Mechanism for Minimally Invasive Laserosteotome," in *The yearly meeting of the Biomedical Photonics Network 2019 (BMPN)*, (2019).
128. H. Abbasi and A. Zam, "LIBS for Smart Laserosteotomy," in (International Conference on Biomedical Photonics, 2018).
129. H. Abbasi, "Pilot ex vivo study of laser induced breakdown spectroscopy for hard and soft tissue differentiation as a feedback system for tissue-specific laser surgery," in *8th International Graduate Summer School Biophotonics '17*, (2017), 1-3.
130. S. Rupprecht, K. Tangermann-Gerk, S. Schultze-Mosgau, F. W. Neukam, and J. Ellrich, "Neurophysiological monitoring of alveolar nerve function during sensor-controlled Er:YAG laser corticotomy in rabbits," *Lasers in Surgery and Medicine* **36**, 186-192 (2005).
131. J. Yun, Y.-T. Hong, K.-H. Hong, and J.-H. Lee, "Ex vivo identification of thyroid cancer tissue using electrical impedance spectroscopy on a needle," *Sensors and Actuators B: Chemical* **261**, 537-544 (2018).
132. S. M. Rahman, M. A. Ali, O. Altwijri, M. Alqahtani, N. Ahmed, and N. U. Ahamed, "Ensemble-Based Machine Learning Algorithms for Classifying Breast Tissue Based on Electrical Impedance Spectroscopy," in *International Conference on Applied Human Factors and Ergonomics*, (Springer, 2019), 260-266.
133. J. Kim, M. A. Abbasi, T. Kim, K. D. Park, and S. Cho, "Lock-in Amplifier-Based Impedance Detection of Tissue Type Using a Monopolar Injection Needle," *Sensors* **19**, 4614 (2019).
134. M. Apelt, G. Ugen, L. Häni, A. Raabe, J. Ansó, and K. Seidel, "Tissue Impedance Spectroscopy to Guide Resection of Brain Tumours," in *International Conference on Electrical Bioimpedance*, (Springer, 2019), 133-138.
135. R. D. Butler and R. J. Halter, "Gauging electrical properties of bone with a bioimpedance-sensing drill," *Physiological Measurement* **40**, 01NT01 (2019).
136. L. F. E. Huerta-Nuñez, G. Gutierrez-Iglesias, A. Martinez-Cuazitl, M. M. Mata-Miranda, V. D. Alvarez-Jiménez, V. Sánchez-Monroy, A. Golberg, and C. A. González-Díaz, "A biosensor capable of identifying low quantities of breast cancer cells by electrical impedance spectroscopy," *Scientific Reports* **9**, 6419 (2019).
137. Z. Cheng, A. L. C. Carobbio, L. Soggiu, M. Migliorini, L. Guastini, F. Mora, M. Fragale, A. Ascoli, S. Africano, D. G. Caldwell, F. R. M. Canevari, G. Parrinello, G. Peretti, and L. S. Mattos, "SmartProbe: a bioimpedance sensing system for head and neck cancer tissue detection," *Physiological Measurement* **41**, 054003 (2020).
138. M. Adank, J. Fleischer, J. Dankelman, and B. H. Hendriks, "Real-time oncological guidance using diffuse reflectance spectroscopy in electrosurgery: the effect of coagulation on tissue discrimination," *Journal of Biomedical Optics* **23**, 115004 (2018).

139. S. A. Amiri, C. M. Van Gent, J. Dankelman, and B. H. W. Hendriks, "Intraoperative tumor margin assessment using diffuse reflectance spectroscopy: the effect of electrosurgery on tissue discrimination using ex vivo animal tissue models," *Biomedical Optics Express* **11**, 2402-2415 (2020).
140. F. Mollerus, "The integration of diffuse reflectance spectroscopy into the electrosurgical knife used during breast-conserving surgery: Determining and overcoming the challenge of tissue debris adhering to the 'smart' electrosurgical knife," (2018).
141. C. van Gent, "The Integration of Diffuse Reflectance Spectroscopy into the Electrosurgical Knife: Clarifying and Preventing Diffuse Reflectance Spectroscopy Signal Deterioration during Use of the Smart Electrosurgical Knife," (2019).
142. B. H. W. Hendriks, T. J. M. Ruers, G. W. Lucassen, M. Mueller, J. J. Horikx, W. C. J. Bierhoff, J. Klewer, M. Van Der Voort, N. N. Kahya, and C. Reich, "Electro-surgical system, an electro-surgical device, and a method for operating an electro-surgical system," (Google Patents, 2018).
143. W. C. J. Bierhoff, B. H. W. Hendriks, F. M. A. M. Van Gaal, T. M. Bydlon, V. V. Pully, and C. Reich, "Optical tissue feedback device for an electrosurgical device," (Google Patents, 2018).
144. F. Stelzle, K. Tangermann-Gerk, W. Adler, A. Zam, M. Schmidt, A. Douplik, and E. Nkenke, "Diffuse reflectance spectroscopy for optical soft tissue differentiation as remote feedback control for tissue-specific laser surgery," *Lasers in Surgery and Medicine* **42**, 319-325 (2010).
145. F. Stelzle, A. Zam, W. Adler, A. Douplik, K. Tangermann-Gerk, E. Nkenke, F. W. Neukam, and M. Schmidt, "Diffuse reflectance spectroscopy for optical nerve identification: Preliminary ex vivo results for feedback controlled oral and maxillofacial laser surgery," *Physics Procedia* **5**, 647-654 (2010).
146. S. Keller, N. Bibinov, A. Neugebauer, and P. Awakowicz, "Electrical and spectroscopic characterization of a surgical argon plasma discharge," *Journal of Physics D: Applied Physics* **46**, 025402 (2012).
147. I. Bürger, N. Bibinov, A. Neugebauer, M. Enderle, and P. Awakowicz, "Electrical, optical and spectroscopic characterisation of a radio frequency discharge used for electrosurgical cutting," *Plasma Processes and Polymers* **14**, 1600229 (2017).
148. D. Spether, M. Scharpf, J. Hennenlotter, C. Schwentner, A. Neugebauer, D. Nüßle, K. Fischer, H. Zappe, A. Stenzl, F. Fend, A. Seifert, and M. Enderle, "Real-time tissue differentiation based on optical emission spectroscopy for guided electrosurgical tumor resection," *Biomedical Optics Express* **6**, 1419-1428 (2015).
149. I. Bürger, M. Scharpf, J. Hennenlotter, D. Nüßle, D. Spether, A. Neugebauer, N. Bibinov, A. Stenzl, F. Fend, M. Enderle, and P. Awakowicz, "Tissue differentiation by means of high resolution optical emission spectroscopy during electrosurgical intervention," *Journal of Physics D: Applied Physics* **50**, 035401 (2016).
150. F. Cornaz, S. Valet, and D. C. Meyer, "Spectroscopic characterization of tissue and liquids during arthroscopic radio-frequency ablation," *Medical Physics* **47**, 3703-3709 (2020).
151. A. Kontunen, M. Karjalainen, J. Lekkala, A. Roine, and N. Oksala, "Tissue Identification in a Porcine Model by Differential Ion Mobility Spectrometry Analysis of Surgical Smoke," *Annals of Biomedical Engineering* **46**, 1091-1100 (2018).
152. M. Sutinen, A. Kontunen, M. Karjalainen, J. Kiiski, J. Hannus, T. Tolonen, A. Roine, and N. Oksala, "Identification of breast tumors from diathermy smoke by differential ion mobility spectrometry," *European Journal of Surgical Oncology* **45**, 141-146 (2019).
153. G. Sukhikh, V. Chagovets, X. Wang, V. Rodionov, V. Kometova, A. Tokareva, A. Kononikhin, N. Starodubtseva, K. Chingin, and H. Chen, "Combination of Low-Temperature Electrosurgical Unit and Extractive Electrospray Ionization Mass Spectrometry for Molecular Profiling and Classification of Tissues," *Molecules* **24**, 2957 (2019).

154. J. Balog, L. Sasi-Szabó, J. Kinross, M. R. Lewis, L. J. Muirhead, K. Veselkov, R. Mirnezami, B. Dezső, L. Damjanovich, A. Darzi, J. K. Nicholson, and Z. Takáts, "Intraoperative Tissue Identification Using Rapid Evaporative Ionization Mass Spectrometry," *Science Translational Medicine* **5**, 194ra193-194ra193 (2013).
155. E. R. St John, J. Balog, J. S. McKenzie, M. Rossi, A. Covington, L. Muirhead, Z. Bodai, F. Rosini, A. V. M. Speller, S. Shousha, R. Ramakrishnan, A. Darzi, Z. Takats, and D. R. Leff, "Rapid evaporative ionisation mass spectrometry of electrosurgical vapours for the identification of breast pathology: towards an intelligent knife for breast cancer surgery," *Breast Cancer Research* **19**, 59 (2017).
156. D. L. Phelps, J. Balog, L. F. Gildea, Z. Bodai, A. Savage, M. A. El-Bahrawy, A. V. M. Speller, F. Rosini, H. Kudo, J. S. McKenzie, R. Brown, Z. Takáts, and S. Ghaem-Maghami, "The surgical intelligent knife distinguishes normal, borderline and malignant gynaecological tissues using rapid evaporative ionisation mass spectrometry (REIMS)," *British Journal of Cancer* **118**, 1349-1358 (2018).
157. J. Alexander, L. Gildea, J. Balog, A. Speller, J. McKenzie, L. Muirhead, A. Scott, C. Kontovounisios, S. Rasheed, J. Teare, J. Hoare, K. Veselkov, R. Goldin, P. Tekkis, A. Darzi, J. Nicholson, J. Kinross, and Z. Takats, "A novel methodology for in vivo endoscopic phenotyping of colorectal cancer based on real-time analysis of the mucosal lipidome: a prospective observational study of the iKnife," *Surgical Endoscopy* **31**, 1361-1370 (2017).
158. B. Fatou, P. Saudemont, E. Leblanc, D. Vinatier, V. Mesdag, M. Wisztorski, C. Focsa, M. Salzert, M. Ziskind, and I. Fournier, "In vivo Real-Time Mass Spectrometry for Guided Surgery Application," *Scientific Reports* **6**, 25919 (2016).
159. N. Ogrinc, P. Saudemont, J. Balog, Y.-M. Robin, J.-P. Gimeno, Q. Pascal, D. Tierny, Z. Takats, M. Salzert, and I. Fournier, "Water-assisted laser desorption/ionization mass spectrometry for minimally invasive in vivo and real-time surface analysis using SpiderMass," *Nature Protocols* **14**, 3162-3182 (2019).
160. M. Wurlitzer, E. Hessling, K. Rinas, M. Fuh, H. Petersen, F. Ricklefs, K. Lamszus, J. Regelsberger, S. Maier, S. Kruber, N.-O. Hansen, R. Müller, and H. Schlüter, "Mass Spectrometric Lipid Profiles of Picosecond Infrared Laser-Generated Tissue Aerosols Discriminate Different Brain Tissues," *Lasers in Surgery and Medicine* **52**, 228-234 (2020).
161. Y. Gündoğdu and H. Ş. Kiliç, "A new method for investigation of different tissues using femtosecond laser mass spectrometry," *Photomedicine and laser surgery* **36**, 548-554 (2018).
162. Y. Gündoğdu, H. Alptekin, P. Karabağlı, M. Şahin, and H. Ş. Kiliç, "Discrimination of cancerous and healthy colon tissues: A new laser-based method," *Lasers in Surgery and Medicine* **51**, 363-369 (2019).
163. P. Saudemont, J. Quanicco, Y.-M. Robin, A. Baud, J. Balog, B. Fatou, D. Tierny, Q. Pascal, K. Minier, M. Pottier, C. Focsa, M. Ziskind, Z. Takats, M. Salzert, and I. Fournier, "Real-Time Molecular Diagnosis of Tumors Using Water-Assisted Laser Desorption/Ionization Mass Spectrometry Technology," *Cancer Cell* **34**, 840-851.e844 (2018).
164. M. F. Keating, J. Zhang, C. L. Feider, S. Retailleau, R. Reid, A. Antaris, B. Hart, G. Tan, T. E. Milner, K. Miller, and L. S. Eberlin, "Integrating the MasSpec Pen to the da Vinci Surgical System for In Vivo Tissue Analysis during a Robotic Assisted Porcine Surgery," *Analytical Chemistry* **92**, 11535-11542 (2020).
165. H. Nguendon Kenhagho, G. Rauter, R. Guzman, P. C. Cattin, and A. Zam, *Comparison of acoustic shock waves generated by micro and nanosecond lasers for a smart laser surgery system*, SPIE BiOS (SPIE, 2018), Vol. 10484.
166. H. Nguendon Kenhagho, S. Shevchik, F. Saeidi, N. Faivre, B. Meylan, G. Rauter, R. Guzman, P. Cattin, K. Wasmer, and A. Zam, "Characterization of ablated bone and muscle for long-pulsed laser ablation in dry and wet conditions," *Materials* **12**, 1338 (2019).

167. H. Nguendon Kenhagho, F. Canbaz, T. E. Gomez Alvarez-Arenas, R. Guzman, P. Cattin, and A. Zam, "Machine Learning-Based Optoacoustic Tissue Classification Method for Laser Osteotomes Using an Air-Coupled Transducer," *Lasers in Surgery and Medicine* (2020).
168. H. K. Nguendon, N. Faivre, B. Meylan, S. Shevchik, G. Rauter, R. Guzman, P. C. Cattin, K. Wasmer, and A. E. D. L. Zam, "Characterization of ablated porcine bone and muscle using laser-induced acoustic wave method for tissue differentiation," in *Medical Laser Applications and Laser-Tissue Interactions VIII*, SPIE Proceedings (Optical Society of America, 2017), 104170N.
169. M. Morris, P. Matousek, M. Towrie, A. Parker, A. Goodship, and E. Draper, "Kerr-gated time-resolved Raman spectroscopy of equine cortical bone tissue," *Journal of Biomedical Optics* **10**, 014014 (2005).
170. E. R. Draper, M. D. Morris, N. P. Camacho, P. Matousek, M. Towrie, A. W. Parker, and A. E. Goodship, "Novel Assessment of Bone Using Time-Resolved Transcutaneous Raman Spectroscopy," *Journal of Bone and Mineral Research* **20**, 1968-1972 (2005).
171. F. Légaré, C. L. Evans, F. Ganikhanov, and X. S. Xie, "Towards CARS Endoscopy," *Optics Express* **14**, 4427-4432 (2006).
172. X. S. Xie, F. Légaré, F. Ganikhanov, and C. Evans, "System and method for coherent anti-Stokes Raman scattering endoscopy," (Google Patents, 2008).
173. A. J. Au - Nichols and C. L. Au - Evans, "Video-rate Scanning Confocal Microscopy and Microendoscopy," *JoVE*, e3252 (2011).
174. G. C. Dacey, "Optical Masers in Science and Technology," *Science* **135**, 71-74 (1962).
175. F. Breech and L. Cross, "Optical microemission stimulated by a ruby maser," *Appl. Spectrosc* **16**, 1 (1962).
176. M. Baudelet and B. W. Smith, "The first years of laser-induced breakdown spectroscopy," *Journal of Analytical Atomic Spectrometry* **28**, 624-629 (2013).
177. T. R. Loree and L. J. Radziemski, "Laser-induced breakdown spectroscopy: Time-integrated applications," *Plasma Chemistry and Plasma Processing* **1**, 271-279 (1981).
178. L. J. Radziemski and T. R. Loree, "Laser-induced breakdown spectroscopy: Time-resolved spectrochemical applications," *Plasma Chemistry and Plasma Processing* **1**, 281-293 (1981).
179. V. Palleschi, "Laser-induced breakdown spectroscopy: principles of the technique and future trends," *ChemTexts* **6**, 18 (2020).
180. K. Lotfy, S. M. Khalil, and H. A. El-Raheem, "Inactivation by helium cold atmospheric pressure plasma for Escherichia coli and Staphylococcus aureus," *Journal of Theoretical and Applied Physics* **14**, 37-45 (2020).
181. Z. Matinzadeh, F. Shahgoli, H. Abbasi, M. Ghoranneviss, and M. K. Salem, "Degradation of bromophenol blue molecule during argon plasma jet irradiation," *Journal of Theoretical and Applied Physics* **11**, 97-102 (2017).
182. H. Abbasi, M. Nazeri, S. Mirpour, and N. J. Farahani, "Measuring electron density, electric field and temperature of a micro-discharge air plasma jet using optical emission spectroscopy," in *2015 2nd International Conference on Knowledge-Based Engineering and Innovation (KBEI)*, 2015), 1139-1141.
183. Z. Matinzadeh, F. Shahgoli, H. Abbasi, M. Ghoranneviss, and M. K. Salem, "Decomposition of Bromocresol Green Using a Nonthermal Atmospheric Pressure Plasma Jet," *Proceedings* **67**, 14 (2020).
184. G. Cristoforetti, A. De Giacomo, M. Dell'Aglio, S. Legnaioli, E. Tognoni, V. Palleschi, and N. Omenetto, "Local Thermodynamic Equilibrium in Laser-Induced Breakdown Spectroscopy: Beyond the McWhirter criterion," *Spectrochimica Acta Part B: Atomic Spectroscopy* **65**, 86-95 (2010).
185. I. Mehboob, J. Iqbal, M. Rafique, M. A. Baig, and R. Ahmed, "Optical Spectroscopic Study of Laser-Produced Aluminum Plasma," *IEEE Transactions on Plasma Science* **46**, 2920-2929 (2018).

186. S. Messaoud Aberkane, A. Safi, A. Botto, B. Campanella, S. Legnaioli, F. Poggialini, S. Raneri, F. Rezaei, and V. Palleschi, "Laser-Induced Breakdown Spectroscopy for Determination of Spectral Fundamental Parameters," *Applied Sciences* **10**, 4973 (2020).
187. F. J. Fortes, J. Moros, P. Lucena, L. M. Cabalín, and J. J. Laserna, "Laser-Induced Breakdown Spectroscopy," *Analytical Chemistry* **85**, 640-669 (2013).
188. E. Tognoni, V. Palleschi, M. Corsi, and G. Cristoforetti, "Quantitative micro-analysis by laser-induced breakdown spectroscopy: a review of the experimental approaches," *Spectrochimica Acta Part B: Atomic Spectroscopy* **57**, 1115-1130 (2002).
189. J. E. Sansonetti and W. C. Martin, "Handbook of Basic Atomic Spectroscopic Data," *Journal of Physical and Chemical Reference Data* **34**, 1559-2259 (2005).
190. S. Maurice, S. M. Clegg, R. C. Wiens, O. Gasnault, W. Rapin, O. Forni, A. Cousin, V. Sautter, N. Mangold, and L. Le Deit, "ChemCam activities and discoveries during the nominal mission of the Mars Science Laboratory in Gale crater, Mars," *Journal of Analytical Atomic Spectrometry* **31**, 863-889 (2016).
191. S. J. Rehse, H. Salimnia, and A. W. Miziolek, "Laser-induced breakdown spectroscopy (LIBS): an overview of recent progress and future potential for biomedical applications," *Journal of Medical Engineering & Technology* **36**, 77-89 (2012).
192. R. Gaudio, N. Melikechi, Z. A. Abdel-Salam, M. A. Harith, V. Palleschi, V. Motto-Ros, and B. Busser, "Laser-induced breakdown spectroscopy for human and animal health: A review," *Spectrochimica Acta Part B: Atomic Spectroscopy* **152**, 123-148 (2019).
193. K. Bardarov, I. Buchvarov, T. Yordanova, and P. Georgiev, *Laser-induced break down spectroscopy for quantitative analysis of electrolytes (Na, K, Ca, Mg) in human blood serum*, International Conference on Quantum, Nonlinear, and Nanophotonics 2019 (ICQNN 2019) (SPIE, 2019), Vol. 11332.
194. A. Khumaeni, W. S. Budi, A. Y. Wardaya, H. Niki, and K. H. Kurniawan, "Identification of elements in human blood serum using laser-induced breakdown spectroscopy," *AIP Conference Proceedings* **2202**, 020001 (2019).
195. N. Melikechi, H. Ding, S. Rock, A. Marcano O., and D. Connolly, *Laser-induced breakdown spectroscopy of whole blood and other liquid organic compounds*, SPIE BiOS (SPIE, 2008), Vol. 6863.
196. X. Chen, X. Li, S. Yang, X. Yu, and A. Liu, "Discrimination of lymphoma using laser-induced breakdown spectroscopy conducted on whole blood samples," *Biomedical Optics Express* **9**, 1057-1068 (2018).
197. A. El-Hussein, A. K. Kassem, H. Ismail, and M. A. Harith, "Exploiting LIBS as a spectrochemical analytical technique in diagnosis of some types of human malignancies," *Talanta* **82**, 495-501 (2010).
198. S. Moncayo, F. Trichard, B. Busser, M. Sabatier-Vincent, F. Pelascini, N. Pinel, I. Templier, J. Charles, L. Sancey, and V. Motto-Ros, "Multi-elemental imaging of paraffin-embedded human samples by laser-induced breakdown spectroscopy," *Spectrochimica Acta Part B: Atomic Spectroscopy* **133**, 40-44 (2017).
199. A. Kumar, F.-Y. Yueh, J. P. Singh, and S. Burgess, "Characterization of malignant tissue cells by laser-induced breakdown spectroscopy," *Appl. Opt.* **43**, 5399-5403 (2004).
200. J. Kaiser, K. Novotný, M. Z. Martin, A. Hrdlička, R. Malina, M. Hartl, V. Adam, and R. Kizek, "Trace elemental analysis by laser-induced breakdown spectroscopy—Biological applications," *Surface Science Reports* **67**, 233-243 (2012).
201. M. D. Adamson and S. J. Rehse, "Detection of trace Al in model biological tissue with laser-induced breakdown spectroscopy," *Appl. Opt.* **46**, 5844-5852 (2007).
202. E. M. Emara, H. Imam, M. A. Hassan, and S. H. Elnaby, "Biological application of laser induced breakdown spectroscopy technique for determination of trace elements in hair," *Talanta* **117**, 176-183 (2013).

203. Z. A. Abdel-Salam, S. A. M. Abdel-Salam, I. I. Abdel-Mageed, and M. A. Harith, "Evaluation of proteins in sheep colostrum via laser-induced breakdown spectroscopy and multivariate analysis," *Journal of Advanced Research* **15**, 19-25 (2019).
204. Y. Moon, J. H. Han, J. J. Lee, and S. Jeong, "Influence of water content on the laser-induced breakdown spectroscopy analysis of human cell pellet," *Spectrochimica Acta Part B: Atomic Spectroscopy* **114**, 27-33 (2015).
205. A. C. Samuels, F. C. DeLucia, K. L. McNesby, and A. W. Miziolek, "Laser-induced breakdown spectroscopy of bacterial spores, molds, pollens, and protein: initial studies of discrimination potential," *Appl. Opt.* **42**, 6205-6209 (2003).
206. M. Mordmueller, C. Bohling, A. John, and W. Schade, *Rapid test for the detection of hazardous microbiological material*, SPIE Security + Defence (SPIE, 2009), Vol. 7484.
207. C. A. Munson, F. C. De Lucia, T. Piehler, K. L. McNesby, and A. W. Miziolek, "Investigation of statistics strategies for improving the discriminating power of laser-induced breakdown spectroscopy for chemical and biological warfare agent simulants," *Spectrochimica Acta Part B: Atomic Spectroscopy* **60**, 1217-1224 (2005).
208. J. D. Hybl, G. A. Lithgow, and S. G. Buckley, "Laser-Induced Breakdown Spectroscopy Detection and Classification of Biological Aerosols," *Appl. Spectrosc.* **57**, 1207-1215 (2003).
209. F.-Y. Yueh, H. Zheng, J. P. Singh, and S. Burgess, "Preliminary evaluation of laser-induced breakdown spectroscopy for tissue classification," *Spectrochimica Acta Part B: Atomic Spectroscopy* **64**, 1059-1067 (2009).
210. R. K. Gill, *Development of a Feedback Control System for Femtosecond Pulsed Laser Surgery* (University of California, Davis, 2015).
211. D. E. Lewis, J. Martinez, C. A. Akpovo, L. Johnson, A. Chauhan, and M. D. Edington, "Discrimination of bacteria from Jamaican bauxite soils using laser-induced breakdown spectroscopy," *Analytical and Bioanalytical Chemistry* **401**, 2225 (2011).
212. S. Morel, N. Leone, P. Adam, and J. Amouroux, "Detection of bacteria by time-resolved laser-induced breakdown spectroscopy," *Appl. Opt.* **42**, 6184-6191 (2003).
213. S. J. Rehse, J. Diedrich, and S. Palchadhuri, "Identification and discrimination of *Pseudomonas aeruginosa* bacteria grown in blood and bile by laser-induced breakdown spectroscopy," *Spectrochimica Acta Part B: Atomic Spectroscopy* **62**, 1169-1176 (2007).
214. M. Baudelet, L. Guyon, J. Yu, J.-P. Wolf, T. Amodeo, E. Fréjafon, and P. Laloi, "Femtosecond time-resolved laser-induced breakdown spectroscopy for detection and identification of bacteria: A comparison to the nanosecond regime," *Journal of Applied Physics* **99**, 084701 (2006).
215. H. Abbasi, M. Bani, and M. Nazeri, "Resolving Spectral Lines Using a Simple Spectrometer with Sub-angstrom Accuracy," in (The second national electronic conference on physics applications, 2014),
216. W. Demtröder, "Spectroscopic Instrumentation," in *Laser Spectroscopy 1* (Springer, 2014), pp. 113-256.
217. M. A. Bani, M. Nazeri, H. Abbasi, and A. Sajedi, "External Cavity Tunability of Some NIR Semiconductor Lasers," *Óptica pura y aplicada* **51**, 50014 (2018).
218. A. Balooch, M. Nazeri, and H. Abbasi, *Implementation of webcam-based hyperspectral imaging system*, SPIE OPTO (SPIE, 2018), Vol. 10539.
219. H. Abbasi and M. Nazeri, "LIF spectroscopy of fruits: study of excitation wavelength independence," in *The third Iranian Conference on Engineering Electromagnetic (ICEEM)*, 2014).
220. H. Abbasi, M. Nazeri, and S. A. Mireei, "Design and development of a LabVIEW-based LED-induced fluorescence spectroscopy system with applications in non-destructive quality assessment of agricultural products," *Journal of Physics: Conference Series* **672**, 012010 (2016).
221. K.-Y. Zang, Y. Yao, E.-T. Hu, A.-Q. Jiang, Y.-X. Zheng, S.-Y. Wang, H.-B. Zhao, Y.-M. Yang, O. Yoshie, Y.-P. Lee, D. W. Lynch, and L.-Y. Chen, "A High-Performance Spectrometer with Two Spectral Channels Sharing the Same BSI-CMOS Detector," *Scientific Reports* **8**, 12660 (2018).

222. T. Han, W.-M. Ni, P. Zhou, H.-Y. You, J.-H. Jia, S.-Y. Wang, L.-Y. Chen, and D. W. Lynch, "A new spectrometer using multiple gratings with a two-dimensional charge-coupled diode array detector," *Review of Scientific Instruments* **74**, 2973-2976 (2003).
223. M.-H. Liu, S.-X. Pan, Y.-R. Chen, Y.-F. Wu, Q.-Y. Cai, P.-H. Mao, Y.-X. Zheng, and L.-Y. Chen, "Path-folded infrared spectrometer consisting of 10 sub-gratings and a two-dimensional InGaAs detector," *Optics express* **17**, 14956-14966 (2009).
224. A.-Q. Jiang, K.-Y. Zang, H.-T. Tu, J.-K. Chen, W.-J. Lu, O. Yoshie, X.-P. Wang, X.-D. Xiang, Y.-P. Lee, B. Chen, Y.-X. Zheng, S.-Y. Wang, H.-B. Zhao, Y.-M. Yang, and L.-Y. Chen, "Ultrahigh-resolution spectrometer based on 19 integrated gratings," *Scientific Reports* **9**, 10211 (2019).
225. Y.-R. Chen, B. Sun, T. Han, Y.-F. Kong, C.-H. Xu, P. Zhou, X.-F. Li, S.-Y. Wang, Y.-X. Zheng, and L.-Y. Chen, "Densely folded spectral images of a CCD spectrometer working in the full 200–1000 nm wavelength range with high resolution," *Optics express* **13**, 10049-10054 (2005).
226. G. Y. Belay, W. Hoving, A. van der Put, M. Vervaeke, J. Van Erps, H. Thienpont, and H. Ottevaere, "Miniaturized broadband spectrometer based on a three-segment diffraction grating for spectral tissue sensing," *Optics and Lasers in Engineering* **134**, 106157 (2020).
227. T. Eversberg and K. Vollmann, "Fundamentals of echelle spectroscopy," in *Spectroscopic Instrumentation* (Springer, 2015), pp. 193-227.
228. M. Hoehse, D. Mory, S. Florek, F. Weritz, I. Gornushkin, and U. Panne, "A combined laser-induced breakdown and Raman spectroscopy Echelle system for elemental and molecular microanalysis," *Spectrochimica Acta Part B: Atomic Spectroscopy* **64**, 1219-1227 (2009).
229. M. Sabsabi, V. Detalle, M. A. Harith, W. Tawfik, and H. Imam, "Comparative study of two new commercial echelle spectrometers equipped with intensified CCD for analysis of laser-induced breakdown spectroscopy," *Appl. Opt.* **42**, 6094-6098 (2003).
230. P. Fichet, D. Menut, R. Brennetot, E. Vors, and A. Rivoallan, "Analysis by laser-induced breakdown spectroscopy of complex solids, liquids, and powders with an echelle spectrometer," *Appl. Opt.* **42**, 6029-6035 (2003).
231. S. Florek, C. Haisch, M. Okruss, and H. Becker-Ross, "A new, versatile echelle spectrometer relevant to laser induced plasma applications," *Spectrochimica Acta Part B: Atomic Spectroscopy* **56**, 1027-1034 (2001).
232. H. Abbasi, G. Rauter, R. Guzman, P. Cattin, and A. Zam, *Design and implementation of a compact high-throughput echelle spectrometer using off-the-shelf off-axis parabolic mirrors for analysis of biological samples by LIBS (Conference Presentation)*, SPIE Optical Metrology (SPIE, 2019), Vol. 11060.
233. K. Kaleris, Y. Orphanos, M. Bakarezos, V. Dimitriou, M. Tatarakis, J. Mourjopoulos, and N. A. Papadogiannis, "On the correlation of light and sound radiation following laser-induced breakdown in air," *Journal of Physics D: Applied Physics* **53**, 435207 (2020).
234. M. Nazeri, A. E. Majd, R. Massudi, S. H. Tavassoli, A. Mesbahinia, and H. Abbasi, "Laser-Induced Breakdown Spectroscopy Via the Spatially Resolved Technique Using Non-Gated Detector," *Journal of Russian Laser Research* **37**, 164-171 (2016).
235. A. J. R. Bauer and S. G. Buckley, "Novel Applications of Laser-Induced Breakdown Spectroscopy," *Appl. Spectrosc.* **71**, 553-566 (2017).
236. M. Mueller, I. B. Gornushkin, S. Florek, D. Mory, and U. Panne, "Approach to Detection in Laser-Induced Breakdown Spectroscopy," *Analytical Chemistry* **79**, 4419-4426 (2007).
237. S. K. Hussain Shah, J. Iqbal, P. Ahmad, M. U. Khandaker, S. Haq, and M. Naeem, "Laser induced breakdown spectroscopy methods and applications: A comprehensive review," *Radiation Physics and Chemistry* **170**, 108666 (2020).
238. H. Abbasi, G. Rauter, R. Guzman, P. C. Cattin, and A. Zam, "Toward finding the best machine learning classifier for LIBS-based tissue differentiation," in (First International Conference on Biomedical Engineering (ICBE), 2018).

239. H. Abbasi, G. Rauter, R. Guzman, P. C. Cattin, and A. Zam, "LIBS for real-time monitoring of laser-induced thermal damage in laserosteotomy: from dehydration to full carbonization," in 10th Euro-Mediterranean Symposium on Laser-Induced Breakdown Spectroscopy (EMSLIBS, 2019).
240. C. Duverney, H. Abbasi, L. M. Beltrán Bernal, T. Stauber, J. G. Snedeker, P. C. Cattin, A. Zam, and G. Rauter, "Robot- and Laser-Assisted Bio-Sample Preparation: Development of an Integrated, Intuitive System," in *New Trends in Medical and Service Robotics* (Springer International Publishing, 2021), 219-226.